Study on CVD Growth of non-van der Waals 2D Bi_2O_2Se and its Hybrid Integration for Optoelectronic Applications

A Thesis Submitted to
Indian Institute of Technology Guwahati
For the Degree of
Doctor of Philosophy

By
MD TARIK HOSSAIN

Department of Physics
Indian Institute of Technology Guwahati
Guwahati-781039, India
July 2023

Dedicated to
My beloved family

Department of Physics
Indian Institute of Technology Guwahati
Guwahati-781039, India

STATEMENT

The work contained in the thesis entitled "**Study on CVD Growth of non-van der Waals 2D Bi_2O_2Se and its Hybrid Integration for Optoelectronic Applications**" has been carried out by me at the Indian Institute of Technology Guwahati under the supervision of **Prof. P. K. Giri**, Professor, Department of Physics and Centre for Nanotechnology, Indian Institute of Technology Guwahati. This work has not been submitted elsewhere for the award of any degree.

Md Tarik Hossain

Roll No. - **186121014**

Senior Research Fellow
Department of Physics
Indian Institute of Technology Guwahati
Guwahati-781039, India

Prof. P. K. Giri
Professor
Department of Physics
and Centre for Nanotechnology
Indian Institute of Technology Guwahati
Guwahati-781039, India
Phone: ***+91 361 2582703****, Fax:* ***+91 361 2690762***
Email: giri@iitg.ac.in

CERTIFICATE

This is to certify that the work contained in the thesis entitled " **Study on CVD Growth of non-van der Waals 2D Bi_2O_2Se and its Hybrid Integration for Optoelectronic Applications**" has been carried out by **Mr. Md Tarik Hossain** at Indian Institute of Technology Guwahati under my supervision. This work has not been submitted elsewhere for the award of any degree.

Prof. P. K. Giri

Thesis supervisor

ACKNOWLEDGEMENT

This thesis evolves into a reality with numerous people's kind support and encouragement. I am pleased to thank those persons for their assistance, support, and inspiration.

First and foremost, I would like to express my sincere gratitude to my thesis supervisor, Prof. P. K. Giri, for his inspiring guidance, valuable discussion, constant support, and helpful suggestions. I sincerely thank him for allowing me to work under his guidance. His fruitful conversation, necessary consent, consistent motivation, and priceless tips made the completion of my Ph.D. possible. His vast wisdom and devotion to science have greatly inspired me and shaped my perception of scientific research. I also thank him for providing me full liberty in my research work and the necessary arrangements, laboratory facilities, and moral support throughout my Ph.D. work to achieve the goal.

I sincerely thank my Doctoral Committee members, Prof. A. K. Sarma, Prof. U. N. Maiti, and Prof. P. S. G. Pattader, for their routine review of my work, constructive comments, and invaluable suggestions. I am grateful to our Head of the Department of Physics, other faculty members of the Department of Physics and Centre for Nanotechnology, members of the Central Instruments Facilities, and the Centre for Nanotechnology for providing me with a research-friendly environment with up-to-date research facilities.

A special thanks to the scientific/technical officers/staff, Dr. Sidananda Sarma, Indrajit Talukdar, Kaustubh Acharya, Sujit Deb, Milan Mahadani, Rupok, Emlin Elsa Abraham, and Reena Dey for their help and cooperation in completing my work. I am also thankful to the Central Workshop, Department of Mechanical Engineering, for fabricating essential components in my experimental setup. I immensely admire the Indian Institute of Technology Guwahati for offering me a fellowship, suitable accommodation on this beautiful campus, and a pleasant working environment.

I want to thank Prof. Minoru Fujii and Dr. Sugimoto from Kobe University, Japan, for the XPS and NIR photoluminescence measurements. I am grateful to our collaborators Prof. Subhradip Ghosh and Ms. Mandira Das, for the theoretical calculations. I also thank Dr. Manabendra Sarma and Ms. Upasana Nath from the Department of Chemistry, IITG, for helping with the theoretical calculations.

I want to convey my appreciation and thanks to my friends and lab-mates for their help and good company. I share my sincere gratitude to my seniors Dr. Kamal Kumar Paul, Dr.

Larionette P. L. Mawlong, Dr. Sumona Paul, Dr. Joydip Ghosh, Dr. Ruma Das, Dr. Sumaiya Parveen, Dr. Somorjit Singh, Dr. Abhilasha Bora, and Neda for their aid in research and their welcoming gesture. Many thanks to my labmates, Tadasha, Abdul, Ravinder, Koushik, Sirshendu, Sanju, Subhankar, Debabrata, Shipra, and Sanjoy, for their support and assistance in making the thesis reality. I like to thank my close friends for their positive support.

I am thankful to my family members for their persistent encouragement to pursue higher study. I am highly grateful to my grandparents (Late. Wahed Ali and Late. Nesha) for their positive influence during my childhood. I greatly thank my beloved brother Md Mehebub Hossain for his cheerful encouragement. Finally, I deeply thank my parents, Md Mokbul Hossain & Tajel Khatun, for their love, blessing, and constant support. They are instrumental in building my character, morality, and personality.

Md Tarik Hossain
IIT Guwahati

CONTENTS

Chapter 2: Temperature-dependent Raman studies and Thermal conductivity of direct CVD grown non-van der Waals layered Bi_2O_2Se

Chapter 3: Room Temperature Exciton Formation and Robust Optical Properties of CVD-Grown Ultrathin Bi_2O_2Se Crystals on Arbitrary Substrates

Chapter 4: Interfacial Charge Transfer in the CVD-grown $Bi_2O_2Se/CsPbBr_3$ Nanocrystal Heterostructure and its Exploitation in Superior Photodetection

Chapter 5: Interlayer Charge Transfer Induced Photoluminescence Quenching and Enhanced Photoconduction in Two-Dimensional Bi_2O_2Se/MoS_2 Type-II Heterojunction

Chapter 6: Defect-Induced Photogating Effect and its Modulation in Ultrathin Free-Standing Bi_2O_2Se Nanosheets with Visible-to-Near-Infrared Photoresponse

Chapter 7: Summary and Outlook

Synopsis

Since the discovery of graphene in 2004, two-dimensional (2D) materials have been the cradle for fundamental research and routine applications due to their unique planar structure with distinctive physical, electronic, and chemical properties. The nonexistence of band gap (0 eV) in graphene limits its semiconducting properties confining its applications in nano-electronics. Two decades after, researchers found numerous 2D materials (2Ds) such as transition metal dichalcogenides (TMDs), perovskites, black phosphorus, hexagonal boron nitride (hBN), 2D oxides, MXene and so on. Conventional 2Ds are found with an internal gap, known as van der Waal (vdW) gap, that led to several limitations, such as high air sensitivity and performance under ambient conditions. In contrast, recently emerged Bismuth oxichalcogenides are found with a formal bond (non-van dar Waal (nvdW)) that assembles high ambient air stability, which is desirable for regular applications.

Bismuth oxy-chalcogenides are moderate bandgap (~ 0.8-2.2 eV) semiconductors of the type Bi_2O_2X, where X is a chalcogen atom (S, Se, or Te). Typically, one unit cell of X-terminated Bi_2O_2X consists of two cation layers of $[Bi_2O_2]^{2+}$ and three '$[X]^{2-}$' anion layers. Therefore, the monolayer thickness of Bi_2O_2X consists of one $[Bi_2O_2]^{2+}$ layer between two '$[X]^{2-}$' layers. 50% of atoms of 'X' layer in a monolayer and 50% of another monolayer merge and form a covalent bond with weak electrostatic interaction with a nvdW gap. Forming formal bonds between two Bi_2O_2 layers through 'X' layer makes Bi_2O_2X challenging to synthesize ultrathin Bi_2O_2X. In addition, the structural, optical, and electronic properties are somewhat different from the vdW counterparts due to the nvdW characteristics of Bi_2O_2X. Bi_2O_2X exhibits high carrier mobility, room temperature ferroelectricity, low lattice thermal conductivity, close-lying electronic band structure with indirect bandgap, favourable electronic and thermoelectric properties, which make them interesting for fundamental studies and applications in cutting-edge electronics, optoelectronics, flexible electronics, neuromorphic computing, and biomedical sciences.

Among the Bi_2O_2X, Se-terminated compound, Bi_2O_2Se has been frequently studied due to its outstanding structural stability at ambient conditions. It possesses carrier mobility of ~28900 $cm^2V^{-1}s^{-1}$ at 1.9 K and 450 $cm^2V^{-1}s^{-1}$ at room temperature. The unique combination of high air stability and high-carrier mobility with a tunable bandgap of Bi_2O_2Se make them a suitable optical material for ultra-violet (UV) to infrared (IR) electronics compatible with the mature silicon-based platform. 2D Bi_2O_2Se has received special research attention in various applications, including photodetectors, gas sensors, solar cells, artificial synapses, and integrated devices. Among the applications, 2D Bi_2O_2Se photodetectors have shown great interest due to their high air stability, carrier mobility, and absorption coefficient. Fabrication of 2D Bi_2O_2Se-based high-performance photodetectors might pave the way for ultrasensitive photodetection for a wide range of fields (such as optical communication, spectroscopy, biomedical imaging, environmental monitoring, chemical sensing, security, fire detection, night vision, motion detection, video imaging, etc.). However, more thorough and systematic studies are required to bridge the fundamentals to commercial application, especially material synthesis, understanding underlying physical and chemical properties, and practical device engineering.

Substantial synthesis processes have been developed to grow Bi_2O_2Se for studying structural, optical, and electrical properties. The synthesis processes, such as chemical vapor deposition (CVD), molecular beam epitaxy, and chemical reaction, are reported for growth and property studies. Among them, CVD has been demonstrated to produce a high-quality 2D Bi_2O_2Se with high crystallinity favorable for fundamental investigative studies and device fabrication. Different growth processes are responsible for intrinsic defects that modify properties such as carrier concentration. Thus, it is crucial to understand the unavoidable intrinsic defects and control them for appropriate device fabrication. Moreover, designing a suitable heterostructure (HS) is fascinating in studying the basics and developing high-performance devices. In this regard, heterostructure with conventional vdW 2D TMDs, 0D perovskites is expected to provide enriched electronic properties due to interfacial charge transfer at the atomically thin hetero-interface.

This thesis presents a systematic study on the controlled growth of 2D ultrathin Bi_2O_2Se and freestanding nanosheets of few-layer to monolayer Bi_2O_2Se and a thorough understanding of their structural, optical, and electronic properties. It explained the CVD-growth strategies on arbitrary substrates and their impact on optical properties that would assist in choosing the appropriate substrate for device engineering. It discovers new physical phenomena, such as room temperature multiple exciton formation and defect-induced negative persistent photoconductivity in ultrathin Bi_2O_2Se, which will largely contribute to developing 2D-Bi_2O_2X-based optoelectronics. It also includes unveiling underlying optoelectronic properties via integrating with 0D perovskites and 2D MoS_2 for efficient photodetection. We probe into the interlayer charge transfer mechanism and optical properties of 2D $Bi_2O_2Se/CsPbBr_3$ perovskites nanocrystals and 2D MoS_2/Bi_2O_2Se hetero-layers for ensuing photodetector applications. We believe these studies are significant in understanding the fundamentals of 2D Bi_2O_2Se and related nvdW materials and overcoming the challenges of multifunctional optoelectronic applications of 2D materials. The complete thesis work has been organized into seven chapters, as detailed below:

Chapter 1 briefly introduces the inherent structural, optical, and electronic properties of nvdW Bi_2O_2Se, including their various optoelectronics applications. We begin with the differences between nvdW Bi_2O_2Se and vdW TMDs (e.g., MoS_2). After that, the electronic band structure of Bi_2O_2Se is discussed to realize the band gaps and to check the suitability as optoelectronic candidates. Then we emphasized the outstanding properties of Bi_2O_2Se, such as high carrier mobility, low lattice thermal conductivity, room temperature ferroelectricity, etc. In addition, some other unique properties, such as excimer formation and bolometric effects, are also highlighted. We discussed Raman modes and intrinsic and extrinsic defect-induced properties crucial for material and device characterization. Further, we briefly explained the different growth approaches (including bottom-up and top-down) and the significant challenges for large-area, scalable, and reproducible Bi_2O_2Se growth. Transfer methods for transferring Bi_2O_2Se layers from the growth substrate to a new substrate are elaborated. The critical aspects of 2D Bi_2O_2Se and its multifunctional applications, including photodetector and sensor, are discussed in this chapter. The problems, challenges, and emphasis on limitations have been provided for the synthesis and applications of 2D Bi_2O_2Se. The focus and organization of the thesis are briefly outlined at the end of the chapter.

Chapter 2 presents a systematic study for optimizing the synthesis protocols for 2D Bi_2O_2Se by chemical vapor deposition (CVD) technique. Our results demonstrate the controlled formation of ultrathin Bi_2O_2Se depending upon the synthesis parameters adopted. It highlights the successful synthesis of ultrathin Bi_2O_2Se with high structural and chemical uniformity despite its challenging growth due to the weak electrostatic interaction among layers. The growth temperature is tuned to obtain ultra-smooth single crystals of few-layer Bi_2O_2Se. This chapter also includes temperature-dependent Raman studies of a few-layer Bi_2O_2Se for estimating the in-plane thermal conductivity of ultrathin Bi_2O_2Se by a non-contact measurement technique. Temperature-dependent (78 - 293 K) Raman studies reveal that the A_{1g} phonon mode of Bi_2O_2Se varies linearly with the temperature with a first-order temperature coefficient (α) of $-0.017\,87 \pm 0.0011$ cm^{-1} K^{-1}. The in-plane thermal conductivity is estimated to be ~1.6 W/mK, which is significantly low compared to graphene (~4840 W/mK). It demonstrates 2D Bi_2O_2Se, a suitable thermoelectric material. The results of this chapter elucidate the CVD growth of ultrathin Bi_2O_2Se on mica substrates and develop insights into electron-phonon and phonon-phonon interactions in nvdW 2D materials.

Chapter 3 presents novel optoelectronic properties of nvdW 2D Bi_2O_2Se grown by CVD on various growth substrates (mica, sapphire, SiO_2, quartz, glass). This chapter carefully demonstrates the effect of growth substrates on structural and optoelectronic properties, including morphology, lattice strain, optical bandgap, and photo-carrier dynamics. This study reveals that the formation of multiple excitons, even at room temperature, results in broadband absorption and photoluminescence (PL) at visible to near-infrared (NIR) regions in nvdW Bi_2O_2Se. Experimentally, the observations conclusions are established with absorption, reflectivity, and PL measurement and explained via a theoretical understanding of the band structure obtained from DFT calculations. The effect of growth substrates on the structural and optical properties of Bi_2O_2Se is understood quantitatively by utilizing a series of spectroscopic characterizations, indicating that substrate-induced strain/doping is significant in regulating those properties. These results are essential for developing nvdW Bi_2O_2Se for ensuing applications.

Chapter 4 presents an investigation of interfacial charge transfer in the $Bi_2O_2Se/CsPbBr_3$ hybrid structure through various microscopic and spectroscopic tools corroborated with density functional theory calculations. Here, we integrated $CsPbBr_3$ nanocrystals (a high light-harvesting perovskite) on top of a few-layer Bi_2O_2Se nanosheet (a superior electron mobility material) for efficient broadband photodetection. The band alignment reveals a type-I heterojunction, and the device under reverse bias displays a fast response time of 12 μs/24 μs (rise time/fall time) and an improved responsivity in the 390 to 840 nm range due to the effective interfacial charge transfer and efficient interlayer coupling at the $Bi_2O_2Se/CsPbBr_3$ interface. A photodetector with a better light on/off ratio and a peak responsivity of $\sim 10^3$ A/W^{-1} was achieved in the $Bi_2O_2Se/CsPbBr_3$ hybrid photodetector due to the synergistic effects in the hybrid structure under ambient conditions. The DFT analysis of the density of states and charge density plots in the hybrid structure revealed a net transfer of electrons/holes from perovskite nanocrystals to Bi_2O_2Se layers and additional density of states in Bi_2O_2Se. These results are significant for developing nvdW hybrid structure-based high-performance, low-powered photodetectors.

Chapter 5 presents layer-by-layer stacking of a vdW 2D MoS_2 (monolayer) with a nvdW Bi_2O_2Se layer and studies the interlayer electron-phonon coupling and charge transfer across the hetero-layer interface. It may be noted that the stacking of atomically thin vdW materials has been studied extensively, while the stacking of vdW materials with nvdW materials is least explored. Interlayer charge transfer based on band alignment is vital in various optoelectronic applications. Therefore, this chapter investigated the interlayer charge transfer at the unique 2D Bi_2O_2Se/MoS_2 hetero-layer interface through different spectroscopic, microscopic measurements, and DFT calculations. It unveils that significant photogenerated charge transfer occurs across the hetero-layers due to the favorable band alignment of type-II across the p-n junction. Low-temperature PL studies show that the robust interlayer coupling between the hetero-layers enhances the charge transfer process. Upon photoexcitation, the trion-phonon coupling is stronger than the exciton-phonon coupling in the heterogeneous system. These results are significant for understanding the interaction between vdW and nvdW 2D heterostructures and further exploring such vdW/nvdW 2D heterostructures in future optoelectronic applications.

In **Chapter 6**, we studied the structural/optoelectronic properties of ultrathin Bi_2O_2Se nanocrystals synthesized via a chemical reaction process (colloidal synthesis), which is different from CVD growth, as discussed in previous chapters. It provides the scalable (amount) and rapid synthesis (which are the limitations in the case of CVD synthesis) of freestanding Bi_2O_2Se nanosheets with controllable defects. The understanding of this chapter reveals that vacuum annealing is a simple but effective way to control intrinsic defects of Bi_2O_2Se. Interestingly, we found a new physical phenomenon: self-powered negative persistent photoconductivity (negative PPC) in highly defective Bi_2O_2Se and positive photoconductivity (positive PC) in annealed/less defective Bi_2O_2Se. The mechanistic origin of such conversion from negative PPC to positive PC is discussed in detail, providing a thorough understating of the defect-induced photo-gating effect in ultrathin Bi_2O_2Se nanosheets. The observation of negative PPC in Bi_2O_2Se is novel, and the PPC model describes the origin. The intrinsic defect-induced photo-gating effect plays a significant role in tuning the electronic properties of chemically synthesized Bi_2O_2Se. Besides being a superior optoelectronic material, the inherent defects and further structural tuning via vacuum annealing in Bi_2O_2Se can profoundly affect its transport properties, which are fundamental to electronic devices. We believe these findings shed light on the next-generation novel Bi_2O_2Se-based electronics devices.

Chapter 7 summarizes the work done in the thesis and highlights its contributions to studying the 2D Bi_2O_2Se growth with optoelectronic properties and their hybrid structures with other materials for photodetector applications. Finally, the outlook for future studies on Bi_2O_2Se and its relative chalcogenides is presented.

List of Publications

a. In peer-reviewed journals

Thesis relevant publications

1. Md Tarik Hossain, P. K. Giri, Temperature-dependent Raman studies and thermal conductivity of direct CVD grown non-Van der Waals layered Bi_2O_2Se, J. Appl. Phys. 129, 175102 (2021). *This Article is chosen as Editor's Pick.*

2. Md Tarik Hossain, Mandira Das, Joydip Ghosh, Subhradip Ghosh, P. K. Giri, Understanding the interfacial charge transfer in the CVD grown $Bi_2O_2Se/CsPbBr_3$ nanocrystal heterostructure and its exploitation in superior photodetection: experiment vs. theory, Nanoscale 13, 14945-14959 (2021). *Most popular 'Nanoscale' 2021 articles.*

3. Md Tarik Hossain, Tadasha Jena, Subhankar Debnath, P. K. Giri, Defect-induced Photogating effect and its modulation in ultrathin freestanding Bi_2O_2Se Nanosheets with Visible Near-infrared photoresponse, J. Mater. Chem. C 11, 6670-6684 (2023).

4. Md Tarik Hossain, Tadasha Jena, Upasana Nath, Manabendra Sarma, P. K. Giri, Room temperature exciton formation and robust optical properties in ultrathin Bi_2O_2Se crystals on arbitrary substrates, Nanoscale 15, 11222-11236 (2023).

5. Md Tarik Hossain, Larionette P. L. Mawlong, Tadasha Jena, Abhilasha Bora, Upasana Nath, Manabendra Sarma, P. K. Giri, Interlayer Charge-Transfer-Induced Photoluminescence Quenching and Enhanced Photoconduction in Two-Dimensional Bi_2O_2Se/MoS_2 Type-II Heterojunction, ACS Appl. Nano Mater. (2023) DOI: 10.1021/acsanm.3c00759.

Other publications

1. Abhilasha Bora, Sumana Paul, Md Tarik Hossain, P K Giri, Quantitative Understanding of the Photoluminescence Modulation and Doping of Monolayer WS_2 by Heterostructuring with Non-van der Waals 2D Bi_2O_2Se Quantum Dots, J. Phys. Chem. C 126, 12623-12634 (2022).
2. Sumana Paul, Sanju Nandi, Mandira Das, Abhilasha Bora, Md Tarik Hossain, Subhradip Ghosh, P K Giri, Two-dimensional Bismuth Oxyselenide Quantum Dots as Nanosensor for Selective Metal Ion Detection Over a Wide Dynamic Range: Sensing Mechanism and Selectivity, Nanoscale (2023), DOI: 10.1039/D3NR02029K.

3. Tadasha Jena, Md Tarik Hossain, P. K. Giri, Temperature-dependent Raman study and determination of anisotropy ratio and in-plane thermal conductivity of low-temperature

CVD grown $PdSe_2$ using unpolarized laser excitation, J. Mater. Chem. C 9, 16693-16708 (2021).

4. Sumana Paul, Md Tarik Hossain, Abdul Kaium Mia, P K Giri, Europium Doping in 2D Topological Insulator Bi_2Se_3 Nanosheets Enables High Absorption, Suppressed Negative Photoconductivity and High-Performance Photodetection, ACS Appl. Nano Mater. 4, 12527-12540 (2021).
5. Sumana Paul, Joydip Ghosh, Md Tarik Hossain, Hiroaki Hasebe, Hiroshi Sugimoto, Minoru Fujii, P K Giri, Interfacial Charge Transfer Induced Enhanced Near-Infrared Photoluminescence and Enhanced Visible Photodetection in Two Dimensional/Zero-Dimensional $Bi_2Se_3/CsPbBr_2I$ Heterojunctions with Type-I Band Alignment, J. Phys. Chem. C 126, 16721-16731 (2022).
6. Tadasha Jena, Md Tarik Hossain, Upasana Nath, Hiroshi Sugimoto, Minoru Fujii, Manabendra Sarma, P. K. Giri, Evidence for intrinsic defects and nanopores as hotspots in 2D $PdSe_2$ dendrites for plasmon free SERS substrate with a high enhancement factor, NPJ 2D Mater. Appl. 7, 8 (2023).

b. Manuscript under review/preparation

1. Abdul Kaium Mia, Abhilasha Bora, Md Tarik Hossain, S. Sinha, P. K. Giri, Ultra-Sensitive Detection of Staphylococcus aureus using thiol-Functionalized WS_2 Quantum Dots and Bi_2O_2Se Nanosheets Hybrid Through Fluorescence Recovery Mechanism, (**Under review**)
2. Md Tarik Hossain, Tadasha Jena, P. K. Giri, Recent progress on synthesis, properties, applications, and prospects of non-van der Waals 2D Bi_2O_2X (X=S, Se, Te), **(Under preparation)**

c. Oral/poster presentation at Conferences

1. Md Tarik Hossain, Larionette P. L. Mawlong, Tadasha Jena, Abhilasha Bora, P. K. Giri, "Spectroscopic Signatures of Photoinduced Charge Transfer and Interlayer Coupling in Two-dimensional Bi_2O_2Se/MoS_2 Heterostructure", Research & Industrial Conclave-Integration'23' (**RIC 2023**), May 14-16, 2023, IIT Guwahati, India. (**Oral**)
2. Md Tarik Hossain, Mandira das, Joydip Ghosh, Subhradip Ghosh, P. K. Giri, "Efficient interfacial charge transfer in CVD-grown non-van der Waals $Bi_2O_2Se/CsPbBr_3$ type-I heterostructure for improved photodetection", 12th edition of largest European Conference

& Exhibition in Graphene and 2D materials (**Graphene 2022)**, Aachen, Germany, July 6-8, 2022. (**Poster**)

3. Md Tarik Hossain, P. K. Giri, "Interlayer charge transfer in CVD grown $Bi_2O_2Se/CsPbBr_3$ heterostructure", North-East Research Conclave and Assam Biotech Conclave 2022 (**NERC-2022**), May 20-22, 2022, IIT Guwahati, India. (**Oral**)
4. Md Tarik Hossain, P. K. Giri, "CVD growth of non-Van der Waals layered Bi_2O_2Se and its in-plane thermal conductivity", International Conference on Materials for the Millennium (**MATCON-2021**), March 15-19, 2021, CUSAT, India. (**Oral**)
5. Md Tarik Hossain, P. K. Giri, Layer controlled growth of two-dimensional bismuth oxyselenide and their optical properties, International conference on functional materials (**ICFM 2020**), Jan 6-8, 2020, IIT Kharagpur, India. (**Poster**)

d. Conference/Workshops attended

1. 'Research & Industrial Conclave-Integration'23', (**RIC 2023**) May 14-16, 2023, IIT Guwahati, India.
2. 12th edition of largest European Conference & Exhibition in Graphene and 2D materials (**Graphene 2022**), July 5-8, 2022, Aachen, Germany.
3. North-East Research Conclave and Assam Biotech Conclave 2022 (**NERC 2022**), May 20-22, 2022, IIT Guwahati, India.
4. Virtual '**Optical School 2021**' jointly organized by Indian Association of Science and Cultivation (IACS) and HORIBA Scientific India from Sept. 6-8. 2021.
5. International Conference on Materials for the Millennium (**MATCON-2021**), March 15-19, 2021, Department of Applied Chemistry, Cochin University of Science and Technology, India.
6. International Virtual Conference on Advanced Nanomaterials Applications **(VCAN 2020**), June 17-19, 2020, Centre for nanotechnology research (CNR), VIT, Vellore, India.
7. International conference on functional materials (**ICFM 2020**), Jan. 6-8, 2020, Materials Science centre, Indian Institute of Technology Kharagpur, West Bengal, India
8. SERB school on '**Plasma Processing of Materials 2019**', June 3-22, 2019, Department of Metallurgical Engineering & Materials Science, Indian Institute of Technology Bombay, Mumbai, India.

List of abbreviations

Abbreviation	***Description***
0D	Zero Dimensional
1D	One Dimensional
2D	Two Dimensional
1-L	Monolayer
CDD	Charge Density Distribution
CVD	Chemical Vapor Deposition
CT	Charge Transfer
DRS	Diffuse Reflectance Spectroscopy
EDX	Energy Dispersive X-ray Spectroscopy
EQE	External Quantum Efficiency
FESEM	Field Emission Scanning Electron Microscopy
FETEM	Field Emission Transmission Electron Microscopy
FWHM	Full Width at Half Maxima
GGA	Generalized Gradient Approximation
HRTEM	High Resolution Transmission Electron Microscopy
HS	Heterostructure
KPFM	Kelvin Probe Force Microscopy
NC	Nanocrystal
NIR	Near Infrared
nvdW	Non Van der Waals
PBE	Perdew-Burke-Ernzerhof
PD	Photodetector

PL	Photoluminescence
QD	Quantum Dot
SAED	Selected Area Electron Diffraction
STEM	Scanning Transmission Electron Microscopy
TEM	Transmission Electron Microscopy
TMD	Transition Metal Dichalcogenides
TRPL	Time-Resolved Photoluminescence
UV-Vis	Ultraviolet-Visible
vdW	Van der Waals
XPS	X-ray Photoelectron Spectroscopy
XRD	X-ray Diffraction

Chapter 1

Introduction

Two-dimensional (2D) materials are among the most competitive candidates for next-generation optoelectronics due to their intrinsic atomic thickness, flexibility, and dangling-bond-free surfaces. Since the discovery of graphene, a vast family of 2D materials has been investigated, including transition metal dichalcogenides (TMDs), noble metal TMDs, hexagonal boron nitride (hBN), black phosphorus (BP), borophene, Mxene, etc. An interesting fact for all these 2Ds is van der Waals (vdW) stacking among the layers. For example, in the case of TMDs, two monolayers of MX_2 (M= transition metal, X= chalcogenide) consist of an internal gap among the layers to form a bilayer of MX_2, as shown in **Fig 1.1a**. Recently developed, air-stable, and high-mobility 2D bismuth oxichalcogenides (Bi_2O_2X) are non-van der Waals (nvdW) materials with electrostatically attached layers (**Fig. 1.1b**). Among the Bi_2O_2X, 2D bismuth oxyselenide (Bi_2O_2Se) has outstanding advantages such as stability, making it uniquely favorable in the electronics, medical, and energy applications.

1.1. Properties of Bi_2O_2Se

1.1.1. Crystal structure of Bi_2O_2Se

Bi_2O_2Se is a layered material in which each unit is composed of two $[Bi_2O_2]$ layers sandwiched between three Se (X) atomic layers (**Fig. 1.1b**). Bi_2O_2Se possesses inversion symmetry with *I4/mmm* group.[1] Depending on the arrangement of the atoms, the structure of Bi_2O_2Se is tetragonal structure (a=b=3.88 Å, c=12.16 Å).[2] Typically, one unit cell of Se-terminated Bi_2O_2Se consists of two cation layers of $[Bi_2O_2]^{2+}$ and three '$[Se]^{2-}$' anion layers.

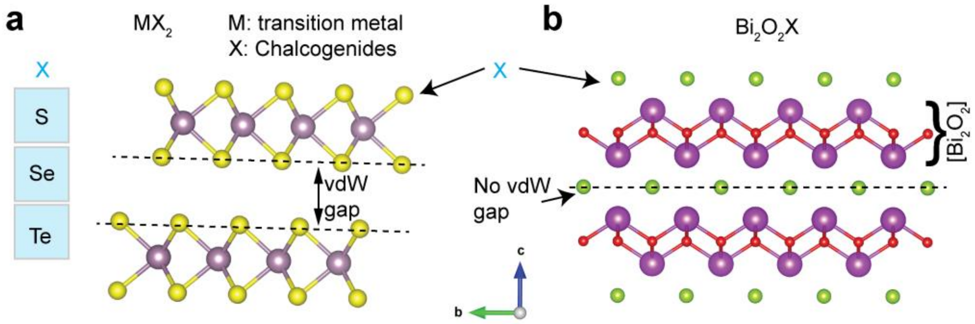

Fig. 1.1: Difference between vdW and nvdW materials: Schematic displaying the difference between vdW and nvdW crystals. (a) TMDs (MX_2) showing the vdW gap, (b) Bi_2O_2X exhibits no vdW gap between the layers.

Therefore, a monolayer thickness of Bi_2O_2Se consists of one $[Bi_2O_2]^{2+}$ layer between two '$[Se]^{2-}$' layers. Here, 50% of atoms of 'Se' layer in a monolayer and 50% of another monolayer merge and covalently bonded with weak electrostatic interaction with no-vdW gap (**Fig. 1.1b**), unlike conventional 2D materials with vdW gap (**Fig. 1.1a**) such as TMDs. The formation of formal bonds between two Bi_2O_2 layers through 'Se' layer makes Bi_2O_2Se challenging to synthesize monolayer Bi_2O_2Se. Nevertheless, there has been some advances in the synthesis of few layer Bi_2O_2Se.

1.1.2. Band structure and optical properties

The electronic band structure of a material determines electronic and optical characteristics. Therefore, the knowledge of the relationship between electronic and optical bandgaps is the key to understanding the suitability of the material in optoelectronics. Generally, two types of bandgaps can co-exist in a semiconducting material. 1. electronic bandgap or structural bandgap, which can be tuned by changing the structure of the material. 2. Optical bandgap, which depends on exciton formation between VBM to CBM due to absorption or emission of energy. Both the bandgaps are supposed to be the same for direct bandgap semiconductors. In the case of indirect bandgap material, it (electronic and optical bandgap) varies due to VBM and CBM lying at two different symmetry points. Computational study of the electronic band structure of Bi_2O_2Se indicates that it is an indirect bandgap semiconductor with bandgap of 0.89 eV (see **Fig. 1.2a**).[3] Experimentally, from the transmittance measurement, the derived bandgap of Bi_2O_2Se is 1.37 eV in bulk, and it increases to 1.9 eV at monolayer thickness with an indirect bandgap.[4] The indirect bandgap is attributed to exciton formation at valance band maxima of X to conduction band minima of Γ symmetry points. Interestingly, being a nvdW material, Bi_2O_2Se exhibits thickness-dependent bandgap due to modulated configuration of energy valleys, i.e., the absence of density of states close to the Fermi energy further suggests Bi_2O_2Se behaves as a 2D material (i.e., it shows thickness-dependent bandgap change). Although the bandgap changes significantly from monolayer to bilayer (by 0.8 eV), above bilayer thickness, the change in bandgap is minor.[5] The possible reason for the minor change in the bandgap for the bilayer is the formation of the unit cell, as we know that the two Bi_2O_2 layers with three Se layers form a unit cell. An incomplete unit cell in monolayer Bi_2O_2Se probably give rise to dramatic change (1.9 -1.2 = 0.7 eV) in the bandgap. Ghosh et al. found that the optical bandgap changes from 2.3 (monolayer) to 1.7 eV (tri-layer) from DFT calculation and 1.9 (monolayer) to 1.45 eV (trilayer) from experimental observation (refer to **Fig. 1.2b**).[6] The higher optical band gap is ascribed to the overlap of symmetry points in the Brillouin zone. They found that the indirect bandgap changes from 2.0 eV (monolayer) to 1 eV (tri-layer) from DFT calculation. As the optical bandgaps are related to the formation of excitons at Γ symmetry point, the optical bandgaps differ from the indirect gap observed in the electronic band structure. Thus, a moderately robust bandgap with a close-lying electronic structure may facilitate Bi_2O_2Se for rich ultra-broadband (UV to infrared beyond 7 μm) optoelectronics.

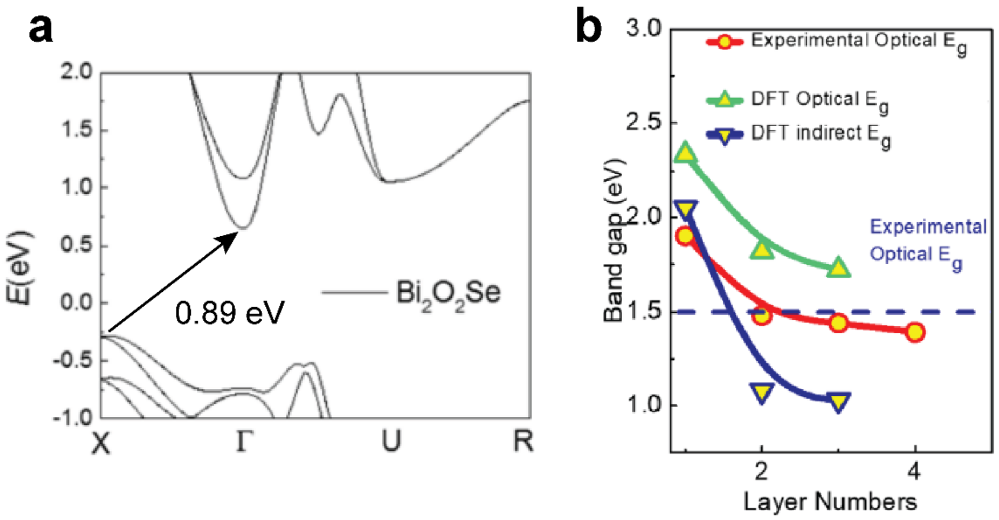

Fig. 1.2: (a) Electronic band structure of Bi_2O_2Se bulk. Adopted from ref [3]. (b) Layer-dependent experimental and DFT calculated band gap of Bi_2O_2Se. Adopted from ref [6].

1.1.3. Carrier mobility

2D Bi_2O_2Se possesses high carrier mobility, which is crucial for high-performance electronics. It exhibits an electron mobility of ~20,000 $cm^2 V^{-1} s^{-1}$ at 2K & 313 $cm^2 V^{-1} s^{-1}$ at room temperature (**Fig. 1.3a,** left y-axis).[4] At the same time, it holds a carrier concentration of ~5×10^{18} cm^{-3} at 2K and ~11×10^{18} cm^{-3} at room temperature (**Fig. 1.3a,** right y-axis). Hence, there is room for achieving even higher carrier mobility by reducing the carrier density. In addition, carrier mobility varies with thickness; in the few layers (<6 nm), the carrier mobility decreases, and in multilayer samples (>6 nm), the carrier mobility increases, which makes multilayer samples more suitable for optoelectronics.[7] The typical carrier mobility of 2D Bi_2O_2Se is relatively lower than that of Silicon (~10^3 $cm^2 V^{-1} s^{-1}$ at 300 K), but it is higher than that of 2D MoS_2 (~10-18 $cm^2 V^{-1} s^{-1}$ at 300 K).

1.1.4. Room temperature ferroelectricity

In addition to high carrier mobility, it is predicted by first-principles calculations that Bi_2O_2Se possesses ferroelectricity/ferroelasticity.[3] The unique combination of high carrier mobility with ferroelectricity/ferroeleasticity makes Bi_2O_2Se a potential candidate for future non-volatile memory (NVMs), energy harvesting, strain-tuned electronics, artificial brain, neuromorphic sensors, etc. Experimentally, room-temperature ferroelectricity is observed in Bi_2O_2Se.[6] The hysteric behaviour in the 'off state' piezo-response signal shows the existence of a spontaneous polarization state and its switching behaviour under an externally applied electric field (**Fig. 3b, c**). The 2D high mobility, along with ferroelectricity/ferroelasticity renders the scope for integration of functional NVMs with Bi_2O_2Se.

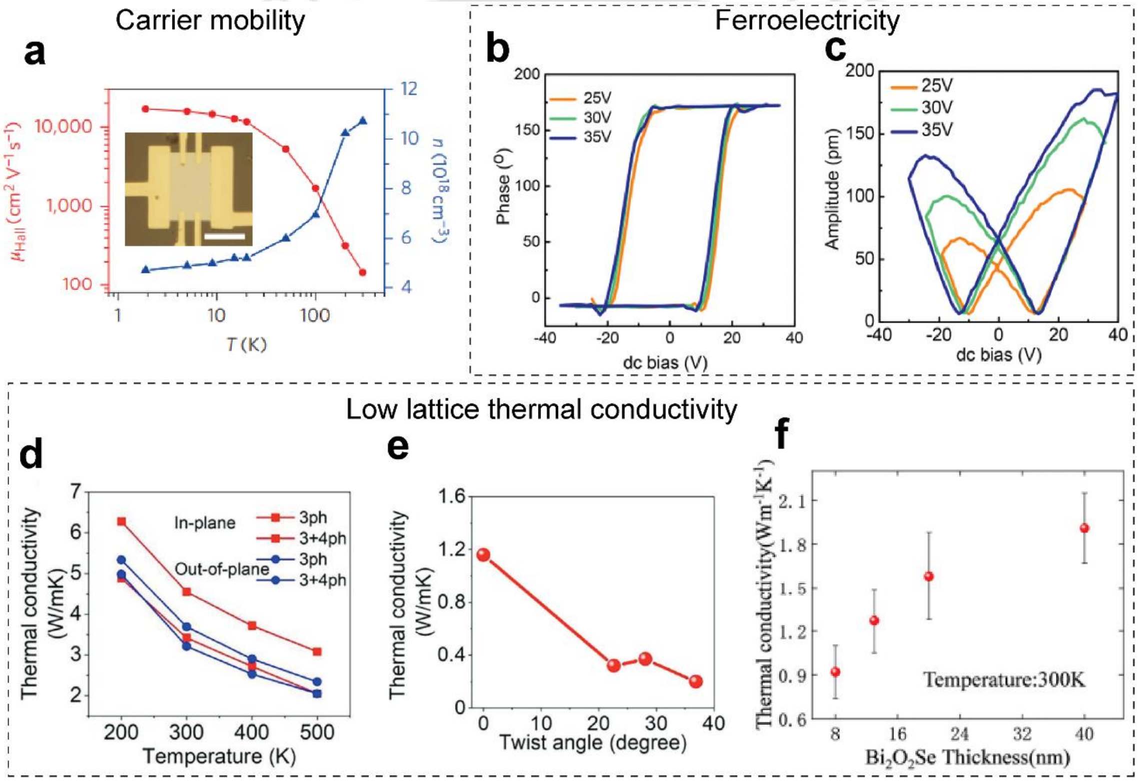

Fig. 1.3: (a) Carrier mobility (left y-axis) and carrier concentration (right y-axis) as a function of temperature. Adopted from ref [4]. (b, c) phase and amplitude hysteresis curve showing ferroelectric property of Bi_2O_2Se at room temperature. Adopted from the ref [6]. Thermal conductivity as a function of (d) temperature, (e) twist angle, and (f) thickness. Adopted from ref [8,9].

1.1.5. Low lattice thermal conductivity

Besides, the above discussed properties Bi_2O_2Se possesses ultralow lattice thermal conductivity. Ultralow lattice thermal conductivity is demanding for thermal barrier coatings, thermoelectric energy harvesting, and data storage devices. According to the theoretical study, thermal conductivity of Bi_2O_2Se varies from 2.34 -5.33 W/mK along out-of-plane direction and 3.08-6.28 W/mK along in-plane direction while temperature changes from 200K to 500K.[8] Experimentally, room temperature out-of-plane and in-plane thermal conductivity of bulk Bi_2O_2Se pellet (highly *00l* oriented) is ≈ 1.0 and 1.2 W/mK.[10] The chemical vapour deposition of Bi_2O_2Se provides *00l*-oriented growth resulting in thickness-dependent in-plane thermal conductivity. Room temperature in-plane thermal conductivity of completely *00l*-oriented layered Bi_2O_2Se ranges from 0.9 (8 nm thick) to 1.6 W/mK (38 nm).[9,11] Therefore, we can attribute the deviation of theoretically and experimentally calculated thermal conductivities to a few factors such as crystal orientation, defects, thickness, and temperature. One way to tune the crystal orientation is layer-by-layer twisting. Taking advantage of the twisting, Sun et al. observed thermal conductivity decreases from 1.2 W/mK (pristine structure) to 0.2 W/mK when the layers are twisted at an angle of 36.87° at 300 K.[8] It could be speculated that the twisted heterostructure may provide a platform for achieving ultralow thermal conductivity.

1.1.6. Other inherent properties

Bi_2O_2Se possesses many other inherent properties, a few of which are mentioned below. Due to its unique nvdW structure, the formation of excimer is observed, resulting in broadband absorption and emission.[12] Excimer states alter the internal geometry of the Bi_2O_2Se due to the built-in-dipolar electric field along the c-direction and, thus, the band structure. Therefore, photoluminescence of Bi_2O_2Se has been observed in the visible range.[12] However, due to its indirect band gap, it shows limited intensity photoluminescence. Besides these properties, Bi_2O_2Se exhibits the bolometric effect[13] (which changes the carrier density with heat) and excellent air stability (due to their dangling bond-free Se-layer termination). The low ambient stability of conventional 2Ds limits the sustainability of electronic devices wherever Bi_2O_2Se-based electronics can serve as better alternatives. Bi_2O_2Se exhibits high bending stability, making it suitable for flexible and wearable electronics. Li et al. reported that Bi_2O_2Se is stable even after 500 times 180-degree bendings.[14] Besides, Bi_2O_2Se is promising as a superior co-catalyst for renewable energy sources due to its high carrier mobility.[15]

1.1.7. Spectral property/Raman spectra of Bi_2O_2Se

Raman spectroscopy is a non-invasive and powerful technique to characterize the crystal phase and structure of Bi_2O_2Se. According to group theory and first principal calculations by Cheng et al. [16], highly symmetric Bi_2O_2Se crystals exhibit four Raman active vibrational modes (A_{1g}, B_{1g}, E_g^1, and E_g^2) at the Γ-symmetry point. The atomic vibrations of Bi and O atoms result in the Raman active modes. The E_g^1 and E_g^2 mode arises due to in-plane vibration of the Bi and O atom **(Fig 1.4a)**. The out-of-plane vibration of Bi and O atoms results in the breathing modes; A_{1g} and B_{1g} **(Fig 1.4a)**. Computationally calculated, the Raman modes are at 67.99 cm^{-1} (E_g^1), 159.89 cm^{-1} (A_{1g}), 364.02 cm^{-1} (B_{1g}), and 428.68 cm^{-1} (E_g^2) (**Fig 1.4b**). Experimentally, the A_{1g} peak is observed at 160 cm^{-1} in Bi_2O_2Se (**Fig 1.4c**). To generate all the Raman active modes of Bi_2O_2Se, only the Bi_2O_2 layer participates. Therefore, all modes lie at <600 cm^{-1}.[16] Raman modes exhibit blueshift while decreasing layer thickness (from bulk to 2-3 layers) of Bi_2O_2Se due to relaxation in the interlayer coupling. Consequently, the monolayer thickness of Bi_2O_2Se does not show a measurable Raman signal.[17] Also, all the Raman modes exhibit blueshift/redshift due to uniaxial compressive/tensile strain.[16]

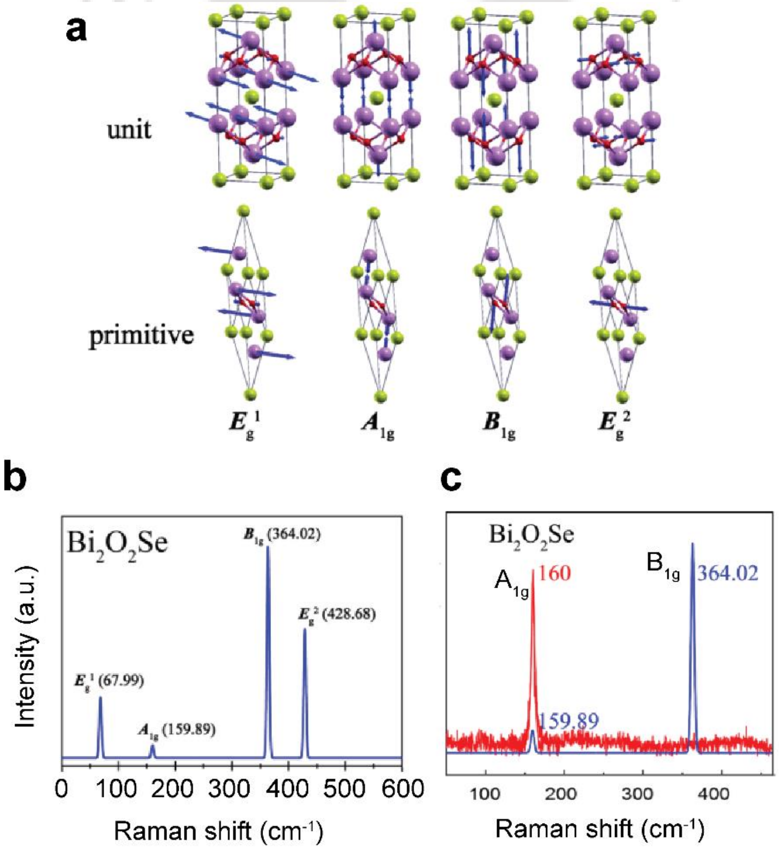

Fig. 1.4: (a) Atomic vibration responsible for different Raman modes in Bi_2O_2Se. (b) Computational results of Raman active modes. (c) Comparison of Experimentally (red line) and computationally (blue line) obtained A_{1g} and B_{1g} mode. Adopted from ref [16].

1.1.8. Defect-induced properties

Defects are beneficial for regulating materials' structural, optical, and electronic properties.[18] These properties can be tuned by monitoring intrinsic and extrinsic defects in Bi_2O_2Se. Defects in Bi_2O_2Se have been investigated widely through substantial theoretical and experimental studies.[14,19-21] Multiple point defects can form depending on their formation energy during the growth. In the growth process of any 2D materials, intrinsic defects are unavoidable occurrences. Therefore, studying the defects is crucial for understanding the mechanism of property modulation and its effect on device performance. It is consistently believed that there are two most probable outcomes after Bi_2O_2Se growth[22,23], i) Se poor, Bi rich, and ii) Se rich and Bi poor. According to first principle calculations, Se vacancy (V_{Se}) is the most stable defect in Se poor Bi rich condition.[14] After that, the sequence of stable point defects are oxygen vacancy (V_O), Bi replacing Se vacancy (Bi_{Se}), interstitial oxygen (O_{in}), interstitial Se (Se_{in}), Bi vacancy (V_{Bi}), Se replacing Bi vacancy (Se_{Bi}), interstitial Bi (Bi_{in}), Bi replacing O vacancy (Bi_O), and O replacing Bi vacancy (O_{Bi}). Therefore, an unintentional n-type doping may be observed in Se poor and Bi rich condition due to V_{Se} and V_O. In Se-rich and Bi-poor conditions, their formation energy increases, making p-type doped Bi_2O_2Se. In the case of Se vacancies (V_{Se}), the donor sites (V_{Se}) are spatially separated; thus, it results in high mobility. On the other hand, Se_{Bi} donor sites lie on the Bi_2O_2 layer, disrupting mobility and resulting in low carrier mobility.[23] Intrinsic defects can be tuned by regulating various experimental parameters such as precursor amount, controlling growth pressure, temperature, varying growth medium, etc. Extrinsically, surface defects can be created by plasma etching[24], annealing, etc. To characterize defects, Raman and HRTEM analyses are effective techniques. Kim et al. recently reported a signature peak at ~55 cm^{-1} due to line defects in Bi_2O_2Se.[20] With such defect engineering, Liu et al.[18] achieved a NIR (λ~1.0 µm) femtosecond solid-state laser with Bi_2O_2Se nanoplates as the saturable absorber (SA) with a high output power (~665 mW) and ultrashort pulse width (~266 fs). It has been reported that the bandgap varies with different Se concentrations via introducing mid-gap states (except ~50% of Se vacancy due to structural symmetry).[25,26] Therefore, controlling the intrinsic and extrinsic defects is essential to see the efficient performance of Bi_2O_2Se-based nanodevices. All the properties mentioned above make 2D Bi_2O_2Se, a suitable candidate for future optoelectronics and nanotechnology.

1.2. Synthesis of 2D Bi_2O_2Se

Many efforts have been dedicated to preparing large-scale, uniform atomic layer growth of 2D Bi_2O_2Se using numerous top-down and bottom-up methods, including chemical vapour deposition (CVD), molecular beam epitaxy (MBE) chemical reaction (solution assisted, ion template-assisted, solvothermal), salt assisted CVD and mechanical exfoliation. Most of the reported data primarily relied on the CVD growth process[4,27-31] due to atomically uniform and favourable nucleation of nvdW 2D Bi_2O_2Se. Although the exfoliation method provides high-quality vdW 2Ds, the built-in formal bonds in Bi_2O_2Se limit the large-scale atomic uniformity, including the difficulties in exfoliation down to monolayer thickness. Taking advantage of formal bonds, chemical reaction route is also employed for scalable production and fundamental studies of Bi_2O_2Se.[6,32] Nevertheless, chemically integrated Bi_2O_2Se is highly likely to form chemical bonds with foreign molecules (such as oxygen) during the reaction process. Very recently, solution assisted and salt-assisted (e.g., sodium chloride; NaCl) CVD methods have been employed to obtain high-quality Bi_2O_2Se with wafer-scale and thickness-controlled growth. Methods for the preparation of Bi_2O_2Se films can be classified into three main categories as shown in **Fig. 1.5**: (1) atomic deposition (CVD, MBE), (2) chemical reaction (solution assisted), (3) mechanical exfoliation. Here, a few recently developed synthesis techniques of Bi_2O_2Se with their pros and cons are discussed from the perspectives of mechanism, structure, thickness, domain size, and quality.

1.2.1. Physical growth techniques

1.2.1.1. Chemical vapour deposition

Chemical vapour deposition (CVD) enables tunable deposition (large-scale, thickness etc.) with an atomically smooth surface of Bi_2O_2Se. Bismuth oxide (Bi_2O_3) and bismuth selenide (Bi_2Se_3) are primarily used precursors. The CVD schematic is shown in **Fig. 1.5a** (left panel). From the Bi_2O_3 and Bi_2Se_3, [Bi_2O_2] and [Se] layers assemble and crystalize to tetragonal Bi_2O_2Se. Because of the tetragonal crystal phase, growth with square morphology is favourable with lattice-matching growth substrate (e.g., mica), as shown in **Fig. 1.5a** (right panel). Depending upon Bi_2O_3 and Bi_2Se_3 weight ratio and the growth temperature (T_G), the crystal shape varies, where a higher T_G (~670-720 °C) with a nearly equal weight ratio (~1-1.7) provides the square morphology.[30] At a similar temperature window (~670-720 °C), with a relatively higher precursor weight ratio (~1.7-3.5), mixed-shape (truncated square, inclined structure, nanoribbons) is observed.[30] With lower T_G, irregular structures are found with a wide variation of the weight ratio of precursors from 1 to 3, and the higher weight ratio of precursor results in nanoribbons formation.[20] Thus, the growth morphology could be tuned by T_G and precursor weight ratio. Further, NaCl salt-driven CVD has been adopted for large-area uniform growth with controlled thickness.[33] Salts act as catalysis to enhance lateral growth rather than vertical growth. In addition, a mixture of salt and precursor material can reduce the evaporation temperature, eventually decreasing the T_G stepping towards low-temperature growth. High-quality growth at low temperatures is essential for fabricating wearable electronics on a flexible substrate. Recently, Khan et al. have demonstrated the salt-assisted low-temperature CVD growth of mm-size high-quality Bi_2O_2Se flakes.[33]

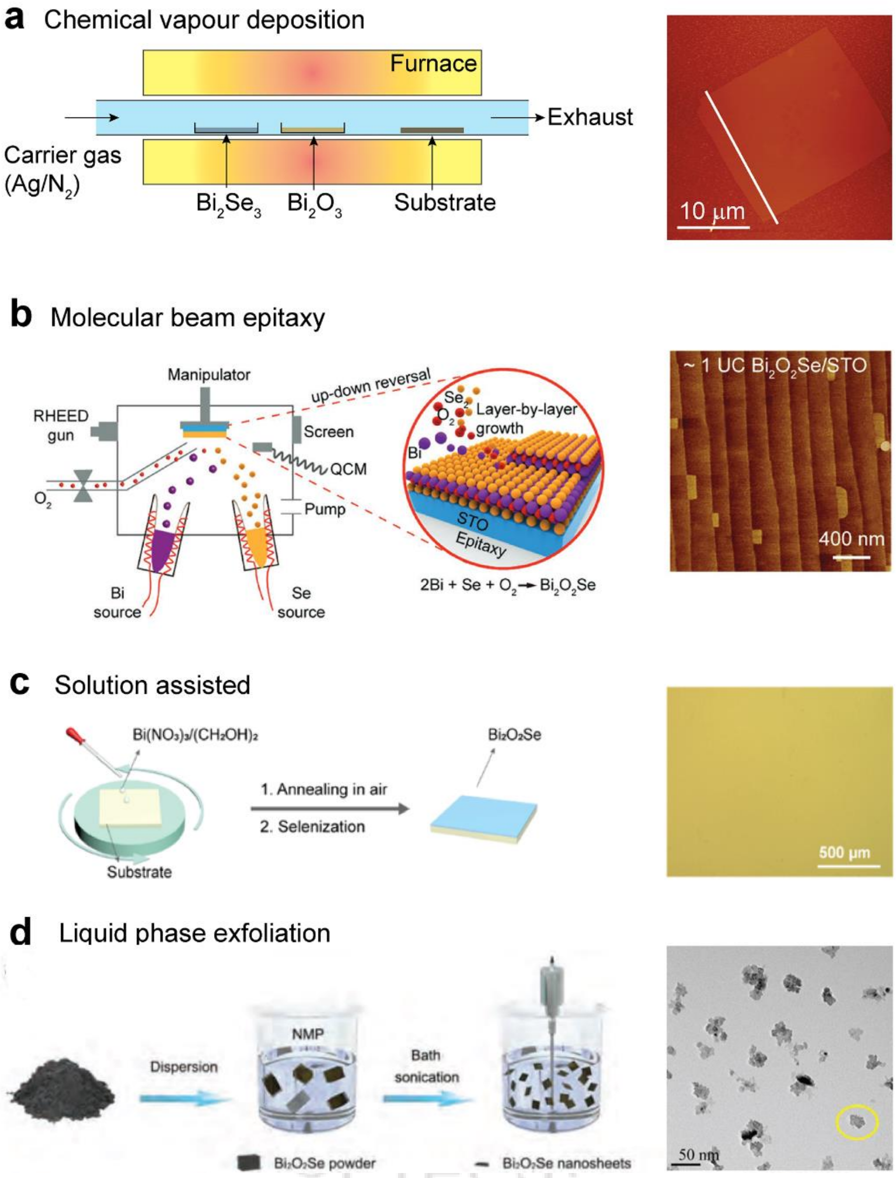

Fig. 1.5: Growth methods of Bi_2O_2Se: (a) chemical vapor deposition (b) molecular beam epitaxy. (c) solution assisted. (d) liquid phase exfoliation. Adopted from the ref [11,34-36].

1.2.1.2. Molecular beam epitaxy

Molecular beam epitaxy (MBE) is another approach for synthesizing Bi_2O_2Se through atomic deposition with precise thickness tunability. **Fig 1.5b** (left panel) shows a schematic representation of atomically thin Bi_2O_2Se films preparation by the MBE method. For the growth of Bi_2O_2Se, Bi, and Se sources are evaporated via standard effusion cells in the precisely controlled oxygen atmosphere.[34] Due to reasonable lattice matching with high thermal stability, mica with an insulating feature and Nb-doped STO (≈ 0.5% mismatch) with excellent conductivity feature are suitable substrates for growth. For MBE growth, control of the Se/Bi flux ratio, oxygen pressure, and T_G is crucial. T_G should be in-between the two sources evaporation temperatures (e.g., $T_{Bi} > T_G > T_{Se}$) for precise thickness control and preventing bulk crystal growth associated with impurities, such as Se-rich/poor. As the evaporation temperature of Se lies within 100 to 350 °C, it is possible to do low-temperature growth of Bi_2O_2Se. A lower flux ratio (Se/Bi) and higher oxygen pressure help produce a pure Bi_2O_2Se phase avoiding Bi_2Se_3 impurities. Liang et al. synthesized pure Bi_2O_2Se phase of the one-unit cell on STO terraces at T_G = 290 °C.[34] The thickness of Bi_2O_2Se was monitored with the variation of growth time. With increasing growth time, monolayer islands merge and form a uniform large area growth; over time, many monolayers merge electrostatically for multilayer growth. Although this method facilitates the low-temperature high-quality growth of 2D Bi_2O_2Se, it requires high-end instrument facilities, which limit the approachability.

1.2.2. Solution-assisted method

Recently, the solution-assisted method has been developed by Zhang et al. for facile, rapid, and scalable synthesis of Bi_2O_2Se thin films on flexible muscovite substrates, as shown in **Fig 1.5c**.[35] They employed the selenization technique for Bi_2O_2Se growth. $Bi(NO_2)_3/(CH_2OH)_2$ is the source for BiO layer, and Se are sources for chalcogenide layers to grow layered Bi_2O_2Se. A uniform layer of $Bi(NO_2)_3/(CH_2OH)_2$ can be spin-coated with different rotation speeds (**Fig. 1.5c**) to tune the layer thickness. Dang et al. optimized the ion template-assisted method for Bi_2O_2Se growth in KOH medium for uniform few layers with oxygen deficiencies.[37] This well-known hydro/solvothermal method can be tuned to obtain Bi_2O_2Se nanostructures with different morphologies and defects for modulating electronic properties. Another simple technique for Bi_2O_2Se growth is the self-assembling of BiO and Se layers via a chemical reaction. For this process, one needs a source for the BiO layer, which could be $Bi(NO_3)_2$, $5H_2O$, and Se layer which could be $Se(NH_2)_2$ for Bi_2O_2Se. The room temperature synthesis of free-standing Bi_2O_2Se nanosheets is possible through this technique under atmospheric conditions.[6] The involvement of solvent and byproducts in this method might reduce the quality of the flakes and is likely to introduce defects and impurities. Hence, careful characterization is necessary before understanding the properties of pure Bi_2O_2Se grown via this method.

1.2.3. Top-down synthesis processes/ liquid-phase exfoliation method

Another approach for synthesizing 2D Bi_2O_2Se is exfoliating the bulk powder, as shown in **Fig. 1.5d**. Bi_2O_2Se nanosheets are obtained from bulk Bi_2O_2Se by liquid exfoliation method.[36] Bi_2O_2Se quantum dots can be synthesized via commonly used bath and probe sonication. Ultrasmall Bi_2O_2Se QDs can be obtained by combining three steps i) grinding the bulk to prepare fine powder, ii) bath sonication of the fine powder, and iii) then ice bath probe sonication for several hours. To prepare Bi_2O_2Se QDs, the bulk powder is ground into fine powders and dispersed in N-methyl-2-pyrrolidone (NMP), followed by liquid exfoliation for a few hours involving ice-bath sonication and ultrasound-probe sonication.[36] Later, to change the solvent, centrifugal separation or solvent removal (with a magnetic stirrer on a hot plate) of the QDs must be done and dispersed in the desired solvent.

1.3. Transfer methods

Transfer of Bi_2O_2Se flakes on a new substrate/target is essential for making a heterostructure or engineering a device. The electrostatic force between ultrathin Bi_2O_2Se and growth substrate (e.g., mica) creates difficulty in transferring this 2D sheet without any damage. Therefore, a clean and easy transfer is required for easy characterization and better performance of the Bi_2O_2Se device. For the transfer of ultrathin Bi_2O_2Se, we need a sacrificial layer that adheres to the material's surface for peeling off the Bi_2O_2Se layer from the growth substrate. After peeling off the sacrificial layer, along with the Bi_2O_2Se layer on a new substrate, the sacrificial layer has to remove from the sample via post-treatment (chemical cleaning/ heating). Few transfer methods have been developed for the transfer of Bi_2O_2Se, which are summarized below.

1.3.1. PMMA-assisted transfer

PMMA-assisted transfer process (**Fig. 1.6a**) is very commonly used.[38,39] For this method, first, one has to deposit a thin PMMA (sacrificial layer) followed by baking at 90 °C. After that, PMMA-adhered Bi_2O_2Se is immersed into the 2% HF solution for several hours to detach it from the substrate. Then, it is rinsed with DI water and fished with the targeted substrate. To remove the PMMA, finally it is dipped into the acetone, followed by isopropanol cleaning. Thus, the sample is transferred from the growth substrate to the target substrate. This method is most widely employed transfer technique. Nevertheless, the PMMA residues and HF partially damages the Bi_2O_2Se layer quality. Therefore, the transferred sample need to be verified to confirm they are PMMA residue-free and good quality for use in device fabrications.

1.3.2. PDMS-assisted transfer

The lower adhesion and brittleness of PMMA limits the large area transfer of Bi_2O_2Se. For better adhesion between the sacrificial layer and Bi_2O_2Se, PDMS provides higher adhesion than only PMMA sacrificial layer. Recently developed by Chen et al.[40], the PDMS-mediated transfer method offers a more straightforward time-saving route for transferring Bi_2O_2Se flakes. Due to the high adhesive force and the flexibility of PDMS, strong adhesion with the thin flakes offers a more convenient and effective transfer of thinner Bi_2O_2Se flakes and large wafer. The freestanding nature of ultrathin Bi_2O_2Se may lead to wrinkle formation during the transfer process. Several factors are likely to be involved in wrinkle formation. For example, the adhesion energy and interactions between the sample and the target substrate depend on the topography of the substrate. Thus, one should delicately etch the freestanding Bi_2O_2Se layer on a highly cleaned (e.g., hydrophilic) substrate to avoid wrinkles on the transferred sample. In contrast, wrinkle formation is helpful for realistic applications (e.g., Sensors). The formation of wrinkles enables physical surface modification, such as strain engineering, which modulates electrical properties. Therefore, to control the performance of electronic devices and meet the requirements for the excellent performance of 2D Bi_2O_2Se-based devices wrinkles are speculated to be advantageous.

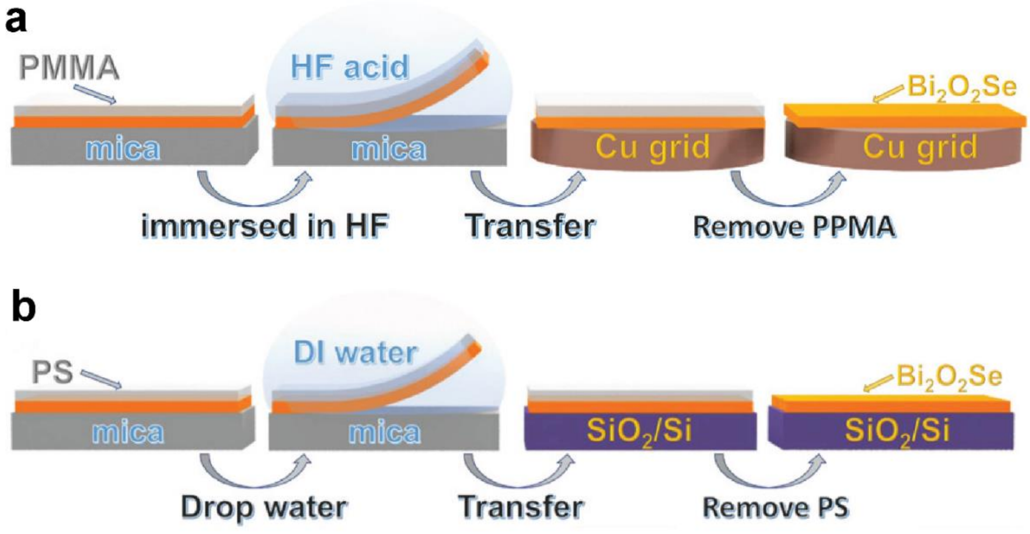

Fig. 1.6: Transfer methods of Bi_2O_2Se: schematic of (a) PMMA and (b) PS-assisted transfer process. Ref [39]

1.3.3. Polystyrene (PS)-assisted transfer

To avoid HF and PMMA, polystyrene (PS) can be coated as a sacrificial layer. Fu et al. developed a PS-assisted transfer method (**Fig. 1.6b**) for the Bi_2O_2Se layer.[38] In this case, PS is coated over Bi_2O_2Se/substrate and heated at 80°C for 15 min. After that, PS/Bi_2O_2Se/substrate is dipped into deionized (DI) water to delaminate the PS along with the Bi_2O_2Se layer from the growth substrate. Finally, it is washed with toluene to remove the PS. Hence the 2D Bi_2O_2Se is transferred to the new substrate. This method offers damage-free and PMMA-free transfer of the film.

1.4. Applications of 2D Bi_2O_2Se

Semiconducting properties with high carrier mobility made Bi_2O_2Se a feasible candidate for many applications such as photodetectors (PD)[27,41-44], sensors[45], memory and storage[46], solar cell[47], biomedical treatment[36], optical switches[48], artificial synapses[49], hydrogen evolution reactions[15], etc. Ferroelectric and ferroelastic properties could be utilized for nonvolatile memory (NVM) devices.[50] Therefore, the unique inherent properties of Bi_2O_2Se are beneficial for multifunctional applications. A few reported applications of 2D Bi_2O_2Se are highlighted in the following section,

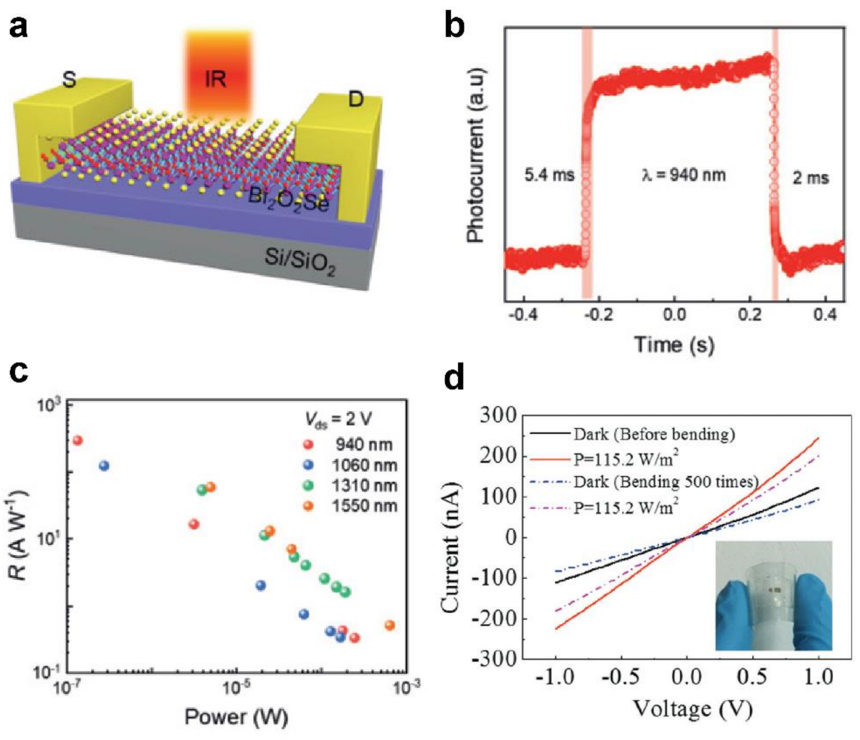

Fig. 1.7: 2D Bi_2O_2Se-based PD: (a) schematic of a Bi_2O_2Se PD. (b) Photo response of the device. (c) Responsivity as a function of illuminated power of 940 nm, 1060 nm, 1310 nm, and 1550 nm laser sources. Adopted from ref [41]. (d) I-V characteristics of a flexible PD. Adopted from ref [27].

1.4.1. 2D Bi_2O_2Se-based Photodetectors

A photodetector (PD) is a device that can convert a light signal to an electrical signal. Broadband (UV-IR) light detection is embedded in modern technology and human society. Due to a relatively higher bandgap, conventional 2Ds limit their detection limit up to the visible wavelength. With a unique combination of lower bandgap with rich electronic properties and good light-matter interactions, 2D Bi_2O_2Se provides a material platform for next-generation broadband photodetection at room temperature. Broadband PDs should have high responsivity, fast response speed, high sensitivity, and atmospheric stability, which are rare to meet simultaneously in a single 2D material. Due to low bandgap with tunability (0.89 eV – 2.00 eV)[6,7] with high absorption coefficient (of order of 10^5), Bi_2O_2Se can harvest light largely and detect a wide range of wavelengths (UV to IR). **Fig. 1.7a** shows a schematic of the Bi_2O_2Se-based photodetector. The response time of the Bi_2O_2Se device at 940 nm is 5.4/2 ms (rise/fall) (**Fig. 1.7b**).[41] The IR region responsivity of the Bi_2O_2Se photodetector is shown in **Fig. 1.7c** as a function of powers at 940, 1060, 1310, and 1550 nm.[41] The peak responsivities are in order of 10^2 AW^{-1} in the IR region. **Fig. 1.7d** shows the flexibility test of Bi_2O_2Se-based PD. Although the dark current and light current decrease after bending (500 times), the photocurrent remains nearly the same (**Fig. 1.7d**), indicating the robust durability of Bi_2O_2Se based flexible device.[27] Overall, the unique combination of high responsivity, ultrafast photo response, mechanical flexibility, and environmental stability makes 2D Bi_2O_2Se a promising material for realizing ultrafast and sensitive broadband PD and high-quality UV and IR imaging applications. However, Bi_2O_2Se-based PD limits their applications due to a few points, such as the high dark current because of their indirect, low bandgap, and moderate responsivity in UV-visible wavelengths. Moreover, the physics and impact of defects of Bi_2O_2Se on the performance of PD is largely unknown, which need to be addressed to understand the application potential of Bi_2O_2Se-based PD.

1.4.2. 2D Bi_2O_2Se and its hybrid PD

Integrating heterostructures (HS)/hybrid structures with similar chalcogenide 2Ds, other group 2Ds, 1Ds, and 0Ds is an efficient approach to enhance the performance of Bi_2O_2Se-based PD. Due to the electronic band bending (type-I and type-II) after the formation of HS, carrier transfer at the interface significantly alters the carrier concentration and mobility, influencing the photoelectric device's performance. **Fig. 1.8a** depicts the schematic of

WSe_2/Bi_2O_2Se HS PD. The band alignment (**Fig. 1.8b**) shows the type-II HS formation, which results in efficient charge transfer across the WSe_2 to Bi_2O_2Se heterojunction. The maximal on/off ratio is ~1.46 at +5V, and the peak responsivity is 483 mA/W (**Fig. 1.8c**). According to Luo et al. [42], the integrated WSe_2/Bi_2O_2Se HS exhibits self-powered photodetection with high on/off (10^5) and fast response speed (2.6 μS). It detects 365 to 2000 nm wavelength, indicating that such HS can be promising for broadband photodetection. Wang et al. fabricated 2D Bi_2O_2Se/1D Te HS PD with type-II bending that exhibits responsivity of order of 10^2 A/W and the response time 330 μS/430 μS.[51] **Fig. 1.8d** shows a 2D Bi_2O_2Se/0D PbSe hybrid structure PD. The corresponding PD with type-II hybrid structure formation (**Fig. 1.8e**) can detect beyond 2 μm with a responsivity of ~10^3 A/W (**Fig. 1.8f**).[43] Performances of a few Bi_2O_2Se and Bi_2O_2Se HS/ hybrid structures-based PD have been compared in **Table 1.1**. It is evident that a practical pathway for achieving the better performance of Bi_2O_2Se-based devices is making heterostructure.

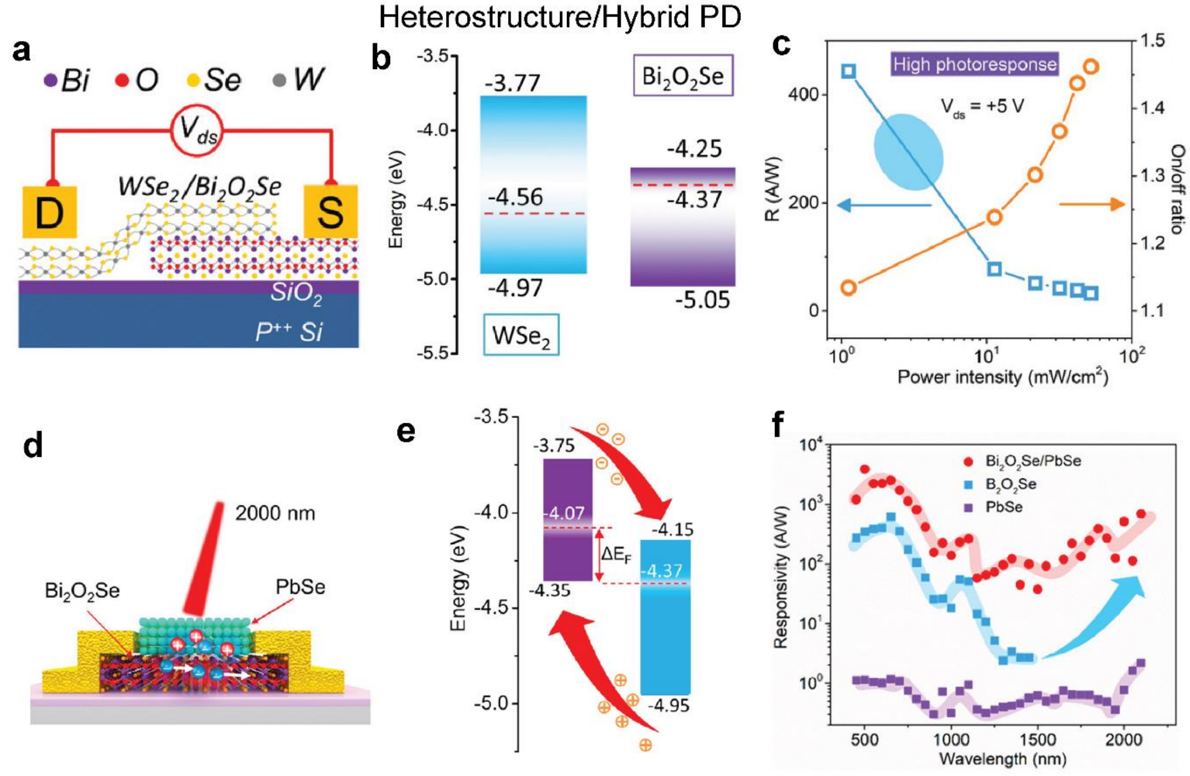

Fig. 1.8: 2D Bi_2O_2Se HS PD: (a) Schematic diagram of WSe_2/Bi_2O_2Se HS PD. (b) Energy band alignment of WSe_2/Bi_2O_2Se HS. (c) Responsivity and current on/off ratio of WSe_2/Bi_2O_2Se HS under varied light intensities at V_{ds}= +5 V. Adopted from the ref [42]. (d) Schematic illustration of the hybrid PD. (e) Energy band alignment of $PbSe/Bi_2O_2Se$ hybrid structure. (f) Responsivity as a function of wavelength of Bi_2O_2Se, PbSe, and $PbSe/Bi_2O_2Se$ hybrid PD. Adopted from ref [43].

Table 1.1: *Photodetector performance of Bi_2O_2Se and Bi_2O_2Se based HS/hybrid structure device.*

Material	Illuminated wavelength (nm)	Responsivity (A/W)	Response time (rise/fall)	Ref.
Bi_2O_2Se	1550	58	150/15 mS	41
Bi_2O_2Se	808	0.48	3.2/4.6 mS	27
Bi_2O_2Se	405	~100	62/601 µS	52
Bi_2O_2Se nanoribbons	650	327	2.1/3.2 µS	53
Bi_2O_2Se nanowires	808	~10-100	4.31/4.74 mS	54
Bi_2O_2Se/PbSe	2000	~1000	-/4mS	43
Bi_2O_2Se/ 1D Te	532	~100	330/430 µS	51

1.4.3. Other applications

The application of Bi_2O_2Se is not limited to photodetector; due to rich electronic properties with intrinsic absorption sites at Se vacancies, it has been demonstrated as a good material for oxygen gas sensors.[45] **Fig. 1.9a** shows the arrays of Bi_2O_2Se sensors, which are parallelly connected and used to detect sub-2 to sub-0.25 ppm oxygen (**Fig. 1.9b** and **Fig. 1.9c**).[45] The trace oxygen detection at room temperature facilitates the integration of 2D Bi_2O_2Se gas sensor for commercialization. In addition, Bi_2O_2Se is suitable for integrated optoelectronics and memory and storage, solar cell[47], optical switch[18], artificial synapses[49], and cancer detection[36].

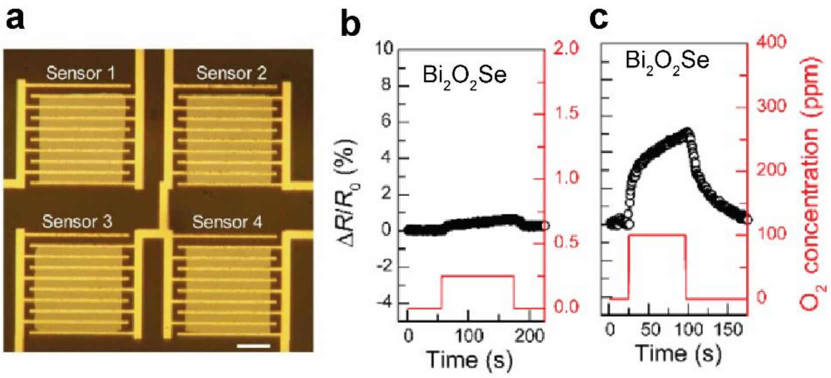

Fig. 1.9: Applications of 2D Bi_2O_2Se: (a) Optical photograph of the sensor array. Scale bar: 30 μm. (b, c) Responses of 2D Bi_2O_2Se to different oxygen concentrations. (b) 0.25 ppm and (c) sub-2 ppm at room temperature. Ref [45]

1.5. Challenges in synthesis and applications of 2D Bi_2O_2Se and its heterostructure

Although significant research has been carried out on synthesis, discovering inherent properties, and applications of 2D Bi_2O_2Se, several challenges remain in studying ultrathin B_2O_2Se.

i. Ultrathin layered growth is challenging due to the nvdW feature of Bi_2O_2Se. The CVD technique is a promising bottom-up synthesis approach with a high yield for the production of Bi_2O_2Se. However, it has several limitations, such as large area monolayer/few-layer growth, high quality, and scalable growth, which need further investigation. Controlling T_G, and choice of the growth substrate, carrier gas, etc., are crucial to tune the Bi_2O_2Se growth. Hence, the controlled growth strategies need to be developed.

ii. As a relatively new material, many unknown structural and optical properties are obstacles to fabricating devices and their integration for heterostructure formation. Therefore, further investigation of novel properties is desirable for efficient device applications.

iii. Further, integration of 2D Bi_2O_2Se with conventional nanomaterials, such as 0D, 1D, 2D materials, can bring unique properties due to the nvdW characteristic of this material. However, integration of heterostructure/hybrid structure is challenging with desired properties.

iv. Defects are inevitable in nanomaterials. However, their control and understanding of the effect are essential to regulate the charge transport and optoelectronic properties.

Thus, a thorough understanding of growth strategy on various substrates, optical and transport properties, and defect-induced properties requires further investigations to make better use of the material and develop 2D Bi_2O_2Se-based nanodevices.

1.6. Focus of the present thesis

2D Bi_2O_2Se, a potential optoelectronic material, has lacuna in controlled growth, and understanding its optoelectronic properties is still preliminary. Therefore, the present dissertation introduces controlled growth, including information on structural and optoelectronic properties of 2D Bi_2O_2Se and its hybrid integration for developing next-generation multifunctional applications. The focus of the present thesis is

1. CVD growth of ultrathin Bi_2O_2Se on mica substrate and its temperature-dependent optical studies for evaluating the in-plane thermal conductivity by employing non-destructive Raman measurement technique.
2. CVD growth of ultrathin Bi_2O_2Se on arbitrary growth substrates, including mica, sapphire, quartz, glass, SiO_2, etc., and observation of multiple exciton formations at room temperature.
3. Hybrid integration of 2D Bi_2O_2Se with 0D halide perovskite for understanding the interlayer charge transfer and their exploitation in superior photodetection.
4. Studies on charge transfer across the 2D nvdW Bi_2O_2Se and vdW MoS_2 layer.
5. Study of defect-induced photo-gating effect in ultrathin free-standing Bi_2O_2Se nanosheets with broadband (Vis-NIR) photodetection.

1.7. Organization of thesis

The thesis work contains seven chapters. **Chapter 1** provides introduction to 2D Bi_2O_2Se with a brief overview of reported research on crystal structure, properties, synthesis routes, and applications of Bi_2O_2Se. **Chapter 2** presents a systematic study of the CVD growth of 2D Bi_2O_2Se and temperature-dependent optical analysis of few-layer Bi_2O_2Se. **Chapter 3** presents the CVD-growth of ultrathin Bi_2O_2Se on arbitrary growth substrates and the observation of multiple exciton formations at room temperature. **Chapter 4** highlights the study of interfacial charge transfer on the hybrid 2D Bi_2O_2Se and 0D $CsPbBr_3$ perovskite for enhanced photodetection. **Chapter 5** investigates the stacking of vdW MoS_2 and nvdW Bi_2O_2Se to understand the interlayer charge transfer-induced photoluminescence quenching. **Chapter 6** presents the defect-induced photo-gating effect in colloidally-grown ultrathin Bi_2O_2Se and the modulation of photoconduction from negative to positive via vacuum annealing. **Chapter 7** contains a summary of the significant findings and conclusions of the thesis with future scopes.

References

1 Yan, M.-Y. *et al.* Reversible and Nonvolatile Manipulation of the Spin-Orbit Interaction in Ferroelectric Field-Effect Transistors Based on a Two-Dimensional Bismuth Oxychalcogenide. *Physical Review Applied* **18**, 044073, doi:10.1103/PhysRevApplied.18.044073 (2022).

2 Wang, F. *et al.* Emerging two-dimensional bismuth oxychalcogenides for electronics and optoelectronics. *InfoMat* **3**, 1251-1271, doi:https://doi.org/10.1002/inf2.12215 (2021).

3 Wu, M. & Zeng, X. C. Bismuth Oxychalcogenides: A New Class of Ferroelectric/Ferroelastic Materials with Ultra High Mobility. *Nano Letters* **17**, 6309-6314, doi:10.1021/acs.nanolett.7b03020 (2017).

4 Wu, J. *et al.* Controlled Synthesis of High-Mobility Atomically Thin Bismuth Oxyselenide Crystals. *Nano Letters* **17**, 3021-3026, doi:10.1021/acs.nanolett.7b00335 (2017).

5 Wei, Q. *et al.* Quasi-Two-Dimensional Se-Terminated Bismuth Oxychalcogenide (Bi2O2Se). *ACS Nano* **13**, 13439-13444, doi:10.1021/acsnano.9b07000 (2019).

6 Ghosh, T. *et al.* Ultrathin Free-Standing Nanosheets of Bi2O2Se: Room Temperature Ferroelectricity in Self-Assembled Charged Layered Heterostructure. *Nano Letters* **19**, 5703-5709, doi:10.1021/acs.nanolett.9b02312 (2019).

7 Wu, J. *et al.* High electron mobility and quantum oscillations in non-encapsulated ultrathin semiconducting Bi2O2Se. *Nature Nanotechnology* **12**, 530-534, doi:10.1038/nnano.2017.43 (2017).

8 Sun, J. *et al.* Ultralow Thermal Conductivity of Layered Bi2O2Se Induced by Twisting. *Advanced Functional Materials* **32**, 2209000, doi:https://doi.org/10.1002/adfm.202209000 (2022).

9 Yang, F. *et al.* Thermal transport and energy dissipation in two-dimensional Bi2O2Se. *Applied Physics Letters* **115**, 193103, doi:10.1063/1.5123682 (2019).

10 Gibson, Q. D. *et al.* Low thermal conductivity in a modular inorganic material with bonding anisotropy and mismatch. *Science* **373**, 1017-1022, doi:10.1126/science.abh1619 (2021).

11 Hossain, M. T. & Giri, P. K. Temperature-dependent Raman studies and thermal conductivity of direct CVD grown non-van der Waals layered Bi2O2Se. *Journal of Applied Physics* **129**, 175102, doi:10.1063/5.0049368 (2021).

12 Yu, J. *et al.* Excimer Formation in the Non-Van-Der-Waals 2D Semiconductor Bi2O2Se. *Advanced Materials* **34**, 2204227, doi:https://doi.org/10.1002/adma.202204227 (2022).

13 Yang, H. *et al.* Bolometric Effect in Bi2O2Se Photodetectors. *Small* **15**, 1904482, doi:https://doi.org/10.1002/smll.201904482 (2019).

14 Li, H. *et al.* Native point defects of semiconducting layered Bi2O2Se. *Scientific Reports* **8**, 10920, doi:10.1038/s41598-018-29385-8 (2018).

15 Ding, D., Jiang, Z., Ji, D., Nosang Vincent, M. & Zan, L. Bi2O2Se as a novel co-catalyst for photocatalytic hydrogen evolution reaction. *Chemical Engineering Journal* **400**, 125931, doi:https://doi.org/10.1016/j.cej.2020.125931 (2020).

16 Cheng, T. *et al.* Raman Spectra and Strain Effects in Bismuth Oxychalcogenides. *The Journal of Physical Chemistry C* **122**, 19970-19980, doi:10.1021/acs.jpcc.8b05475 (2018).

17 Khan, U. *et al.* Controlled Vapor–Solid Deposition of Millimeter-Size Single Crystal 2D Bi2O2Se for High-Performance Phototransistors. *Advanced Functional Materials* **29**, 1807979, doi:https://doi.org/10.1002/adfm.201807979 (2019).

18 Liu, J. *et al.* High output mode-locked laser empowered by defect regulation in 2D Bi2O2Se saturable absorber. *Nature Communications* **13**, 3855, doi:10.1038/s41467-022-31606-8 (2022).

19 Wei, Q. *et al.* Physics of intrinsic point defects in bismuth oxychalcogenides: A first-principles investigation. *Journal of Applied Physics* **124**, 055701, doi:10.1063/1.5040690 (2018).

20 Kim, U. J. *et al.* Visualizing Line Defects in non-van der Waals Bi2O2Se Using Raman Spectroscopy. *ACS Nano* **16**, 3637-3646, doi:10.1021/acsnano.1c06598 (2022).

21 Pan, L. *et al.* Significant Optimization of Electron–Phonon Transport of n-Type Bi2O2Se by Mechanical Manipulation of Se Vacancies via Shear Exfoliation. *ACS Applied Materials & Interfaces* **11**, 21603-21609, doi:10.1021/acsami.9b05470 (2019).

22 Li, P. *et al.* Mobility-Fluctuation-Controlled Linear Positive Magnetoresistance in 2D Semiconductor Bi2O2Se Nanoplates. *ACS Nano* **14**, 11319-11326, doi:10.1021/acsnano.0c03346 (2020).

23 Fu, H., Wu, J., Peng, H. & Yan, B. Self-modulation doping effect in the high-mobility layered semiconductor ${\mathrm{Bi}}_{2}{\mathrm{O}}_{2}\mathrm{Se}$. *Physical Review B* **97**, 241203, doi:10.1103/PhysRevB.97.241203 (2018).

24 Gao, M. *et al.* Defect Engineering in Thickness-Controlled Bi2O2Se-Based Transistors by Argon Plasma Treatment. *ACS Applied Materials & Interfaces* **14**, 15370-15380, doi:10.1021/acsami.1c24260 (2022).

25 Ge, Z. *et al.* Effect of surface Se concentration on stability and electronic structure of monolayer Bi2O2Se. *Applied Surface Science* **611**, 155528, doi:https://doi.org/10.1016/j.apsusc.2022.155528 (2023).

26 Chen, C. *et al.* Electronic structures and unusually robust bandgap in an ultrahigh-mobility layered oxide semiconductor, Bi2O2Se. *Science Advances* **4**, eaat8355, doi:10.1126/sciadv.aat8355.

27 Li, J. *et al.* High-Performance Near-Infrared Photodetector Based on Ultrathin Bi2O2Se Nanosheets. *Advanced Functional Materials* **28**, 1706437, doi:https://doi.org/10.1002/adfm.201706437 (2018).

28 Kang, M. *et al.* Low-Temperature and High-Quality Growth of Bi2O2Se Layered Semiconductors via Cracking Metal–Organic Chemical Vapor Deposition. *ACS Nano* **15**, 8715-8723, doi:10.1021/acsnano.1c00811 (2021).

29 Sagar, R. U. R. *et al.* Transfer-Free Growth of Bi2O2Se on Silicon Dioxide via Chemical Vapor Deposition. *ACS Applied Electronic Materials* **2**, 2123-2131, doi:10.1021/acsaelm.0c00344 (2020).

30 Khan, U. *et al.* Catalyst-Free Growth of Atomically Thin Bi2O2Se Nanoribbons for High-Performance Electronics and Optoelectronics. *Advanced Functional Materials* **31**, 2101170, doi:https://doi.org/10.1002/adfm.202101170 (2021).

31 Wu, J. *et al.* Low Residual Carrier Concentration and High Mobility in 2D Semiconducting Bi2O2Se. *Nano Letters* **19**, 197-202, doi:10.1021/acs.nanolett.8b03696 (2019).

32 Hossain, M. T., Jena, T., Debnath, S. & Giri, P. K. Defect-Induced Photogating Effect and its Modulation in Ultrathin Free-Standing Bi2O2Se Nanosheets with Visible to Near-Infrared Photoresponse. *Journal of Materials Chemistry C*, doi:10.1039/D3TC01129A (2023).

33 Khan, U. *et al.* Salt-Assisted Low-Temperature Growth of 2D Bi2O2Se with Controlled Thickness for Electronics. *Small* **19**, 2206648, doi:https://doi.org/10.1002/smll.202206648 (2023).

34 Liang, Y. *et al.* Molecular Beam Epitaxy and Electronic Structure of Atomically Thin Oxyselenide Films. *Advanced Materials* **31**, 1901964, doi:https://doi.org/10.1002/adma.201901964 (2019).

35 Zhang, C. *et al.* High-Mobility Flexible Oxyselenide Thin-Film Transistors Prepared by a Solution-Assisted Method. *Journal of the American Chemical Society* **142**, 2726-2731, doi:10.1021/jacs.9b11668 (2020).

36 Xie, H. *et al.* Biodegradable Bi2O2Se Quantum Dots for Photoacoustic Imaging-Guided Cancer Photothermal Therapy. *Small* **16**, 1905208, doi:https://doi.org/10.1002/smll.201905208 (2020).

37 Dang, L.-Y. *et al.* Organic Ion Template-Guided Solution Growth of Ultrathin Bismuth Oxyselenide with Tunable Electronic Properties for Optoelectronic Applications. *Advanced Functional Materials* **32**, 2201020, doi:https://doi.org/10.1002/adfm.202201020 (2022).

38 Fu, Q. *et al.* Ultrasensitive 2D Bi2O2Se Phototransistors on Silicon Substrates. *Advanced Materials* **31**, 1804945, doi:https://doi.org/10.1002/adma.201804945 (2019).

39 Chen, W. *et al.* High-Fidelity Transfer of 2D Bi2O2Se and Its Mechanical Properties. *Advanced Functional Materials* **30**, 2004960, doi:https://doi.org/10.1002/adfm.202004960 (2020).

40 Chen, W. *et al.* High-Fidelity Transfer of 2D Bi2O2Se and Its Mechanical Properties. *Advanced Functional Materials* **n/a**, 2004960, doi:10.1002/adfm.202004960 (2020).

41 Chen, Y. *et al.* Broadband Bi2O2Se Photodetectors from Infrared to Terahertz. *Advanced Functional Materials* **31**, 2009554, doi:https://doi.org/10.1002/adfm.202009554 (2021).

42 Luo, P. *et al.* Self-Driven WSe2/Bi2O2Se Van der Waals Heterostructure Photodetectors with High Light On/Off Ratio and Fast Response. *Advanced Functional Materials* **31**, 2008351, doi:https://doi.org/10.1002/adfm.202008351 (2021).

43 Luo, P. *et al.* PbSe Quantum Dots Sensitized High-Mobility Bi2O2Se Nanosheets for High-Performance and Broadband Photodetection Beyond 2 µm. *ACS Nano* **13**, 9028-9037, doi:10.1021/acsnano.9b03124 (2019).

44 Tan, C. *et al.* Exploitation of Bi2O2Se/graphene van der Waals heterojunction for creating efficient photodetectors and short-channel field-effect transistors. *InfoMat* **1**, 390-395, doi:10.1002/inf2.12025 (2019).

45 Xu, S. *et al.* Exploiting Two-Dimensional Bi2O2Se for Trace Oxygen Detection. *Angewandte Chemie International Edition* **59**, 17938-17943, doi:https://doi.org/10.1002/anie.202006745 (2020).

46 Xia, Y. *et al.* 2D Heterostructure of Bi2O2Se/Bi2SeOx Nanosheet for Resistive Random Access Memory. *Advanced Electronic Materials* **8**, 2200126, doi:https://doi.org/10.1002/aelm.202200126 (2022).

47 Huang, C. & Yu, H. Two-Dimensional Bi2O2Se with High Mobility for High-Performance Polymer Solar Cells. *ACS Applied Materials & Interfaces* **12**, 19643-19654, doi:10.1021/acsami.0c01364 (2020).

48 Tian, X. *et al.* An Ultrabroadband Mid-Infrared Pulsed Optical Switch Employing Solution-Processed Bismuth Oxyselenide. *Advanced Materials* **30**, 1801021, doi:https://doi.org/10.1002/adma.201801021 (2018).

49 Yang, C.-M. *et al.* Bidirectional All-Optical Synapses Based on a 2D Bi2O2Se/Graphene Hybrid Structure for Multifunctional Optoelectronics. *Advanced Functional Materials* **30**, 2001598, doi:https://doi.org/10.1002/adfm.202001598 (2020).

50 Yan, J.-M. *et al.* Optoelectronic Coincidence Detection with Two-Dimensional Bi2O2Se Ferroelectric Field-Effect Transistors. *Advanced Functional Materials* **31**, 2103982, doi:https://doi.org/10.1002/adfm.202103982 (2021).

51 Wang, W. *et al.* Highly Efficient Full van der Waals 1D p-Te/2D n-Bi2O2Se Heterodiodes with Nanoscale Ultra-Photosensitive Channels. *Advanced Functional Materials* **32**, 2203003, doi:https://doi.org/10.1002/adfm.202203003 (2022).

52 Hossain, M. T., Das, M., Ghosh, J., Ghosh, S. & Giri, P. K. Understanding the interfacial charge transfer in the CVD grown Bi2O2Se/CsPbBr3 nanocrystal heterostructure and its exploitation in superior photodetection: experiment vs. theory. *Nanoscale* **13**, 14945-14959, doi:10.1039/D1NR04470B (2021).

53 Wei, Y. *et al.* High-Performance Visible to Near-Infrared Broadband Bi2O2Se Nanoribbon Photodetectors. *Advanced Optical Materials* **10**, 2201396, doi:https://doi.org/10.1002/adom.202201396 (2022).

54 Li, J. *et al.* Oriented layered Bi2O2Se nanowire arrays for ultrasensitive photodetectors. *Applied Physics Letters* **114**, 151104, doi:10.1063/1.5094192 (2019).

Chapter 2

Temperature-dependent Raman studies and Thermal conductivity of direct CVD grown non-van der Waals layered Bi_2O_2Se

In this chapter, we systematically study the CVD of 2D Bi_2O_2Se. The growth of nvdW layered Bi_2O_2Se is challenging due to the weak electrostatic interaction among layers, as discussed in **Chapter 1**. Here, we present the CVD of an ultrathin Bi_2O_2Se with high structural and chemical uniformity. By tuning the growth temperature (T_G), we obtained ultra-smooth single crystals of few-layer Bi_2O_2Se (LBOS) on mica and quartz substrates, as confirmed by X-ray diffraction, micro-Raman, and high-resolution TEM analyses. Furthermore, a temperature-dependent Raman study has been conducted to study phonon dispersion in the as-grown LBOS. It is observed that the A_{1g} phonon mode frequency of LBOS varies linearly with the temperature with a first-order temperature coefficient (α) of $-0.017\,87 \pm 0.0011$ $cm^{-1}K^{-1}$. A phonon lifetime of 2.08 ps is found for LBOS at absolute zero temperature. Finally, the in-plane thermal conductivity of LBOS is estimated by a non-contact measurement technique in a relatively straightforward way. The in-plane thermal conductivity of LBOS is estimated to be ~1.6 W/mK, which is significantly low compared to other 2D materials. These results pave the way for CVD of large-area ultrathin LBOS on mica and quartz substrates and developing insights into electron-phonon and phonon-phonon interactions in nvdW 2D materials.

2.1. Introduction

Ultrathin Bi_2O_2Se layers have been synthesized in several ways, such as the solution process[1, 2], CVD[3-9], and modified[10, 11] CVD. Among the growth methods, CVD-grown ultrathin materials provide large single-domain sizes, chemically uniform samples, and structural uniformity. Thus CVD-grown samples are more beneficial for investigating the fundamental properties and device applications. Therefore, a Bi_2O_2Se growth study is required to explore the properties and device applications.

On the other hand, the performance of electronic devices has a fundamental dependency on the thermal conductivity of the materials used. The thermal conductivity of a material is often a unique parameter to understand the nano-systems better for scheming heat transport in broad areas of technological applications. There are vast applications where we demand remarkably low thermal conductivity, such as thermal barrier coatings[12], thermoelectric energy reaping, and solid-state cooling.[13] In this regard, 2D thermoelectric materials gained massive attention due to their outstanding electrical and mechanical properties.[14] These properties depend on the material's atomic bonding, including the atomic vibration caused by thermal excitation. Thus, the vibrational properties of 2D Bi_2O_2Se are fundamental to learning the electron-phonon interaction and the transport attributes and their profound influence on the performance of electronic devices.[15, 16]

The literature report says that in atomically thin graphene, the in-plane thermal conductivity is significantly higher than the cross-plane because the layers in such cases are accumulated with soft vdW forces.[17] Unlike graphene-like materials, in nvdW Bi_2O_2Se, the layers stacked with soft electrostatic forces might lead to lower in-plane thermal conductivity than cross-plane. Although experimental studies of thermal conductivities of vdW 2D materials (such as MoS_2, WS_2, etc.) have been broadly studied, it is very limited in the case of nvdW 2D materials. Hence, it is interesting to measure the thermal conductivity of ultrathin Bi_2O_2Se straightforwardly using the Raman measurement technique and compare it with other conventional 2D materials.

In this chapter, we have grown a few-layer (~3 layer) single crystal Bi_2O_2Se with a domain size of 25-µm with high chemical and structural uniformity on mica substrates via the CVD technique. Various structural and optical studies (such as XRD, Raman, TEM, etc.) are conducted to evaluate the structural and compositional uniformity of the samples. Temperature-dependent (78K-293K) Raman studies are made on a few-layer nanosheet of Bi_2O_2Se to study the nature of electron-phonon interactions and the phonon lifetime in the as-grown sample. We estimated the in-plane thermal conductivity of free-standing Bi_2O_2Se by a very straightforward approach by taking into account the heat circulation through the suspended sample from the laser spot toward the edge of the flakes and finally to the heat sink. Here, the heat sink is a Cu grid. In this measurement technique, the laser source is used as a source as well as the excitation source, making it more beneficial. The results are compared with the literature reports on other 2D materials.

2.2. Experimental details

2.2.1. Growth of 2D Bi_2O_2Se

2D Bi_2O_2Se crystals were synthesized inside a homemade low-pressure CVD system furnished with a long quartz tube (length 120 cm and diameter 35 mm). Bi_2O_3 powder (Alfa Aesar, 99.999%) and Bi_2Se_3 powder (Sigma Aldrich) were taken as precursors for the growth. **Fig. 2.1a** displays the schematic of the growth setup. Bi_2O_3 powder was located in the hot center, and Bi_2Se_3 powder was located upstream 5 cm away from the hot center for vaporization. Argon was engaged as the carrier gas to carry the vapor precursor to the cold region (8-12 cm downstream), where freshly cleaved mica resided as growth substrates. Typical growth conditions were as ensued. The quartz tube is brought to a base pressure of 1.9×10^{-2} using a rotary pump and repeatedly flushed with the Ar carrier gas (~250 sccm) at room temperature to remove O_2 contamination. After that, the furnace temperature was elevated to ~525 °C with a ramping rate of ~14 °C/min for 35 min with a gas flow rate of ~35 sccm (Note that, during this period, the temperature was ramped up rapidly towards T_G since the evaporation temperature of the precursor is ~525 °C). Then the ramping rate was slowed down 50% (~7 °C/min) to reach ~695 °C and held there for 25 mins before being allowed to cool naturally (**Fig. 2.1b**). The pressure was maintained at 400-500 mbar during the growth period. It may be noted that the electrostatic interaction between the layers could promote

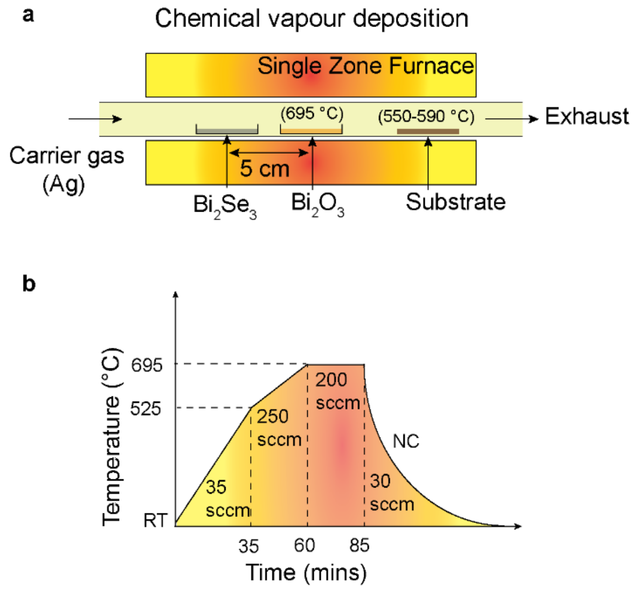

Fig. 2.1: (a) Schematic of CVD setup. (b) corresponding temperature profile and growth parameters for the growth of layered Bi_2O_2Se.

vertical growth instead of lateral growth, consistent with our observation. Consequently, chamber pressure and gas flow rate were maintained appropriately to obtain large-area lateral growth of the 2D Bi_2O_2Se crystal. The growth was conducted on a mica substrate at different T_G for optimization. The substrate was kept at 9, 10, 11, 12 cm away from the hot center to obtain different T_G. For comparison, growth was also conducted on quartz substrates.

2.2.2. Transfer of Bi_2O_2Se layer

To perform TEM analysis and power-dependent Raman study, we transferred the as-grown Bi_2O_2Se from the mica substrate to a TEM Cu grid. We have transferred the LBOS using the PMMA solution-based transfer method. Extracting the LBOS from the mica substrate to other desired places is difficult due to strong lattice matching and boding between the sample and growth substrate. Therefore, a highly efficient etchant is desirable to delaminate ultrathin Bi_2O_2Se from growth substrate (e.g. mica). We used hydrofluoric (HF) acid as an etchant. First, the PMMA solution is spin-coated on the sample at 3000 rpm for 60 s and baked on a hot plate at 90 °C. Subsequently, the spin-coated sample is dipped into the as-prepared HF solution for a few hours, then transferred into distilled water in a Petri dish for fishing the PMMA-coated LBOS flakes. The PMMA-coated flakes are fished on the TEM grid. The sample is dipped into acetone and kept for about 12 h to remove the PMMA layer from the LBOS. Finally, it is washed with isopropanol and dried for a few hours. Thus, the samples are transferred for further characterization.

2.2.3. Characterization techniques

The structural morphology of the sample has been identified by the Olympus optical microscope (BX51M). The as-grown samples' crystal structure has been collected from x-ray diffraction (XRD) patterns (Rigaku RINT 2500 TTRAX-III, Cu kα radiation). The crystalline phase in the as-grown LBOS has been examined by high-resolution micro-Raman spectroscopy (LabRam HR800, Jobin Yvon) with an excitation wavelength (λ_{ex}) of 488 nm (Ar ion laser). The excitation laser light was converged with a 100× objective lens to a spot size of ~1 μm, with an 80 μW laser power, lessening the possibility of laser heating-induced damage, and the generated signal was collected by a charge-coupled device (CCD) in a backscattering geometry conveyed through a multimode fiber grating of 1800 grooves mm^{-1}. The acquisition time has been kept constant while taking the Raman spectra. The as-grown sample thickness was estimated via atomic force microscopy (AFM) (Cypher, Oxford Instruments) in non-contact mode scanning. X-ray photoelectron spectroscopy (XPS) measurement was performed using a

PHI X-tool automated photoelectron spectrometer (ULVAC-PHI, Japan) with an Al Kα x-ray beam (1486.6 eV) at a beam current of 20 mA for the analysis of the chemical compositions. The high magnification surface morphology and crystal lattice arrangement of the pristine LBOS have been investigated employing TEM (JEOL-JEM 2010 ran at 200 kV). TEM study is conducted on a carbon-coated Cu grid of 300 mesh sizes (Pacific Grid, USA). The temperature-dependent Raman spectra comparisons were brought out, adopting a temperature stage with a remote functioning span of 50× objective with liquid nitrogen as the coolant. The power-based spectra in ambient temperature states are obtained by a 100× objective owning NA = 0.9 by utilizing various power of a 488 nm laser power source. To get the exact power experienced by the as-grown sample, we have calibrated the power at the same location, emitted through the 100× objective by a power meter.

2.3. Results and Discussion

2.3.1. Controlled CVD-growth of LBOS

The control over growth parameters such as growth temperature (T_G), carrier gas, precursors, and substrate location is crucial in the CVD method. We utilized a single-zone tube furnace with argon as the carrier gas, as illustrated schematically in **Fig. 2.1a,** for LBOS growth. We used freshly cleaved mica and quartz as the growth substrates for the optimization. The substrates were placed downstream in a comparatively lower temperature zone than the

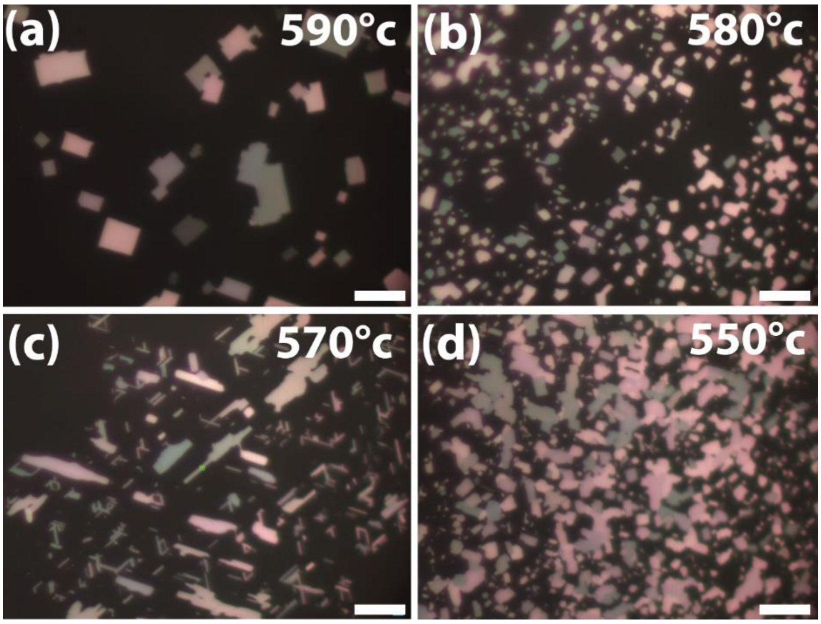

Fig. 2.2: OM images of LBOS at the different growth temperatures. The scale bar is 10 mm in each case.

precursor (Bi_2Se_3 and Bi_2O_3 powder) temperature zone. The complete temperature profile for CVD of LBOS is shown in **Fig. 2.1b,** discussed in **section 2.2.1**.

Depending on the T_G, different morphologies were observed by locating the mica substrate in various positions inside the quartz tube. Note that other growth parameters such as source temperature, the flow rate of carrier gas, chamber pressure, amount of the precursor, and location of the precursors were kept fixed. Optical microscopy (OM) images (**Fig. 2.2(a-d)**) confirm the different morphologies of CVD-grown samples at different T_G. At a relatively low T_G of 540–550 °C, LBOS exhibited inter-connected growth (**Fig. 2.2d**). Such growth behaviour might be ascribed to the generation of multi-nucleation centres at low T_G. As the T_G is increased to 560 °C, rod-like morphology was observed, and at 570 °C, square-shaped morphology began to appear along with the rod-like shape (**Fig. 2.2c**); at 580 °C, the majority of LBOS followed the squared morphology with smaller domain size (**Fig. 2.2b**). Interestingly,

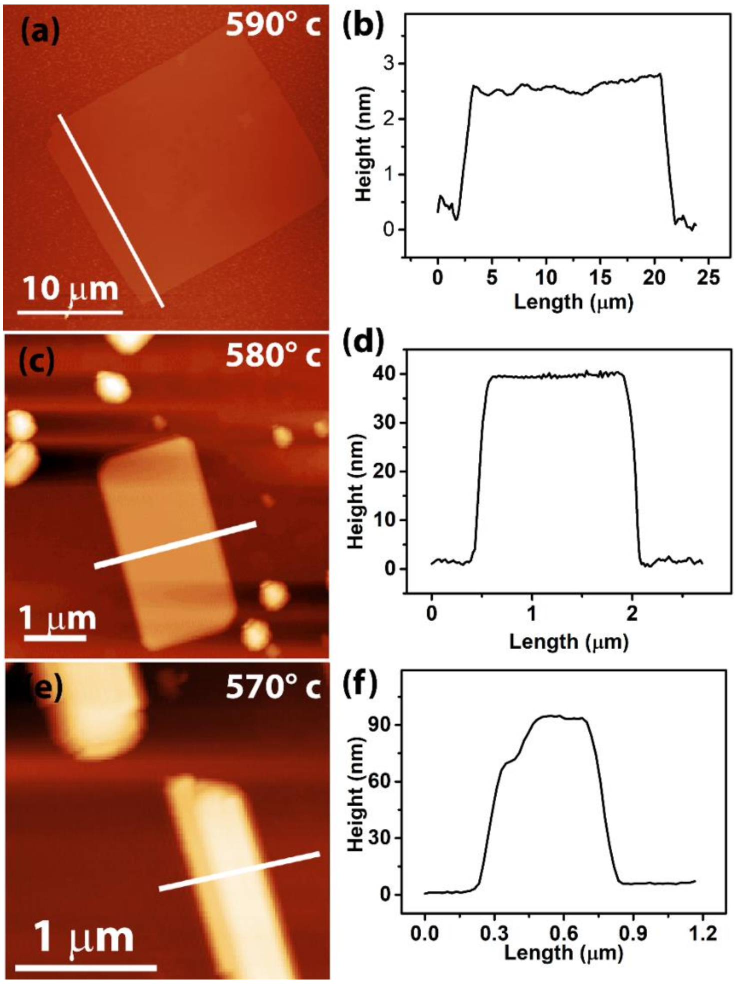

Fig. 2.3: AFM topography images of Bi_2O_2Se flakes grown on mica substrate at different substrate-temperatures: (a) 590° C (d) 580° C (e) 570° C, and (b,d,f) the corresponding height profiles, respectively.

at 590 °C, it achieves the large-area crystal domain of LBOS **(Fig. 2.2a)**. We did not observe LBOS growth at a temperature >600 °C. From our observation, the required thermal energy lies within 70 -75 meV for the CVD of 2D Bi_2O_2Se. The chemical reaction follows the Arrhenius nature with the increasing temperature up to 600 °C. Beyond 600 °C, the reverse reaction might occur, stopping further growth. In addition, the nucleation activation energy of the 2D Bi_2O_2Se on the growth surface is responsible for such exceptions. However, we cannot separate the accurate reason due to a lack of information about the nucleation activation energy of 2D Bi_2O_2Se. Besides, it suggests that the growth morphology of LBOS significantly depends upon the broad temperature range from 530 to 600 °C. Thus, we can obtain the LBOS growth based on the required morphology for applications by varying T_G. The high formation energy at high T_G is probably responsible for planar Bi_2O_2Se than inclined growth at lower T_G.

At the nanoscale range, the thickness of 2D material renders many intriguing properties. Thus, the knowledge of the thickness of the material is mandatory. However, according to the

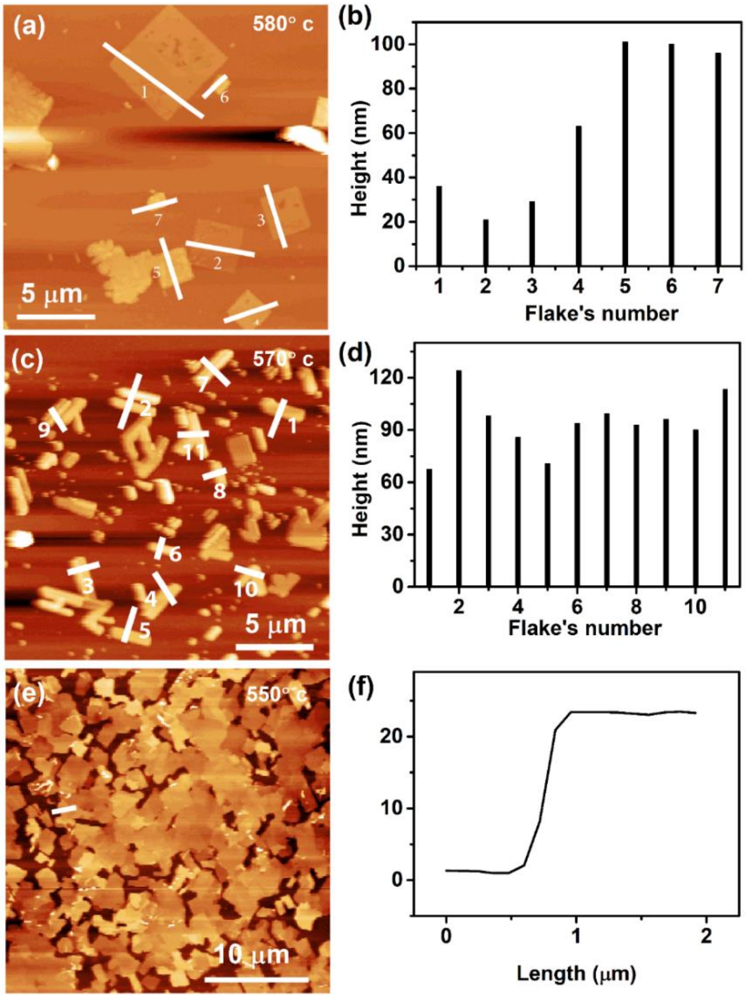

Fig. 2.4: (a, c, e) AFM images and (b, d, f) their corresponding height profile of as-grown LBOS grown at substrate temperatures of 580°C, 570°C, 550°C.

literature, the carrier mobility remains almost constant (~200 $cm^2V^{-1}s^{-1}$) for multilayer Bi_2O_2Se (> 6.2 nm) but dropped for few-layer (< 6.2 nm) thickness[18] suggesting multilayer samples are advantageous for high-performance optoelectronic devices. Therefore, we focussed on few-layer to multilayer Bi_2O_2Se rather than monolayer thickness. Thus, the thickness of Bi_2O_2Se was further investigated via AFM to learn about the thickness modulation with T_G. Detailed analyses of the surface topography and height of the as-grown Bi_2O_2Se are shown in **Fig. 2.3**. The height profile of an LBOS (**Fig. 2.3a**) at 590°C attests that it has a thickness of ~2.2 nm (**Fig. 2.3b)**, which corresponds to only three layers of Bi_2O_2Se. The thickness of the one-layer Bi_2O_2Se is 0.61 nm.[3] The uniform contrast on the flake shows an even thickness of the flake. The slight noise in the height profile near the edges may be due to the substrate's precursor residue or the tiny nucleus of the growth where the nucleation occurred. The flake size is smaller, and the thickness is higher at a relatively lower T_G (**Fig. 2.3c**). **Fig. 2.3d** shows a height of 38 nm, indicating multilayer growth of Bi_2O_2Se. A comparative histogram of four flakes shown in **Fig. 2.4b** depicts that as-grown Bi_2O_2Se flakes are of multilayer thickness. At 570 °C,

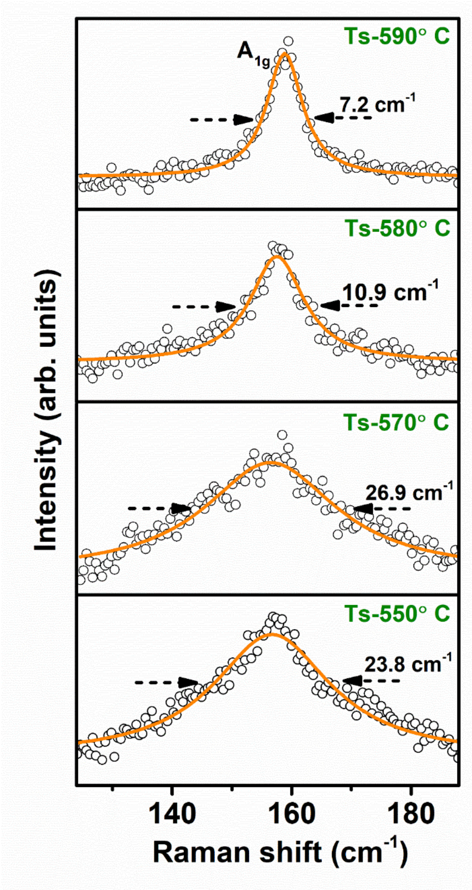

Fig. 2.5: Raman spectra of characteristics A_{1g} mode of Bi_2O_2Se for different substrate temperatures (Ts)/growth temperature (T_G). Symbols refer to the experimental data, while the solid line depicts the Lorentz fit. Inset values are of FWHM for each spectrum.

LBOS exhibits rod-like shape (**Fig. 2.3e**) with higher thickness (**Fig. 2.3f**), which is due to the inclined/vertical growth of the flakes. A histogram of height profiles for 9 flakes is depicted in **Fig. 2.4d**. At lower temperatures (~550°C), the flakes are interconnected (**Fig. 2.4e**) and multi-layered (**Fig. 2.4f**).

Micro-Raman measurement was performed to identify the characteristic Raman mode A_{1g} for LBOS grown at different T_G, as shown in **Fig. 2.5**. The observation of the characteristic A_{1g} Raman mode for all squared, rod-like and self-assembled morphologies confirms the growth of Bi_2O_2Se grown at different T_G. A comparison of Lorentz-fitted peak parameters for various T_G is given in **Table 2.1**. The full width at half maximum (FWHM) of the A_{1g} mode shows higher values for growth at lower T_G, indicating lower crystallinity for lower T_G (refer to **table 2.1**). But, the FWHM of the A_{1g} mode for the 550 °C case is lower than that of 570 °C (see **Table 2.1**). The growth at 570 °C is inclined or vertical. In contrast, at 550 °C, planar interconnected multilayer growth, as revealed in **Fig. 2.4**. Planar growth might result in a thicker layer with higher crystallinity and lower FWHM. In contrast, inclined growth shows slightly higher FWHM.

Table 2.1: *Comparison of Raman peak position and FWHM of A_{1g} mode in LBOS grown at different T_G.*

Substrate temperature (T_S)/growth temperature (T_G)	A_{1g} peak position (cm^{-1})	FWHM (cm^{-1})
590°C	158.8	7.2
580°C	157.5	10.9
570°C	156.5	26.9
550°C	156.7	23.8

XRD pattern is recorded for samples grown at different T_S/T_G, as shown in **Fig. 2.6.** It is apparent that growth at T_G gives rise to XRD peaks with other orientations due to the inclined growth on the mica substrate. We observe strong (*00l*) orientated growth of Bi_2O_2Se at 590 °C on mica substrate, whereas other orientated growth is observed in the case of lower T_G. The other peaks are attributed to the inclined crystal growth of Bi_2O_2Se. Line shape analysis of the XRD pattern corresponding to the (004) plane of LBOS grown at different T_G is summarized in **Table 2.2**, showing higher FWHM and lower peak intensity for lower T_G growth, indicating lower T_G growth crystallinity consistent with the Raman analyses. Furthermore, the growth process was also conducted on a quartz substrate. A comparison of XRD pattern and Raman spectra of LBOS grown on quartz and mica substrates is shown in **Figs. 2.7c** and **2.7d**, respectively. In the case of growth on a quartz substrate, we observe different orientations probably because of the lattice mismatch of Bi_2O_2Se and quartz substrate. Evidently, growth on mica substrate yields higher intensity and lower linewidth (0.13°) of XRD pattern and narrow Raman linewidth (FWHM: 5.5 cm^{-1}) at 590 °C, indicating the higher crystallinity of the films on mica substrate as compared to that on the quartz substrate. Based on the above, further

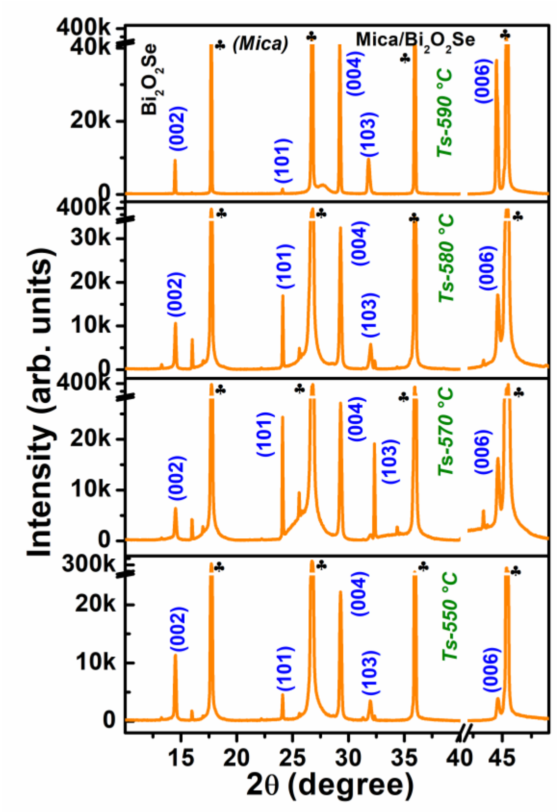

Fig. 2.6: XRD pattern of 2D Bi_2O_2Se grown on mica at different substrate/growth temperatures (T_S/T_G). '♣' Symbols refer to the mica substrate peak.

studies were conducted on LBOS grown on mica substrate with square morphology in this chapter. It may be noted that a thorough study on the impact of growth substrate is discussed in **Chapter 3**.

Table 2.2: *Comparison of (004) peak position, FWHM, and the peak intensity in the XRD pattern of LBOS grown at different* T_G.

T_G	(004) peak position (2θ) in degrees	FWHM (degree)	(004) peak position intensity (arb. units)
590°C	29.24°	0.13°	41773
580°C	29.29°	0.18°	30748
570°C	29.31°	0.19°	26223
550°C	29.29°	0.19°	21486

Fig. 2.7(a) shows the optical microscopy (OM) images of as-grown square-shaped LBOS. From the OM image, the domain size distribution is plotted and shown in **Fig. 2.7(b)**.

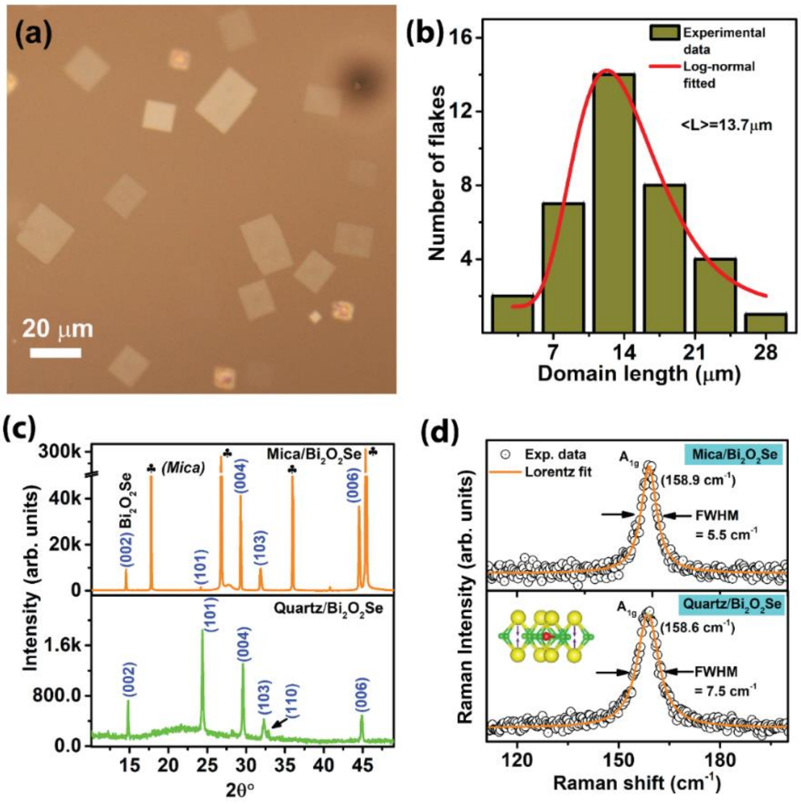

Fig. 2.7: a) Optical microscopy images of CVD-grown LBOS flakes. b) A histogram of the flakes' size distribution in an area of interest. c) Comparison of XRD patterns for crystalline Bi_2O_2Se flakes on quartz and mica substrates. '♣' symbol corresponds to the peak of the substrate.

The domain length distribution plot exhibits a maximum of ~25 μm size LBOS flakes grown at 590 °C. We have fitted the size distribution plot with lognormal distribution (**Fig. 2.7(b)**), which reveals an average flake size of 13.7 μm.

The comparative XRD pattern (**Fig. 2.7c**.) shows the intense peaks of LBOS on quartz and mica substrates. Mica substrate peaks are symbolized with "♣." XRD patterns of LBOS flakes on mica substrate consist of peaks at 2θ values of 14.49°, 29.23°, 31.79°, and 44.47° corresponding to (002), (004), (103), and (006) planes of Bi_2O_2Se, respectively. XRD pattern of LBOS flakes grown on quartz substrate exhibits intense peaks at 2θ values of 14.49°, 23.98°, 29.23°, 31.79°, 32.51°, and 44.47° corresponding to (002), (101) (004), (103), (110), (006), and (008) planes of Bi_2O_2Se, respectively. The measured and indexed peak position matches well with the tetragonal phase of Bi_2O_2Se (JCPDS Card No. 01-070-1549). Thus, we have successfully grown LBOS with high crystallinity on both mica and quartz substrates.

Further information on the crystallinity of LBOS (T_G ~ 590°C) is obtained from Raman spectroscopic measurement. Raman spectroscopy is a versatile tool to perform an in-depth analysis. For example, the knowledge of phonon dispersion mechanism, interlayer interactions, layer number, and doping could be obtained from the Raman peak or frequency shift of 2D materials. In the case of phonon decay in LBOS, A_{1g} Raman mode exhibit redshift, which results from the increment in the phonon dispersion similar to that of other 2D materials[15]. We discussed the phonon dispersion behaviour of A_{1g} mode in detail in **Sec. 2.3.2**. The micro-Raman spectrum (**Fig. 2.7d)** of as-grown LBOS flakes on quartz and mica substrate displays the characteristic A_{1g} mode, which is an out of plane mode originating from the vibration of two "Bi" atoms of two back-to-back $[Bi_2O_2]_n^{2n+}$ layers to "O" atoms (inset of **Fig. 2.7d**). The A_{1g} peak positions are 158.6 cm^{-1} on quartz and 158.9 cm^{-1} on a mica substrate. The FWHM of LBOS is 5.5 cm^{-1} grown on mica and 7.5 cm^{-1} grown on quartz substrates, suggesting a better crystallinity of as-grown LBOS on the mica substrate. The better crystallinity of LBOS on mica

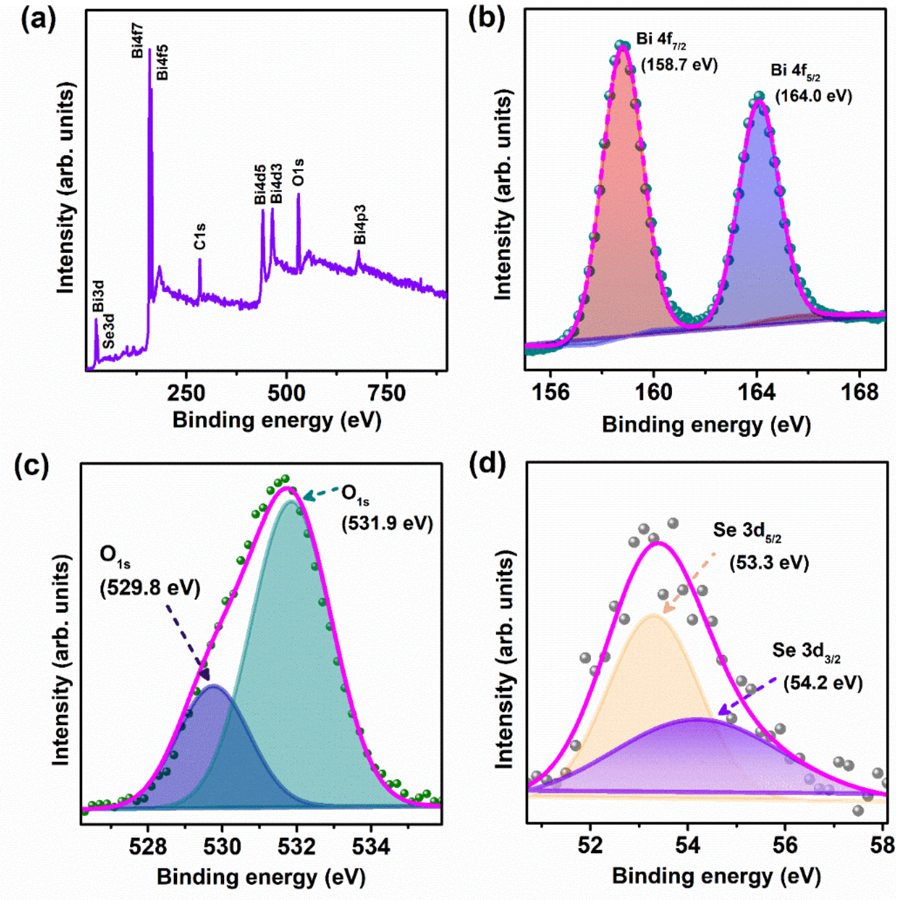

Fig. 2.8: (a) XPS survey scan spectrum of LBOS showing the presence of Bi, O and Se. High-resolution XPS spectra of as-grown LBOS on mica for (b) Bi 4f, (c) O 1s, and (d) Se 3d. The symbols represent the experimental data and the solid lines refer to fitted spectra.

is ascribed to a similar layered structure of mica.[19] It may be noted that more details of the Raman study depending on growth substrates are highlighted in **Chapter 3**.

We performed the XPS measurement to know the chemical composition of as-grown LBOS. **Fig. 2.8a** shows the survey scan XPS spectrum, confirming the presence of the Bi, O, and Se elements in LBOS. High-resolution XPS spectra (**Fig. 2.8(b-d)**) were recorded for Bi 4f, O 1s, and Se 3d states. The binding energies (BEs) are 158.7 eV and 164.0 eV of Bi $4f_{7/2}$ and Bi $4f_{5/2}$, respectively (**Fig. 2.8b**). The O 1s BEs are at 529.8 eV and 531.9 eV (**Fig. 2.8c**). For Se atoms, the BEs of Se $3d_{5/2}$ and Se $3d_{3/2}$ are 53.3 and 54.2 eV, respectively (**Fig. 2.8d**). The BEs of all the chemical components are consistent with literature[20], confirming the successful formation of Bi_2O_2Se.

The high-resolution features of LBOS are identified from the TEM images (**Figs. 2.9(a), 2.9(c), and 2.9(e)). Figs. 2.9(a)** and **2.9(c)** show the images of comparatively smaller size flakes, while **Figs. 2.9(b)** and **2.9(d)** depict the corresponding selected area electron diffraction (SAED) patterns. **Fig. 2.9(e)** shows the TEM image of a bigger flake of LBOS. The images reflect the uniform and square shape growth of the flakes. The SAED pattern (**Fig. 2.9(b))** reveals that the set of plane or lattice orientations are (110), (200), $(1\bar{1}0)$, $(0\bar{2}0)$, $(\bar{1}\bar{1}0)$, $(\bar{2}00)$, $(\bar{1}10)$, and (020). Careful observation shows that the intensity of the diffraction spots of the SAED pattern in **Fig. 2.9(d)** is reduced compared to the diffraction pattern in **Fig. 2.9(b)**. The lower intensity of diffraction spots is ascribed to the higher thickness and folded crystal of LBOS. The SAED pattern (**Fig. 2.9d**) of the folded LBOS (green dashed box in **Fig. 2.9c**) resembles a 90° rotation in the crystal orientation relative to the underneath layer. The planes of folded LBOS are displayed by $(110)'$, $(1\bar{1}0)'$, and $(200)'$ planes (**Fig. 2.9d**). HRTEM images of LBOS (**Fig. 2.9(f)**) show the lattice spacing of 0.29 nm ((110), $(1\bar{1}0)$) and 0.20 nm (200). It is obvious that the angle between the (110) and (110) planes is 90°, and the angle with the (200) plane of each particular plane is 45°, which further confirms the tetragonal crystal structure of Bi_2O_2Se. The cross-sectional atomic lattice arrangement of tetragonal Bi_2O_2Se is depicted in **Fig. 2.9(f)** (inset) with a clear view of the atoms' positions based on the literature to show the experimental results are consistent with the reported result.[3] The HRTEM analysis reveals that the CVD-grown 2D Bi_2O_2Se are high-quality single crystals.

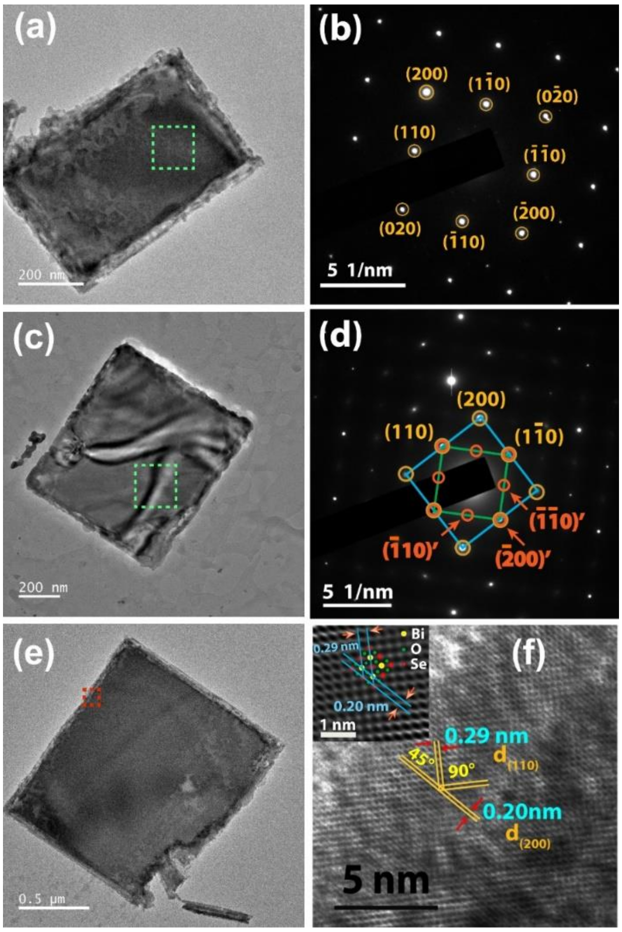

Fig. 2.9: (a, c) TEM images of LBOS flakes and (b, d) the respective SAED patterns. (e) TEM image of a bigger LBOS flake, and (f) the corresponding HRTEM lattice image. The inset shows the atomic positions of different elements.

STEM imaging was studied to check the elemental uniformity of the single Bi_2O_2Se crystal. The STEM image (**Fig. 2.10a**) with corresponding elemental mapping (**Figs. 2.10b-2.10d**] confirms the uniform elemental distribution of each component (Bi, O, and Se) in the LBOS. The LBOS single crystal exhibits atomic percentage of 41.95% (Bi), 38.91% (O), and 19.14% (Se) (**Fig. 2.10e**), which corresponds to the atomic ratio of ~2:2:1. In some LBOS, we perceived the deficiency of oxygen that may occur during the HF transfer process from the mica to the TEM grid. Thus, we confirmed the growth of high-quality single-crystal LBOS with high chemical uniformity. Further, this chapter carried out the studies with high-quality LBOS.

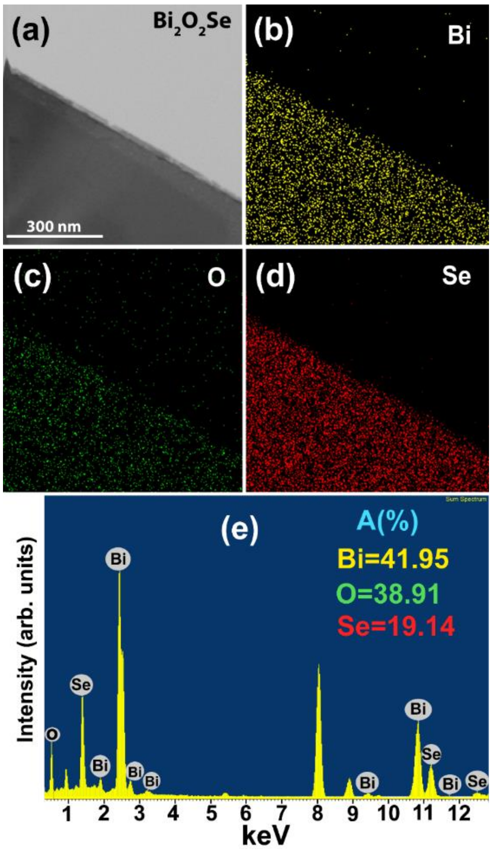

Fig. 2.10: (a) Scanning TEM image of LBOS flake, and (b-d) STEM elemental mapping of Bi, O, and Se atoms, respectively, present in the flake. (e) EDX spectrum of LBOS showing the atomic percentage of different elements.

2.3.2. Low-temperature Raman study

Temperature-dependent (78-293 K) Raman study has been conducted to understand the phonon dispersion and find the lattice thermal conductivity in LBOS. This study is interesting due to the unique nvdW structure of LBOS. The temperature dependency of frequency shift, FWHM broadening, and intensity modulation of characteristics A_{1g} Raman mode are discussed in detail.

2.3.2.1. Frequency shift

Fig. 2.11a displays the temperature-dependent Raman spectra of LBOS. The ascending order of peak shift of the A_{1g} (blue shift compared to room temperature peak position) is discerned in LBOS by lowering the temperature. The blue shift is due to anharmonicity in the lattice wave.[15] The Raman plots are adequately fitted with the Lorentzian line shape, and the elicited Raman peak position is plotted with temperature in **Fig. 2.11b**. The frequency (ω) of the Raman mode as a function of temperature (T) can be expressed by[15]

$$\omega = \omega 0 + \alpha T \qquad \mathbf{(2.1)}$$

, where $\omega 0$ is the frequency of the A_{1g} mode at absolute zero temperature and α is the first-order temperature coefficient of A_{1g} mode. From the linear fit of **Fig. 2.11b**, we obtained the value of α, which is -0.017 87 ± 0.0011 $cm^{-1}K^{-1}$. It may be noted that we did not consider the higher-order temperature coefficients because these terms are notable only at high temperatures.[15] Interestingly, the α is higher than the α of MoS_2 and $MoSe_2$, which are -0.0123 and -0.0094 $cm^{-1}K^{-1}$, respectively.[15, 21] This is expected because of the electrostatic interaction between the layers of LBOS.

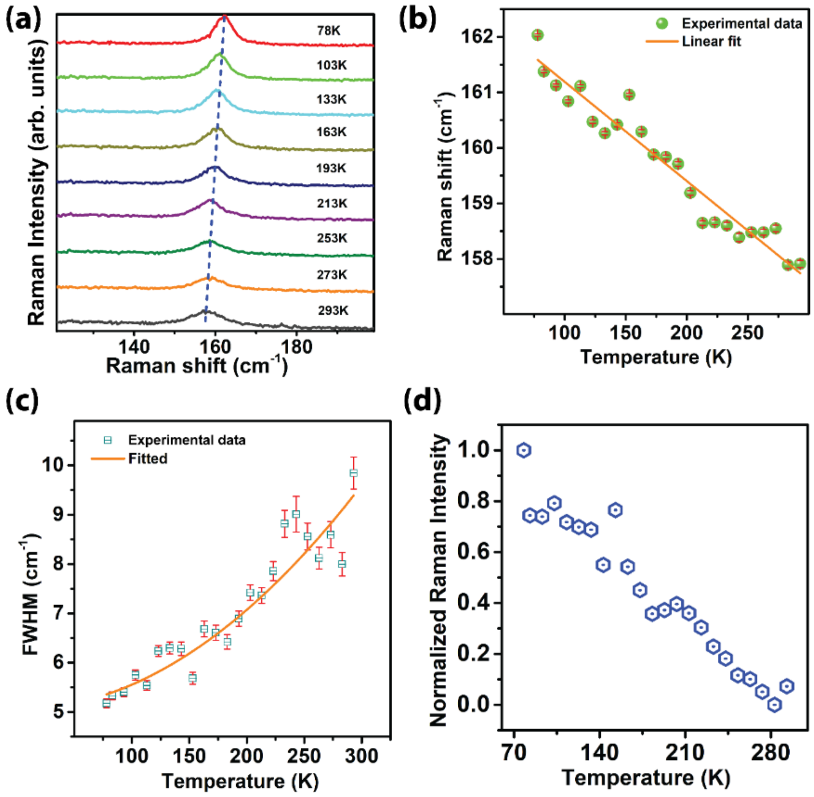

Fig. 2.11: (a) Temperature dependent (78K-293K) Raman spectra. (b) The peak positions (symbols) of characteristics A_{1g} mode as a function of temperature. The solid line depicts the linear fitting. (c,d) Variation of FWHM of the characteristics A_{1g} mode. The symbols represent the experimental data, and the solid line refers to the fitted data using **Eq. (2.2)** assuming an anharmonic phonon dispersion process. (d) Variation of A_{1g} mode intensity (normalized) as a function of temperature.

2.3.2.2. FWHM

Fig. 2.11c shows FWHM of the A_{1g} mode increases with the increase in temperature. To understand the broadening of the FWHM due to the temperature rise, we contemplate a qualitative analysis of temperature dependency of the A_{1g} mode. The contribution from the pure temperature effect mainly considers the anharmonic effects of three and four-phonon processes. Based on the report by Balkanski et al.,[22] the light scattering process can be viewed as involving the absorption of a photon, the emission of a photon, and the creation of an optical phonon, which then decays via anharmonicity into two phonons, three phonons, etc. The production of two and three phonons is called the three-phonon and four-phonon processes, respectively. The pure temperature effect, including three and four-phonon processes, can be described by a semi-quantitative simple model[23] given by

$$\Gamma(T) = \Gamma 0 + a\left[1 + \frac{2}{e^{c/2T} - 1}\right] + b\left[1 + \frac{3}{e^{c/3T} - 1} + \frac{3}{\left(e^{c/3T} - 1\right)^2}\right] \qquad \textbf{(2.2)}$$

, where $c=\hbar\omega/kB$, Γ0 is FWHM of the corresponding Raman peak at absolute zero temperature, and a and b are the second and third-order anharmonic constants, respectively. The above equation rightly fits the variation of FWHM as a function of temperature for three-phonon decay shown in **Fig. 2.11c**. The FWHM of A_{1g} Raman peak at absolute zero temperature is 5.1 cm^{-1}. It resembles a phonon lifetime of 2.08 ps at absolute zero temperature considering the relation between Raman FWHM and the phonon lifetime, i.e., lifetime $=1/\pi^*\Gamma$.[24] where Γ is the FWHM in the frequency scale. The values of the second and third-order constants are -0.124 ± 0.067 and 0.109, respectively.

2.3.2.3. Temperature-dependent Raman intensity

The variation of the Raman intensity of the A_{1g} mode with temperature **(Fig. 2.11d)** shows the systematic increases of Raman intensity with decreasing temperature. Su et al. reported that the temperature-dependent hot stimulated phonons of the vibrational state could be mathematically represented by the Bose-Einstein distribution function [25],

$$\eta(\omega, T) = \frac{1}{[e^{x} - 1]} \qquad \textbf{(2.3)}$$

, where $x=\hbar\omega/k_BT$. As the temperature increases, the single phonon decays into two, three, or multiple phonons. From the temperature-dependent Raman data, it is discerned that as the temperature decreases, the Raman frequency of the A_{1g} mode increases (**Fig. 2.11b**).

Consequently, in **equation 2.3**, the value of “x” increases, implying that the Bose-Einstein distribution function value will decrease and the number of stimulated phonons of the vibrational state in LBOS will decrease. Reduction in the number of stimulated phonons leads to a higher cumulative scattered photon of the same frequency at a fixed data acquisition time. Hence the higher intensity of the Raman signal is observed at a lower temperature. On the other hand, increasing the temperature increases the stimulated phonons, which eventually reduces the cumulative scattered photons of the same frequency. Due to energy conservation, the scattered photons of different frequencies lead to lower Raman intensity at a particular frequency and a higher FWHM. Thus, the intensity of the A_{1g} mode reduces along with FWHM broadening/phonon dispersion take place as the temperature increases in CVD-grown Bi_2O_2Se.

2.3.3. Thermal conductivity

As noted in the preceding discussion, the A_{1g} mode in LBOS is very sensitive to temperature. According to the power-dependent Raman study[15], laser excitation develops a significant local temperature on a sample. The rise of local temperature is advantageous for understanding the phonon behaviour inside the ultrathin sample. Power-dependent Raman measurement of ultrathin samples might be conducted on a supported or suspended film to estimate thermal conductivity. A supported LBOS is not a good choice for studying the power dependency of the phonon mode due to the quick dissipation of local heat to the substrate.[26] Therefore, the quick dissipation of heat need to be avoided to estimate the power coefficient accurately. To eliminate the heat dissipation through the supporting substrate, we have transferred our sample to a coating-free Cu grid, where the LBOS is suspended (schematically displayed in **Fig. 2.12(**a) and the optical microscopy image is shown in **Fig. 2.12(**b)). Thus, the conduction of the laser-generated heat occurs entirely through a suspended LBOS. The heat circulation of the laser source through the sample can determine the thermal conductivity of the LBOS. Heat can be disseminated in two ways. (a) Radially from the middle of the laser spot to the sample's border when the laser spot size is similar to the sample domain area. (b) Longitudinally from the laser spot to the sample's border if the laser spot area is smaller than the sample domain area. Heat circulation through a sample follows the following equation[26],

$$\frac{dQ}{dt} = -k.\oint \nabla T.dS \qquad \textbf{(2.4)}$$

, where dQ/dt is the rate change of heat through the sample radially, k is the thermal conductivity, ∇T is the temperature change, and S is the cross-sectional area through which the heat is transported. Since the flake is suspended, the in-plane distribution of the generated local heat due to laser excitation is faster than the cross-plane distribution toward the heat sink (Cu grid). The exact configuration of the heat propagation through LBOS is unknown and depends on the shape of the flake and its edges. In our case, the laser spot size is smaller than the flake size of LBOS. Assuming the laser heat is uniformly transporting from the flakes' middle to the border, the sample thermal conductivity is estimated. Balandin et al.[17] have calculated the thermal conductivity k of single-layer graphene using the formula,

$$k = \frac{1}{2\pi h}\left(\frac{dP}{dT}\right) \qquad \textbf{(2.5)}$$

, where dT is a change in temperature due to a change in power dP, and h is the flake's thickness. Sahoo et al.[15] simplified it for calculating the thermal conductivity of few-layer MoS_2 by taking the derivative of **Eq. (2.1)** with respect to the power (p) and substituting the value of dp/dT from **Eq. (2.5)** into it, expressed as

$$k = \frac{1}{2\pi h}\alpha\left(\frac{d\omega}{dP}\right) \qquad \textbf{(2.6)}$$

, where $d\omega$ is a shift in the A_{1g} peak position due to the variation of dP on the sample surface. “h” is the thickness of the LBOS. We observed a systematic red shift in the characteristic A_{1g} Raman peak position and broadening in linewidth with the increase in the laser power, as shown in **Fig. 2.12c.** The broadening of the A_{1g} peak of LBOS indicates localized heating due to the laser beam. The excitation power increment improved the intensity count along with the red shift of the A_{1g} peak. The reason for the enhanced intensities of the first-order Raman mode is the higher quantity of the incident photons associated with the increased laser power, resulting in more phonons participating in the scattering.[25] At relatively high laser power(>250 μW), we noticed laser-induced etching of the samples. It depends on the layer number of the sample. As the layer number shrinks, a higher possibility of etching at lower power is likely. The variation of the Raman peak position with the incident laser power variation is displayed in **Fig. 2.12d**. The systematic red shift in peak position with increasing power indicates a rise in the local temperature in the middle of the suspended LBOS. The slope of the corresponding plot gives the value of $d\omega/dP$ as $-0.046\,04 \pm 0.0008\ cm^{-1}\mu W^{-1}$.

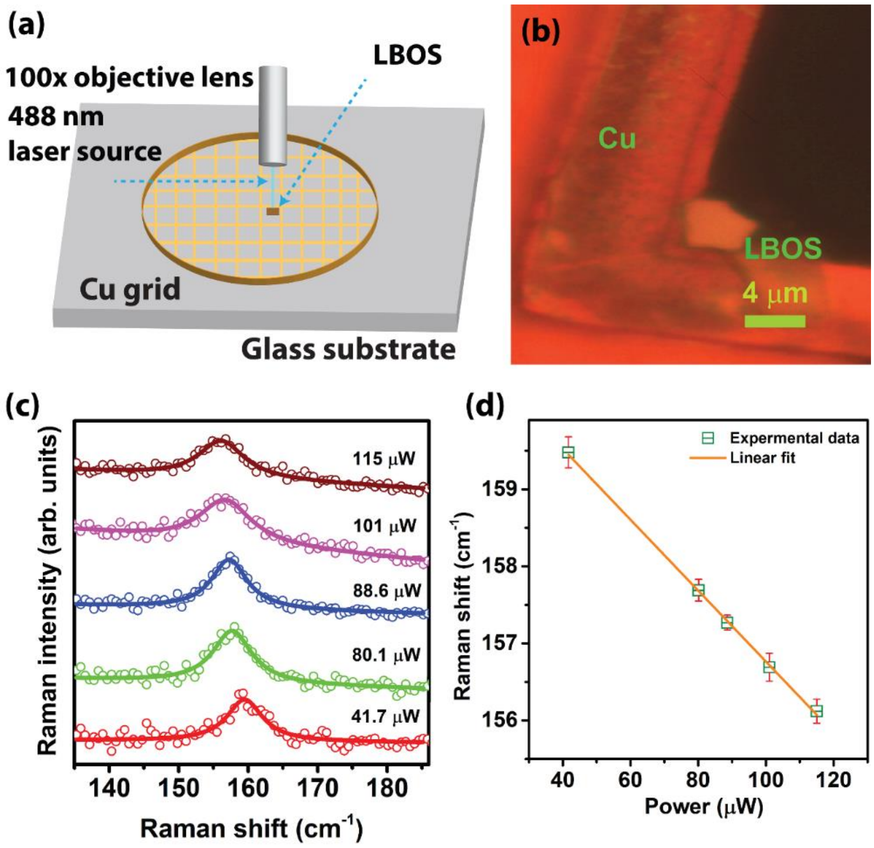

Fig. 2.12: (a) Schematic of power-dependent Raman measurement on LBOS, (b) optical image of LBOS flakes suspended on a Cu grid, (c) incident laser power-dependent Raman spectra of LBOS, and (d) corresponding Raman shift as a function of laser power. The solid line indicates the linear fit.

Finally, considering the fact that the heat is transporting radially from the middle of the suspended flake of LBOS, the in-plane thermal conductivity (k) can be estimated using Eq. (**2.6**). The in-plane thermal conductivity is evaluated with a flake thickness of ∼38 nm for the small flake size. The value of first-order temperature coefficient (α) is -0.017 87 ± 0.0011 $cm^{-1}K^{-1}$, and the value of $d\omega/dP$ is -0.046 04 ± 0.0008 $cm^{-1}\mu W^{-1}$. The in-plane thermal conductivity of the LBOS sample is thus estimated to be ∼ 1.6 ± 0.1 W/mK. A comparison chart of thermal conductivity and its experimental methods with different 2D materials is given in **Table 2.3**. The table shows that the LBOS exhibits very low thermal conductivity compared to conventional vdW TMDs and graphene. The lower ‘k’ might be attributed to the unique nvdW feature of LBOS. Interestingly, our estimated ‘k’ value is consistent with the recently reported thermal conductivity value of LBOS in **Ref.** [27]. Note that we adopted a more straightforward method to measure the ‘k’ value in LBOS. Despite the relatively high thickness of the LBOS flake, the estimated ‘k’ value is very close to that for the few-layer LBOS.[27] Thus, the low k, even for a multilayer sample, suggests that the multilayer ultrathin Bi_2O_2Se could be used for thermal barrier coating. Due to the ultrathin nature of LBOS, it is apparent that the cross-plane contribution to the thermal conductivity is much smaller than the in-plane contribution for the case of LBOS. However, more studies are required to isolate the individual contributions.

Table 2.2: *Comparison of thermal conductivity and its methodology for different 2D materials.*

Material	**Thermal conductivity (W/mK)**	**Measurement mode**	**Method**	**Reference**
Single-layer graphene	~ 4840-5300	Suspended in SiO_2 substrate	Micro-Raman	[17]
free-standing silicon nanowire	~ 53	Suspended	Micro-Raman	[26]
Few layer MoS_2	~ 52	Suspended at the edge of a Cu grid	Micro-Raman	[15]
Few layer WS_2	~ 32-53	Suspended in SiO_2 substrate	Micro-Raman	[28]
1L & 2L $MoSe_2$	~ 59 ± 18 , ~42 ± 13	Suspended in SiO_2 substrate	Micro-Raman	[21]
Few layer Black Phosphorus	~ 10-40	Suspended in SiN substrate	Micro-Raman	[29]
Few layer h-BN	~ 250-360	Suspended	Microbridge	[30]
Few layer InSe	~ 28.7-53.4	Supported in holey Si_3N_4/Si substrate	Micro-Raman	[31]
Bi_2O_2Se	~ 0.92-1.91	Suspended in whole mesh of a Cu grid	Micro-Raman	[27]
LBOS	~1.6 ± 0.1	Suspended at the edge of a Cu grid	Micro-Raman	*This work*

2.4. Conclusions

We have successfully synthesized 2D layered nvdW Bi_2O_2Se flakes by adopting a bottom-up CVD technique. We demonstrated that the LBOS flakes grown on mica substrates at relatively high T_G have excellent chemical uniformity and high crystallinity. The as-grown LBOS are of few-layer to multilayer thickness with a single crystalline nature. The interpretation of the temperature-dependent Raman spectral linewidth (FWHM) of LBOS reveals that an anharmonic phonon decay occurs when the temperature increases. The thermal conductivity of LBOS is estimated comparatively straightforwardly, considering the laser source's heat circulation. The calculated thermal conductivity value is $\sim 1.6 \pm 0.1$ W/mK at room temperature. which is beneficial for thermal insulation and thermoelectric devices. These results are essential for further investigating the temperature dependency and insights into electron-phonon and phonon-phonon interactions in nvdW 2D materials, such as 2D bismuth oxichalcogenides.

References

1. X. Tian, H. Luo, R. Wei, C. Zhu, Q. Guo, D. Yang, F. Wang, J. Li and J. Qiu, *Advanced Materials*, 2018, **30**, 1801021.
2. T. Ghosh, M. Samanta, A. Vasdev, K. Dolui, J. Ghatak, T. Das, G. Sheet and K. Biswas, *Nano Letters*, 2019, **19**, 5703-5709.
3. J. Wu, C. Tan, Z. Tan, Y. Liu, J. Yin, W. Dang, M. Wang and H. Peng, *Nano Letters*, 2017, **17**, 3021-3026.
4. J. Li, Z. Wang, Y. Wen, J. Chu, L. Yin, R. Cheng, L. Lei, P. He, C. Jiang, L. Feng and J. He, *Advanced Functional Materials*, 2018, **28**, 1706437.
5. U. Khan, Y. Luo, L. Tang, C. Teng, J. Liu, B. Liu and H.-M. Cheng, *Advanced Functional Materials*, 2019, **29**, 1807979.
6. S. Liu, C. Tan, D. He, Y. Wang, H. Peng and H. Zhao, *Advanced Optical Materials*, 2020, **8**, 1901567.
7. C. Tan, S. Xu, Z. Tan, L. Sun, J. Wu, T. Li and H. Peng, *InfoMat*, 2019, **1**, 390-395.
8. P. Luo, F. Zhuge, F. Wang, L. Lian, K. Liu, J. Zhang and T. Zhai, *ACS Nano*, 2019, **13**, 9028-9037.
9. Q. Fu, C. Zhu, X. Zhao, X. Wang, A. Chaturvedi, C. Zhu, X. Wang, Q. Zeng, J. Zhou, F. Liu, B. K. Tay, H. Zhang, S. J. Pennycook and Z. Liu, *Advanced Materials*, 2019, **31**, 1804945.
10. T. Tong, Y. Chen, S. Qin, W. Li, J. Zhang, C. Zhu, C. Zhang, X. Yuan, X. Chen, Z. Nie, X. Wang, W. Hu, F. Wang, W. Liu, P. Wang, X. Wang, R. Zhang and Y. Xu, *Advanced Functional Materials*, 2019, **29**, 1905806.
11. Z. Wu, G. Liu, Y. Wang, X. Yang, T. Wei, Q. Wang, J. Liang, N. Xu, Z. Li, B. Zhu, H. Qi, Y. Deng and J. Zhu, *Advanced Functional Materials*, 2019, **29**, 1906639.
12. N. P. Padture, M. Gell and E. H. Jordan, *Science*, 2002, **296**, 280-284.
13. G. Tan, L.-D. Zhao and M. G. Kanatzidis, *Chemical Reviews*, 2016, **116**, 12123-12149.
14. D. Li, Y. Gong, Y. Chen, J. Lin, Q. Khan, Y. Zhang, Y. Li, H. Zhang and H. Xie, *Nano-Micro Letters*, 2020, **12**, 36.
15. S. Sahoo, A. P. S. Gaur, M. Ahmadi, M. J. F. Guinel and R. S. Katiyar, *The Journal of Physical Chemistry C*, 2013, **117**, 9042-9047.

16. K. H. Lee, H.-J. Shin, J. Lee, I.-y. Lee, G.-H. Kim, J.-Y. Choi and S.-W. Kim, *Nano Letters*, 2012, **12**, 714-718.
17. A. A. Balandin, S. Ghosh, W. Bao, I. Calizo, D. Teweldebrhan, F. Miao and C. N. Lau, *Nano Letters*, 2008, **8**, 902-907.
18. J. Wu, H. Yuan, M. Meng, C. Chen, Y. Sun, Z. Chen, W. Dang, C. Tan, Y. Liu, J. Yin, Y. Zhou, S. Huang, H. Q. Xu, Y. Cui, H. Y. Hwang, Z. Liu, Y. Chen, B. Yan and H. Peng, *Nature Nanotechnology*, 2017, **12**, 530-534.
19. G. Franceschi, P. Kocán, A. Conti, S. Brandstetter, J. Balajka, I. Sokolović, M. Valtiner, F. Mittendorfer, M. Schmid, M. Setvín and U. Diebold, *Nature Communications*, 2023, **14**, 208.
20. M. Gao, W. Wei, T. Han, B. Li, Z. Zeng, L. Luo and C. Zhu, *ACS Applied Materials & Interfaces*, 2022, **14**, 15370-15380.
21. X. Zhang, D. Sun, Y. Li, G.-H. Lee, X. Cui, D. Chenet, Y. You, T. F. Heinz and J. C. Hone, *ACS Applied Materials & Interfaces*, 2015, **7**, 25923-25929.
22. M. Balkanski, R. F. Wallis and E. Haro, *Physical Review B*, 1983, **28**, 1928-1934.
23. J. Menéndez and M. Cardona, *Physical Review B*, 1984, **29**, 2051-2059.
24. G. Nilsson and G. Nelin, *Physical Review B*, 1971, **3**, 364-369.
25. Z. Su, J. Sha, G. Pan, J. Liu, D. Yang, C. Dickinson and W. Zhou, *The Journal of Physical Chemistry B*, 2006, **110**, 1229-1234.
26. S. Sahoo, S. K. Mallik, M. C. Sahu, A. Joseph, S. Singh, S. K. Gupta, B. Rout, G. K. Pradhan and S. Sahoo, *Nanotechnology*, 2020, **31**, 505701.
27. F. Yang, R. Wang, W. Zhao, J. Jiang, X. Wei, T. Zheng, Y. Yang, X. Wang, J. Lu and Z. Ni, *Applied Physics Letters*, 2019, **115**, 193103.
28. N. Peimyoo, J. Shang, W. Yang, Y. Wang, C. Cong and T. Yu, *Nano Research*, 2015, **8**, 1210-1221.
29. Z. Luo, J. Maassen, Y. Deng, Y. Du, R. P. Garrelts, M. S. Lundstrom, P. D. Ye and X. Xu, *Nature Communications*, 2015, **6**, 8572.
30. I. Jo, M. T. Pettes, J. Kim, K. Watanabe, T. Taniguchi, Z. Yao and L. Shi, *Nano Letters*, 2013, **13**, 550-554.
31. V. D. Botcha, M. Zhang, K. Li, H. Gu, Z. Huang, J. Cai, Y. Lu, W. Yu and X. Liu, *Journal of Alloys and Compounds*, 2018, **735**, 594-599.

Chapter 3

Room Temperature Exciton Formation and Robust Optical Properties of CVD-Grown Ultrathin Bi_2O_2Se Crystals on Arbitrary Substrates

This chapter thoroughly investigates the CVD of ultrathin 2D Bi_2O_2Se crystals on arbitrary substrates, including the growth substrates' effect on the structure and optical properties. In addition, this chapter discovers room temperature multiple exciton formation in ultrathin Bi_2O_2Se. The appealing success of nvdW 2D Bi_2O_2Se crystals in optoelectronics provides an exciting avenue to explore its photo-physical properties. Substantial studies have been reported to understand the properties of 2D Bi_2O_2Se, usually grown on mica substrates. Hence, a gap still persists in realizing the effect of arbitrary growth substrates on the structure and optical properties (such as absorbance and photoluminescence (PL)) of 2D Bi_2O_2Se. More importantly, the origin of broadband absorption and PL of new-age nvdW Bi_2O_2Se at visible and near-infrared wavelengths is rarely taken care of. We demonstrate that forming multiple excitons in momentum valleys is responsible for broadband absorption and visible PL from a 2D Bi_2O_2Se. Moreover, this study unfolds that the growth substrates (mica, sapphire, quartz, SiO_2, glass) introduce strain/doping in CVD-grown Bi_2O_2Se crystals, and consequently, the morphology, lattice constant, absorption coefficient, optical bandgap, refractive index, and PL properties are modulated. In addition, the possible direct/indirect multiple exciton formation at the valance band to conduction band at different symmetry points of Bi_2O_2Se is experimentally understood and corroborated with the theoretical electronic band structure calculation. These findings are significant for the futuristic optoelectronic applications of Bi_2O_2Se and the choice of growth substrates on the directly fabricated nanodevices.

3.1. Introduction

2D Bi_2O_2Se is extensively studied to fabricate electronic devices. The unique combination of outstanding air stability and carrier mobility with the built-in charged surface renders open scope for discovering inherent properties of 2D Bi_2O_2Se. In fact, little is known about the photo-carrier/exciton dynamics in ultrathin Bi_2O_2Se. Fundamentally, a semiconductor of a direct bandgap nature results in PL emissions through direct exciton formation, for example, A and B excitons in monolayer MoS_2.[1] On the other hand, a unique geometry with intralayer/interlayer electrostatic attractions in 2D Bi_2O_2Se with broad absorption could show PL in visible and near-infrared (NIR) regions. It is indeed interesting to investigate the exciton dynamics in ultrathin Bi_2O_2Se layers, despite its indirect gap nature. In addition, it is necessary to develop materials on the desired substrate surface based on their application. Depending upon research and application, 2D materials have been prepared on different substrates, such as quartz, mica, SiO_2, glass, sapphire, $SrTiO_3$, etc. Bi_2O_2Se has been grown on mica substrate[2-7], $SrTiO_3$[8], and SiO_2 substrate[9]. Many reports have been devoted to exploring the structural and optical properties of Bi_2O_2Se, and optoelectronic applications.[10] Nevertheless, to date, there is no study on the influence of growth substrates of Bi_2O_2Se crystals on their structural and optical properties. To address the lacunae, we explored the effect of growth substrates on the structural and optical properties of Bi_2O_2Se crystals grown via CVD.

In this chapter, we studied the substrate-induced effects on the microstructure and optical absorption and emission properties of directly CVD-grown Bi_2O_2Se crystals. The morphology of the crystals changes not only with growth temperature but also due to physical roughness, chemical activity, and lattice structure compatibility of the substrate. We show that with the growth at 580 °C, mica substrate promotes squared morphology of Bi_2O_2Se crystals with sharp edges due to its positively charged surface, consistent with the studies of **Chapter 2**[11]**.** However, the sapphire substrate exhibits different morphology due to its lattice incompatibility (hexagonal crystal surface). Similarly, studies on other substrates are analyzed in detail. At 560 °C, sapphire shows non-uniform irregular multilayer growth, and similar to mica substrate, SiO_2 produces rod-like multilayer growth, unraveling the role of substrate crystallinity and surface chemistry, including surface roughness.[11] Thus, the surface of the substrate makes the structure and optical properties of crystals to vary. All the substrates (mica, SiO_2, sapphire, glass, quartz) introduce an out-of-plane compressive strain in the as-grown Bi_2O_2Se layer. Lattice parameters and induced strain have been quantified via XRD analyses. We observe a broad optical transition in visible and NIR wavelength ranges. We identified the absorption peaks of Bi_2O_2Se depending upon the growth substrates, revealing the peak shift primarily due to the substrate-induced strain. Subsequently, the optical bandgap of Bi_2O_2Se can be modulated based on growth substrates. It is worth mentioning that the carrier mobility remains almost constant (~200 $cm^2V^{-1}s^{-1}$) for multilayer Bi_2O_2Se (> 6.2 nm), but dropped for few-layer (< 6.2 nm) thickness[2] suggesting multilayer samples are promising for optoelectronic devices. Thus, exploiting the effect of growth substrate in a multilayer sample is indeed crucial for designing a device with known functionalities.

Additionally, the origin of PL from Bi_2O_2Se film in the visible-NIR region has been explored using reflectivity and PL spectroscopy measurements. Through a combined experimental and theoretical calculation, our results demonstrate the multiple exciton formation, which inevitably results in the broad absorption and broad PL peak for Bi_2O_2Se. The PL intensity can be tuned depending on the growth substrate, mainly due to the change in carrier density/induced intrinsic strain. We evaluate the exciton binding energy of Bi_2O_2Se, which is lower than that of conventional TMDC, such as MoS_2 and WS_2. The implication of these results on the fundamental understanding of structural and optical properties of Bi_2O_2Se, including its photo-excited carrier dynamics, are discussed.

3.2. Experimental details

3.2.1. Materials

Bi_2O_3 (99%, Alfa Aeser) and Bi_2Se_3 (99.995%, Sigma Aldrich) are the precursors for Bi_2O_2Se growth, similar to **Chapter 2**. Commercial quartz, mica, sapphire, SiO_2, and glass substrates were purchased and used as growth substrates. Quartz, mica, and sapphire were used without further cleaning; however, SiO_2 and glass were cleaned before use. Since commercial SiO_2 and glass were purchased in bulk and kept in a laboratory atmosphere, we conducted Acetone, IPA, and DI water cleaning utilizing a bath sonicator to remove the microdust. However, commercial quartz, mica, and sapphire were purchased with high purity and came as properly sealed pieces. Hence, we did not do further cleaning for quartz, mica, and sapphire substrates.

3.2.2. Preparation

To prepare 2D Bi_2O_2Se crystals, we followed **section 2.2.1**. Similar to the discussion in **section 2.2.1**, we have kept the quartz, sapphire, SiO_2, and glass substrates in place of the mica substrate. Bi_2O_3 and Bi_2Se_3 were kept at the center and away from the center (i.e., against the gas flow) of the heating-temperature zone, respectively. The substrate was kept 9 to 12 cm away from the top high-temperature region in the gas flow direction. The 9 to 12 cm distance is chosen for keeping the growth substrates at the different T_G. The temperature gradient varies from 580 °C to 540 °C in increasing order of distance (9-12 cm) from the centre of the heating zone. The location of the growth substrate mica, sapphire, and SiO_2 is at 9-11 cm (T_G~560-580 °C), and glass and quartz are at 11-12 cm (T_G~540 °C). Note that the different substrates were used in different sets of experiments.

3.2.3. Characterization techniques

XRD, AFM, and Raman characterization details are similar to **section 2.2.2**. Absorption and reflectivity measurement was performed operating a commercial spectrophotometer (PerkinElmer, Lambda 950). X-ray photoelectron spectroscopy (XPS) measurement was performed using a PHI 5000VersaProbe III (M/s Physical electronics, USA) with a monochromated K-Alpha X-ray source (1486.7 eV) for the analysis of the chemical compositions. We adopted a temperature stage with a remote functioning span of 50× objective for temperature-dependent PL measurement with an excitation wavelength of 488 nm. Liquid nitrogen was used as the coolant.

3.3. Computational details

First-principles calculations were carried out through density functional theory (DFT), as incorporated in the Quantum ESPRESSO software package [12]. The geometry of bulk Bi_2O_2Se

was optimized by using generalized gradient approximation with Perdew-Burke-Ernzerhof (GGAPBE)[13] exchange-correlation methods, including Grimme's DFT-D3[14]. The projector augmented wave (PAW)[15] approach described core-valence electron interaction, and a plane wave basis cut-off was set at 80 Ry. Monkhorst-Pack k-point[16] mesh of 8 × 8 × 3 [51] was used for geometry optimization and density of states (DOS) calculation. Self-consistency was obtained by employing a force of 10^{-2} eV/Å. To get the bandgap appropriately for such a strong correlation system, the Hubbard parameter (U) of the generalized gradient approximation (GGA+U) has been used[52]. The U was added for Bi and Se elements (Bi = 2.5 eV, Se = 2.0 eV).

3.4. Results and Discussion

3.4.1. CVD-growth of 2D Bi_2O_2Se on arbitrary substrates

At first, Bi_2O_2Se crystals were grown on different substrates via chemical vapor deposition (detailed information is depicted in **Fig. 3.1**). Our earlier study (**Chapter 2**) reveals that the morphology of the Bi_2O_2Se grown on mica substrates varies with growth temperature (T_G).[11] In the present chapter, the samples were grown on sapphire, SiO_2, quartz, glass, and mica substrates. The substrates exhibit different surface properties, such as physical roughness and chemical activity, which impact the nucleation over the surface during the growth. To check the physical roughness of the substrates, we conducted atomic force microscopy and the topography represented in **Fig. 3.1 (a-e)**. The mica is a smoother surface with very low roughness (R_q) of 15 pm (**Fig. 3.1a**). Favorably, squared morphology (**Fig. 3.1f**) of Bi_2O_2Se flakes with sharp edges with 90° angle (inset of **Fig. 3.1f**) was observed on mica substrate at a T_G of 580 °C, consistent with the earlier study.[11] The sapphire substrate exhibits a smooth surface with a roughness of 25 pm (**Fig. 3.1b**). On sapphire, Bi_2O_2Se growth shows a rectangular truncated hexagonal edge with an angle of 120° (inset of **Fig. 3.1g**) at T_G~ 580°C. Sharp edges of Bi_2O_2Se on mica are attributed to lattice matching at the substrate/sample interface, whereas rectangular truncated hexagon edges might arise due to sapphire's hexagonal crystal surface. T_G and vapor pressure variations are critical in changing the morphology of as-grown Bi_2O_2Se. At T_G~560 °C, the growth on sapphire and SiO_2 show non-uniform irregular and rod-like morphology (see **Fig. 3.1h and i** and their inset), respectively, with multilayer thickness similar to mica case, as studied in the earlier chapter.[11] Growth on quartz and glass results in the agglomeration of Bi_2O_2Se crystals at ~540 °C. Note that at a higher T_G (~580 °C), we did not observe any film growth on quartz, glass, and SiO_2 due to unsuitable thermodynamic conditions. SiO_2 possesses a surface with a comparatively higher roughness (~90 pm) due to its amorphous nature with active dangling bonds (shown in **Fig. 3.1c**). Dangling bonds and defects over the surface make the surface chemically reactive. SiO_2 exhibits rod-like morphology of Bi_2O_2Se crystals on amorphous and chemically active surfaces. Interestingly, mica results in similar rod-like vertical growth at the same temperature window.[11] However, the thickness and area of Bi_2O_2Se crystal are different in both substrates. Mica produces higher thicknesses with a larger area of Bi_2O_2Se crystals than SiO_2. This indicates faster nucleation over the mica surface than the SiO_2 substrate. Faster nucleation on the mica surface is ascribed to its cleaved surface with lattice matching. The similar rod-like structure of Bi_2O_2Se on SiO_2 and mica suggests that the favorable formation energy of rod-like Bi_2O_2Se is ~560 °C. Mica and sapphire both have smoother and crystalline surfaces, though mica shows distinct squared morphology of Bi_2O_2Se crystals due to the similar layered structure, which accelerates the nucleation via electrostatic interaction with Se-atoms underneath the surface of Bi_2O_2Se. During nucleation, electrostatic attachment is generated at the Bi_2O_2Se/mica interface, stimulating the form of sharp edge squared shape morphology. Nevertheless, a charged surface is lacking in sapphire, which results in rectangular truncated hexagonal edge growth. Although the quartz substrate is crystalline with a smooth surface, as shown in **Fig. 3.1d** (roughness ~50 pm), lower T_G (~540°C) results in agglomerated growth over the surface. A similar kind of agglomerated growth was observed on the glass substrate due to a highly rough surface (R_q~

140 pm, **Fig. 3.1e**). However, the film thickness (~25 nm) on quartz substrate is ~five times lower than that on the glass substrate (~120 nm) (**Fig. 3.1v** and **3.1w**). At lower T_G, vapor pressure/ molecular density is lower than at higher T_G, and it may initiate multiple nucleation centers over a particular region, resulting in agglomerated growth. Higher vapor pressure/density at high T_G can create only a few nucleation centers in the same surface area. Now, for the same growth duration, it leads to individual nucleation with larger lateral growth. Sequentially, at high T_G, a few micrometers (2-5 micrometers) of individual flakes were obtained, and at lower T_G, non-uniform agglomerated growth was obtained over a large area. Since positively charged $[Bi_2O_2]^+$ and negatively charged $[Se]^-$ are forming a layered structure with weak electrostatic force, in contrast to other conventional vdW 2D materials (such as

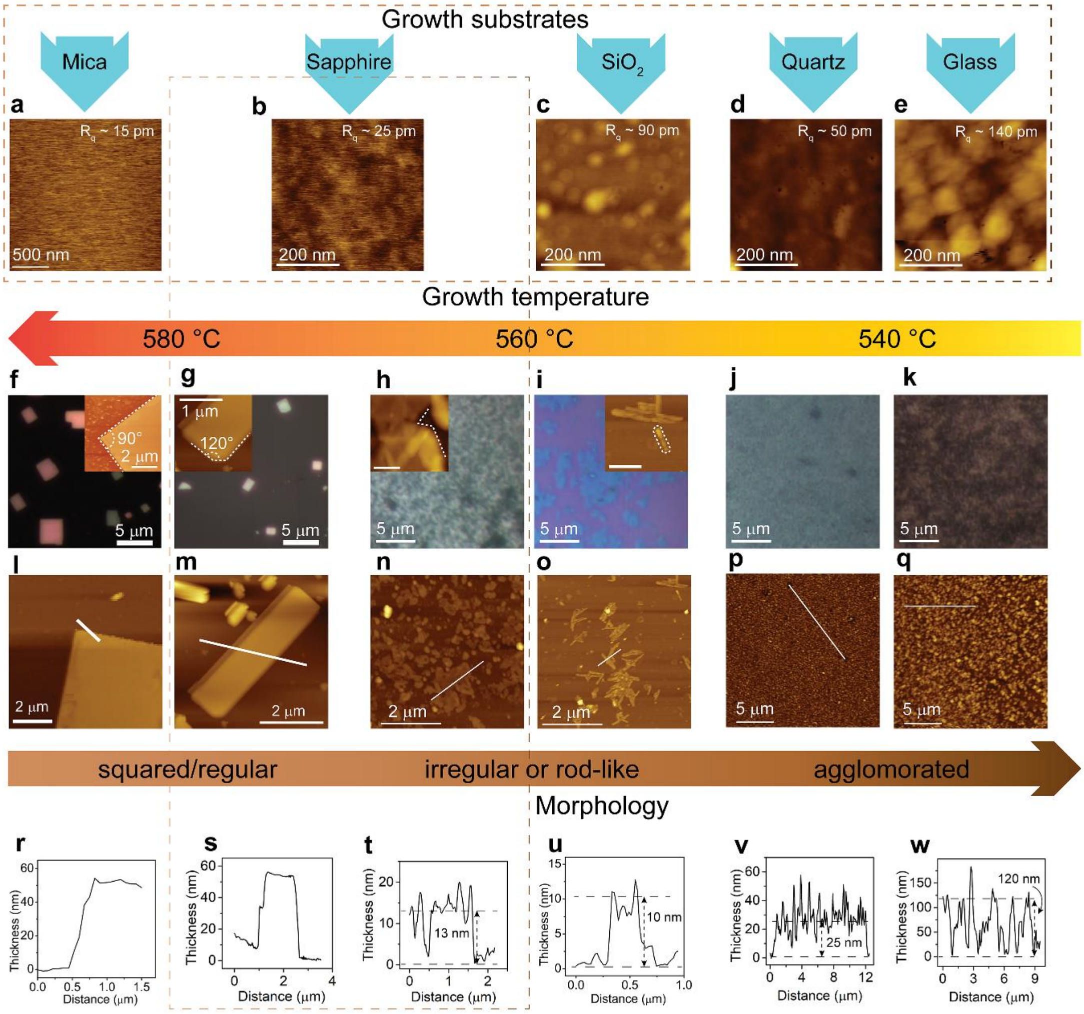

Fig. 3.1: (a-e) Atomic force microscopy images of mica, sapphire, SiO_2, quartz, and glass substrate denoting the roughness of the surface. (f-k) Optical microscopy images of as-grown samples on different substrates. (j-q) Topography images of as-grown samples and (r-w) their corresponding height profile. Inset of (f-i) highlights the edge morphology of the synthesized Bi_2O_2Se. Inset of (h and i) has the scale bar of 0.2 and 0.5 mm.

TMDCs), it is likely to grow vertically (along the C-axis), instead of the usual lateral growth for conventional vdW materials. Therefore, it is possible to grow a multilayer sample on each substrate. Mica possesses positively charged $[K]^+$ on the top surface, which is further connected with negatively charged $[Se]^-$ and then to positively charged $[Bi_2O_2]^+$, and the sequence repeats during growth. So, it is expected to observe a uniform layered surface of Bi_2O_2Se grown on K^+ terminated mica surface. However, the case is different for the growth of Bi_2O_2Se on other substrates (e.g., SiO_2, sapphire, glass, quartz), and therefore we observe irregularly shaped flakes.

3.4.2. Structural properties

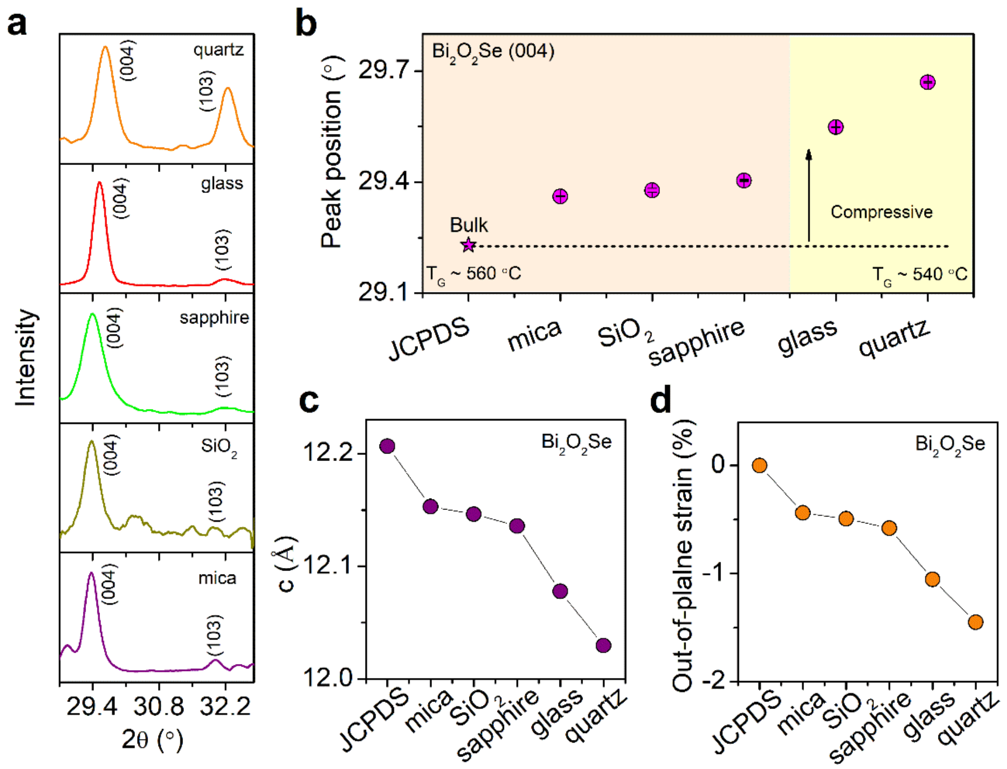

Fig. 3.2: (a) Stacked XRD pattern showing (004) peak of Bi_2O_2Se crystals grown on different substrates. The symbols are the experimental data, while solid lines refer to the Gaussian-fitted spectra. (b) The 2θ vs. growth substrate plot obtained from Gaussian fitting of (004) peak demonstrates the peak shift. Two color panel denotes two growth temperature (T_G ~ 560℃: light orange and T_G ~ 540℃: light yellow). (c) The lattice parameter (*c*) of Bi_2O_2Se extracted from the respective peak on different samples using Bragg's law. (d) The intrinsic out-of-plane strain (%) for different growth substrates estimated via $\frac{\Delta c}{c} \times 100$.

To evaluate the structural features of the flakes grown on different substrates, directly grown CVD samples on arbitrary substrates were characterized with XRD analyses (**Fig. 3.2**). Note that the XRD patterns were acquired on mica, sapphire, and SiO_2 under identical growth conditions (T_G ~ 560 °C). Additionally, the XRD pattern are recorded on Bi_2O_2Se/quartz and Bi_2O_2Se/glass at the T_G of ~540 °C since we did not observe growth at 560 °C on quartz and glass. **Fig. 3.2a** reflects the comparative XRD pattern corresponding to the (004) and (103) planes of Bi_2O_2Se. The fitted Gaussian line shape of the (004) peak reveals that the peak position differs on different substrates. In JCPDS data (PDF Card No.: 01-070-1549), the 2θ value for the (004) plane lies at 29.23°. Noticeably, the corresponding peak position on all the substrates is shifted to a higher 2θ value (**Fig. 3.2b**). This indicates compressive strain (out-of-plane) on the Bi_2O_2Se crystals introduced by the substrates during the growth. Further, the lattice parameter (c) is deduced using Bragg's law ($2d \sin\theta = n\lambda$) and $\frac{1}{d^2} = \frac{h^2+k^2}{a^2} + \frac{l^2}{c^2}$ owning the tetragonal phase of Bi_2O_2Se. **Fig. 3.2c** shows a plot of 'c' for different substrates. A strain-free Bi_2O_2Se crystal exhibits a 'c' value of 12.21 Å (PDF Card No.: 01-070-1549). However, the obtained 'c' values are 12.15 Å (mica), 12.14 Å (SiO_2), 12.13 Å (sapphire), 12.08 Å (glass), and 12.03 Å (quartz). The variation of the 'c' can be associated with strain/charge doping from the substrate surface and charge impurities.[17, 18] In order to identify the quantitative effect of substrates on the 'c' value, the out-of-plane strain has been estimated by calculating $\frac{\Delta c}{c}$. Interestingly, the multilayer Bi_2O_2Se (~50 nm) grown over mica holds minimum out-of-plane compressive strain (-0.43 %) among all the substrates (**Fig. 3.2d**). SiO_2 and sapphire induce -0.49 % and -0.58 % compressive strain, respectively, on the multilayer Bi_2O_2Se with the thickness of ~10-13 nm and at an identical T_G (~560 °C). Thus, even with similar thickness and identical T_G, the strain variations imply that the substrate induces a strain in the as-grown Bi_2O_2Se crystals. On the other hand, Bi_2O_2Se grown over quartz shows maximum out-of-plane compressive strain (-1.44 %), among various substrates, as shown in **Fig. 3.2d.** For the same T_G (~540 °C), the glass substrate exhibits -1.05 % compressive strain, which is lower than that for the quartz (-1.44 %) case, indicating that the influence of substrate is more than the T_G. Due to the higher thickness of Bi_2O_2Se on glass (~120 nm) than quartz (~25 nm), strong coupling within the layers may increase the compressive strain on the glass compared to quartz, which is not observed. Therefore, the lower lattice compression in glass compared to quartz indicates that the thickness has little role in the lattice strain (refer to **Fig. 3.2d**). Hence, the substrate-induced strain is believed to be the key reason behind the change in lattice constant.

Furthermore, Raman spectra were recorded to evidence the difference in structure and electronic properties induced by the growth substrates during the CVD growth. **Fig. 3.3a** shows

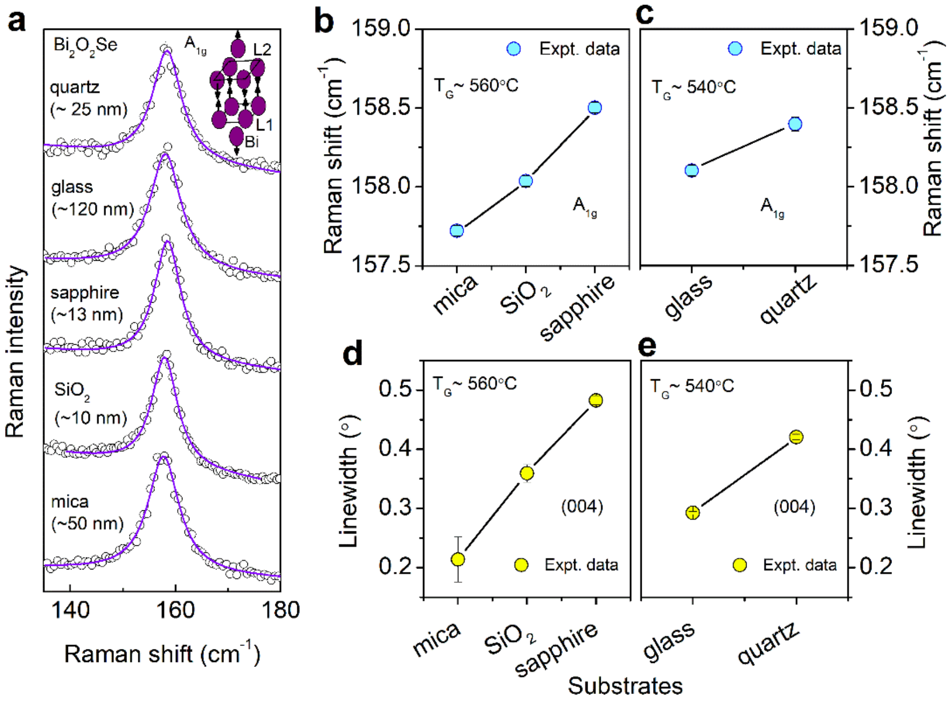

Fig. 3.3: (a) Stacked Raman spectra of characteristics A_{1g} Raman mode of Bi_2O_2Se grown on different substrates (symbols) with Lorentzian fit (solid lines). (b-c) The Lorentzian fitted peak position of A_{1g} Raman mode on different growth substrates at T_G ~560 ℃ and T_G ~540℃. (d-e) The linewidths of the (004) plane peak on growth substrates, which were obtained from XRD analyses with two T_G (d: ~560 ℃ and e: ~540℃).

the stacked Raman spectra of characteristic Raman mode A_{1g} of Bi_2O_2Se on different substrates. Lorentzian fitted parameters reveal the relative shift in the A_{1g} mode peak position with respect to theoretical value 159.89 cm^{-1}.[19] A shift of the A_{1g} mode can be associated with the strain, change in electron density, and layer thickness in 2D Bi_2O_2Se. Here we have studied the multilayer thickness samples, which have less influence on out-of-plane vibration mode in nvdW Bi_2O_2Se compared to few-layer/monolayer samples. According to the literature, the peak position of A_{1g} remains steady for multilayer samples (≥10 nm).[20] As this study is more focused on the multilayer samples (≥10 nm), we presume that the layer thickness has a negligible effect on the observed Raman modes. Thus, it suggests that the change in charge doping density/doping-induced strain or substrate-induced mechanical strain in Bi_2O_2Se influences the Raman modes. This is fully consistent with the XRD analysis showing a lower lattice constant than its standard value (c:12.21 Å). Note that due to the robust tetragonal crystal structure of Bi_2O_2Se, it is apparent that a decrease in the out-of-plane lattice constant (*i.e.*, compressive strain) can result in an increase of in-plane lattice constant and thus introduce an in-plane tensile strain. Accordingly, the out-of-plane vibration of Bi atoms in Bi_2O_2Se crystals grown at identical T_G results in the redshift of Raman peak (**Fig. 3.3b)** with respect to the theoretically calculated peak position of A_{1g} mode of Bi_2O_2Se at 159.89 cm^{-1}.[19]. Although sapphire and SiO_2 substrate show multilayer Bi_2O_2Se with similar thickness, the higher redshift (0.5 cm^{-1}) on SiO_2 than sapphire might be due to the effect of the substrate-induced strain. The higher redshift on SiO_2 than sapphire signifies a decrease in compressive strain. The compression increases in the order of mica → SiO_2 → sapphire according to XRD data (**Fig. 3.2d**). This is consistent with the blueshift in the order of mica → SiO_2 → sapphire in the Raman data (**Fig. 3.3b**) and it indicates an increase in compressive strain. Similarly, a relative peak shift (0.3 cm^{-1}) for quartz than glass with T_G ~ 540°C is attributed to substrate-induced strain/layer thickness (**Fig. 3.3c**). To correlate the origin of peak shift, the XRD linewidth of (004) peak is analysed. The linewidth of the XRD (004) peak follows the same trend as the Raman peak shift indicating that the substrate-induced non-uniform strain is dominant on directly CVD-grown samples (**Fig. 3.3d** and **3.3e**). The substrate indued strain can be categorized into two effects, (i) substrate-induced out-of-plane mechanical strain and (ii) substrate-induced charge doping density modulation, which partially contributing to the Raman peak shift.

XPS measurement has been employed to assess the chemical states, the electronic band structure, and carrier doping for different growth substrates. **Fig. 3.4** shows the survey scan spectra of Bi_2O_2Se grown over SiO_2 (**Fig. 3.4a**), quartz (**Fig. 3.4b**), sapphire (**Fig. 3.4c**), mica (**Fig. 3.4d**), and glass (**Fig. 3.4e**) and show that the as-grown samples contained characteristics Bi 4f, Se 3d, and O1s peak, indicating the formation of the crystals. Further, a high-resolution spectrum was acquired for Bi 4f, O 1s, and Se 3d elements to identify the oxidation states, as shown in **Fig. 3.5(a-c),** and the binding energies (BEs) are tabulated in **Table 3.1**. On the sapphire substrate, Bi 4f BEs are 158.8 eV (Bi 4f $_{7/2}$) and 164.2 eV (Bi 4f $_{5/2}$). On SiO_2, the BEs are 159.2 eV and 164.5 eV. Hence on SiO_2, the BEs are upshifted by ~ 0.4 eV towards higher binding energy, indicating reduced electron density in Bi_2O_2Se gown on SiO_2 than sapphire. It is attributed to the higher charge impurities lying over the surface of SiO_2 than sapphire. In general, higher binding energy means reduced electron density. In addition, the binding energies of O 1s are 530.0 eV (O1s(I)) and 531.9 eV (O1s(II)) for SiO_2 and 530.1 eV (O1s(I)) and 530.8 eV (O1s(II)) for sapphire as shown **Table 3.1.** The contribution of O 1s(II) centered at 531.9 eV is higher on SiO_2 than sapphire. This may be partly due to the presence of Bi_2SeO_5, as samples were exposed to the ambient air prior to the XPS measurements[21], and partly due to the larger scan area, which might be affected by the substrate oxygen states. According to a previous study, in the case of oxide formation on the surface of the Bi_2O_2Se, characteristic Raman mode (A_{1g}) would not be observed.[22] Therefore, the native Bi_2SeO_5 formation is not

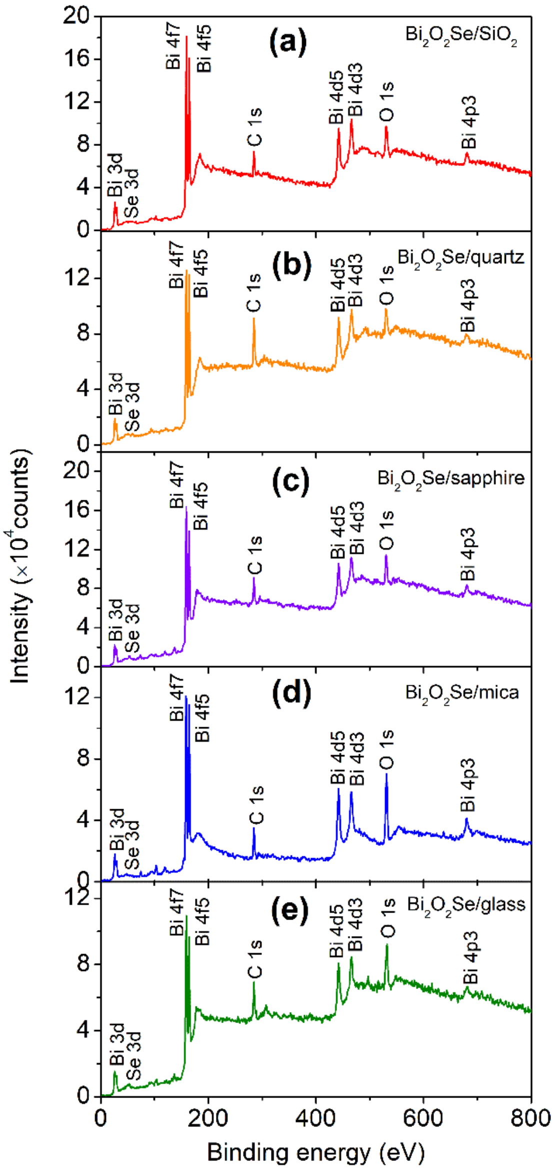

Fig. 3.4: Comparative XPS survey scan spectra of Bi_2O_2Se on (a) SiO_2, (b) quartz, (c) sapphire (d) mica, and (e) glass substrates.

due to atmospheric exposure on top of Bi_2O_2Se, as the Raman characteristics A_{1g} is present even after air exposure. Thus, native oxide formation at the interface between the exposed surface of oxygen-contained growth substrates (SiO_2) and Bi_2O_2Se is more likely than the Bi_2OSe_5 formation on the surface of Bi_2O_2Se. Note that the XPS instrument can analyze only ~5-10 nm of the top surface. Moreover, we know the XPS scanning area is larger than the lateral sample size in the present scenarios. Therefore, it is likely to have the Se^{4+} oxidation state due to native oxide (Bi_2SeO_5) formation on the substrate surface (SiO_2).

The Se 3d BEs are 52.8 eV, 53.7 eV, 58.8 eV, 59.9 eV on SiO_2, and 53.0 eV, 53.8 eV, 58.5, and 59.3 eV on sapphire (**Table 3.1**). This indicates the presence of Se^{4+} states caused by forming an oxide layer. The higher contribution from O 1s on the SiO_2 substrate indicates that the formation of an oxide layer is more favorable on SiO_2 substrates than sapphire, consistent with relative contribution from the Se^{4+} state, as shown in **Fig. 3.5c** (upper and lower panel). The amorphous oxide layer probably influences the formation of the oxide layer faster than the crystalline sapphire surface. As the O-terminated surface is chemically reactive, the characteristics of the first Se layer are significantly modified by the formation of the strong Se-

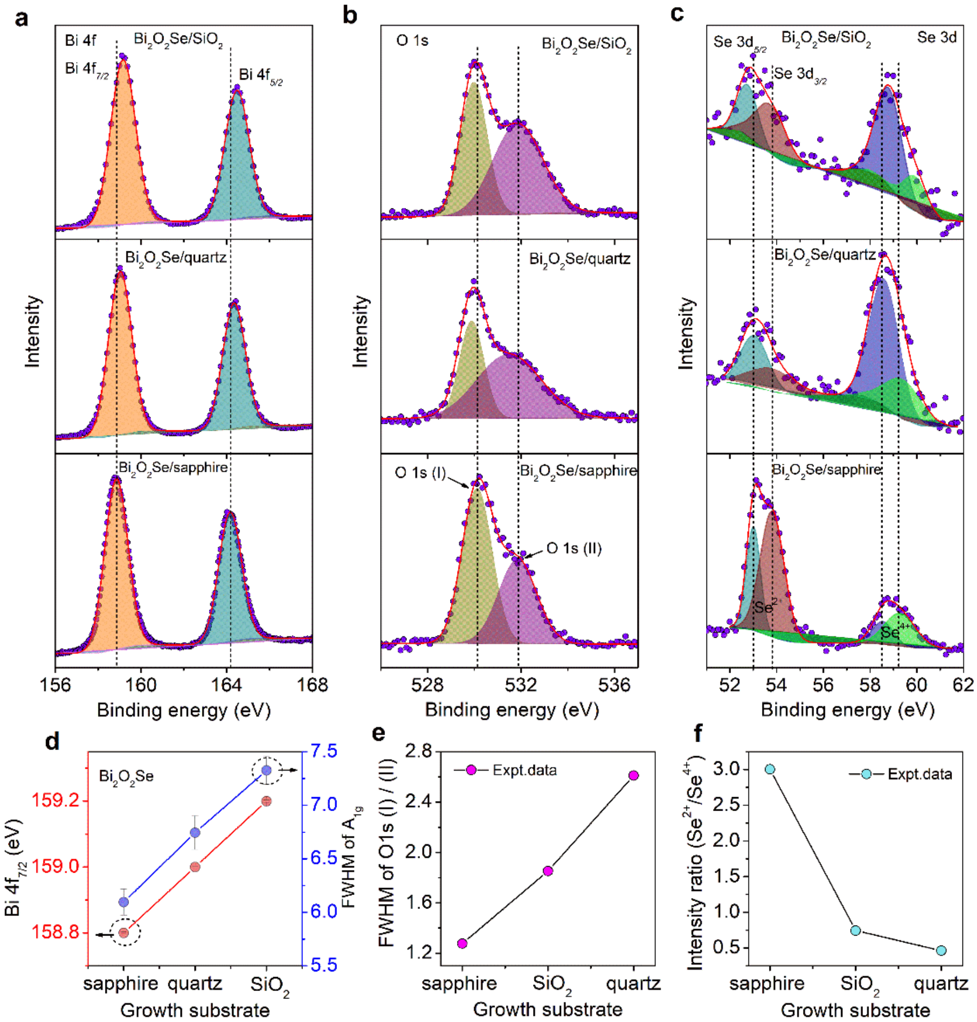

Fig. 3.5: (a-c) Stacked Bi 4f, O 1s, and Se 3d spectra for Bi_2O_2Se on sapphire, quartz, and SiO_2 substrates. Experimental data are represented using symbols and fitted spectra using solid lines with shaded regions. Shirley's baseline was utilized for XPS spectral fitting. (d) Left y-axis: Bi 4f $_{7/2}$ binding energies and right y-axis: FWHM of A_{1g} mode depending on growth substrates (sapphire, quartz, SiO_2). (e) The ratio of FWHM of O1s (I) and O1s (II) states on sapphire, quartz, and SiO_2 substrates. (f) The intensity ratio of Se^{2+} and Se^{4+} states based on growth substrates.

O bonds (probably the Bi_2SeO_5 phase as it is energetically favorable). Due to the built-in dipolar electric field within two consecutive layers, the formation of Bi_2O_2Se is restored with the next layer of $[Bi_2O_2]^+$ layer. In the metastable interface geometry on the O face, the substrate is weakly bonded to the first Se layer and induces charge doping, which ascribes the charge transfer from the Bi_2O_2Se to the oxygen-dangling bonds.[23-25] Consequently, it results in upshift (~0.4 eV) of Bi 4f state and downshifts (~0.2 eV) of Se 3d (Se^{2+}) in SiO_2 substrate w.r.t. sapphire case. Eventually, it directs that Bi_2O_2Se can be n-doped if the Si-terminated surface has active dangling bonds. Therefore, charge density modulation is achievable by choosing a particular growth substrate. Substrate-dependent changes in the bonding will likely change the optoelectronics performance of the Bi_2O_2Se layers. Additionally, at T_G~540 °C (i.e., lower than sapphire and mica T_G, ~560°C), quartz substrate exhibits Bi $4f_{7/2}$ at 159.0 eV and Bi $4f_{5/2}$ at 164.3 eV and O 1s at 529.9 eV(I) and 531.5(II) eV and Se 3d (Se^{2+}) at 53.1 eV and 53.8 eV and Se^{4+} at 58.6 eV and 59.4 eV. Compared to the SiO_2 case, the bi 4f binding energy is downshifted (~0.2 eV), implying the higher n-type doping of Bi_2O_2Se grown on the quartz substrate than SiO_2, as expected due to crystalline surface/less surface impurities of quartz than SiO_2. This suggests that lower T_G could provide n-type Bi_2O_2Se due to higher Se vacancies consistent with the observations of Se^{4+} i.e., the relative contribution of Se^{4+} to Se^{2+} is higher in quartz case than sapphire (i.e., the intensity ratio of Se^{2+} and Se^{4+} is 3.0 on sapphire and 0.5 on quartz, as depicted in **Fig. 3.5f**). Bi_2O_2Se grown at lower T_G in quartz (**Fig. 3.1v**) exhibits a much higher roughness than that on sapphire (with higher T_G) (**Fig. 3.1(m, n)**) due to higher roughness of the quartz substrate. Due to this surface roughness, there coud be multiple nucleation sites on quartz. At lower T_G, multiple nucleation sites on quartz promote the formation of multi-grain boundaries (GBs) during the growth. Thus, the higher Se vacancies at lower T_G could be ascribed to multi-GBs of Bi_2O_2Se [26]. Additionally, XRD measurements of Bi_2O_2Se grown on a quartz substrate (**Fig. 2.7c,** chapter 2) exhibit diffraction peaks (*101*) and (*103*) along with (*00l*), confirming polycrystalline growth of Bi_2O_2Se on a quartz substrate. Ample Se vacancies along the GBs[26] exist due to the polycrystalline growth of Bi_2O_2Se on quartz.

Table 3.1: *Fitting parameters of XPS spectra showing the binding energies of each element (Bi 4f, O 1s, Se 3d) in Bi_2O_2Se grown on different substrates.*

Growth Substrate	**Growth temperature (°C)**	**Binding energies (eV)**							
		Bi $4f_{7/2}$	Bi $4f_{5/2}$	O1s (I)	O1s (II)	Se^{2+} $3d_{5/2}$	Se^{2+} $3d_{3/2}$	Se^{4+} (I)	Se^{4+} (II)
Sapphire	560	158.8	164.2	530.1	530.8	53.0	53.8	58.5	59.3
Quartz	540	159.0	164.3	529.9	531.5	53.1	53.8	58.6	59.4
SiO_2	560	159.2	164.5	530.0	531.9	52.8	53.7	58.8	59.9

Interestingly, the FWHM of O1s(II) peak on quartz (3.2 eV) is larger than that on sapphire (1.9 eV) as expected and relatable to higher contribution of Se^{4+}/Se vacancies/n-doping on quartz. A qualitative understanding has been employed by calculating the FWHM ratio of O 1s(I), and O1s(II) as shown in **Fig 3.5e,** which reflects that SiO_2 and quartz have higher FWHM of O1s consistent with higher n-doping in SiO_2 and quartz than sapphire, though on quartz it is mainly due to Se vacancies, and on SiO_2 it is mainly due to higher O-dangling bonds. It is evident that substrate/sample interface impurities could be doped as different substrates have different charge impurities.[27] The SiO_2 substrate has higher charge impurities than sapphire substrate over its surface, resulting in higher charge doping in Bi_2O_2Se crystals grown on SiO_2 than the sapphire substrate consistent with the Bi $4f_{7/2}$ peak shift observation

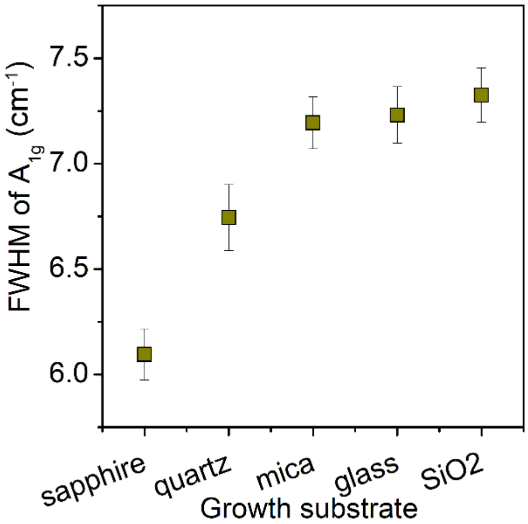

Fig. 3.6: FWHM of Raman A_{1g} Raman mode of Bi_2O_2Se on different growth substrates.

(**Fig. 3.5d;** left y-axis) and Raman FWHM increment[28] (**Fig. 3.5d;** right y-axis). The Bi 4f $_{7/2}$ is upshifted (~0.4 eV) in the SiO_2 case compared to sapphire. Consequently, a higher FWHM is observed in the A_{1g} mode of Bi_2O_2Se crystals under identical growth conditions. However, on quartz, the doping is higher than the sapphire due to Se vacancies. On mica, the presence/absence of K+ ions on mica probably causes charge doping modulation.[29] Mica induces higher n-type doping/(higher FWHM of A_{1g}) in Bi_2O_2Se than sapphire. With an identical T_G (540 °C), glass exhibits higher charge doping/FWHM of A_{1g} than quartz due to lower surface impurities on the quartz substrate than on the glass substrate (**Fig. 3.6**). Therefore, the growth substrate essentially tunes the structural and electronic properties of as-grown Bi_2O_2Se. It is interesting to know how these structural-carrier densities impact the optical properties of Bi_2O_2Se, which are discussed below.

3.4.3. Optical properties

Substrate/sample interface engineering is an effective way to modulate light harvesting behavior in low-dimensional material for improving the light-matter interaction.[30, 31] UV-visible absorption spectra of ultrathin 2D Bi_2O_2Se were collected for different samples grown on different substrates to assess the optical properties. Note that, the UV-visible absorption spectrum could be measured only on optically transparent substrates (quartz, mica and glass). **Fig. 3.6a** (upper panel) shows the respective absorption spectra for different samples. For the non-transparent substrates, sapphire and SiO_2, we adopted diffuse reflectance spectroscopy (DRS) measurement to obtain the absorption behavior. The Kubelka–Munk function, representing the absorption of the as-grown Bi_2O_2Se, is shown in **Fig. 3.6a** (lower panel). Interestingly, the spectra are broad with specific features. Yu et al. reported that the excimer formation causes a broad absorption band (550-740 nm) due to the stacking of positively charged $[Bi_2O_2]^{2+}$ and negatively charged Se^{2-} layers with covalent bonds creating a built-in dipolar electric field along the stacking direction in ultrathin Bi_2O_2Se crystals, which basically modifies the excited states under light irradiation.[32] The light-modified excited state was termed the excimer state. Remarkably, the close-lying electronic states in the band structure can give rise to broad absorption with multiple broad/narrow peaks, consistent with our observations (**Table 3.2**) explained below. On mica, the absorption peak positions for Bi_2O_2Se are ~460 nm, ~490 nm, and ~654 (1.896 eV) nm, with a broad feature, as shown in **Fig. 3.7a** and **b.** Fig. **3.7b** represents the magnified view of the lower-wavelength region to visualize the peaks at ~ 460 and ~ 490 nm. In case of glass substrate, the peaks are ~456 nm, ~484 nm, and ~649 nm (1.911 eV). On quartz, broad peaks were observed at ~435 - 550 nm and ~634 (1.956

eV). On sapphire, absorption peaks were observed at ~450 nm, ~486 nm, and ~651 nm (1.905 eV) for as-grown Bi_2O_2Se crystals. On SiO_2, the absorption peak positions are ~455 nm, ~486 nm, and ~662 nm. These peaks could be assigned to direct/indirect optical transitions between the symmetry points, as discussed below.

Table 3.2: *Absorption peak positions of Bi_2O_2Se on different growth substrates.*

Growth Substrate	Peak positions (nm)
Mica	~460, ~490, ~654
Glass	~456, ~484, ~649
Quartz	~435 - 550, ~634
Sapphire	~450, ~486, ~651
SiO_2	~455, ~486, ~662

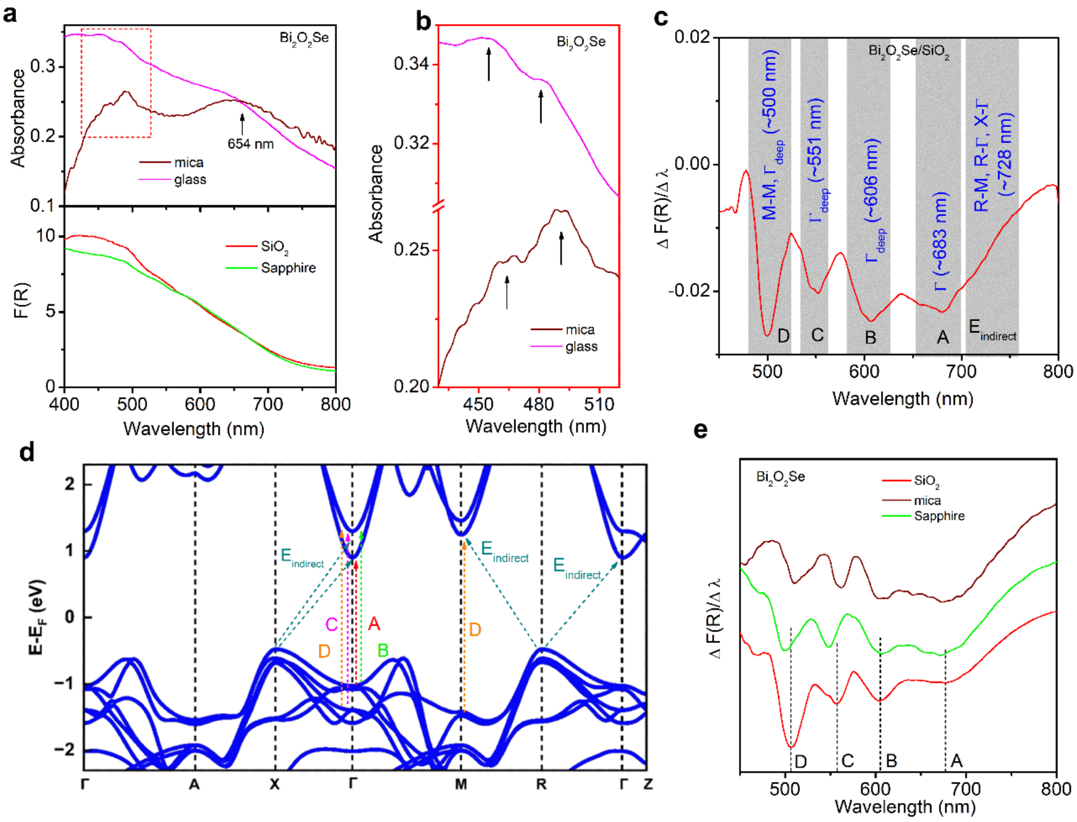

Fig. 3.7: (a) Absorption spectra of Bi_2O_2Se on mica and glass substrates (upper panel), Kubelka Munk plot (F(R)) of Bi_2O_2Se on SiO_2 and sapphire (lower panel). (b) Magnified portions of absorption spectra showing pronounced peaks in the range of 430-520 nm. (c) Differentiated Kubelka-Munk absorption spectrum depicting the multiple exciton peaks. (d) DFT calculated the electronic band structure of bulk Bi_2O_2Se with rescaled CB valleys, depicting the different excitonic transitions (indirect and direct). (e) Differentiated Kubelka-Munk absorption spectra depict multiple exciton peaks of Bi_2O_2Se on different growth substrates.

According to first-principles calculations, the band structure of the 2D Bi_2O_2Se exhibits a low indirect bandgap due to optical absorption edges at the X−Γ point. The theoretical calculation reveals that Γ−Γ direct optical transition is probable, and a strong absorption peak should appear at 596 nm.[32] However, we observed a broad absorption feature deconvoluted with multiple peaks, which might have arisen from the other optical transitions/exciton formation in the visible-NIR range. Due to the close-lying valleys in the band structure, the possible optical transitions/exciton formations are at Γ_{VB} (outer) - Γ_{CB} (outer), Γ_{VB} (inner)−Γ_{CB} (outer), Γ_{VB} (inner)−Γ_{CB} (outer), M_{CB}−M_{VB} (outer/inner), X_{VB}−Γ_{CB} (inner), R_{VB}−Γ_{CB} (inner), R_{VB}−M_{CB} (outer/inner), and Γ_{VB} (outer/inner)−M_{CB} (outer/inner), in the range of 400 to 725 nm according to theoretical electronic band structure.[2, 32] In our case, the broad absorption peak in the range ~590 to 750 nm could be assigned to the combined effect of R−M, X−M, and Γ−Γ points transitions. The peak at 486 nm (2.55 eV) is possibly caused by M_{VB}−M_{CB} (outer), Γ_{VB} (inner) − Γ_{CB} (inner) transitions, and the peak at 456 nm (2.72 eV) is mainly contributed by M_{VB}−M_{CB} (inner) point transitions. To visualize and understand these optical transitions prominently and quantitively, the differentiated data ($\Delta F(R)/\Delta\lambda$) has been plotted in **Fig. 3.7c,** which is further consistent with the theoretical calculations of exciton formations at different momentum valleys. In the differentiated Kubelka-Munk plot, the peaks at ~500 nm, ~551 nm, ~606 nm, ~683 nm, and ~728 nm originate from the exciton formation at M_{VB}−M_{CB} (outer), Γ_{VB} (inner)−Γ_{CB} (inner) transitions (D-exciton), Γ_{VB} (outer)−Γ_{CB} (inner) (C-exciton), Γ_{VB} (inner)−Γ_{CB} (outer) (B-exciton), Γ_{VB}−Γ_{CB} (A-exciton) and X_{VB}−Γ_{CB}, R_{VB}−Γ_{CB} ($E_{indirect}$) transitions, respectively (see **Fig. 3.7d**). To validate our experimental observation, we have calculated the electronic band structure of bulk Bi_2O_2Se by density functional theory (DFT) (see **Fig. 3.7d** for band structure bulk Bi_2O_2Se), and the energy values of CBM and VBM at different K-points are tabulated in **Table 3.3.** The extracted energy gaps at different valleys are tabulated in **Table 3.4**. In line with Yu et al. report[32], the internal geometry of Bi_2O_2Se changes during the excited state due to the built-in-dipolar electric field along the stacking direction, making us to rescale the conduction band valleys. Interestingly, after rescaling (an upshift of 0.3835 eV and 0.1704 eV of outer and inner CB valleys, respectively), the energy gaps between the VB and CB at different symmetry points match very well with the experimental results of different exciton formations. Thus, it is concluded that the multiple exciton formation at the excimer state causes broad features with multiple peaks in the absorption spectrum.

Table 3.3: *Energy value at different high symmetry k-points obtained from the DFT calculation.*

Valance Band (eV)		**Conduction Band (eV)**	
Γ_{VB} (outer)	-0.99	Γ_{CB} (outer)	0.87
Γ_{VB} (inner)	-1.36	Γ_{CB} (inner)	1.27
X_{VB}	-0.44	-	-
M_{VB}	-1.40	M_{CB} (outer)	1.23
-	-	M_{CB} (inner)	1.42
R_{VB}	-0.45	-	-
A_{VB}	-1.52	A_{CB}	2.13
Z_{VB}	-1.13	-	-

Table 3.4: *Summary of energy differences at high symmetry k-points due to different indirect and direct transitions calculated theoretically and observed experimentally.*

	Theoretical values			**Experimental values**
Transitions	**Energy (eV)**	**Wavelength (nm)**	**Exciton**	**Wavelength (nm)**
Γ_{VB} (outer)–Γ_{CB} (outer)	1.86	667	A	683
Γ_{VB} (inner)–Γ_{CB} (outer)	2.23	556	B	606
Γ_{VB} (outer)–Γ_{VB} (inner)	2.26	548	C	551
Γ_{VB} (inner)–Γ_{CB} (inner)	2.63	471	D	500
M_{VB}–M_{CB} (outer)	2.63	471		
M_{VB}–M_{CB} (inner)	2.82	440	E	
X_{VB}–Γ_{CB} (outer)	1.31	946	$E_{indirect}$	970
R_{VB}–Γ_{CB} (outer)	1.32	939		904
X_{VB}–M_{CB} (outer)	1.67	743		833
R_{VB}–M_{CB} (outer)	1.68	738		728
X_{VB}–Γ_{CB} (inner)	1.71	725		
R_{VB}–Γ_{CB} (inner)	1.72	721		
R_{VB}–M_{CB} (inner)	1.87	663		
Γ_{VB} (outer)–M_{CB} (outer)	2.22	559		
M_{VB}–Γ_{CB} (outer)	2.27	546		
Γ_{VB} (outer)–M_{CB} (inner)	2.41	515		
Γ_{VB} (inner)–M_{CB} (outer)	2.59	479		
M_{VB}–Γ_{CB} (inner)	2.67	464		
Γ_{VB} (inner)–M_{CB} (inner)	2.78	446		

Interestingly, we observe the variation in the exciton peak positions depending on the growth substrates. Due to the broad peak, we considered the wavelength of a peak where the absorption is maximum to estimate the quantitative effect of growth substrates. These variations in peak positions depending upon the growth substrate are contributed by the induced intrinsic strain and charge doping[33], resulting in a dislocation in momentum valley transition, including the change in the electronic band structure. The upshift in absorption peak (A-exciton peak) positions are 45 meV, 52 meV, and 60 meV on glass, sapphire, and mica, respectively, compared to quartz, which is significant. **Fig. 3.7e** demonstrates the presence of different excitons depending upon the growth substrate and validates the formation of multiple exciton, which is an exciting feature of ultrathin Bi_2O_2Se. The shift in A-exciton peak position with growth substrate is attributed to charge doping from substrate impurities/growth substrate-induced out-of-plane strain, which further affects the PL emission discussed later (**Fig. 3.12g**).

The absorption coefficient as a function of wavelength has been calculated and plotted in **Fig. 3.8**. It shows an absorption coefficient >10^5, indicating the high light harvesting nature of Bi_2O_2Se crystals.[34] The thickness profile used to calculate the absorption coefficient is provided in **Fig. 3.1(r,t-w)**. Among various substrates, Bi_2O_2Se grown over the quartz substrate shows a higher absorption coefficient due to the low refractive index of the substrate (*n*=1.4).[31, 35] Thus, based on the high absorption, Bi_2O_2Se grown over a quartz substrate might help to engineer an efficient photodetector with a better photo response. In addition, sapphire, mica, and glass have a refractive index (*n*) of 1.77[36],1.56[37], and 1.52[38]. Mica shows a lower absorption coefficient in the 400-680 nm range than quartz as it has a higher refractive index than quartz. However, higher absorption coefficients of Bi_2O_2Se on mica could be attributed to the out-of-plane lower compressive strain of Bi_2O_2Se on mica than quartz. Moreover, sapphire exhibits lower absorption coefficients than mica and quartz due to its higher refractive index.

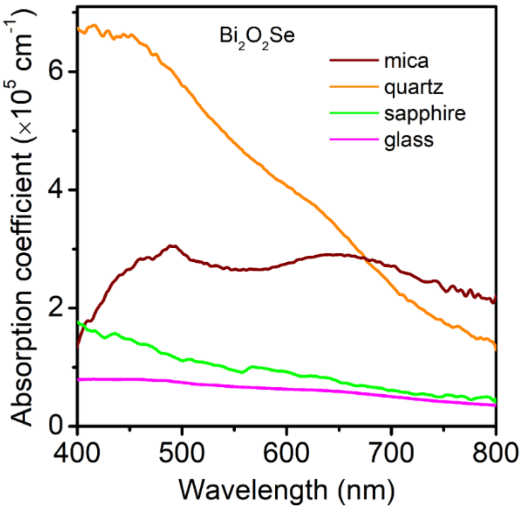

Fig. 3.8: Absorption coefficient of Bi_2O_2Se grown on mica, quartz, sapphire, and glass substrates.

Further, the optical bandgap is deduced by employing the Tauc plot (**Fig. 3.9**). According to photoemission spectroscopy measurements by Wu. et al., the indirect bandgap of

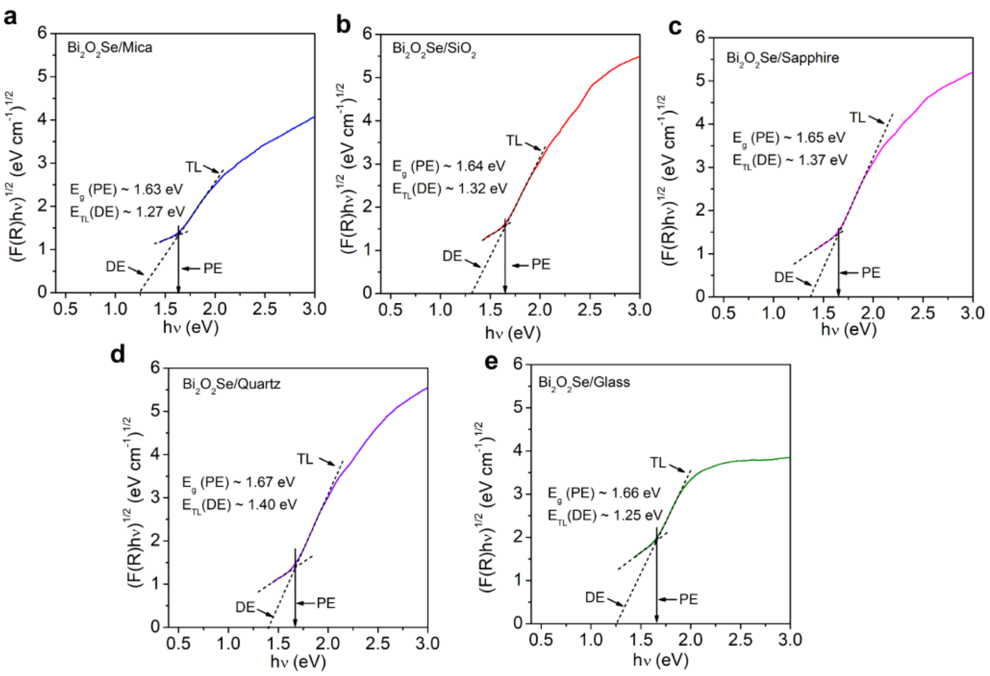

Fig. 3.9: Tauc plot of Bi_2O_2Se crystals considering the indirect bandgap, on (a) mica, (b) SiO_2, (c) sapphire, (d) quartz, and (e) glass substrates. Direct extrapolation (DE) and proper extrapolation (PE) estimate the optical energy gap of as-grown Bi_2O_2Se on different substrates.

Bi_2O_2Se crystals is 0.8 eV.[2] Experimentally, the optical bandgap for CVD-grown samples has been reported to be 1.37 eV (multilayer) to 1.90 eV (monolayer), and chemically synthesized samples as 1.5 eV (few-layer) to 2.34 eV (monolayer).[4, 39] We found that the optical bandgaps of Bi_2O_2Se crystals are 1.63 eV, 1.64 eV, 1.65 eV, 1.66 eV, and 1.67 eV on mica, SiO_2, sapphire, glass, and quartz substrates, respectively considering proper extrapolation (PE) rather than direct extrapolation (DE) in indirect Tauc plot (**Fig. 3.9**). The possible reasons for the variation in the optical bandgap with substrates are induced strain by substrates, Se vacancies, or partial change in the doping density by substrate impurities. Notably, above the bilayer thickness of Bi_2O_2Se, the change in bandgap is minor due to the covalent bonding of Se-atoms between the consecutive layers.[2, 40] It is worth mentioning that with ~ 50% Se deficiencies on the surface of bulk Bi_2O_2Se, the bandgap shows excellent robustness due to an intact covalent bond with no mid-gap states. [10, 41] Guo et al. theoretically predicted that bandgap variation is sensitive to the applied strain, which varies (0.6 to 1.28 eV) with applied in-plane strain (change in 'a/b' lattice constant) for Bi_2O_2Se.[42] It has been reported that the bandgap increases with increasing in-plane lattice constant (a/b).[42] Due to the robust tetragonal crystal structure of Bi_2O_2Se, it is apparent that an increase in the in-plane lattice constant cause a decrease in the out-of-plane lattice constant, thus giving rise to higher out-of-plane strain. Therefore,

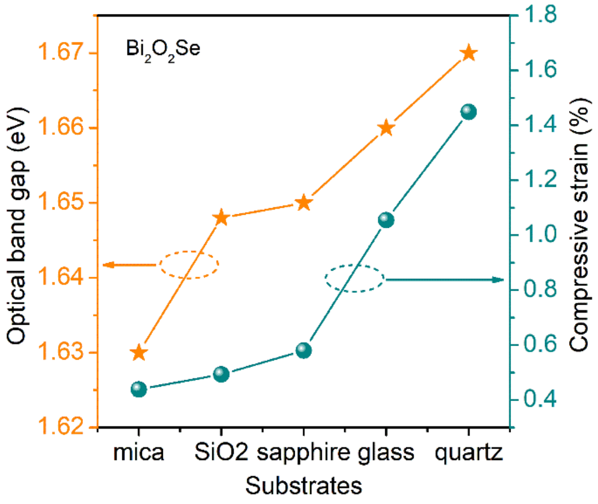

Fig. 3.10: Direct correlation between the measured optical bandgap and strain in Bi_2O_2Se crystals on different substrate.

correlating with the theoretical prediction and experimental data on out-of-plane strain increases the optical bandgap in our case. The out-of-plane strain in the as-grown sample varies from -1.5 % to - 0.4 % depending upon the growth substrates (**Fig. 3.2d**). **Fig. 3.10** (right y-axis) demonstrates a quantitative understanding of compressive strain (out-of-plane) and optical bandgap modulation as a function of growth substrates. Substrate-induced strain/doping is dominant for the modulated optical bandgap. Consequently, we can conclude that the growth substrate-induced strain causes the bandgap variation (1.63 eV to 1.67 eV) in Bi_2O_2Se crystals (**Fig. 3.10**). Note that the optical bandgap variation is quite small, suggesting the robust feature of the optical bandgap of Bi_2O_2Se, irrespective of substrate-induced mechanical strain/doping-induced strain, thickness, and Se vacancies.

According to the literature, the change in absorption coefficients and the optical bandgap induced by strain can influence the semiconductor refractive index, which is crucial for optical devices.[43] The refractive index (*n*) of the as-grown Bi_2O_2Se sample can be correlated with the optical bandgap following the equation[44, 45]

$$n = 3.59 - \log E_g \quad , \qquad (3.1)$$

E_g is the optical bandgap of the semiconductor in eV. The estimated refractive indices of Bi_2O_2Se crystals are 3.378, 3.375, 3.373, 3.370, and 3.367 on different substrates, e.g., mica, SiO_2, sapphire, glass, and quartz, respectively. The refractive index (*n*) of as-grown Bi_2O_2Se and growth substrates is tabulated in **Table 3.5**. According to the terahertz time-domain spectroscopy measurement, the change in light intensity can tune the refractive index of Bi_2O_2Se/Si from 3.41 to 3.37 and thus the absorption coefficient.[46] In the present study, the light intensity was kept constant during absorption measurement; hence, the effect on refractive index variation due to light intensity is insignificant. Among the substrates, Bi_2O_2Se grown over quartz shows the lowest refractive index (3.367) with a high absorption coefficient, which is expected. Bi_2O_2Se grown over mica shows a higher refractive index (3.378) with high absorption coefficient than sapphire (3.375), which is unusual. This unusual feature is due to the lower refractive index of the mica substrate (1.56) than sapphire (1.77). Even with a higher refractive index of mica substrate (1.56) than quartz substrate (1.4), a high refractive index of Bi_2O_2Se (3.378) on mica substrates shows comparable absorption coefficients, which might be attributable to the built-in dipolar electric field at Bi_2O_2Se/mica interface. In addition, Bi_2O_2Se on sapphire shows a lower refractive index (3.373) than on mica (3.378), with a lower absorption coefficient, which might arise from the higher index of sapphire (1.77). Bi_2O_2Se on sapphire shows a higher refractive index (3.373) than on quartz (3.367), resulting in a lower absorption coefficient. Therefore, substrate-induced strain and charge doping/modulation in optical bandgap alter the refractive index and the absorption coefficient of as-grown ultrathin Bi_2O_2Se crystals having multilayer thickness. In addition, the built-in dipolar electric field is related to the higher refractive index (3.367-3.378) of Bi_2O_2Se than conventional low-bandgap semiconductors, such as Si (3.5)[47].

Table 3.5: *'Refractive index (n)' of the as-grown Bi_2O_2Se and the growth substrates.*

Growth substrate	***n* of growth substrate**	***n* of Bi_2O_2Se**
Quartz	1.40	3.367
SiO_2	1.47	3.375
Glass	1.52	3.370
Mica	1.56	3.378
Sapphire	1.77	3.373

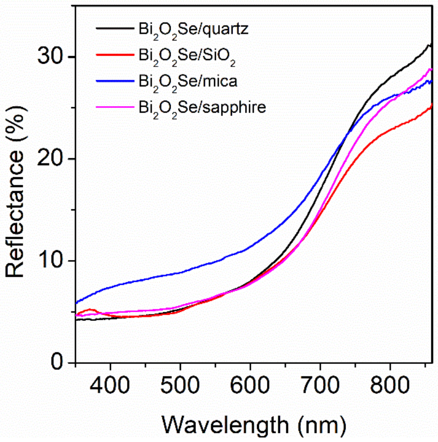

Fig. 3.11: Reflectance spectra of Bi_2O_2Se crystals on mica, quartz, sapphire, and SiO_2 substrates.

Further, the origin of visible PL in 2D Bi_2O_2Se crystals has been investigated. As the absorption features reveal, a multilayer Bi_2O_2Se crystal has multiple optical transition possibilities. Thus, it is expected to show the PL in the visible and NIR region. However, an indirect bandgap possibly results in low PL intensity. Nevertheless, we conducted the PL measurement with the above bandgap excitation (488 nm), and a broad PL spectrum was observed for the as-grown Bi_2O_2Se crystals. Due to their close-lying electronic structure, there may be multiple exciton formations, giving rise to a broad PL spectrum consistent with the absorption features. Reflectance measurement was carried out across the visible to NIR range (see **Fig. 3.11**), and differentiated data was extracted, showing absorption peaks due to exciton formation. Although two peaks (~604 nm and ~685 nm) are observed in the differential reflectance spectrum, the peak lying at a higher wavelength (~685 nm) is significantly broad

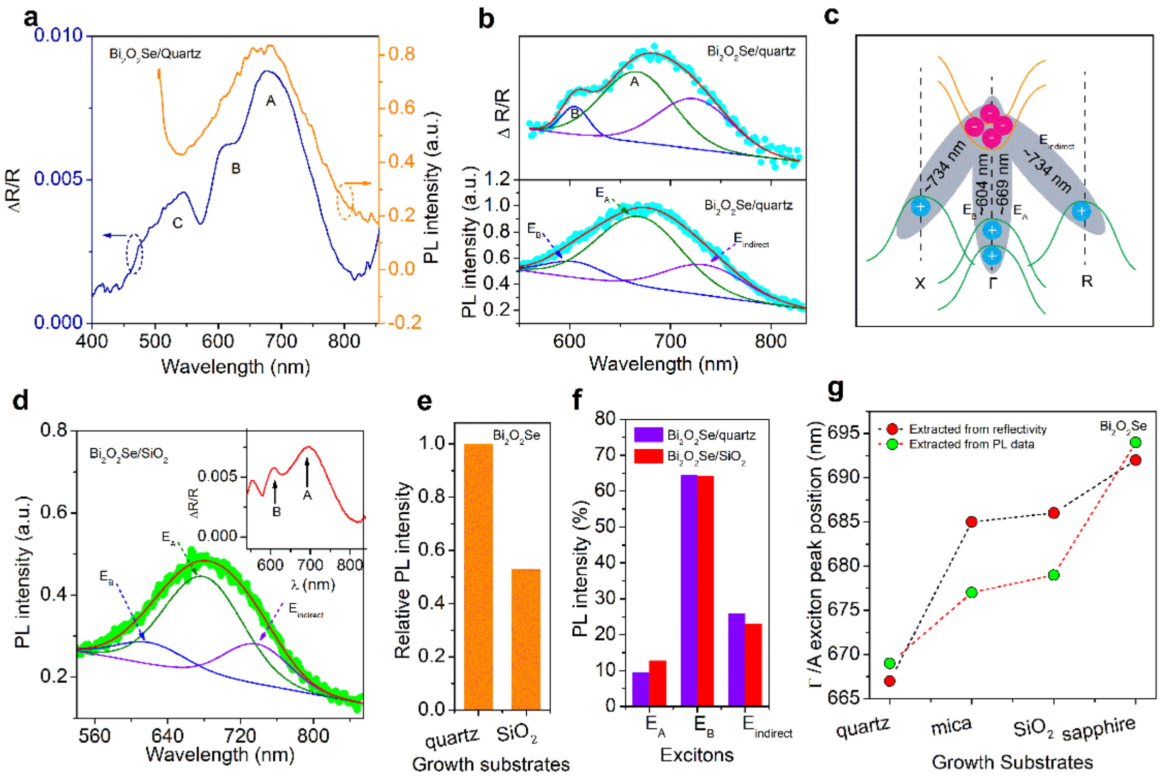

Fig. 3.12: (a) Wavelength-dependent ΔR/R (left y-axis) and PL spectrum (right y-axis) of Bi_2O_2Se crystals grown on quartz substrate showing similar broad spectral features. (b) Deconvoluted ΔR/R (upper panel) and PL spectra (lower panel) of Bi_2O_2Se/quartz showing three exciton peaks in the range 550 nm to 830 nm. (c) A schematic illustration of exciton formation at different momentum valleys resulting in a broad absorption/emission spectrum of Bi_2O_2Se in the visible wavelength. (d) PL spectrum (green symbols) fitted with the excitonic peaks (solid lines) of Bi_2O_2Se crystals grown over SiO_2 substrate. The inset shows the ΔR/R vs. wavelength of the Bi_2O_2Se/SiO_2 substrate. (e) Normalized PL intensity of Bi_2O_2Se on quartz and SiO_2 substrates indicating a difference in charge carrier density. (f) The relative intensity of different excitonic peaks (A, B, indirect) of Bi_2O_2Se on quartz and SiO_2 substrates. (g) Γ/A exciton peak positions for different growth substrates extracted from the reflectivity (red circle with black line) and photoluminescence (green circle with red line) measurement featuring the matching trend.

(~640-790 nm), which is consistent with broad PL spectra of Bi_2O_2Se shown in **Fig. 3.12a**. The broad PL feature of Bi_2O_2Se may be partly associated with excimer geometry (i.e., internal structural change during the excited state).[32] For quantitative analysis of different excimer excitons and to corroborate the exciton formation with PL contribution, we deconvoluted the differential reflectance and PL spectra with three Gaussian peaks, as shown in **Fig. 3.12b**. The measured PL peak positions are 604.9 nm, 669.1 nm, and 734.1 nm (**Fig. 3.12b,** lower panel), which are fully consistent with deconvoluted differential reflectance peak positions 605.1, 667.1, 723.6 nm (**Fig. 3.12b,** upper panel). A typical PL spectrum is seen due to direct exciton formation, named bright exciton; however, as an exception, the exciton can form at different valleys, which are close in energy (called momentum-forbidden exciton).[48] However, due to strain and substrate effect, i.e., an increase in carrier populations, PL could be observed even with indirect bandgap transitions.[49] Relating to the absorption peak, the formation of exciton can be assigned to deep valley exciton formation at ~604 nm (Γ_{deep}/B-exciton), the combined effect of formation of exciton at $\Gamma-\Gamma$ at ~ 669 nm (Γ/A-exciton), and R−M, X−Γ and R−Γ points possibly cause PL at ~734 nm ($E_{indirect}$) consistent with absorption analysis (refer to **Fig. 3.7c**). A schematic illustration of the exciton formation mechanism in multilayer Bi_2O_2Se is shown in **Fig. 3.12c**. As the momentum valleys are very close with a minor energy gap, the exciton formation possibly occurs in three ways: i) Γ_{VB} (inner) to Γ_{CB} (outer)/B-exciton, ii) Γ_{VB} (outer) to Γ_{CB} (outer)/A-exciton, and iii) $X_{VB}-\Gamma_{CB}$, $R_{VB}-\Gamma_{CB}$ ($E_{indirect}$) with same energy gap. Therefore, we believe that the formation of multiple excitons is the reason behind the broad visible PL emission from Bi_2O_2Se. It is noteworthy that due to their close-lying electronic

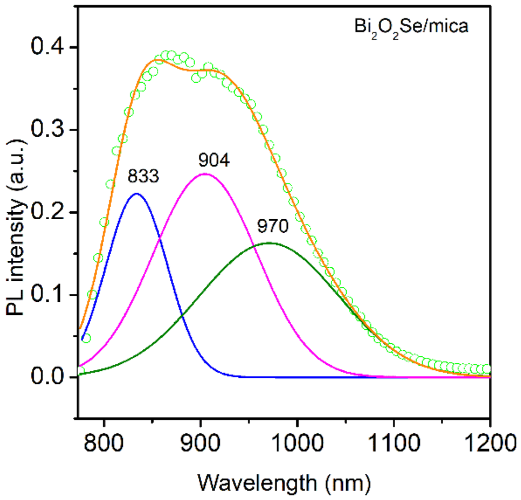

Fig. 3.13: Near IR Photoluminescence spectra of Bi_2O_2Se crystals on mica substrates. The solid spectra are gaussian fitted spectra showing 833, 904, 970 peaks originate from indirect transitions. Symbols represents experimental data.

structure with excimer formation at excited states, the thickness effect on PL emission is negligible in the uniquely structured nvdW Bi_2O_2Se compared to vdW semiconductors, such as TMDs. Recently, visible PL of Bi_2O_2Se has been observed in monolayer[50] and 18 nm thick[32] Bi_2O_2Se crystals with similar broad emission, which indicates layer-independent broad emission. Thus, the observed visible PL of multilayer Bi_2O_2Se is an intrinsic property rather than perturbations such as defect states since the PL spectrum matches well with the absorption spectrum involving formation of multiple excitons. Note that at a higher wavelength (640 nm) of excitation, we observed NIR PL with (see **Fig. 3.13**), which is ascribed to the indirect transitions in 2D Bi_2O_2Se. The asymmetric peak is deconvoluted with three Gaussian peaks centered at 833 nm, 904 nm, and 970 nm, which are well agreeing with the indirect transitions between $R_{VB}-\Gamma_{CB}$ (outer), $X_{VB}-M_{CB}$ (outer), and $X_{VB}-\Gamma_{CB}$ (outer) (**Table 3.4**) as obtained from the band structure.

We performed the PL measurement in Bi_2O_2Se crystals grown over quartz, SiO_2, mica, and sapphire substrates to check the substrate effect. The PL spectrum of Bi_2O_2Se on SiO_2 substrate (**Fig. 3.12d**) shows a similar broad feature of PL as on quartz (**Fig. 3.12b**, lower panel), and it is consistent with the differential reflectance spectrum (inset **Fig. 3.12d**) of Bi_2O_2Se on SiO_2 substrate. However, the relative PL intensity of Bi_2O_2Se on SiO_2 is lower than that on quartz, as shown in **Fig. 3.12e**, which is due to the charge doping from the substrate, consistent with the XPS and Raman FWHM (A_{1g}) analyses discussed earlier. Note that the measurement parameters, such as laser intensity and integration time, were kept identical in all PL measurements. The excimer excitons lie at ~621 nm, ~679 nm, and ~738 nm in Bi_2O_2Se grown on SiO_2/Si (**Fig. 3.12d**), consistent with the reflectivity spectrum (inset of **Fig. 3.12d**).

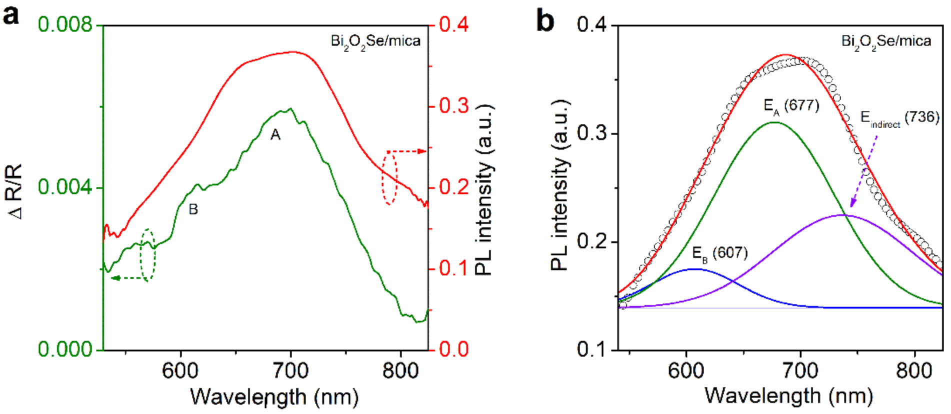

Fig. 3.14: (a) First derivative of reflectance spectrum (left y-axis) and photoluminescence spectrum (right y-axis) of Bi_2O_2Se crystals grown on mica substrate. (b) Deconvoluted PL spectra of Bi_2O_2Se on mica.

The peaks are redshifted compared to the quartz case, indicating electron doping of Bi_2O_2Se grown over SiO_2. Bi_2O_2Se is more n-doped in the case of SiO_2 than quartz. Hence, it exhibits PL quenching with redshift. Individual exciton contribution has been compared for quartz and SiO_2 substrate, which reveals insignificant difference, further validating that the emission is occurring due to the exciton formation in different valleys rather than the formation of charge exciton usually formed in vdW semiconductors (**Fig. 3.12f**). In addition, Bi_2O_2Se on mica exhibits very low-intensity PL, as shown in **Fig 3.14a (**right Y-axis). Like other substrates, Bi_2O_2Se grown over mica shows a broad PL spectrum consistent with the differential reflectance spectrum, as shown in **Fig. 3.14a** (left Y-axis). The low PL intensity of Bi_2O_2Se grown on mica substrate may be attributed to higher electron-phonon coupling due to lattice matching of the sample/substrate surface. Though the intensity is low, assuming the presence of 3 excitonic peaks (**Fig. 3.14b**) similar to PL on quartz and SiO_2 substrates, we obtain the nearly identical individual contribution of excitons, validating the formation of excitons in PL of Bi_2O_2Se. The excimer excitons lie at ~607 nm, ~677 nm, and ~736 nm in Bi_2O_2Se grown on mica (**Fig. 3.14b**). Similarly, Bi_2O_2Se grown over a sapphire substrate shows the PL with a broad range, as shown in **Fig. 3.15a**. The differential reflectance data matches the PL feature, confirming again the exciton formation (**Fig. 3.15a,** left Y-axis). The excimer excitons lie at ~600 nm, ~694 nm, and ~744 nm in Bi_2O_2Se grown on sapphire (**Fig. 3.15b).** Moreover, the A-exciton peak is shifted depending upon the growth substrate (**Fig. 3.12g**), which matches with reflectivity trends, further validating our explanation. Interestingly, the A and B exciton

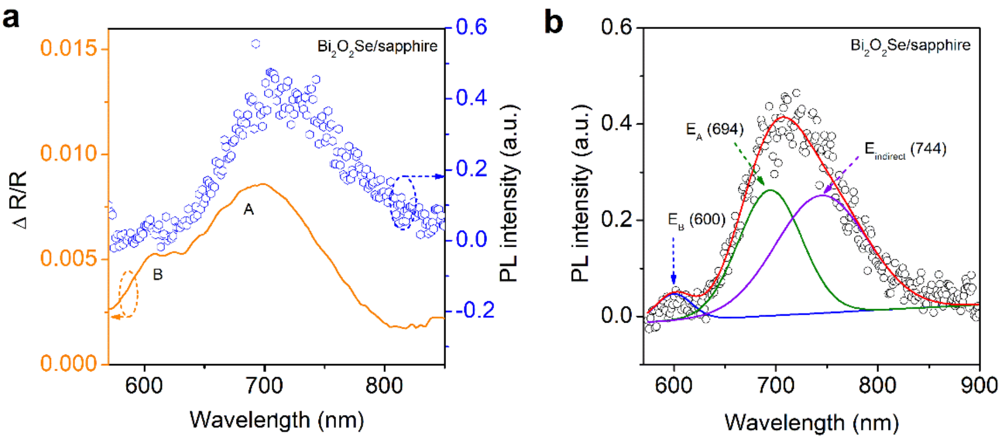

Fig. 3.15: (a) First derivative of reflectance spectrum (left y-axis) and photoluminescence spectrum (right y-axis) of Bi_2O_2Se crystals grown on a sapphire substrate. (b) Deconvoluted PL spectra of Bi_2O_2Se on sapphire.

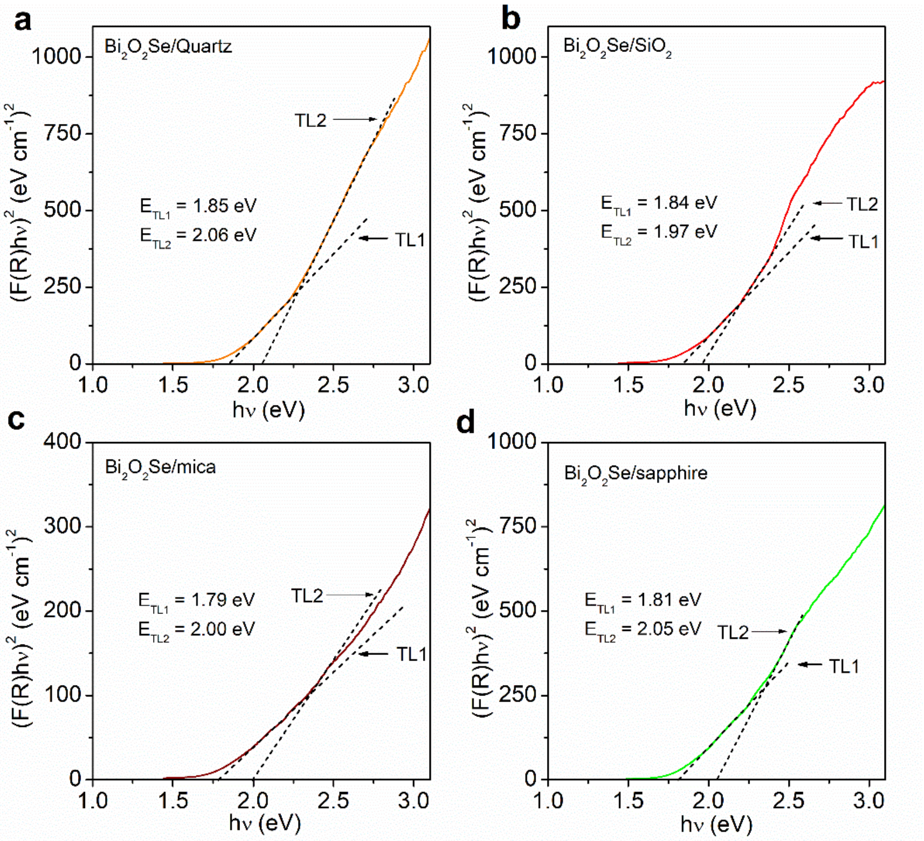

Fig. 3.16: Tauc plot considering the direct bandgap of Bi_2O_2Se crystals on (a) mica, (b) SiO_2, (c)sapphire, (d) quartz, and (e) glass substrates. Tauc line 1 (TL1) defines the first direct optical transition, while Tauc line 2 (TL2) signifies the second direct optical transition.

peak positions are consistent with the Tauc plots, considering the direct transitions, as shown in **Fig 3.16**.

Further, temperature-dependent PL (**Fig. 3.17**) spectra are collected on Bi_2O_2Se/SiO_2 using a 50x objective lens having a long focal length equipped with Linkam temperature stage installed with Raman set up. The evolution of PL spectra with temperature (300-77 K) has been shown in **Fig. 3.17a**. Due to the low-intensity PL of Bi_2O_2Se, the SiO_2 peak (marked with '$*$') arises at low temperatures. To confirm the SiO_2 contribution, we recorded the SiO_2 PL spectrum at 77 K, as shown in **Fig. 3.18a**. Note that for bare SiO_2, we collected the spectrum where the Bi_2O_2Se is not present, as depicted in **Fig. 3.18b**. In addition, the multilayer thickness (~10 nm) between substrate and laser heating rules out the underestimation of Gaussian fitting of the Bi_2O_2Se PL spectrum. However, in the preceding section, the 100x objective lens was used to perform the room-temperature PL spectroscopy. Thus, our obtained results with 3 Gaussian fittings are justified in the previous section.

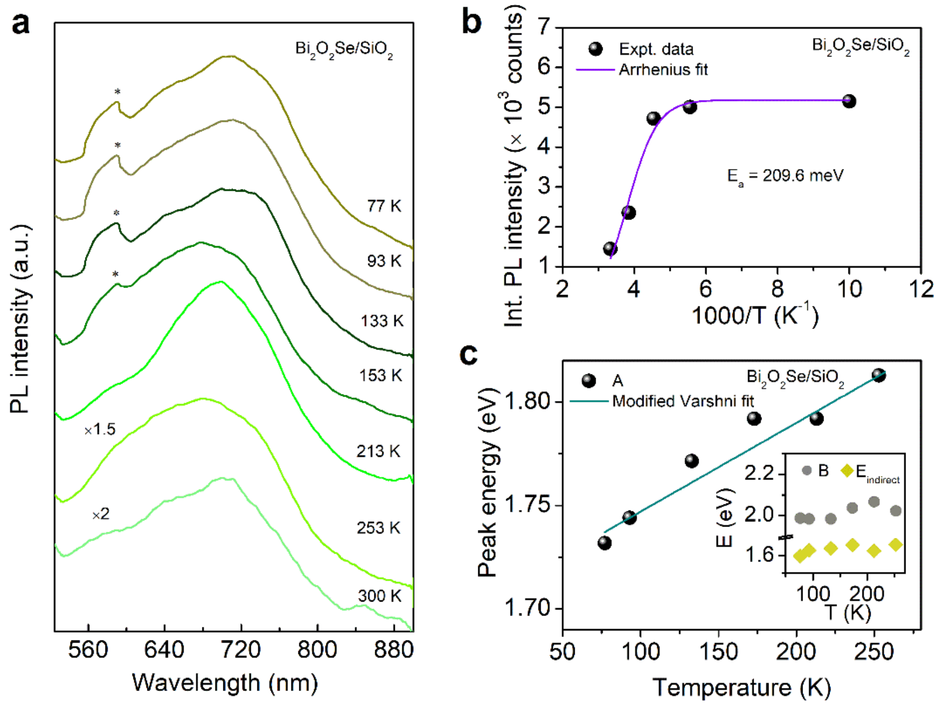

Fig. 3.17: (a) PL spectral evolution of Bi_2O_2Se (on SiO_2 substrate) as a function of temperature (77 - 300 K). The peak marked with '⁎' symbol arises from the substrate. (b) Integrated PL intensity of Γ/A exciton as a function temperature (T), fitted with Arrhenius equation revealing exciton binding energy of 209.6 meV. (c) The corresponding emission peak energy as a function of temperature and fitted with the Varshni equation showing energy gap shrinkage with decreasing temperature.

Therefore, keeping constant with the previous analysis, the temperature-dependent spectra were deconvoluted with 3 Gaussian peaks to understand the photo-carrier dynamics. The integrated PL intensity of each peak is extracted at different temperatures and plotted against 1000/T (**Fig. 3.17b**). The experimental data were fitted with the Arrhenius-type

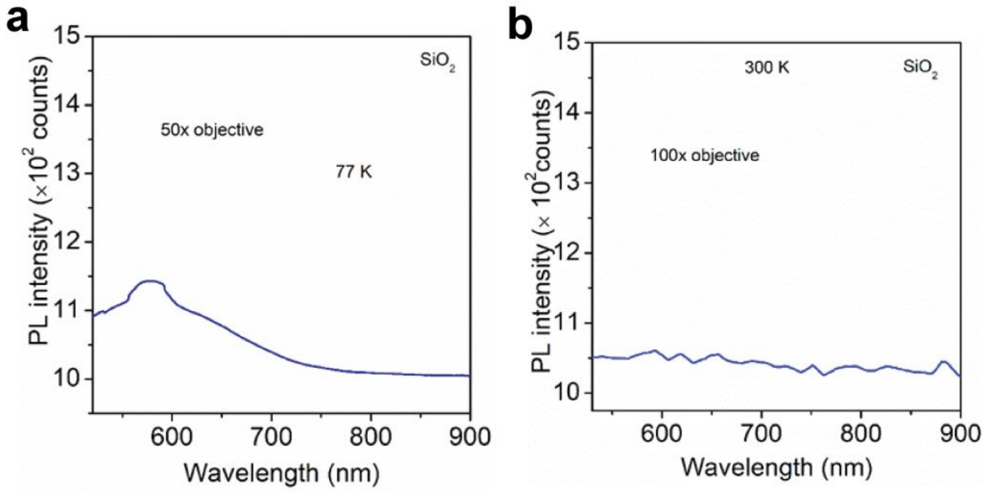

Fig. 3.18: (a) Low temperature (77 K) PL spectrum of bare SiO_2 substrate. (b) Room temperature (300 K) PL spectrum of bare SiO_2 substrate.

equation[51] to estimate the exciton (Γ/A) binding energy, which was found to be 209.6 meV. This exciton binding energy is lower than the conventional van der Waal 2D materials, like MoS_2 and WS_2,[52, 53] probably due to excimer formation in non-van der Waal Bi_2O_2Se. Low exciton binding energy with the formation of multiple exciton in Bi_2O_2Se could be an incentive for superior performance of the photovoltaic device.[54, 55] The PL peak energy is plotted as a function of temperature and fitted with the modified Varshni equation[56] (with negative temperature coefficient) for a quantitative understanding of the energy gap at Γ point (**Fig. 3.17c**). It shows a linear increase in energy gap with increasing temperature, contrary to conventional semiconductors and other vdW 2Ds, like MoS_2[57]. Emission energy of B exciton and $E_{indirect}$ (inset of **Fig. 3.17c**) increases with increasing temperature. When the thermal contribution dominates and direct contribution of electron-phonon interaction is negligible, the bandgap can increase with increasing temperature.[58] Additionally, lattice contraction with lowering temperature is a possible reason behind such variation in Bi_2O_2Se. Consequently, the higher electron-phonon coupling leads to the energy gap shrinkage resulting in PL upshift. This indicates positive temperature coefficients feature at the Γ point, which is contrary to the conventional semiconductors and vdW 2D materials. This seems to be unique for the nvdW Bi_2O_2Se crystals and needs further investigation.

3.5. Conclusions

Our study reveals the formation of multiple excitons even at room temperature in nvdW Bi_2O_2Se, resulting in broadband absorption and PL in the visible to NIR region. Experimentally, the conclusions are established with absorption, reflectance, and PL measurement and explained via theoretical DFT calculation of the band structure. Besides the excimer formation unveiled recently[32], we found multiple excitons at the excimer states resulting in broad PL from ultrathin Bi_2O_2Se in ~580-800 nm range. In addition, we have investigated the effect of substrates on the structural and optical properties of ultrathin Bi_2O_2Se crystals, which mirrors robust landscapes of ultrathin Bi_2O_2Se irrespective of the growth substrate. Our understanding reveals that mica, SiO_2, sapphire, glass, and quartz substrates introduce a compressive (out-of-plane) strain on the CVD-grown Bi_2O_2Se. It is revealed that substrate-impurity doping-induced strain and substrate-induced mechanical strain sway the property modulation. Eventually, the influence of the growth substrate has a noticeable impact on tuning the structure and optical properties, including photo-excited carrier dynamics. The order of best to worst growth substrate is Mica→Sapphire→SiO_2→quartz→glass. We believe these results extend the in-depth understanding of the properties of Bi_2O_2Se for future optoelectronics applications.

References

1. A. Splendiani, L. Sun, Y. Zhang, T. Li, J. Kim, C.-Y. Chim, G. Galli and F. Wang, *Nano Letters*, 2010, **10**, 1271-1275.
2. J. Wu, H. Yuan, M. Meng, C. Chen, Y. Sun, Z. Chen, W. Dang, C. Tan, Y. Liu, J. Yin, Y. Zhou, S. Huang, H. Q. Xu, Y. Cui, H. Y. Hwang, Z. Liu, Y. Chen, B. Yan and H. Peng, *Nature Nanotechnology*, 2017, **12**, 530-534.
3. J. Li, Z. Wang, Y. Wen, J. Chu, L. Yin, R. Cheng, L. Lei, P. He, C. Jiang, L. Feng and J. He, *Advanced Functional Materials*, 2018, **28**, 1706437.
4. J. Wu, C. Tan, Z. Tan, Y. Liu, J. Yin, W. Dang, M. Wang and H. Peng, *Nano Letters*, 2017, **17**, 3021-3026.
5. J. Wu, C. Qiu, H. Fu, S. Chen, C. Zhang, Z. Dou, C. Tan, T. Tu, T. Li, Y. Zhang, Z. Zhang, L.-M. Peng, P. Gao, B. Yan and H. Peng, *Nano Letters*, 2019, **19**, 197-202.
6. Z. Wu, G. Liu, Y. Wang, X. Yang, T. Wei, Q. Wang, J. Liang, N. Xu, Z. Li, B. Zhu, H. Qi, Y. Deng and J. Zhu, *Advanced Functional Materials*, 2019, **29**, 1906639.
7. P. Luo, F. Zhuge, F. Wang, L. Lian, K. Liu, J. Zhang and T. Zhai, *ACS Nano*, 2019, **13**, 9028-9037.
8. Y. Song, Z. Li, H. Li, S. Tang, G. Mu, L. Xu, W. Peng, D. Shen, Y. Chen, X. Xie and M. Jiang, *Nanotechnology*, 2020, **31**, 165704.
9. R. U. R. Sagar, U. Khan, M. Galluzzi, S. Aslam, A. Nairan, T. Anwar, W. Ahmad, M. Zhang and T. Liang, *ACS Applied Electronic Materials*, 2020, **2**, 2123-2131.
10. Y. Sun, J. Zhang, S. Ye, J. Song and J. Qu, *Advanced Functional Materials*, 2020, **30**, 2004480.
11. M. T. Hossain and P. K. Giri, *Journal of Applied Physics*, 2021, **129**, 175102.
12. P. Giannozzi, S. Baroni, N. Bonini, M. Calandra, R. Car, C. Cavazzoni, D. Ceresoli, G. L. Chiarotti, M. Cococcioni, I. Dabo, A. Dal Corso, S. de Gironcoli, S. Fabris, G. Fratesi, R. Gebauer, U. Gerstmann, C. Gougoussis, A. Kokalj, M. Lazzeri, L. Martin-Samos, N. Marzari, F. Mauri, R. Mazzarello, S. Paolini, A. Pasquarello, L. Paulatto, C. Sbraccia, S. Scandolo, G. Sclauzero, A. P. Seitsonen, A. Smogunov, P. Umari and R. M. Wentzcovitch, *Journal of Physics: Condensed Matter*, 2009, **21**, 395502.
13. J. P. Perdew, K. Burke and M. Ernzerhof, *Physical Review Letters*, 1996, **77**, 3865-3868.
14. J. Moellmann and S. Grimme, *The Journal of Physical Chemistry C*, 2014, **118**, 7615-7621.
15. P. E. Blöchl, *Physical Review B*, 1994, **50**, 17953-17979.
16. H. J. Monkhorst and J. D. Pack, *Physical Review B*, 1976, **13**, 5188-5192.
17. W. H. Chae, J. D. Cain, E. D. Hanson, A. A. Murthy and V. P. Dravid, *Applied Physics Letters*, 2017, **111**, 143106.
18. J. Wang, W. Hu, Z. Lou, Z. Xu, X. Yang, T. Wang and X. Lin, *Applied Physics Letters*, 2021, **119**, 081901.
19. T. Cheng, C. Tan, S. Zhang, T. Tu, H. Peng and Z. Liu, *The Journal of Physical Chemistry C*, 2018, **122**, 19970-19980.
20. T. Wang, Z. Xu, Z. Zhu, M. Wu, Z. Lou, J. Wang, W. Hu, X. Yang, T. Sun, X. Zheng, W. Li and X. Lin, *Nano Research*, 2023, **16**, 3224-3230.
21. M. Gao, W. Wei, T. Han, B. Li, Z. Zeng, L. Luo and C. Zhu, *ACS Applied Materials & Interfaces*, 2022, **14**, 15370-15380.
22. T. Tu, Y. Zhang, T. Li, J. Yu, L. Liu, J. Wu, C. Tan, J. Tang, Y. Liang, C. Zhang, Y. Dai, Y. Han, K. Lai and H. Peng, *Nano Letters*, 2020, **20**, 7469-7475.
23. Y.-J. Kang, J. Kang and K. J. Chang, *Physical Review B*, 2008, **78**, 115404.
24. C.-P. Lu, G. Li, J. Mao, L.-M. Wang and E. Y. Andrei, *Nano Letters*, 2014, **14**, 4628-4633.
25. Y. Li, C.-Y. Xu, P. Hu and L. Zhen, *ACS Nano*, 2013, **7**, 7795-7804.
26. Z. G. Yu, Y.-W. Zhang and B. I. Yakobson, *Nano Letters*, 2015, **15**, 6855-6861.

27. M. Buscema, G. A. Steele, H. S. J. van der Zant and A. Castellanos-Gomez, *Nano Research*, 2014, **7**, 561-571.
28. B. Chakraborty, A. Bera, D. V. S. Muthu, S. Bhowmick, U. V. Waghmare and A. K. Sood, *Physical Review B*, 2012, **85**, 161403.
29. A. N. Rudenko, F. J. Keil, M. I. Katsnelson and A. I. Lichtenstein, *Physical Review B*, 2011, **83**, 045409.
30. D. Jariwala, A. R. Davoyan, J. Wong and H. A. Atwater, *ACS Photonics*, 2017, **4**, 2962-2970.
31. L. Wang, Z. N. Nilsson, M. Tahir, H. Chen and J. B. Sambur, *ACS Applied Materials & Interfaces*, 2020, **12**, 15034-15042.
32. J. Yu, Y. Han, H. Zhang, X. Ding, L. Qiao and J. Hu, *Advanced Materials*, 2022, **34**, 2204227.
33. L. P. L. Mawlong, A. Bora and P. K. Giri, *Scientific Reports*, 2019, **9**, 19414.
34. M. T. Hossain, M. Das, J. Ghosh, S. Ghosh and P. K. Giri, *Nanoscale*, 2021, **13**, 14945-14959.
35. E. Kim, J.-W. Cho, T. K. Nguyen, T. T. T. Nguyen, S. Yoon, J.-H. Choi, Y. C. Park, S.-K. Kim, Y. S. Kim and D.-W. Kim, *Nanoscale*, 2018, **10**, 18920-18925.
36. I. H. Malitson, F. V. Murphy and W. S. Rodney, *J. Opt. Soc. Am.*, 1958, **48**, 72-73.
37. A. Castellanos-Gomez, M. Wojtaszek, N. Tombros, N. Agraït, B. J. van Wees and G. Rubio-Bollinger, *Small*, 2011, **7**, 2491-2497.
38. C. Guo, D. Li, D. P. Kelly, H. Li, J. P. Ryle and J. T. Sheridan, *Appl. Opt.*, 2018, **57**, E205-E217.
39. T. Ghosh, M. Samanta, A. Vasdev, K. Dolui, J. Ghatak, T. Das, G. Sheet and K. Biswas, *Nano Letters*, 2019, **19**, 5703-5709.
40. Q. Wei, R. Li, C. Lin, A. Han, A. Nie, Y. Li, L.-J. Li, Y. Cheng and W. Huang, *ACS Nano*, 2019, **13**, 13439-13444.
41. C. Chen, M. Wang, J. Wu, H. Fu, H. Yang, Z. Tian, T. Tu, H. Peng, Y. Sun, X. Xu, J. Jiang, N. B. M. Schröter, Y. Li, D. Pei, S. Liu, S. A. Ekahana, H. Yuan, J. Xue, G. Li, J. Jia, Z. Liu, B. Yan, H. Peng and Y. Chen, *Science Advances*, **4**, eaat8355.
42. D. Guo, C. Hu, Y. Xi and K. Zhang, *The Journal of Physical Chemistry C*, 2013, **117**, 21597-21602.
43. J. Cai, Y. Ishikawa and K. Wada, *Opt. Express*, 2013, **21**, 7162-7170.
44. A. Bahadur and M. Mishra, *Acta Phys. Pol. A*, 2013, **123**, 737-740.
45. M. I. Khan, S. Ali, N. Alwadai, H. Ikram ul, M. Irfan, H. Albalawi, A. H. Almuqrin, M. M. Almoneef and M. Iqbal, *Journal of Materials Research and Technology*, 2022, **20**, 1616-1623.
46. Z. W. Li and J.-S. Li, *Appl. Opt.*, 2020, **59**, 11076-11079.
47. J. Jin, J. W. Kim, C.-S. Kang, J.-A. Kim and T. B. Eom, *Opt. Express*, 2010, **18**, 18339-18346.
48. M. Tebyetekerwa, J. Zhang, Z. Xu, T. N. Truong, Z. Yin, Y. Lu, S. Ramakrishna, D. Macdonald and H. T. Nguyen, *ACS Nano*, 2020, **14**, 14579-14604.
49. A. Steinhoff, J. H. Kim, F. Jahnke, M. Rösner, D. S. Kim, C. Lee, G. H. Han, M. S. Jeong, T. O. Wehling and C. Gies, *Nano Letters*, 2015, **15**, 6841-6847.
50. S. Liu, C. Tan, D. He, Y. Wang, H. Peng and H. Zhao, *Advanced Optical Materials*, 2020, **8**, 1901567.
51. S. Parveen, K. K. Paul and P. K. Giri, *ACS Applied Materials & Interfaces*, 2020, **12**, 6283-6297.
52. H. Shi, H. Pan, Y.-W. Zhang and B. I. Yakobson, *Physical Review B*, 2013, **87**, 155304.
53. T. C. Berkelbach, M. S. Hybertsen and D. R. Reichman, *Physical Review B*, 2013, **88**, 045318.
54. R. J. Ellingson, M. C. Beard, J. C. Johnson, P. Yu, O. I. Micic, A. J. Nozik, A. Shabaev and A. L. Efros, *Nano Letters*, 2005, **5**, 865-871.
55. S. Y. Leblebici, T. L. Chen, P. Olalde-Velasco, W. Yang and B. Ma, *ACS Applied Materials & Interfaces*, 2013, **5**, 10105-10110.
56. K. P. O'Donnell and X. Chen, *Applied Physics Letters*, 1991, **58**, 2924-2926.
57. T. Korn, S. Heydrich, M. Hirmer, J. Schmutzler and C. Schüller, *Applied Physics Letters*, 2011, **99**, 102109.
58. C. Yu, Z. Chen, J. J. Wang, W. Pfenninger, N. Vockic, J. T. Kenney and K. Shum, *Journal of Applied Physics*, 2011, **110**, 063526.

Chapter 4

Interfacial Charge Transfer in the CVD-grown $Bi_2O_2Se/CsPbBr_3$ Nanocrystal Heterostructure and its Exploitation in Superior Photodetection

This chapter demonstrates the understanding of interfacial charge transfer (CT) between the 2D Bi_2O_2Se and 0D $CsPbBr_3$ nanocrystals. Efficient CT in a 2D semiconductor heterostructure (HS) plays a crucial role in high-performance photodetectors and energy-harvesting devices. NvdW 2D Bi_2O_2Se has enormous potential for high-performance optoelectronics, though very little is known about the interfacial charge transport at the corresponding 2D heterojunction. Herein, we studied a combined experimental and theoretical investigation of interfacial CT in the $Bi_2O_2Se/CsPbBr_3$ heterostructure through various microscopic and spectroscopic tools corroborated with DFT calculations. The CVD-grown few-layer Bi_2O_2Se nanosheet possesses high crystallinity and a high absorption coefficient in the visible-NIR region. We integrated the few-layer Bi_2O_2Se nanosheet possessing superior electron mobility and $CsPbBr_3$ nanocrystals with high light-harvesting capability for efficient broadband photodetection. The band alignment reveals a type-I heterojunction, and the device under reverse bias reveals a fast response time of 12 μs/24 μs (rise time/fall time) and an improved responsivity in the 390 to 840 nm range due to the effective interfacial CT and efficient interlayer coupling at the $Bi_2O_2Se/CsPbBr_3$ interface. Notably, a photodetector with a better light on/off ratio and a peak responsivity of $\sim 10^3$ AW^{-1} was achieved in the $Bi_2O_2Se/CsPbBr_3$ HS due to the synergistic effects in the HS under ambient conditions. The DFT analysis of the density of states and charge density plots in the heterostructure revealed a net transfer of electrons/holes from perovskite nanocrystals to Bi_2O_2Se layers and additional density of states in Bi_2O_2Se. These results are significant for developing nvdW HS-based high-performance, low-powered photodetectors.

4.1. Introduction

The layered nature and intriguing optoelectronic properties make 2D Bi_2O_2Se very promising for fabricating electronic devices. Fu et al. have engineered Bi_2O_2Se nanosheet-based phototransistors with a high responsivity of 3.5×10^4 AW^{-1} and detectivity of 9.0×10^{13} Jones.[1] Tong et al. demonstrated CVD-grown Bi_2O_2Se nanosheet-based broadband ultrasensitive phototransistors working in the 360–1800 nm wavelength range.[2] More recently, a PbSe colloidal quantum dot decorated 2D Bi_2O_2Se device has been fabricated by Luo et al., which could detect light up to 2 μm with a relatively high responsivity ($>10^3$ AW^{-1}).[3] Despite the recent developments, there are a few critical drawbacks concerning the slow photoresponse and low photocurrent on/off ratio in Bi_2O_2Se photodetectors: (1) the slower response speed (~ms) due to the bolometric effect and (2) the high dark current ($>10^{-7}$ A at 1V) due to the high intrinsic carrier concentration ($\sim10^{18}$–10^{20} cm^{-3}).[4] Several approaches have been attempted to overcome the current limitations of Bi_2O_2Se photodetectors, such as control in the synthesis process, hybridization with other 0D and 2D materials, etc. However, there are still various aspects of improving the performance of Bi_2O_2Se-based devices by reducing the dark current and improving the photocurrent. It is noteworthy that pristine Bi_2O_2Se has high air stability and exceptional carrier mobility, which are beneficial to design efficient photodetector devices with high responsivity and detectivity.[5] However, due to the the relatively low bandgap and relatively high conductivity, it generally produces a high dark current, limiting its practical applications in industry and domestic use. Decreasing the dark current and improving the photocurrent gain are essential requirements for a sensitive photodetector. Exploiting the photoinduced CT through other light-harvesting materials in a HS could be a viable approach to overcome such limitations. It is noted that CT is a ubiquitous phenomenon commonly witnessed in semiconductor HSs.[6, 7] In a suitably engineered HS, charge travels across heterointerfaces, enabling changes in optical responses and making it helpful in improving the photocurrent. Innovative engineering of the heterostructure materials could enable an improved understanding of device operation/functionality. Thus, the investigation of the CT and electronic band structure of the nvdW semiconductor HS is of fundamental interest to predict its suitability for different optoelectronic and sensing applications.

A 2D material-based heterojunction with other low dimensional semiconductors possessing high optical absorption, such as halide perovskites, is an excellent choice to understand CT and its application in photodetectors. HSs like these could enhance light absorption and initiate a high photocurrent and speedy response because of efficient CT and high carrier mobility of the 2D materials.[8] Among all perovskites, metal halide perovskites have promising potential for optoelectronics and solar cell devices with an efficient performance because of broadband absorption and low-cost synthesis.[9, 10] In contrast to organic perovskites, inorganic metal halide perovskites are more stable. $CsPbX_3$ nanocrystals (NCs), in particular, $CsPbBr_3$ NCs, exhibit fascinating optoelectronic properties with superior stability and high light-harvesting capability.[8] These exciting properties make them unique for superior optoelectronic applications. Thus, integrating 2D materials with a halide perovskite layer could be a feasible approach to understand the origin of CT enabling high-performance photodetection in nvdW 2D materials. Very recently, Fan et al. reported epitaxial growth of perovskite nanowires on few-layer Bi_2O_2Se.[11] However, very little has been understood on the optoelectronic application of such HS. To our knowledge, there is no report on the systematic study of CT mechanism in Bi_2O_2Se/perovskite heterostructure with the support of DFT calculations. The motivation behind choosing the HS system is to explore the synergistic effects of the two interesting nanostructured systems, i.e., 2D Bi_2O_2Se and 0D $CsPbBr_3$, both possessing superior optoelectronic properties and secondly, to understand the interfacial CT mechanism and its impact on the improved photocurrent in the HS. While most studies on HS for photodetection applications have focused on the use of type-II HSs, very few studies have focused on type-I HS for such applications.[12-14] For two semiconductors: A and B, if the band offsets (VBM and CBM) of A stay in between the band offsets of B or vice versa, then the HS is called type-I or straddling gap HS. If the band offsets of A are below the band offsets of B, then they are called type-II or staggered gap HS. In general, type-I HS are more suitable for recombination and light emission application. However, here we have explored the CT and photodetection application of type-I HSs.

To this effect, we investigated the CT mechanism at the $Bi_2O_2Se/CsPbBr_3$ interface primarily through micro-Raman and photoluminescence (PL) measurements. We have fabricated a hybrid structure of CVD-grown 2D Bi_2O_2Se nanoflakes with $CsPbBr_3$ perovskite NCs to analyze the photoelectric performance. Interestingly, the hybrid structure forms a type-I HS. The origin of the high photocurrent and high on/off ratio in the $Bi_2O_2Se/CsPbBr_3$ HS is investigated in detail. The type I interfacial band offset between Bi_2O_2Se and $CsPbBr_3$ speeds up the photoresponse time to a few microseconds, which is much faster than those of other Bi_2O_2Se devices. In the HS, we investigated the mechanism of improved photoconduction through DFT calculations of the band structure and density of states. We attempted to pinpoint the CT sites through charge density plots of the DFT results. Our study addresses the fundamental understanding of the CT across nvdW HSs and sheds light on the enhanced photoresponse properties of the $Bi_2O_2Se/CsPbBr_3$ type-I heterojunction system. Compared to the 1D perovskite nanowire, the $CsPbBr_3$ nanocrystal used in this work is a highly light-absorbing material with a high absorption coefficient and larger surface area, which facilitates higher absorption in the lower wavelength region resulting in an improved photocurrent.

4.2. Experimental details

4.2.1. Growth of 2D few-layered Bi_2O_2Se

For the growth of few-layer Bi_2O_2Se crystals, we conducted CVD-growth technique, where Bi_2O_3 powder (Alfa Aesar, 99.999%) and Bi_2Se_3 powder (Sigma Aldrich 99.999%) were the precursors and the high purity argon (99.999%) was carrier gas. Initially, the quartz tube was evacuated until a base pressure of 2×10^{-2} mbar was reached. Ar gas (~300 sccm) was purged repeatedly at room temperature (RT) to eliminate the O_2 impurity. The source temperature was increased to ~695 °C and maintained for 25 min with a base pressure of 400–500 mbar. The growth substrates were placed downstream (9-12 cm away from the hot center) at ~580–590 °C to grow few-layer Bi_2O_2Se nanosheets.

4.2.2. Synthesis of $CsPbBr_3$ nanocrystals

A nearly solvent-free mechanochemical process was followed to synthesize the $CsPbBr_3$ NCs. The desired amounts of cesium bromide (CsBr, Sigma Aldrich, 99.999%) and lead(II) bromide ($PbBr_2$, Sigma Aldrich, 99.999%) were taken as precursors. At atmospheric pressure and temperature, these two precursors were added with 40 g of zirconia balls of diameter 5 mm in a zirconia vial of volume 50 mL. The sample was ball milled (Retsch, Germany) with a rotation speed of 400 rpm. $CsPbBr_3$ powder is obtained in this way after milling for 2 hours. Subsequently, the surfactant-assisted milling process was continued for 1 h with the addition of 0.1 mL of oleylamine. Finally, the $CsPbBr_3$ NCs were extracted and immersed in 10 mL of toluene. The mixture was kept for 24 h in a culture tube, and the precipitate of the solution was separated, and the colloidal dispersion of $CsPbBr_3$ perovskite NCs was stored for further use.

4.2.3. Fabrication of the hybrid photodetector

To fabricate the $Bi_2O_2Se/CsPbBr_3$ hybrid photodetector, the colloidal dispersion of $CsPbBr_3$ NCs in toluene was drop cast on the layered Bi_2O_2Se grown on mica substrates. Typically, 5 μL of $CsPbBr_3$ NC dispersion was drop cast on the Bi_2O_2Se layer. Subsequently, it was baked at 50 °C for 15 min on a hot plate to grow the perovskite NC film with a shining green color. To make the contact electrodes, a copper grid (without carbon coating) of channel width 10 μm was placed carefully over the sample using an optical microscope, which serves as a shadow mask. Next, a gold film of thickness ~100 nm was deposited on the mask by the thermal deposition method. This resulted in an electrode separation of 10 μm for the photodetector. For the fabrication of the Bi_2O_2Se photodetector, we followed the same masking and Au electrode deposition procedures directly on the Bi_2O_2Se layer.

4.2.4. Characterization techniques

Optical images, AFM, FETEM, XRD, and Raman characterization of the Bi_2O_2Se and $CsPbBr_3$ have been carried out following **section 2.2.3**. The samples' UV–Vis absorption and diffuse reflectance spectra (DRS) were collected following **section 3.3.3**. For the steady-state PL measurements on the perovskite NCs, a commercial fluorimeter (Horiba Jobin Yvon, Fluoromax-4) was used at room temperature. The time-resolved PL (TRPL) decay of different samples was recorded using 375 nm pulsed laser excitation (average power ~1.0 mW), with an instrument time response of <50 ps (LifeSpecII, Edinburgh Instruments). The temporal response of the photocurrent and I–V measurement of the photodetectors were carried out using a microprobe station (ECOPIA EPS-500), a 405 nm laser with TTL modulation (CNI Laser) and a source-measure unit (Keithley 2400). The spectral photo-responsivity of the photodetector was measured using a xenon lamp (Newport) with a manual monochromator (Newport), and a source-measure unit.

4.3. Computational details

We used the density functional theory (DFT) based projector augmented wave (PAW) method as implemented in the Vienna *ab initio* simulation package (VASP).[15-17] We used the Perdew–Burke–Ernzerhof (PBE) functional to implement the generalized gradient approximation (GGA)[18] for exchange-correlation. We used a kinetic energy cut-off of 600 eV for all the calculations. A Monkhorst–Pack[19] grid of 4 × 4 × 1 *k* mesh was used to optimize the 4 × 4 supercell of Bi_2O_2Se. The $CsPbBr_3$ NC was optimized at a single gamma point. The density of states (DOS) of the 4 × 4 supercell of Bi_2O_2Se and the HS was simulated using a 6 × 6 × 1 Monkhorst–Pack *k* grid. We used the Bader charge analysis code[20-23] developed by Henkelman's group to examine the charge transfer.

4.4. Results and Discussion

4.4.1. Morphological characterization

Few-layer atomically thin high-quality Bi_2O_2Se, was grown on freshly cleaved mica substrates through the CVD method (schematically represented in **Fig. 4.1(a)**) similar to

Chapter 1. The optical image (**Fig. 4.1(b)**) exhibits a lateral size of ~12–20 μm of the Bi_2O_2Se flakes with nearly square morphology. The AFM topography of a single Bi_2O_2Se flake (**Fig. 4.1(c)**) and the corresponding height profile (inset of **Fig. 4.1(c)**) shows the flake thickness is ~6.8 nm, which corresponds to ~10 layers of Bi_2O_2Se. The as-synthesized layered Bi_2O_2Se sheets were transferred onto a TEM grid through an HF-etching transfer method following **section 2.2.2** for the atomic resolution study of the structure and morphology. The HRTEM lattice pattern (**Fig. 4.1(d)**) displays d spacing is 0.28 nm, corresponding to the (110) planes of the Bi_2O_2Se crystal.[24] A magnified view of the lattice image (inset of **Fig. 4.1(d))** shows 0.19 nm spacing, which corresponds to the (010) plane. The SAED pattern of the Bi_2O_2Se flakes (**Fig. 4.1(e))** confirms the single tetragonal crystal structure of the as-grown Bi_2O_2Se flake.

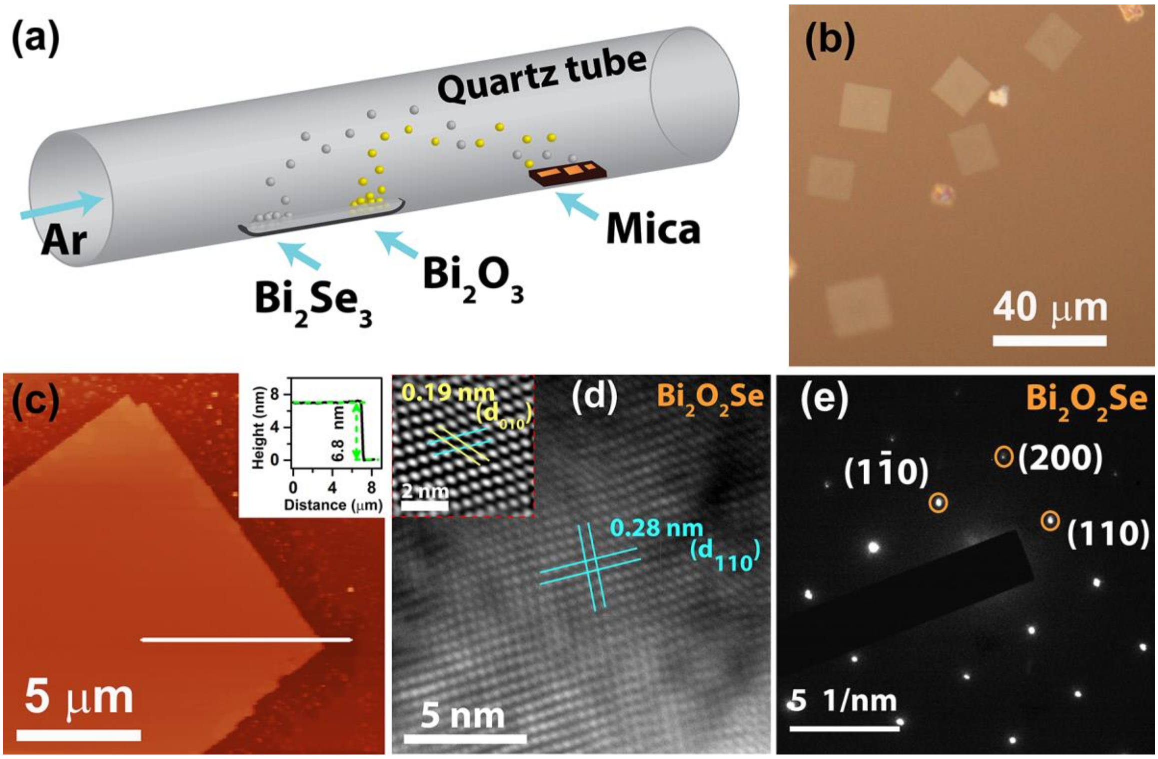

Fig. 4.1: (a) Schematic illustration of the CVD process for the growth of few-layer Bi_2O_2Se. (b) Optical microscopy images of the as-grown Bi_2O_2Se flakes. (c) AFM image of a Bi_2O_2Se flake. The inset shows the height profile of the Bi_2O_2Se layer on the mica substrate. (d) HRTEM lattice fringe of a Bi_2O_2Se crystal; the inset depicts the magnified view of the d(010) spacing. (e) SAED pattern of a Bi_2O_2Se crystal.

The morphology of $CsPbBr_3$ perovskite NCs is cubic (**Fig. 4.2(a)**), as expected.[8] **Fig. 4.2(b)** shows the corresponding size distribution of the NCs. The average size of the NCs was found to be ~11.4 nm. The HTREM lattice fringes of the $CsPbBr_3$ (**Fig. 4.2(c)**) display 'd' spacing of 0.29 nm and 0.41 nm, representing the (200) and (110) planes of $CsPbBr_3$, respectively.

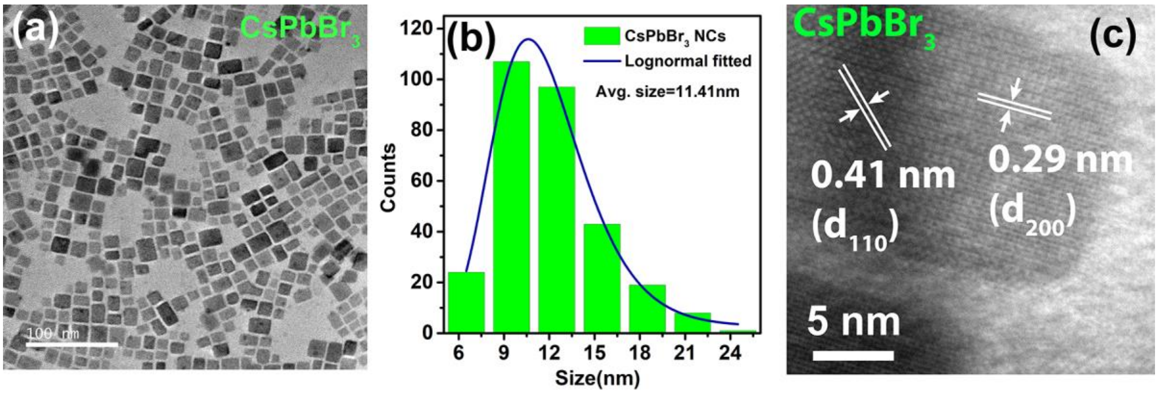

Fig. 4.2: (a) TEM image of as-synthesized $CsPbBr_3$ NCs. (b) A histogram of the size distributions of $CsPbBr_3$ NCs. The solid line shows the corresponding log-normal fitting to determine the average size of the NCs. (c) HRTEM image of a single $CsPbBr_3$ NC.

To fabricate the $Bi_2O_2Se/CsPbBr_3$ HS, an optimum volume (5 μL) of the colloidal solution of $CsPbBr_3$ perovskite NCs was deposited on the as-grown Bi_2O_2Se flakes. The morphology of the $Bi_2O_2Se/CsPbBr_3$ HS was first characterized by TEM analysis. **Fig. 4.3(a)**

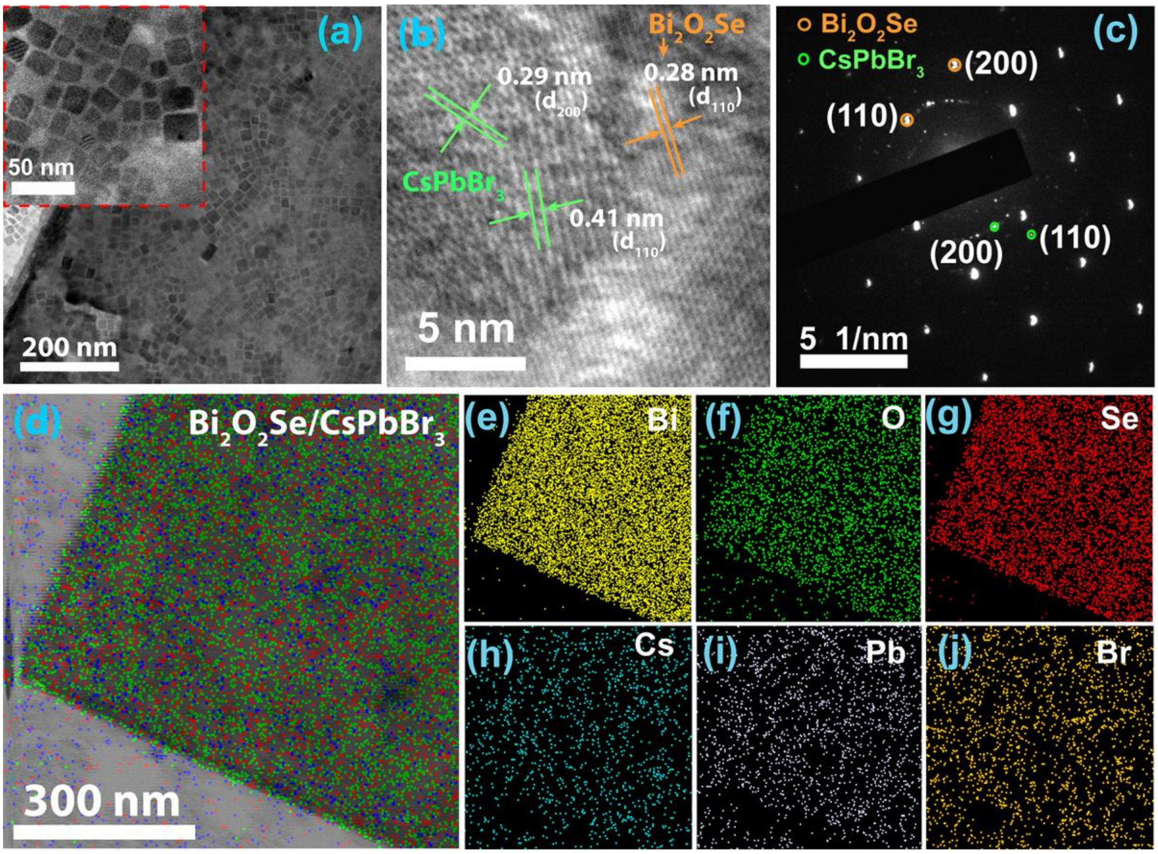

Fig. 4.3: (a) TEM image of the $Bi_2O_2Se/CsPbBr_3$ NC heterostructure. Inset shows the magnified view of $CsPbBr_3$ NCs on a Bi_2O_2Se flake. (b) HRTEM lattice fringes of a Bi_2O_2Se crystal and $CsPbBr_3$ NCs in the $Bi_2O_2Se/CsPbBr_3$ heterostructure. (c) SAED pattern of the $Bi_2O_2Se/CsPbBr_3$ heterostructure. (d) TEM elemental mapping image of the $Bi_2O_2Se/CsPbBr_3$ heterostructure and (e–j) the corresponding elemental mapping for Bi, O, Se, Cs, Pb, and Br respectively.

shows the nearly uniform decoration of $CsPbBr_3$ NCs on the surface of the Bi_2O_2Se flakes. An enlarged view of the $CsPbBr_3$ NCs on the Bi_2O_2Se flake is shown in the inset of **Fig. 4.3(a)**. The HTREM lattice fringes of the HS (**Fig. 4.3(b)**) display ‘d’ spacing of 0.28 nm, representing the plane of Bi_2O_2Se, while the d spacings of 0.29 nm and 0.41 nm, depicting the planes of $CsPbBr_3$. The SAED pattern (**Fig. 4.3(c)**) confirms that crystalline phases of both $CsPbBr_3$ perovskite and 2D Bi_2O_2Se are present. Thus, HRTEM and SAED analyses confirm the formation of a suitable heterojunction between layered Bi_2O_2Se and perovskite NCs, which were further used for studying the CT process and broadband photodetection. To analyze the elemental distribution in the hybrid system, we have performed the scanning transmission electron microscopy (STEM–EDS) analysis, as shown in **Fig. 4.3(d–j)**. The FETEM mapping of the components of the $Bi_2O_2Se/CsPbBr_3$ HS is shown in **Fig. 4.3(d)**. **Fig. 4.3(e–j)** shows the distribution profile of the individual elements Bi, O, Se, Cs, Pb, and Br, respectively. The high contrast of Bi, O, and Se due to the few-layer Bi_2O_2Se flakes, while the presence of Cs, Pb, and Br confirms the presence of $CsPbBr_3$ NCs on top of the Bi_2O_2Se flakes.

4.4.2. Structural characterization

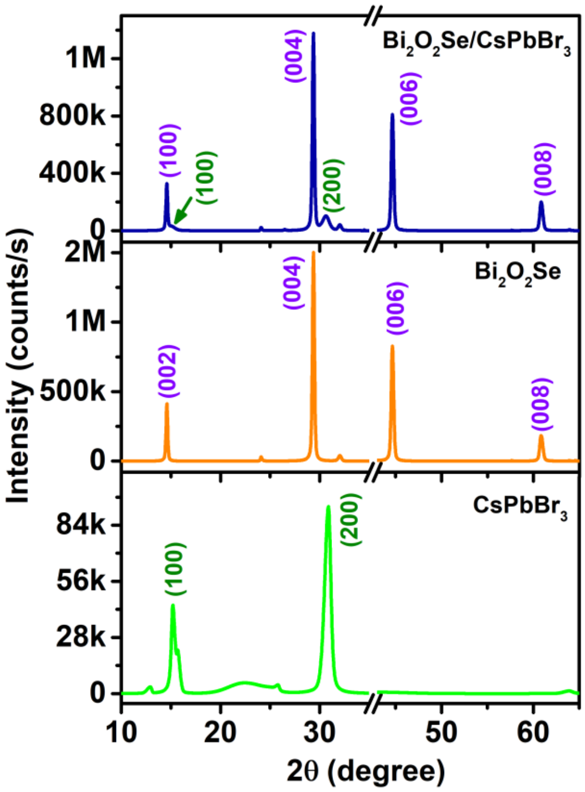

Fig. 4.4: Comparative XRD pattern of $CsPbBr_3$ NCs, pristine Bi_2O_2Se flakes, and their heterostructure.

XRD patterns were acquired to get the crystalline phase and quality of Bi_2O_2Se and $CsPbBr_3$ NCs. The comparative XRD pattern of the $CsPbBr_3$ NC film, pristine few-layer Bi_2O_2Se, and the $Bi_2O_2Se/CsPbBr_3$ heterostructure is shown in **Fig. 4.4**. Cubic $CsPbBr_3$ NCs having diffraction peaks at 15.20° and 30.50° are attributed to the (100) and (200) planes, respectively. The Bi_2O_2Se flakes exhibit major diffraction peaks at 14.49°, 29.23°, and 44.47°, assigned to the (002), (004), and (006) planes, respectively. The diffraction peak positions reveal the tetragonal crystal phase of Bi_2O_2Se (JCPDS card no-01-070-1549).[24] It is noticeable that no significant shift was observed in the XRD peak positions, confirming suitable crystallization of the hybrid system after the drop casting of $CsPbBr_3$.

4.4.3 Optical characterization

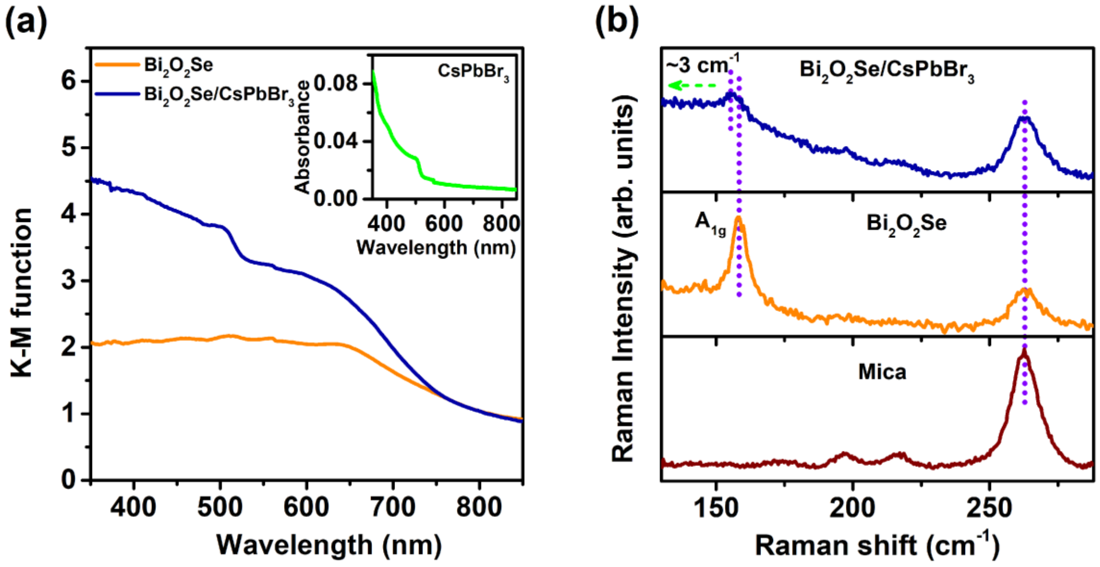

Fig. 4.5: (a) Comparison of the K–M function plot for Bi_2O_2Se flakes and the $Bi_2O_2Se/CsPbBr_3$ NC heterostructure film. Inset shows the UV-vis absorption spectra of $CsPbBr_3$ NCs. (b) Comparative Raman spectra for the bare mica substrate, pristine Bi_2O_2Se layer on mica, and $Bi_2O_2Se/CsPbBr_3$ NC heterostructure on the mica substrate.

To investigate the optical absorption of bare Bi_2O_2Se nanoflakes and the $Bi_2O_2Se/CsPbBr_3$ NC HS, diffuse reflectance spectroscopy (DRS) measurement was carried out. We deduced the Kubelka–Munk function, F(R), from the DRS data. F(R) is a comprehensive measure of the absorption coefficient/absorbance, and F(R) can be calculated using the following equation

$$F(R) = \frac{(1-R)^2}{2R} = \frac{K}{S} \qquad (4.1)$$

where R, K, and S denote diffuse reflectance, absorption, and scattering coefficient, respectively. **Fig. 4.5(a)** presents the F(R) *vs*. wavelength plot for Bi_2O_2Se flakes and the hybrid $Bi_2O_2Se/CsPbBr_3$ NC film. The inset of **Fig. 4.5(a)** represents the absorption spectra of the as-prepared $CsPbBr_3$ NCs. The absorption peak for $CsPbBr_3$ NCs was observed at 514 nm, attributed to the optical transition from the valence band to the conduction band. Interestingly, the absorption coefficient of Bi_2O_2Se is found to be very high, of the order of $\sim 10^5$ cm^{-1}, and for $CsPbBr_3$, it is $\sim 10^4$ cm^{-1}. In **Fig. 4.5(a)**, we observed a significant absorption enhancement in the UV-Visible region for the $Bi_2O_2Se/CsPbBr_3$ NC hybrid compared to pristine Bi_2O_2Se. The enhanced absorption is caused by hybridization of $CsPbBr_3$. High absorption in the UV-visible region for $Bi_2O_2Se/CsPbBr_3$ helps to obtain high photocurrent in heterojunction.

Micro-Raman measurement was performed on pristine Bi_2O_2Se flakes and $Bi_2O_2Se/CsPbBr_3$ NC HS. The comparative Raman spectra of the as-grown Bi_2O_2Se flakes on a mica substrate, $Bi_2O_2Se/CsPbBr_3$ NC HS, and bare mica substrate are shown in **Fig. 4.5(b)**. The peak at $\sim$158.5 cm^{-1} of pristine Bi_2O_2Se corresponds to the characteristic A_{1g} mode, confirming the formation of ultrathin Bi_2O_2Se flakes. In Bi_2O_2Se, in the out-of-plane mode, A_{1g} originates from the vibration of two 'Bi' atoms. Interestingly, the characteristic A_{1g} peak in the $Bi_2O_2Se/CsPbBr_3$ HS was redshifted by 3 cm^{-1}. The redshift in the A_{1g} peak position indicates higher n-type doping in Bi_2O_2Se after the heterojunction formation. It might a result of a possible CT from $CsPbBr_3$, which will be discussed later. The peak at 262.8 cm^{-1} in the spectra is attributed to the mica substrate, and it does not show any shift in the HS, confirming that shift in the A_{1g} Raman mode arises due to the coupling of Bi_2O_2Se with the perovskite NCs. Notably, the CT in the heterojunction can be made beneficial for photodetector application. The doping state of Bi_2O_2Se can be predicted from the out-of-plane A_{1g} mode due to the coupling between electrons and phonons along the c-axis. The Bi_2O_2Se layer may be connected with the perovskite NCs by the van der Waals force in the hybrid structure.

To better understand the origin of the shift in the A_{1g} mode, we have systematically studied the Raman spectra of the $Bi_2O_2Se/CsPbBr_3$ NC HS for different amounts of the perovskite NCs. **Fig. 4.6(a)** shows the results for three different volumes, 2.5 μL, 5 μL, and 10 μL, of $CsPbBr_3$ NCs. With the increase in the volume of the perovskite NCs, the A_{1g} Raman peak of Bi_2O_2Se showed systematically higher shifts towards the lower wavenumber. Thus, the direct correlation between the perovskite NC amount and the redshift of A_{1g} suggests that CT is higher at a higher volume of NCs (up to 5 μL). For a qualitative understanding of the CT process, we plot the Raman peak position (A_{1g} mode) as a function of the perovskite volume,

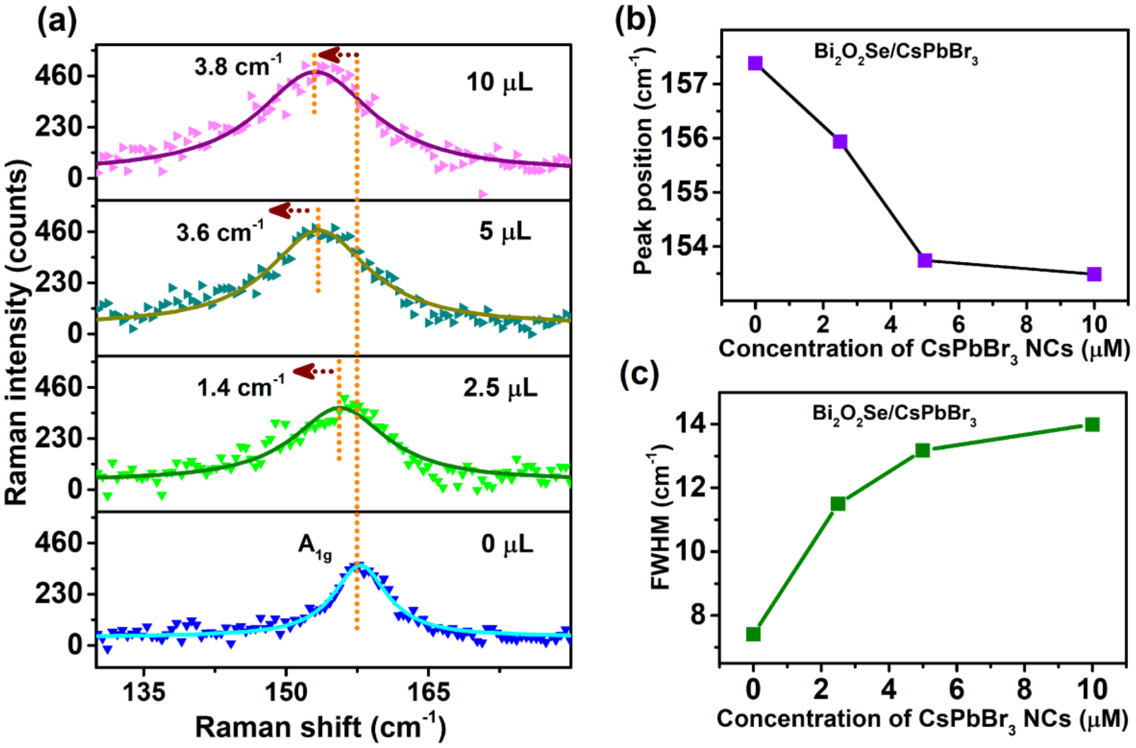

Fig. 4.6: (a) Raman spectra of the characteristic A_{1g} mode of Bi_2O_2Se decorated with $CsPbBr_3$ for different volumes. The solid lines are Lorentz fitted, and the arrow indicates the redshift of the A_{1g} mode in the presence of $CsPbBr_3$. (b) Evolution of the A_{1g} peak position of Bi_2O_2Se as a function of the $CsPbBr_3$ volume. (c) FWHM of the A_{1g} mode for different volumes of $CsPbBr_3$ NCs.

as shown in **Fig. 4.6(b)**. A linear relationship between the Raman shift and NC volume was discerned up to a volume of 5 μL. Note that no further shift in the peak position is observed at a higher volume of perovskites, implying no further CT. Likewise, the FWHM (**Fig. 4.6 (c)**) of the Raman peak significantly increases up to a volume of 5 μL and saturated at a higher volume. It is due to the uniform surface coverage with $CsPbBr_3$ NCs at 5 μL (see **Fig. 4.7**). At 2.5 μL of NCs, we witnessed less coverage of the perovskite NCs over the Bi_2O_2Se layer (see **Fig. 4.7(b)**). If we add a larger amount, it covers more surface area of the Bi_2O_2Se flakes (see

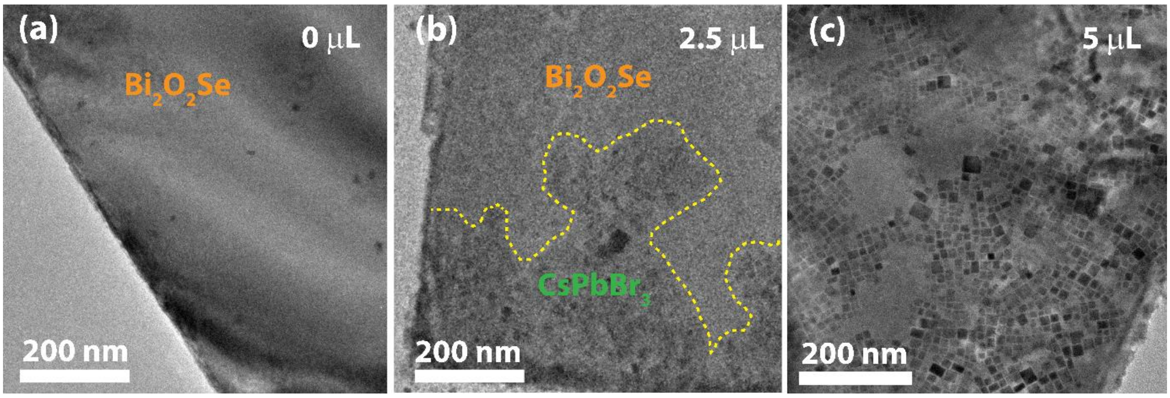

Fig. 4.7: TEM image of Bi_2O_2Se flakes with (a) 0 μL (b) 2.5 μL (c) 5 μL of $CsPbBr_3$ NCs.

Fig. 4.7(c)). With a larger volume of the solution (>5 μL), $CsPbBr_3$ NCs start stacking on each other. The efficiency of the CT depends on the nature of the interface of the perovskite and layered Bi_2O_2Se. It is quite likely that due to the higher bandgap of the perovskite NCs compared to the 2D Bi_2O_2Se, CT takes place from the perovskite layer to the Bi_2O_2Se layer, and this leads to a higher concentration of electrons in the Bi_2O_2Se.The larger FWHM and homogeneous broadening of the Raman peak may originate from the structural relaxation caused by charge accumulation.

The photogenerated CT and recombination dynamics of the photogenerated carriers in the $Bi_2O_2Se/CsPbBr_3$ hybrid system are investigated utilizing steady-state and time-resolved PL measurements. The PL spectra of a bare $CsPbBr_3$ NC film and the $Bi_2O_2Se/CsPbBr_3$ NC film with different volumes of $CsPbBr_3$ are shown in **Fig. 4.8(a)**. The PL intensity is dramatically quenched in the hybrid system as compared to the pristine perovskite NCs. The corresponding data are shown on a magnified scale (5 times) for better visualization. The PL peak at 514 nm corresponds to excitonic recombination near the band edge in $CsPbBr_3$. It is noticeable that the PL intensity of $CsPbBr_3$ is quenched strongly while it is in contact with the Bi_2O_2Se layer. A significant quenching is noticed at 2.5 μL with a quenching efficiency of 93.5% (inset of **Fig. 4.8(a)**), and at 5 μL, the quenching efficiency increases to 96.1%. The

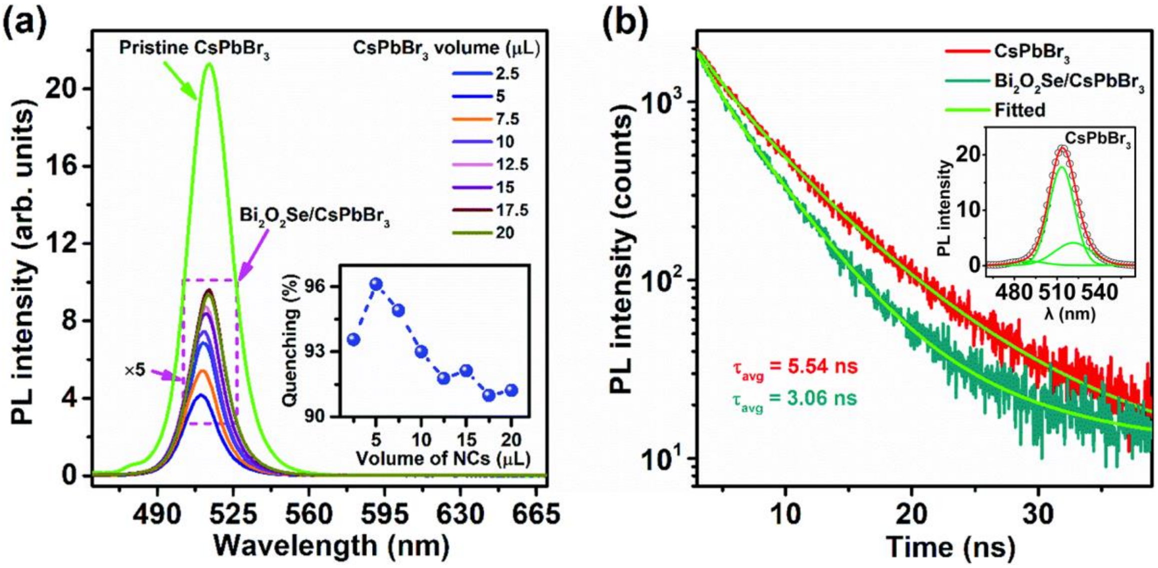

Fig. 4.8: (a) Comparison of PL spectra for $CsPbBr_3$ on the mica substrate and $CsPbBr_3$ on the Bi_2O_2Se/mica substrate at a different volume of $CsPbBr_3$. The inset represents the quenching efficiency as a function of the volume of the NC solution. (b) Comparison of the TRPL decay profiles for $CsPbBr_3$ and $Bi_2O_2Se/CsPbBr_3$. Inset shows the steady-state PL emission spectrum of pristine $CsPbBr_3$ at room temperature. Symbols represent the experimental data, and the solid line shows the Gaussian fitting.

quenching efficiency is highest for 5 μL of the perovskite. Maximum quenching is due to the uniform surface coverage at 5 μL (**Fig. 4.7(c)**). Note that above 5 μL, a systematic reduction in quenching is observed. This is quite expected since at a higher perovskite volume, most of the perovskite NCs are not in direct contact with the Bi_2O_2Se layer, and hence less quenching is justified. Thus, the PL quenching of NCs is attributed to the photoinduced CT from $CsPbBr_3$ to Bi_2O_2Se at the hybrid interface. Due to the interfacial CT, radiative recombination reduces in $CsPbBr_3$ NCs.

Time-resolved photoluminescence (TRPL) measurements were performed to investigate the photoinduced charge recombination kinetics for pristine $CsPbBr_3$ NCs and the $Bi_2O_2Se/CsPbBr_3$ NC hybrid system. The TRPL decay profiles of the $CsPbBr_3$ NC film and the $Bi_2O_2Se/CsPbBr_3$ NC film are shown in **Fig. 4.8(b)**. The TRPL decay profiles are monitored at 514 nm since the steady-state PL spectra revealed a peak at 514 nm for the pristine perovskite NCs. The experimental data are fitted using the following equation[8]

$$A(t) = \sum_{i=1}^{i=2} A_i \exp(-t/\tau_i) \qquad (4.2)$$

which is a bi-exponential decay function. In **equation (4.2)**, A_i and τ_i represent the amplitude and lifetime of the i-th decay component, respectively. The emission dynamics of the fluorophore can be deduced from the average time the fluorophores reside in the excited state. The average lifetime (τ_{avg}) was estimated from the TRPL decay profile using the relation[8]

$$\tau_{avg} = \frac{\sum_{i=1}^{i=2} A_i \tau_i}{\sum_{i=1}^{i=2} A_i} \qquad (4.3)$$

The decay time and amplitude of the $CsPbBr_3$ NC film and the $Bi_2O_2Se/CsPbBr_3$ NC film are tabulated in **Table 4.1**. Noticeably, two prominent peaks are seen from the Gaussian fitting of the steady-state PL spectrum of pristine $CsPbBr_3$ (shown in the inset of **Fig. 4.8(b)**). The fitted TRPL decay profile revealed the average decay time for $CsPbBr_3$ and $Bi_2O_2Se/CsPbBr_3$ NC film as 5.54 ns and 3.06 ns, respectively. The apparent shortening in the average decay time in the $Bi_2O_2Se/CsPbBr_3$ hybrid compared to the pristine $CsPbBr_3$ sample is fully consistent with the interfacial CT proposed earlier. Because of the specific type of band alignment, the generation and transfer of photoinduced electrons/holes occur from $CsPbBr_3$ to Bi_2O_2Se, reducing the probability of recombination results in the PL quenching and faster decay of carriers in the hybrid device.

Table 4.1: *Details of the fitting parameters of time-resolved PL decay profiles for* $CsPbBr_3$ *NCs and* $Bi_2O_2Se/CsPbBr_3$ *HS.*

Sample	τ_1 (ns)	A_1	τ_2 (ns)	A_2	τ_{ave} (ns)
$CsPbBr_3$	8.65	924	4.55	2916	5.54
$Bi_2O_2Se/CsPbBr_3$	4.55	2781	1.60	2828	3.06

4.4.4. Electronic structure calculation of $Bi_2O_2Se/CsPbBr_3$ NCs and mechanism of superior charge transfer

To thoroughly understand the $Bi_2O_2Se/CsPbBr_3$ heterojunction, we investigated the electronic structure of the individual and hybrid system made of the $CsPbBr_3$ NC and bilayer Bi_2O_2Se. The electronic structures of the $CsPbBr_3$ NC and bilayer Bi_2O_2Se are calculated separately to understand the nature of charge transfer and the type of heterojunction formed. Though our Bi_2O_2Se sample is thicker than the bilayer thickness, to save computation time and without the loss of generality, we consider only bilayer Bi_2O_2Se for the DFT calculation. It has been reported from a theoretical study that in the case of layered Bi_2O_2Se, the change in the bandgap with the thickness above two layers is minimal.[25] Hence, it is believed that it will not affect the conclusion on the CT if we consider higher thickness (more than two layers) for the calculation. The total density of states (TDOS) and projected density of states (PDOS) of the

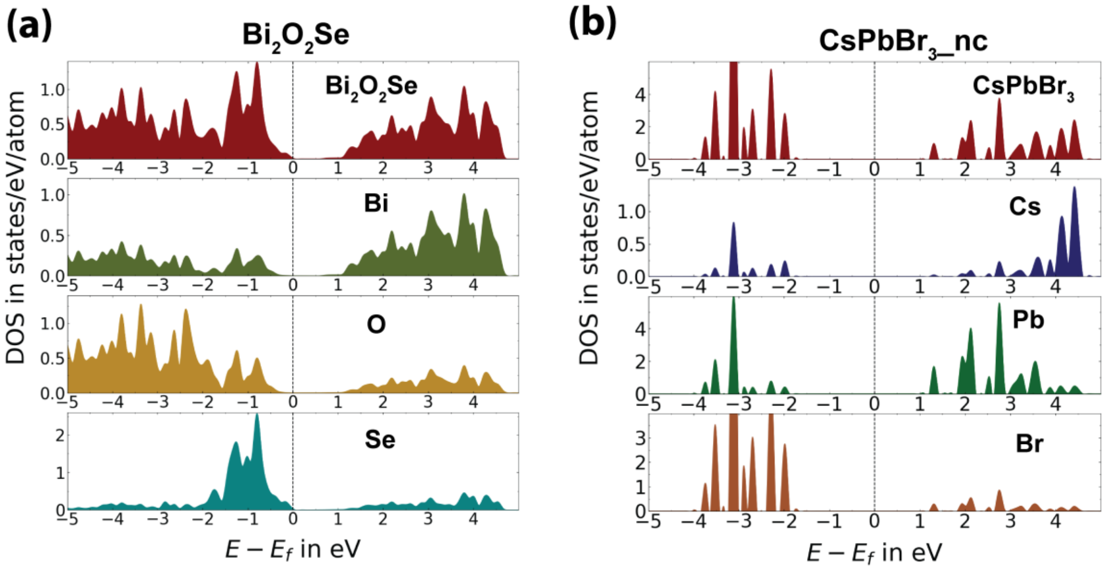

Fig. 4.9: Total density of states (TDOS) and projected density of states (PDOS) for (a) bilayer Bi_2O_2Se (b) $CsPbBr_3$ NCs.

bilayer Bi_2O_2Se and $CsPbBr_3$ NC are shown in **Fig. 4.9(a)** and **(b)**, respectively. From the PDOS data, one can understand the contributions of the valence electrons of each element towards the TDOS of the system. The TDOS of the $CsPbBr_3$ NC and PDOS of each element consists of neither discrete energy levels like isolated molecules/atoms nor bands like a solid system. The electronic states of the NC lie between -2 eV and -4 eV in the valence band region and between 1.25 eV and 4.5 eV in the conduction band region. Unlike the $CsPbBr_3$ NC, we find states close to the Fermi level in the valence band of Bi_2O_2Se, contributed by all three constituents. **Fig. 4.10** shows the TDOS and PDOS of the $Bi_2O_2Se/CsPbBr_3$ NC hybrid structure, which has been obtained from the optimized structure of the hybrid system (**Fig. 4.11(a)**). We observe that in comparison with either of the constituents forming the HS, the TDOS of the HS shifts towards lower energies. The bottom of the conduction band (around 0.5 eV) shows contributions from Bi - 6p, Se - 4p, and O -2p states. The availability of additional states in the conduction band near the Fermi level (in comparison with either of the constituents of the HS) and their characteristics imply that there is CT from the $CsPbBr_3$ NC to bilayer Bi_2O_2Se. The DOS also implies the formation of a type-I heterojunction. The change in the DOS and transfer of charges (electrons/holes) is more evident from **Fig. 4.11(b),** showing the TDOS of Bi_2O_2Se, $CsPbBr_3$ NCs, and the $Bi_2O_2Se/CsPbBr_3$ hybrid system. The red and blue

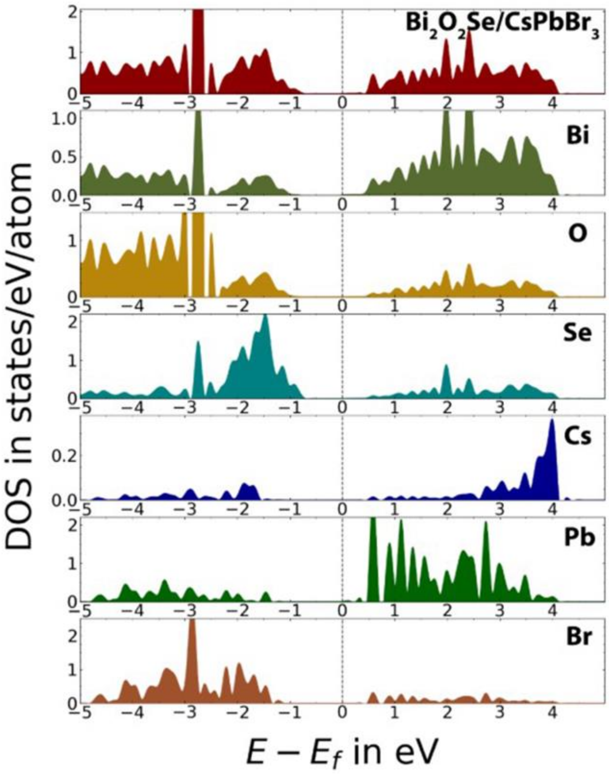

Fig. 4.10: TDOS and PDOS of bilayer $Bi_2O_2Se/CsPbBr_3$ NC heterostructure.

vertical lines show the VBM (valence band maxima) and CBM (conduction band minima) of the systems, respectively. The band positions of the NCs and bilayer Bi_2O_2Se confirm the formation of the type-I heterojunction. The shift of the VBM and CBM in the hybrid/composite system towards the Fermi level suggests electron and hole movement from $CsPbBr_3$ NCs to bilayer Bi_2O_2Se in the conduction and valence bands, respectively. **Fig. 4.11(c)** shows the corresponding charge density plot. The Bader charge analysis corroborates the CT from the NC to Bi_2O_2Se. It shows that the $CsPbBr_3$ NC loses an overall charge of amount 7.68e, which is gained by Bi_2O_2Se. Interestingly, this theoretical interpretation agrees very well with the experimental results of the CT between Bi_2O_2Se and $CsPbBr_3$ systems. Note that the interfacial CT in such a system leads to the superior performance of the hybrid photodetector under

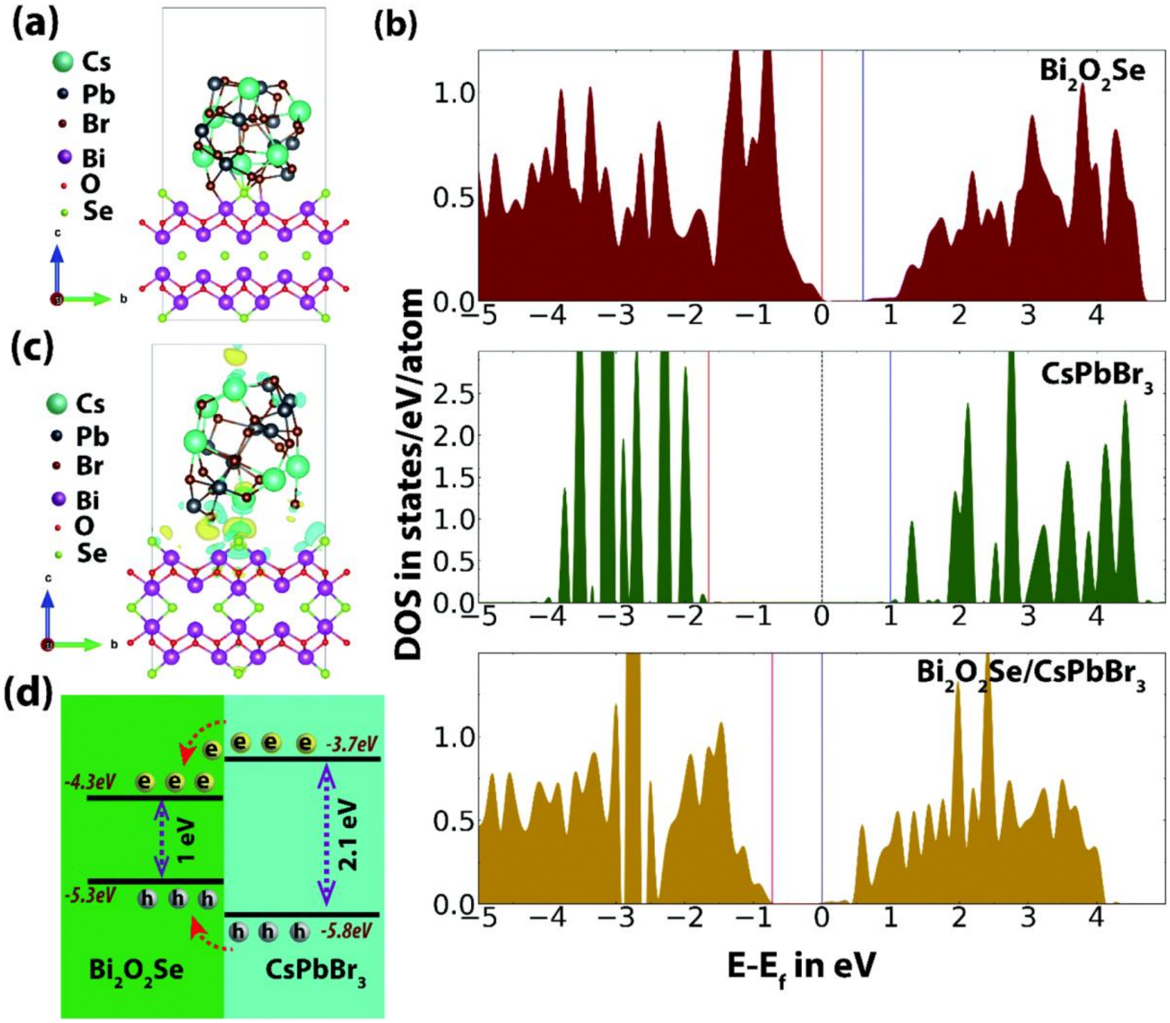

Fig. 4.11: (a) Optimized structure at the minimum energy configuration of the bi-layer $Bi_2O_2Se/CsPbBr_3$ NC heterostructure. (b) TDOS of Bi_2O_2Se, $CsPbBr_3$ NCs and the composite ($Bi_2O_2Se/CsPbBr_3$) system. The red and blue vertical lines show the VBM (valence band maxima) and CBM (conduction band minima) of the systems, respectively. (c) Charge density difference plot ($\Delta\rho = \rho(Bi_2O_2Se/CsPbBr_3) - \rho(Bi_2O_2Se) - \rho(CsPbBr_3)$) for the $Bi_2O_2Se/CsPbBr_3$ heterostructure; the blue (yellow) color represents accumulation (depletion) of electrons. (d) Schematic illustration of the band bending and photo-induced charge transfer process in the $Bi_2O_2Se/CsPbBr_3$ heterostructure.

external bias, as discussed below. The energy band alignment intrinsically determines the charge transport behavior at the vdW HS. The band edges of Bi_2O_2Se and $CsPbBr_3$ suggest a type-I band alignment in the HS, shown in **Fig. 4.11(d).**[13, 14, 26, 27] When the $Bi_2O_2Se/CsPbBr_3$ HS is formed, the higher Fermi level (E_F) of $CsPbBr_3$ facilitates the transfer of its electrons to Bi_2O_2Se until the thermal equilibrium state of the complete system with a merged E_F. Because of the type-I band alignment, photoinduced charges are transferred efficiently at the heterojunction.[12] Though both the electrons and holes are transferred to the underlying Bi_2O_2Se layer, due to the applied external bias, these carriers can avoid recombination and contribute to the photocurrent in the external circuit. It results in an improved photocurrent in the HS device compared to the Bi_2O_2Se device. Thus, the electronic structure calculation confirms the experimental findings. It provides valuable insights into the mechanism of the CT process and its implication for the performance of the photodetector.

4.4.5. Photoresponse properties of the $Bi_2O_2Se/CsPbBr_3$ heterostructure

To study the photoresponse performance of pristine Bi_2O_2Se and the $Bi_2O_2Se/CsPbBr_3$ heterojunction, two-terminal devices were fabricated. A copper grid with a gap of 10 µm is used to pattern the electrodes with Au film. A schematic representation of the hybrid $Bi_2O_2Se/CsPbBr_3$ NC photodetector is shown in **Fig. 4.12(a)** (Inset displays the photograph of the fabricated device). **Fig. 4.12(b)** shows the I-V curves of the $Bi_2O_2Se/CsPbBr_3$ device in the

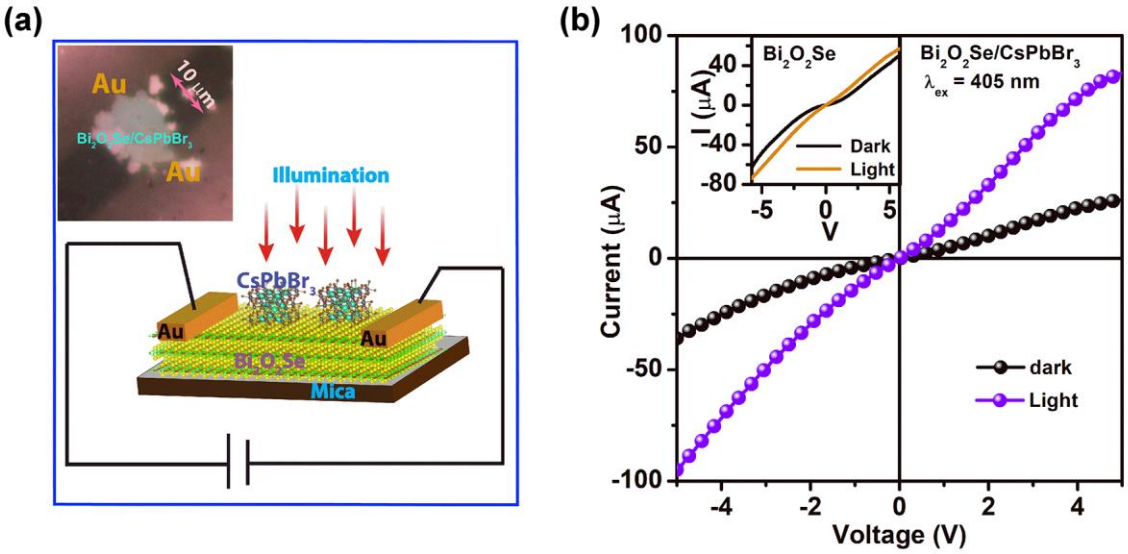

Fig. 4.12: (a) Schematic illustration of the $Bi_2O_2Se/CsPbBr_3$ planar heterojunction photodetector. Inset shows the photograph of the device. (b) I–V characteristics of the $Bi_2O_2Se/CsPbBr_3$ heterostructure device without and with light illumination (405 nm laser). Inset displays the I-V characteristics of the pristine Bi_2O_2Se device.

dark and under light (405 nm laser with an intensity of 2.35 mW.cm^{-2}) at 300 K under atmospheric conditions. Interestingly, the dark current in the $Bi_2O_2Se/CsPbBr_3$ device is lower than that of the pristine Bi_2O_2Se device (see inset of **Fig 4.12(b)**) for the same applied voltage. At the same time, the photocurrent in $Bi_2O_2Se/CsPbBr_3$ is much higher than in the pristine device due to the interfacial CT from the light-harvesting $CsPbBr_3$ NCs to Bi_2O_2Se. **Fig. 4.13(a)** shows the typical photocurrent response of the $Bi_2O_2Se/CsPbBr_3$ device under 405 nm laser (pulsed) illumination at various intensities (0.05 mW cm^{-2} to 20.06 mW cm^{-2}). The current increases with the increase in the laser intensity. The variation of the photocurrent (I_{ph}) with the change in the light intensity (P) is fitted with the power-law as

$$I_{ph} = AP^{\theta} \qquad (4.4)$$

where A and θ are the constant and response parameter for a particular wavelength, respectively. For the $Bi_2O_2Se/CsPbBr_3$ photodetector, the θ value is 0.52 in the low intensity region and 0.28 in the high intensity region (inset of **Fig. 4.13**). The sub-linear behavior originates from the trapping of charge carriers in interfacial trap states in the hybrid system, which helps the photo-excited carriers to recombine.[28] Note that the ligand residue in the $CsPbBr_3$ NCs can trap carriers, leading to photocurrent saturation at a higher intensity. Since our experiments are conducted under ambient conditions, introduction of defects in the perovskite NCs is quite likely since these are susceptible to moisture. Photocurrent measurement has been carried out for different bias voltages, as shown in **Fig. 4.14(a)**. The

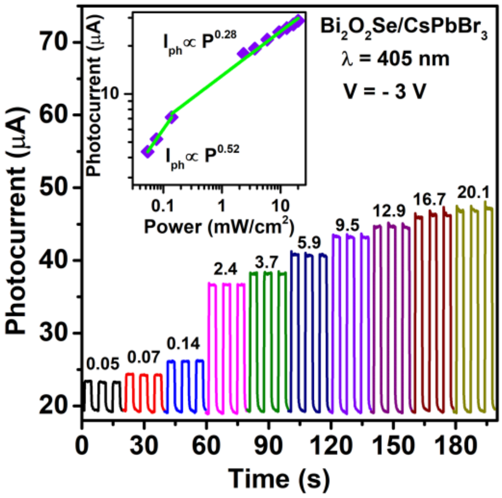

Fig. 4.13: Photocurrent response as a function of the illumination intensity (ON/OFF) for the heterojunction photodetector. The inset shows the power-law fitting to the illumination power dependence of the photocurrent for the heterojunction device.

inset of **Fig. 4.14(a)** shows a nearly linear increment in the photocurrent with the increment in the bias voltage. The photocurrent under the illumination of a 405 nm laser pulse was measured for a prolonged duration to check the light stability of the device (**Fig. 4.14(b)**). The results suggest the high stability of the hybrid device under ambient conditions.

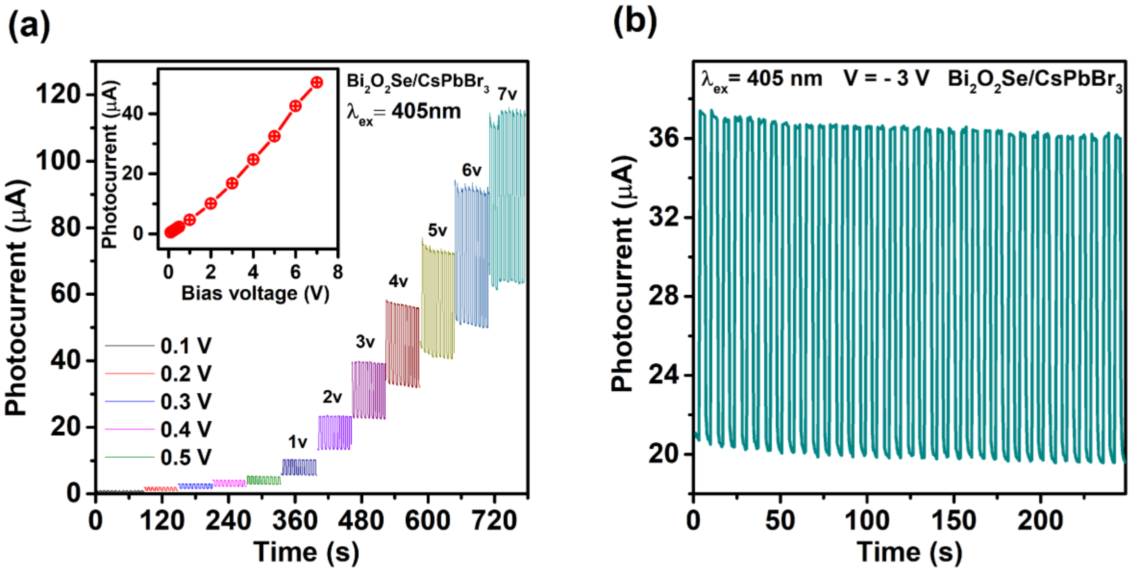

Fig. 4.14: (a) Photocurrent response under different bias voltages in $Bi_2O_2Se/CsPbBr_3$ NCs heterostructure photodetector. Inset depicts the nonlinear increase in photocurrent with the bias voltage. (d) Stability of photocurrent response under prolonged exposure to light pulses.

Furthermore, the photo-responsivity (R) and detectivity (D) were calculated using the following equations

$$R = \frac{I_{ph}}{SP} \qquad (4.5)$$

$$D = \frac{R}{(2qJ_d)^{1/2}} \qquad (4.6)$$

where I_{ph} represents the photocurrent, P is the laser intensity, S is the operative area, J_d is the dark current density, and q is the electronic charge. A comparison of the spectral responsivity of pristine and hybrid photodetectors is shown in **Fig. 4.15(a)** at 3 V (reverse bias) in the wavelength range of 390-840 nm. It reveals a relatively higher responsivity in the wavelength region of 390-640 nm and a lower responsivity in the higher wavelength region. Higher responsivity at the lower wavelength region is primarily due to the higher absorption of the $Bi_2O_2Se/CsPbBr_3$ hybrid, as shown in **Fig. 4.5(a)**. Due to the additional absorption of UV-visible light by the $CsPbBr_3$ layer, responsivity is higher in the lower wavelength region. The internal reflection of light at the interface of the hybrid structure is also partly responsible for higher responsivity of the hybrid device. The highest responsivity was 46 AW^{-1} at 620 nm and 39 AW^{-1} at 400 nm, as shown in **Fig. 4.15(a)**, while for the pristine Bi_2O_2Se device it was 43 AW^{-1} and 34 AW^{-1} at the respective wavelengths. We notice an enhancement in responsivity by ~35% at 500 nm in the hybrid photodetector, which is attributed to the superior photocarrier generation and transport from $CsPbBr_3$ NCs to the Bi_2O_2Se layer and finally to the external circuit due to the bias voltage. Note that the transport of photogenerated carriers avoiding radiative recombination in perovskite NCs was probed by Raman, steady-state, and time-resolved PL measurements, and it was corroborated by DFT-based electronic structure calculations. The obtained responsivity value is higher than those of other conventional $CsPbBr_3$-based photodetectors.[8, 29] The inset of **Fig. 4.15(a)** shows the responsivity of bare Bi_2O_2Se and the heterojunction photodetector as a function of the illumination intensity. The heterojunction photodetector shows a very high responsivity (~10^3 AW^{-1}) at an incident intensity of 0.05 mW cm^{-2} for 405 nm, which is excellent as a low-power photodetector. This is mainly due to the high absorption coefficient of the Bi_2O_2Se layer. We further calculated the specific detectivity of the hybrid photodetectors using **equation (4.6)**. The peak detectivity of the heterojunction photodetector is 2.34×10^{10} Jones, and that of the bare Bi_2O_2Se photodetector is 2.11×10^{10} Jones at 400 nm (**Fig. 4.15(b)**). At 620 nm, the detectivity is 2.73

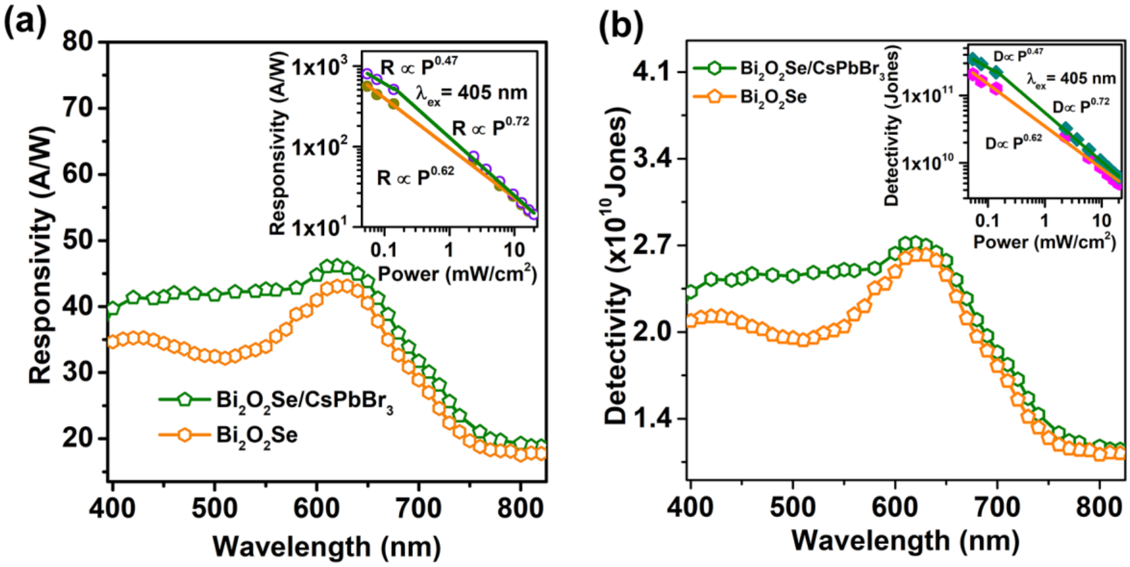

Fig. 4.15: (a) Comparison of the spectral responsivity of the pristine Bi2O2Se photodetector and heterojunction photodetector in the wavelength 390-840 nm under -3 V bias. The inset shows the variation of responsivity with the incident light (405 nm laser) intensity for the pristine Bi_2O_2Se and heterojunction photodetector. (b) Detectivity of pristine semiconducting Bi_2O_2Se and $Bi_2O_2Se/CsPbBr_3$ NCs. heterostructure. The inset shows the respective excitation intensity-dependent detectivity at 405 nm.

× 10^{10} Jones for the HS. Thus, the responsivity and detectivity of the hybrid photodetector are improved compared to the bare Bi_2O_2Se based photodetector.

The response time is a key parameter of a photodetector. The photoresponse speeds of bare Bi_2O_2Se and $Bi_2O_2Se/CsPbBr_3$ heterojunction photodetectors are quantified, as shown in **Fig. 4.16(a) and (b)**, respectively. The experimental data of the photocurrent rise and decay processes are fitted by a single exponential function given by

$$I(t) = I_0 + Ae^{\left(-\frac{t}{\tau}\right)} \qquad (4.7)$$

where τ is the time constant, and I_0 and A represent the constants. The photocurrent growth and decay time are 62 μs and 601 μs for bare Bi_2O_2Se, while it comes out to be 12 μs and 28 μs, respectively, for the $Bi_2O_2Se/CsPbBr_3$ heterojunction photodetector, as shown in **Fig. 4.16(a and b)**. Remarkably, in the heterojunction system, the response time is comparatively faster than the reported values for the bare Bi_2O_2Se based device.[2] The faster photoresponse of the hybrid photodetector compared to the pristine Bi_2O_2Se photodetector is due to the faster interfacial CT in the type-I HS. Note that in general a type-I heterojunction with a Bi_2O_2Se layer can limit the performance of a photodetector, as the photogenerated carriers can recombine in the Bi_2O_2Se layer. However, due to the external bias, the probability of recombination of carriers in the layer is reduced and this leads to an improvement in the photocurrent in the hybrid device. Ideally, a type-II heterojunction on Bi_2O_2Se could lead to a

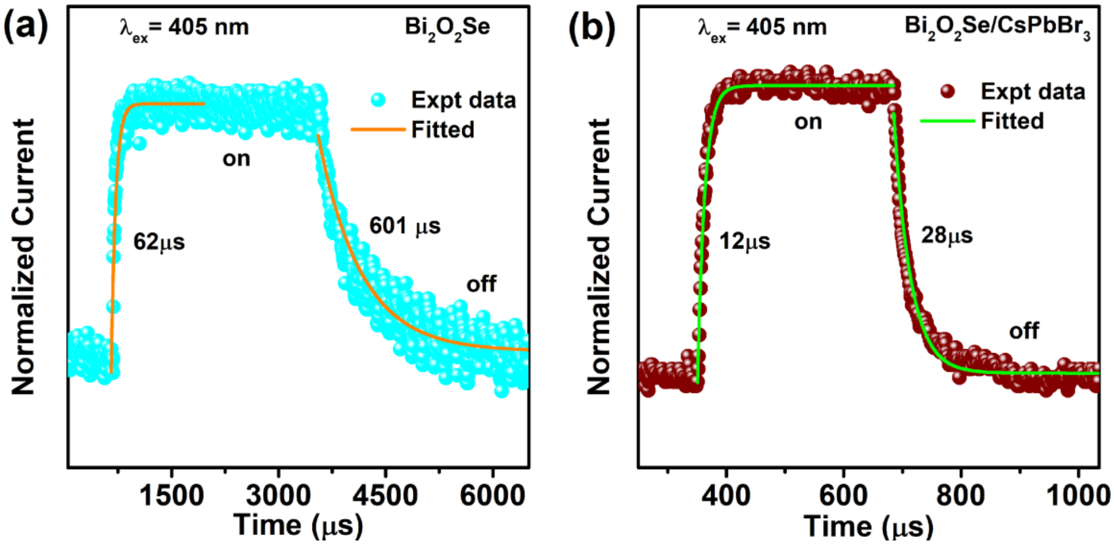

Fig. 4.16: (a) Temporal response of the growth and decay of photocurrent (symbols) in the pristine Bi_2O_2Se device and (b) heterojunction photodetector with single exponential fitting (solid line).

dramatic improvement in the performance of the Bi_2O_2Se photodetector. It would be interesting to explore such systems for future studies.

4.5. Conclusions

We have demonstrated the CVD growth of few-layer 2D Bi_2O_2Se crystals for studying the CT dynamics in the $Bi_2O_2Se/CsPbBr_3$ hybrid structure. Direct evidence from photoinduced CT was provided from the micro-Raman and PL analyses. It is further corroborated by the DFT calculation of the density of states and charge density plots. The CT mechanism was investigated thoroughly by Raman spectral analysis and steady-state and time-resolved PL analyses. Our studies reveal the origin of improved photodetection performance of the $Bi_2O_2Se/CsPbBr_3$ HS compared to bare Bi_2O_2Se layers. It was demonstrated that the improved efficiency of the hybrid photodetector is due to the interfacial CT of photoinduced electrons from the perovskite to the Bi_2O_2Se layer due to the type-I band bending. As a result, we obtain a high responsivity of 46 AW^{-1}, a fast response time of 12 μs, and broadband photodetection from 390 to 840 nm in the hybrid photodetector. More importantly, understanding of the CT process and CT-induced photodetection was first achieved in the $Bi_2O_2Se/CsPbBr_3$ planar HS. Our work on the 2D $Bi_2O_2Se/CsPbBr_3$ HS opens up a promising ground in the field of highly sensitive, fast broadband photodetection.

References

1. Q. Fu, C. Zhu, X. Zhao, X. Wang, A. Chaturvedi, C. Zhu, X. Wang, Q. Zeng, J. Zhou, F. Liu, B. K. Tay, H. Zhang, S. J. Pennycook and Z. Liu, *Advanced Materials*, 2019, **31**, 1804945.
2. T. Tong, Y. Chen, S. Qin, W. Li, J. Zhang, C. Zhu, C. Zhang, X. Yuan, X. Chen, Z. Nie, X. Wang, W. Hu, F. Wang, W. Liu, P. Wang, X. Wang, R. Zhang and Y. Xu, *Advanced Functional Materials*, 2019, **29**, 1905806.
3. P. Luo, F. Zhuge, F. Wang, L. Lian, K. Liu, J. Zhang and T. Zhai, *ACS Nano*, 2019, **13**, 9028-9037.
4. H. Yang, C. Tan, C. Deng, R. Zhang, X. Zheng, X. Zhang, Y. Hu, X. Guo, G. Wang, T. Jiang, Y. Zhang, G. Peng, H. Peng, X. Zhang and S. Qin, *Small*, 2019, **15**, 1904482.
5. M. Wu and X. C. Zeng, *Nano Letters*, 2017, **17**, 6309-6314.
6. D. Kozawa, A. Carvalho, I. Verzhbitskiy, F. Giustiniano, Y. Miyauchi, S. Mouri, A. H. Castro Neto, K. Matsuda and G. Eda, *Nano Letters*, 2016, **16**, 4087-4093.
7. L. P. L. Mawlong, A. Bora and P. K. Giri, *Scientific Reports*, 2019, **9**, 19414.
8. J. Ghosh, L. P. L. Mawlong, M. G. B, A. J. Pattison, W. Theis, S. Chakraborty and P. K. Giri, *Journal of Materials Chemistry C*, 2020, **8**, 8917-8934.
9. J. Ghosh, R. Ghosh and P. K. Giri, *ACS Applied Nano Materials*, 2018, **1**, 1551-1562.
10. J. Ghosh, G. Natu and P. K. Giri, *Organic Electronics*, 2019, **71**, 175-184.
11. C. Fan, B. Dai, H. Liang, X. Xu, Z. Qi, H. Jiang, H. Duan and Q. Zhang, *Advanced Functional Materials*, 2021, **31**, 2010263.
12. M. Z. Bellus, M. Li, S. D. Lane, F. Ceballos, Q. Cui, X. C. Zeng and H. Zhao, *Nanoscale Horizons*, 2017, **2**, 31-36.

13. W. Zheng, B. Zheng, Y. Jiang, C. Yan, S. Chen, Y. Liu, X. Sun, C. Zhu, Z. Qi, T. Yang, W. Huang, P. Fan, F. Jiang, X. Wang, X. Zhuang, D. Li, Z. Li, W. Xie, W. Ji, X. Wang and A. Pan, *Nano Letters*, 2019, **19**, 7217-7225.
14. M. Li, M. Z. Bellus, J. Dai, L. Ma, X. Li, H. Zhao and X. C. Zeng, *Nanotechnology*, 2018, **29**, 335203.
15. P. E. Blöchl, *Physical Review B*, 1994, **50**, 17953-17979.
16. G. Kresse and J. Furthmüller, *Physical Review B*, 1996, **54**, 11169-11186.
17. G. Kresse and D. Joubert, *Physical Review B*, 1999, **59**, 1758-1775.
18. J. P. Perdew, K. Burke and M. Ernzerhof, *Physical Review Letters*, 1996, **77**, 3865-3868.
19. M. Methfessel and A. T. Paxton, *Physical Review B*, 1989, **40**, 3616-3621.
20. W. Tang, E. Sanville and G. Henkelman, *Journal of Physics: Condensed Matter*, 2009, **21**, 084204.
21. E. Sanville, S. D. Kenny, R. Smith and G. Henkelman, *Journal of Computational Chemistry*, 2007, **28**, 899-908.
22. G. Henkelman, A. Arnaldsson and H. Jónsson, *Computational Materials Science*, 2006, **36**, 354-360.
23. M. Yu and D. R. Trinkle, *The Journal of Chemical Physics*, 2011, **134**, 064111.
24. J. Wu, H. Yuan, M. Meng, C. Chen, Y. Sun, Z. Chen, W. Dang, C. Tan, Y. Liu, J. Yin, Y. Zhou, S. Huang, H. Q. Xu, Y. Cui, H. Y. Hwang, Z. Liu, Y. Chen, B. Yan and H. Peng, *Nature Nanotechnology*, 2017, **12**, 530-534.
25. Q. Wei, R. Li, C. Lin, A. Han, A. Nie, Y. Li, L.-J. Li, Y. Cheng and W. Huang, *ACS Nano*, 2019, **13**, 13439-13444.
26. M. T. Hossain, M. Das, J. Ghosh, S. Ghosh and P. K. Giri, *Nanoscale*, 2021, **13**, 14945-14959.
27. Y. H. Zhou, Z. B. Zhang, P. Xu, H. Zhang and B. Wang, *Nanoscale Research Letters*, 2019, **14**, 364.
28. S. Parveen, K. K. Paul and P. K. Giri, *ACS Applied Materials & Interfaces*, 2020, **12**, 6283-6297.
29. C. H. Kang, I. Dursun, G. Liu, L. Sinatra, X. Sun, M. Kong, J. Pan, P. Maity, E.-N. Ooi, T. K. Ng, O. F. Mohammed, O. M. Bakr and B. S. Ooi, *Light: Science & Applications*, 2019, **8**, 94.

Chapter 5

Interlayer Charge Transfer Induced Photoluminescence Quenching and Enhanced Photoconduction in Two-Dimensional Bi_2O_2Se/MoS_2 Type-II Heterojunction

This chapter highlights the investigation of interlayer charge transfer across the 2D/2D hetero-layers of Bi_2O_2Se/MoS_2. Interlayer charge transfer (CT) based on band alignment is vital in high-performing optoelectronic applications, such as PL modulation, superior photoconduction, etc. Stacking atomically thin materials with suitable band alignments is an efficient approach to witness CT. To study interlayer CT, the stacking of ultrathin vdW materials has been studied extensively, while the stacking of vdWs materials with nvdW materials is least explored. In this context, we studied the stacking of vdWs 2D MoS_2 with nvdWs 2D Bi_2O_2Se layer for understanding the interlayer coupling and charge transfer across the 2D interface. Studies through various spectroscopic and microscopic tools and DFT calculations reveal that significant interlayer charge transfer occurs across the hetero-layers due to the favourable band alignment of a type-II across the junction. Interestingly, the CT from the 2D Bi_2O_2Se layer to the monolayer MoS_2 results in photoluminescence (PL) quenching in the MoS_2 layer and enhanced photoconduction in the HS. Low-temperature PL studies reveal that the robust interlayer coupling between the hetero-layers enhances the CT process. The modified Varshni fit reveals that the electron−phonon coupling constant (Huang−Rhys factor) is higher for trions (1.13) than for neutral excitons (0.66) in the heterostructure. Upon photoexcitation, the trion−phonon coupling is stronger than the neutral exciton−phonon coupling in the heterostructure system. The additional doping caused by photogenerated CT was quantified by solving the coupled rate equations using a four-level model, and the results are fully consistent with the CT estimated from the density functional theory (DFT) calculation. These results are significant for understanding the interaction between vdW and nvdW 2D heterostructures and further exploration of such 2D heterostructures in future optoelectronic applications.

5.1. Introduction

2D heterostructures (HS) have been advocated for next-generation electronics and optoelectronics integrated devices due to their novel properties and synergistic effects.[1-4] Numerous efforts have been devoted to understanding the 2D HS due to their fascinating electronic and optical properties.[5-7] Over the past decades, researchers have shown keen interest in 2D-based HS for their applications in broadband, fast photodetection, and on-demand sensing.[8] VdW pairing among the layers is generally weaker than electrostatically attached layers. Many studies[9-12] show vdW pairing within different 2D materials, such as TMD/TMD vdW-layered materials exhibiting efficient interlayer charge transfer (CT). However, the nature and implications of CT across nvdW and vdW stacking have been largely unknown. Earlier studies[13-16] on TMD/ TMD HS have shown efficient CT and separation due to their vdW coupling at the interfaces. HS of 2D layered materials holds a significant lateral contact between the layers with atomically sharp interfaces, which is fundamentally different from the interfaces in other HS, like 0D/2D and 1D/2D. Within the 2D/2D HS, very little has been explored about the CT dynamics in vdW 2D/ nvdW 2D HS. MoS_2, a well-known TMD, belongs to the vdW family, whereas Bi_2O_2Se is an nvdW 2D material with weak electrostatic staking of layers. Therefore, forming heterostructures by staking of MoS_2 with new age 2D Bi_2O_2Se and investigating the fundamental as well as applications of stacked MoS_2 and Bi_2O_2Se layers, specifically, charge transport dynamics at the interface is of great interest for futuristic optoelectronic applications of such unique heterolayer interface.

The interlayer CT phenomenon is intrinsic in the 2D HS, facilitating superior properties. Notably, efficient photoinduced hot carriers in semiconductors create a nonequilibrium distribution of electrons and holes above and below the Fermi energy with superior kinetic energy.[17] Exploration of CT for nvdW stacking is still warranted for their ensuing applications. It is also crucial for the fundamental understanding of inherent interfacial optoelectronic properties. In addition, obtaining good-quality 2D materials for stacking is challenging. The CVD process has partly solved the problem, as it is a quality approach for obtaining highly crystalline 2D materials[18, 19]. Thus, CVD-grown layered materials are an excellent choice for 2D stacking rather than chemically synthesized 2D materials to study the CT properties. Usually, a shift in the peak in Raman and PL spectra is observed in 2D HS due to induced strain, temperature, layer shrinkage, defects, and CT. Several studies [20-23] have demonstrated that CT primarily contributes to the observed peak shift. Therefore, Raman and PL measurements are essential tools to investigate the CT at the HS interface. HS-based devices can alter the intrinsic doping and chemical reactivity [24, 25] and improve the performance of the devices.

In this article, we elucidate the CT mechanism in 2D Bi_2O_2Se/1L-MoS_2 hetero-layers via different microscopic and spectroscopic tools, and the experimental results are corroborated with DFT calculations. A proper stacking of two different layers was confirmed by TEM

(HRTEM) imaging and AFM analyses. We show that the redshift of a specific Raman peak and the quenching/redshift of the PL peak in the heterojunction could be explained systematically through the transfer of photogenerated excess carriers from Bi_2O_2Se to the 1L-MoS_2, and as a result, the 1L-MoS_2 becomes more n-type. Further evidence of the CT process is gathered from the optical absorption and PL of the HS system. XPS analysis also indicates an electrostatic interface between vdW MoS_2 and nvdW Bi_2O_2Se with probable Mo-O bond formation. The nature of the interface and CT is further confirmed by the DFT calculations and KPFM measurements. Temperature-dependent PL spectra of HS were acquired to justify the temperature effect on CT efficiency. In addition, the electron/exciton-phonon coupling in the heterogeneous system could be assessed from a modified Varshni equation fit. We show that due to photogenerated CT from Bi_2O_2Se to 1L-MoS_2, the MoS_2 layer becomes more n-type doped, and trion population is correspondingly increased through the conversion of neutral exciton. We collectively estimated the photogenerated charge doping density by solving the coupled rate equation involving the four-energy level model and the law of mass-action and compared it with the DFT-calculated CT and show that the results are fully consistent with each other.

5.2. Experimental details

5.2.1. Preparation of 2D Bi_2O_2Se

For this study, the ultrathin layer of Bi_2O_2Se crystals was grown on mica substrate via CVD process in a single-zone tube furnace, following **section 2.2.1** of this thesis. Briefly, Bi_2O_3 powder (Alfa Aesar, 99.999%) and Bi_2Se_3 powder (Sigma Aldrich 99.999%) were used as the precursors and the high purity argon (99.999%) was used as carrier gas. The quartz tube was evacuated and Ar gas (~300 sccm) was purged repeatedly at room temperature (RT) to eliminate the O_2 impurity. The source temperature was increased to ~695 °C with a ramping rate of 11 °C/minute and maintained for 25 min with a base pressure of 400–500 mbar. The growth substrates were placed downstream (9-12 cm away from the hot center) at ~580–590 °C to grow few-layer 2D Bi_2O_2Se.

5.2.2. Preparation of 2D MoS_2

1L-MoS_2 was grown on sapphire and SiO_2 substrate via CVD process in a two-zone furnace, following the earlier reported process.[21] In a typical procedure, a quartz boat containing sulfur powder was placed 15 cm upstream inside a quartz tube away from the quartz boat containing MoO_3 powder. A quartz mask with circular openings was placed on the boat containing MoO_3 powder, and Si/SiO_2 substrates were kept over the mask. The mask allows local control of vapor pressure to grow monolayer and bilayer regions separately. High-purity Ar gas (99.999%) served as the carrier gas, and a high flow rate of Ar (~300 sccm) was used at first to purge the surface-adsorbed impurities of the sapphire substrates and the tube. Afterward, S and MoO_3 source temperatures were raised to 150 and 700 °C with ramping rates of 15 and 3.5 °C/min, respectively. An Argon flow rate of 10 sccm was maintained for 5 min for the growth of MoS_2. Then, the system was allowed to cool down to room temperature at a cooling rate of 6.5 °C/min. The 1L-MoS_2 film was grown on each substrate only on the substrate region covered by the quartz mask. In contrast, the directly exposed areas were deposited with few-layer and multilayer MoS_2. Note that further experiments were performed on monolayer MoS_2 only.

5.2.3. 2D Bi_2O_2Se/1L-MoS_2 heterostructure preparation

The few-layer Bi_2O_2Se flakes were transferred to the direct CVD-grown MoS_2 layer grown on sapphire and SiO_2 to prepare the Bi_2O_2Se/1L-MoS_2 vertical-type HSs. PMMA-based transfer method was adopted following the standard protocol.[26] In brief, the PMMA solution was spin-coated over the 1L-MoS_2 with a spin rate of 2000 rpm for 60 s. Subsequently, it was heated for 15 minutes on a hot plate for proper adhesion of PMMA on MoS_2. Once it dried adequately, it was introduced into a 5% NaOH solution to lift off the sample and kept for a few hours. Then the floated PMMA-adhered MoS_2 was scooped on a Cu grid for TEM characterization. For the TEM characterization, Bi_2O_2Se was transferred using the HF transfer process following **section 2.2.2**. Similarly, Bi_2O_2Se layer is transferred on 1L-MoS_2 to form the HSs. A gentle heat treatment (50°C) was given for proper stacking of the HSs.

For the spectroscopic measurement of the HS, we transferred the 2D Bi_2O_2Se layer onto 1L-MoS_2 grown on a sapphire/SiO_2 substrate by optimizing the HF transfer method. Au electrodes of thickness ~100 nm were deposited through a carbon-free Cu grid (mask) by thermal evaporation to fabricate an HS device to measure the photo I-V characteristics on the sapphire substrate.[27]

5.2.4. Characterization techniques

Raman spectroscopy (instrument details same as **section 2.2.3**) is utilized to obtain the crystalline phase of the different samples. AFM (instrument details same as **section 2.2.3**) was used in tapping mode to examine the topography of the CVD-grown Bi_2O_2Se and MoS_2 layer individually as well as for HS. The morphology and structural properties of fabricated HS were analysed using a FETEM (instrument details same as **section 2.2.3**). Room temperature PL spectra were acquired using a micro-Raman instrument. X-ray photoelectron spectroscopy details are the same as in **section 2.2.3**. Surface contact potential difference was measured using Kelvin probe force microscopy (KPFM) tool incorporated in the above AFM setup. UV–Vis absorption measurements were carried out using a commercial spectrophotometer (PerkinElmer, Lamda 950). A temperature stage with a remote functioning span of 50X objective was integrated with the micro-Raman setup to collect the temperature-dependent PL spectra. Liquid nitrogen was used as the coolant. The I-V measurement of the HS device was carried out using a microprobe station (ECOPIA EPS-500), a 405 nm laser, and a source meter (Keithley 2400) interfaced through a computer.

5.3. Computational details

All the calculations were performed using plane-wave DFT-based Quantum ESPRESSO code, including projector-augmented wave (PAW) pseudopotential [28, 29] The exchange-correlation term was approximated using the generalized gradient approximation (GGA) functional of Perdew-Burke-Ernzerhof (PBE) [30] Monkhorest pack k-point [31] 12×12×1 was chosen for the unit cell of the Bi_2O_2Se/MoS_2 HS, and a 5×5×1 grid was utilized for the supercell k-points. The plane-wave cutoff energy 80 Ry was used. The Grimme-D3 [32] method was used to incorporate the long-range dispersion correction, and a vacuum of 40 Å was considered along the z-axis to remove periodic image interaction. The convergence of the energy threshold is set at 1×10^{-6} Ry. Since the change in the electronic properties above the bilayer-Bi_2O_2Se is minimal [33], we are simply considering bilayer Bi_2O_2Se to reduce computing time.

To determine the charge density distribution (CDD) between the MoS_2 and Bi_2O_2Se layers, **equation 5.1**[34] was used, and the figure (see results and discussions) was visualized by using the VESTA code[35].

$$\rho_{cdd} = \rho_{MoS_2/Bi_2O_2Se} - \rho_{MoS_2} - \rho_{Bi_2O_2Se} \qquad (5.1)$$

Here, ρ_{MoS_2/Bi_2O_2Se}, ρ_{MoS_2}, and $\rho_{Bi_2O_2Se}$ represent the charge density of MoS_2/Bi_2O_2Se heterostructure, MoS_2 monolayer, and Bi_2O_2Se bilayer, respectively.

5.4. Results and Discussion

5.4.1. Growth and characterization of 2D Bi_2O_2Se and MoS_2

2D Bi_2O_2Se were grown following **section 2.2.1,** and monolayer MoS_2 was grown by CVD process, as discussed above[21]. Before fabricating HS, the individual morphology and phases of as-grown 2D Bi_2O_2Se and monolayer MoS_2 have been confirmed using optical microscopy (OM), Raman spectroscopy, AFM, and TEM imaging, as shown in **Fig. 5.1**. The OM image (**Fig. 5.1a**) and Raman spectrum (**Fig. 5.1b**) with characteristic A_{1g} mode at 160.7 cm^{-1} confirm the crystallinity of 2D Bi_2O_2Se flakes. AFM (inset of **Fig. 5.1b**) and TEM imaging, including SAED pattern (**Fig. 5.1c**), confirmed the growth of multilayer flakes (thickness ~13 nm) with tetragonal phase. The OM image in **Fig. 5.1d** shows the growth of large area 1L-MoS_2. The characteristic Raman mode at 386.6 cm^{-1} (E_{2g}) and 405.9 cm^{-1} (A_{1g}) confirms the 1L-MoS_2 growth (**Fig. 5.1e**). The inset of **Fig. 5.1e** depicts the AFM image and

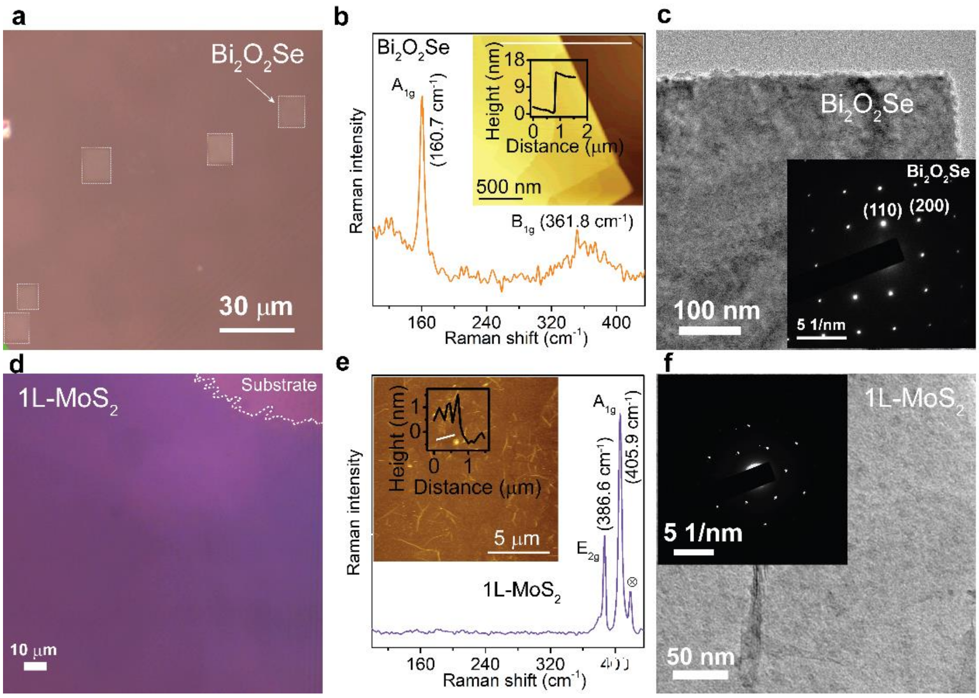

Fig. 5.1: (a) Optical microscopy images of as-grown square-shaped flakes of 2D Bi_2O_2Se. (b) Raman spectrum of the 2D Bi_2O_2Se and the inset shows the corresponding height profile along the black line (c) TEM image of 2D Bi_2O_2Se. Inset depicts the SAED pattern of single crystalline tetragonal 2D Bi_2O_2Se. (d) Optical microscopy images of as-grown large area 1L-MoS_2. (e) AFM image of the MoS_2, including the height profile (along the white line) at the top right corner. (f) TEM image of 1L-MoS_2. Inset shows the SAED pattern that confirms the hexagonal crystal structure of MoS_2.

corresponding height profile that further validates the monolayer thickness of as-grown MoS_2. The TEM characterization (**Fig. 5.1f**) approves monolayer hexagonal MoS_2.

5.4.2. Fabrication and characterization of HS

Bi_2O_2Se/1L-MoS_2 HSs are prepared by standard PMMA transfer techniques (see section **5.2.3** for detailed information). After fabricating HS, the HSs were first examined with OM, TEM, and Raman spectroscopy (**Fig. 5.2** & **5.3**). **Fig. 5.2a** illustrates the OM image of the HS with the Bi_2O_2Se flake on top of the 1L-MoS_2 film. Further, the Raman spectrum (**Fig. 5.2b)** of HS consists of characteristics A_{1g} mode (160.4 cm^{-1}) of Bi_2O_2Se and E′ (386.4 cm^{-1}) and A'_1 (404.5 cm^{-1}) modes of monolayer MoS_2, suggesting successful stacking of the HS. The fabricated HS used for Raman characterization is shown schematically in the inset of **Fig. 5.2b,** demonstrating a vertical stacking of vdW monolayer MoS_2 and nvdW 2D Bi_2O_2Se. In addition, Mo-O bond vibration (B_{2g} at ~280 cm^{-1}, shown in **Fig. 5.3a**) is identified only in the HS,

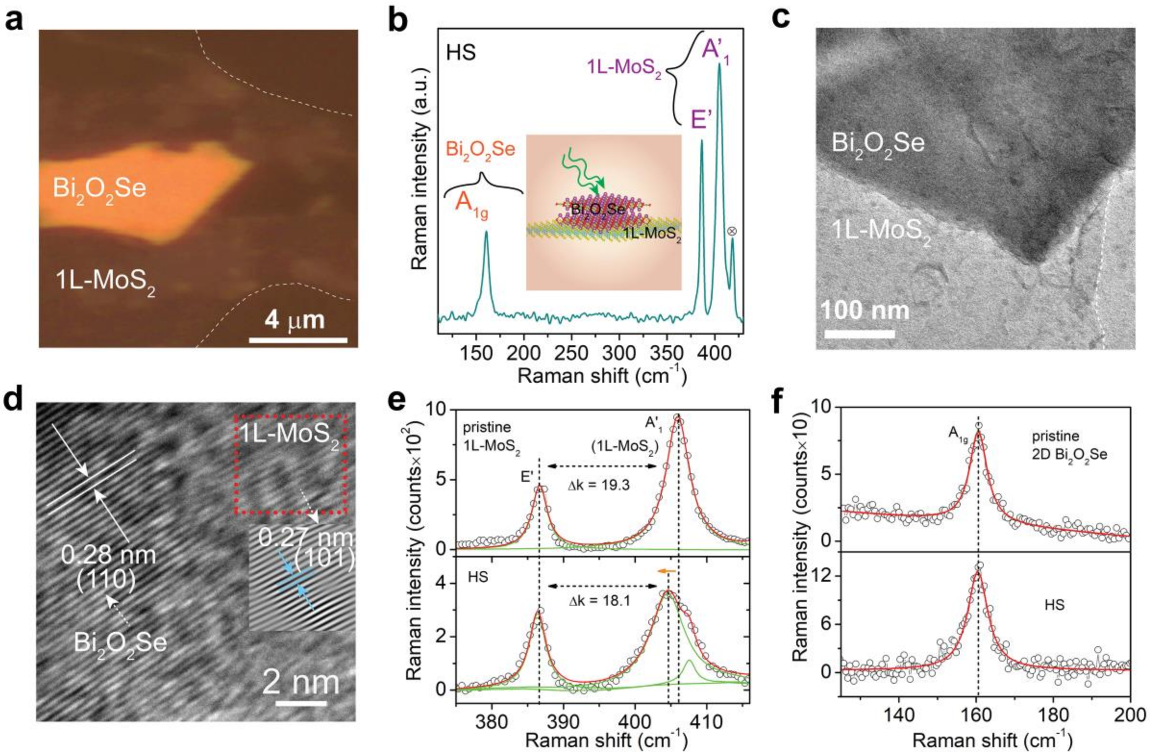

Fig. 5.2: (a) optical microscopy image showing the transferred multilayer Bi_2O_2Se on 1L-MoS_2 for 2D Bi_2O_2Se/1L-MoS_2 heterostructure formation. (b) Characteristics Raman spectrum of the HS. Inset shows the schematic of HS formed by vertical stacking of 1L-MoS_2 (bottom) and 2D Bi_2O_2Se (top) considered for Raman measurement. '⊗' symbol shows the sapphire substrate peak. (c) Transmission electron microscopy image of HS. (d) High-Resolution TEM image of HS contains 0.28 nm (110) d-spacing of Bi_2O_2Se and 0.27 nm (101) d-spacing of monolayer MoS_2. (e) Lorentzian fitted Raman spectra of A_{1g} and E_{2g} Raman modes (1L-MoS_2) for pristine and HS, which shows peak shift with reduced Δk. (f) Lorentzian fitted Raman spectra of A_{1g} mode (Bi_2O_2Se) for pristine and HS. Symbols refer to experimental data, whereas solid lines refer to fitted spectra.

indicating the incorporation of O in the 1L-MoS_2 crystal structure[36, 37] due to the formation of HS with Bi_2O_2Se, which is consistent with the XPS spectra discussed later. Such Mo-O bond might be formed by incorporating oxygen antisites (present at Se vacancy (O_{Se}) of the outer Bi_2O_2Se surface) at the vacant sulfur site of MoS_2 surface. For the TEM analyses of the HS, we transferred MoS_2 and Bi_2O_2Se in the same TEM grid via HF and sodium hydroxide (NaOH) solution-assisted transfer methods (refer to **section 5.2.3**). **Fig. 5.2c** represents a TEM image of a typical HS. **Fig. 5.2d** exhibits a high-resolution TEM image of the heterostructure with a d-spacing of 0.28 nm corresponding to the (110) plane of Bi_2O_2Se and 0.27 nm corresponding to (101) of MoS_2. **Fig. 5.3b** shows the atomic arrangement of the HS with tetragonal (red square) Bi_2O_2Se and hexagonal 1L-MoS_2 (cyan color), indicating the formation of a formal bond at the interface, where the O atom is sitting at the vacant sulphur site (red circled at one edge of hexagon) of MoS_2 lattice, consistent with Raman and XPS observations. Thus, these results confirm the formation of HS with a probable Mo-O bond that is further used for understanding the interlayer CT and electron-phonon coupling. It may be noted that the present work was conducted at room temperature by a standard wet transfer of few-layered Bi_2O_2Se on as-grown MoS_2 (monolayer) without any post-treatment. Therefore, structural reconstruction is unlikely in the present case, though the sample was heated at 50 °C during the transfer process.

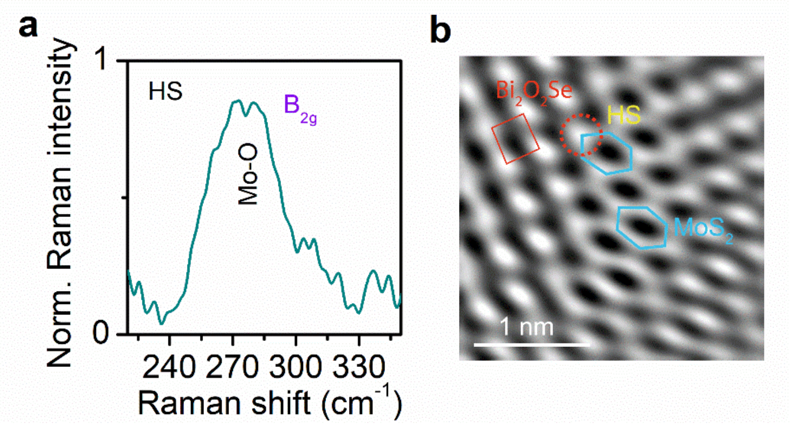

Fig. 5.3: (a) B_{2g} Raman mode (Mo-O vibrations) observed in the Raman spectrum of HS. (b) Atomic resolution lattice image of Bi_2O_2Se/1L-MoS_2 HS with tetragonal Bi_2O_2Se (red square) and hexagonal MoS_2 (cyan color). HS junction, i.e., red dashed circle at the edge of cyan hexagon indicates the oxygen sitting at a vacant sulfur lattice and forms a Mo-O bond.

5.4.3. Charge transfer studies

Raman spectroscopy is a powerful tool for understanding the interlayer CT in 2D HSs. Graphene and TMD monolayers show a spectral shift due to the electron-phonon coupling and CT at the interface, leading to charge doping.[38] The coupling effect and CT at the Bi_2O_2Se/1L-

MoS_2 interface have been verified via optical measurements. Individually, the characteristic Raman mode was observed at 160 cm^{-1} (A_{1g}) for Bi_2O_2Se and at 386.6 cm^{-1} (E′) and 405.9 cm^{-1} (A'_1) for 1L-MoS_2. Although all the respective modes were also observed for the HS (**Fig. 5.2b**), a distinct redshift (1.4 cm^{-1}) in A'_1 mode for 1L-MoS_2 was noticed, while no apparent shift in the E′ mode, as shown in **Fig. 5.2e**. In the TMD monolayer, the A'_1 Raman mode is more sensitive to changes in the charge doping density than a change in strain, stress, and temperature.[38] The contribution of strain to the observed shift can be ruled out since the strain would shift all the peaks instead of a selective peak, and it is consistent with the reduction in in-plane E′ and A'_1 peak difference (Δk). It is noticeable that due to the red shift of one peak, the Δk has been reduced (**Fig. 5.2e**) from 19.3 cm^{-1} to 18.1 cm^{-1}. The redshift of A'_1 mode on different locations of the HS sample (**Fig. 5.4**) validates the uniformity of the layer and the repeatability of the results. Further, we fabricated the HS on the SiO_2 substrate to compare the results of charge doping with sapphire case. The statistics of reduced Δk vary from 18.2 to 18.8 cm^{-1} on SiO_2 substrate, as depicted in **Fig. 5.5a**. It's worth highlighting that the redshift is

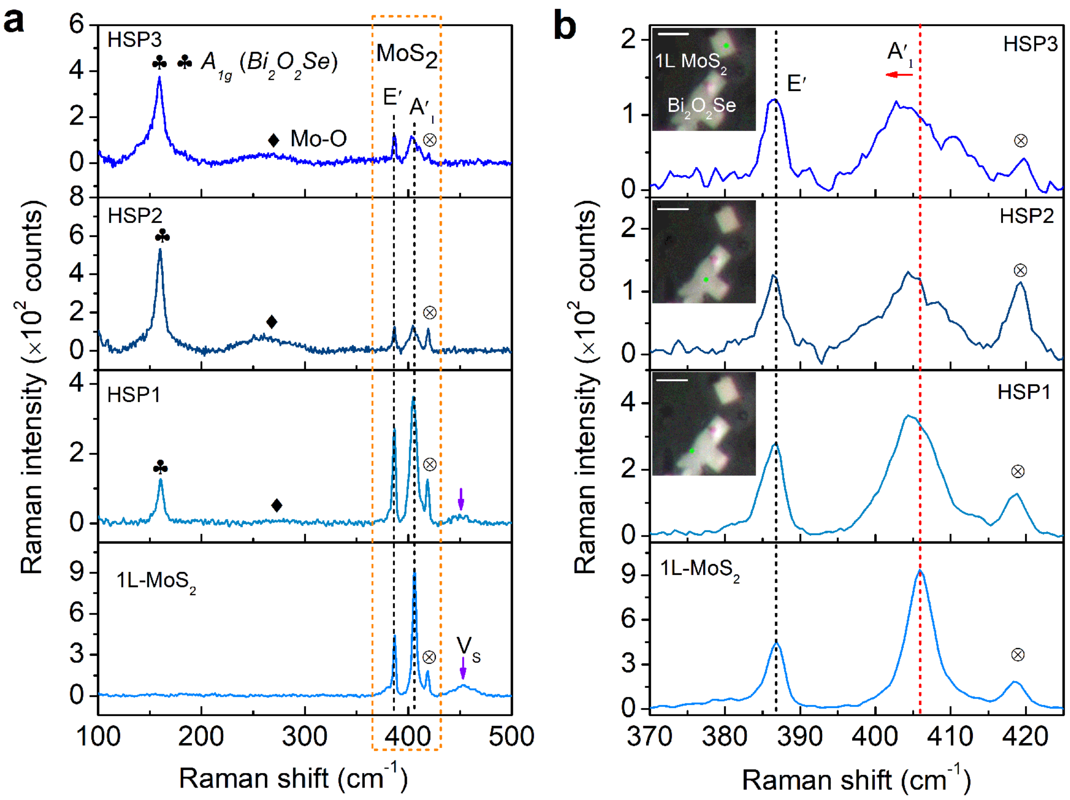

Fig. 5.4: (a) Comparison of Raman spectra of 1L-MoS_2 and HS in pristine and the different HS positions on a sapphire substrate. (b) Comparison of Raman spectra of 1L-MoS_2 E′ and A'_1 peaks of the highlighted box of (a) displaying the A'_1 peak redshift in HS. Inset are the corresponding images where the scale bar is 5 μm. The Raman peak marked with the '⊗' symbol represents the sapphire substrate peak.

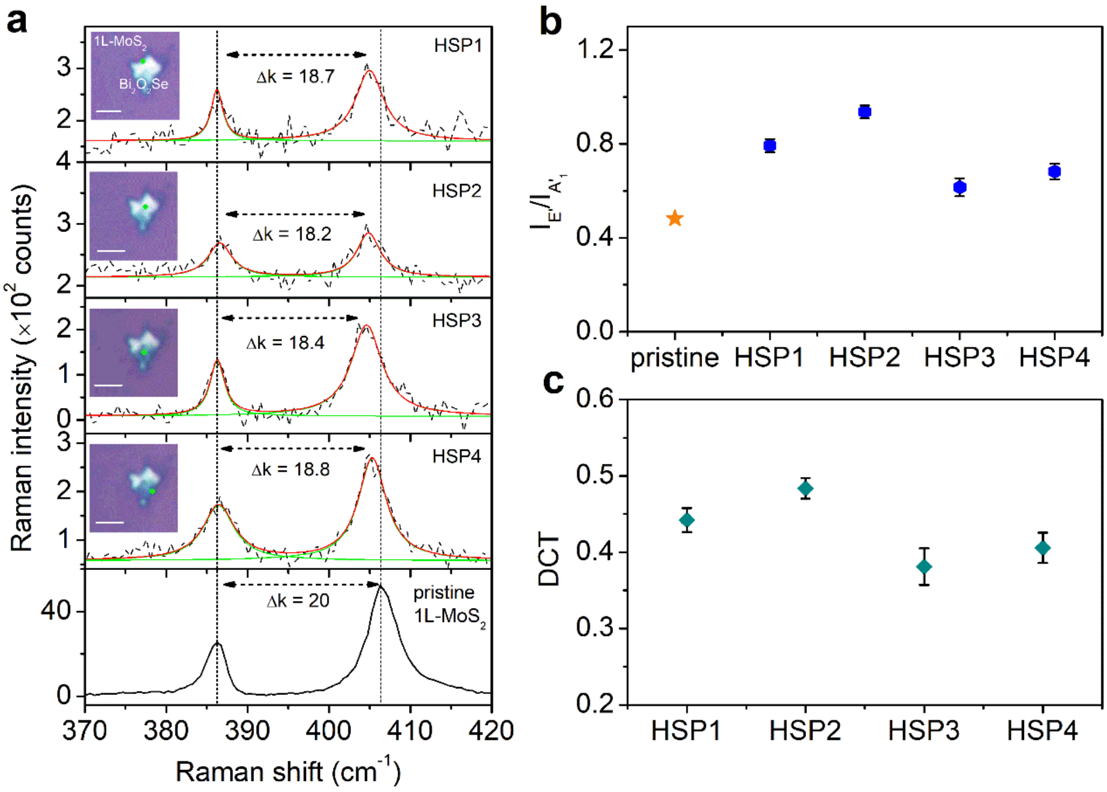

Fig. 5.5: (a) Stacked Raman spectra of 1L-MoS$_2$ E′ and A′$_1$ peaks in pristine and the different HS positions. Inset are the corresponding images where the scale bar is 5 μm. (b) The intensity ratio of E′ and A′$_1$ Raman mode (c) Calculated DCT at the different spots across the sample.

mainly in A'$_1$ mode on both substrates. Thus, irrespective of the choice of the substrate, the red shift of A′$_1$ of MoS$_2$ in HS as compared to the pristine MoS$_2$ sample indicates that the photoinduced charge doping in the MoS$_2$ layer originated from the interlayer CT between the layers. Moreover, Δk is reduced on both substrates, and the change is similar in both cases. Note that the Δk value for monolayer MoS$_2$ is found to be ~19.3 cm^{-1} on the sapphire substrate and ~20.0 cm^{-1} on the SiO$_2$ substrate. Therefore, the significant reduction of Δk in HS compared to the bare MoS$_2$ is attributed to charge doping instead of any strain effect. In fact, any compressive strain associated with the transfer of Bi$_2$O$_2$Se layer over the 1L-MoS$_2$ layer would cause a blue shift of the A′$_1$ mode, which is contrary to the observed red shift. Thus, the red shift in A′$_1$ mode primarily arises from the change in charge doping density in the 1L-MoS$_2$ layer. Consequently, the different energy band structures might be significantly affected by the interlayer coupling in the interface of the HS.[39] It has been found (**Table 5.1**) that the FWHM of A′$_1$ mode (of 1L-MoS$_2$) is higher (by 1.8 cm^{-1}) in HS than in pristine 1L-MoS$_2$. This may be related to charge doping-induced strain caused by the formation of HS. Particularly, it might be caused by the formation of Mo-O bond at hetero-interface. In the HS, the additional peak on the right side of the A′1 mode (**Fig. 5.2e**) possibly originates from the S vacancy.[40] We observe a broad Raman peak at ~ 450 cm^{-1} in pristine MoS_2, revealing the presence of S vacancy (V_S)[40] and the corresponding peak intensity reduces in the HS, and a peak at ~280 cm^{-1} appears (**Fig. 5.4a**). This suggests the reduction in S vacancy in MoS_2 by forming Mo-O bond after stacking the Bi_2O_2Se. After the formation of HS, the out-of-plane vibration of S-Mo-S (A′1) is affected by the out-of-plane vibration of breathing mode (caused by Mo-O bond), resulting in an increase of FWHM significantly (by 1.8 cm^{-1}). However, the in-plane vibration of S-Mo-S (E′) is barely altered by the additional Mo-O bond vibration, and therefore the increase in FWHM is relatively small (0.5 cm^{-1}). Further, we calculated the intensity ratio of in-plane E′ and out-of-plane A′1 modes, which reveals an increase in ratio $(I_{E'}/I_{A'_1})$ after the formation of HS (**Table 5.1**). We relate the variation in intensity ratio $(I_{E'}/I_{A'_1})$ with interlayer CT. Following the earlier report, we estimated the degree of charge transfer (DCT) using the modified relation[41, 42]: DCT= $\alpha/(1 + \alpha)$, where $\alpha = (I_{E'}/I_{A'_1})$. The intensity of E′ mode at 386.6/386.4 cm^{-1} and the A′1 mode at 405.9/404.5 cm^{-1} for 1L-MoS_2/HS have been considered for calculating α and DCT. The values for pristine 1L-MoS_2 are $\alpha = 0.48$ and DCT = 0.32, whereas the values for HS are $\alpha = 0.82$ and DCT = 0.45. The α and DCT values across the HS (**Fig. 5.5b,c**) shows that these values are higher for HS than for the pristine 1L-MoS_2. The higher DCT in HS indicates a stronger interfacial coupling between heterolayers attributed to an electrostatic environment across the interface. **Fig. 5.2f** shows the Lorentzian fitted spectra of A_{1g} Raman mode (Bi_2O_2Se) for pristine Bi_2O_2Se and HS. Note that we did not observe any measurable shift in the A_{1g} mode of Bi_2O_2Se after the formation of HS, which might be attributed to its multilayer nature. In HS, we noticed an apparent reduction and enhancement in the Raman intensity of the A′1 mode of 1L-MoS_2 and the A_{1g} mode of Bi_2O_2Se, respectively (see **Table 5.1**), indicating a robust interfacial coupling between the heterolayers in the HS. Raman intensity quenching/enhancement is highly correlated with changes in layer numbers, lattice orientation, type of stacking, defects, doping, stress/strain, temperature, laser source, the variation of electronic and lattice vibration properties, and it could be related to CT, dipole-dipole coupling, and CT with dipole-dipole coupling.[43] We observe a significant quenching (60%) in the intensity of the A′1 Raman mode of 1L-MoS_2 and enhancement (82%) of A_{1g} mode in Bi_2O_2Se in the HS (**Table 5.1**), and it is primarily due to the absorption/reflection of light at the top Bi_2O_2Se layer, which causes the lower intensity of light to reach the bottom MoS_2 layer, and as a result, lower intensity of A′1 mode. The multilayer nature of HS possibly has multiple interference effects of backscattering of light, which may partly be responsible for the reduction in A′1 mode intensity.

Table 5.1 *Summary of the Lorentzian fitted parameters (peak positions, FWHM, Raman intensity) in Pristine Bi_2O_2Se, and 1L-MoS_2 and HS and ΔK (separation in peak positions of E′ and A′1 Raman mode) and intensity ratio of E′ and A′1 of MoS_2 Raman modes in pristine 1L-MoS_2 and HS.*

Sample	E′ (MoS_2)			A′1 (MoS_2)			ΔK (cm^{-1})	Intensity ratio $I_{E'}/I_{A'_1}$	A_{1g} (Bi_2O_2Se)
	Peak position (cm^{-1})	FWHM (cm^{-1})	Intensity (counts)	Peak position (cm^{-1})	FWHM (cm^{-1})	Intensity (counts)			Intensity (counts)
Bi_2O_2Se		-	-		-	-		-	68
1L-MoS_2	386.6	2.3	460	405.9	3.9	956	19.3	0.48	-
HS	386.4	2.8	282	404.5	5.7	341	18.1	0.82	124

To explore further the CT and exciton behaviour of the HS, we conducted the absorption spectroscopy measurement. **Fig. 5.6a** shows the absorption spectra for the pristine 1L-MoS_2, pristine Bi_2O_2Se, and the HS. The vertical dotted lines correspond to the A, B, and C exciton peaks for MoS_2. For pristine 1L-MoS_2, three excitonic peaks are located at ~ 1.845 eV (672 nm), ~ 2.009 eV (620 nm), and ~ 2.780 eV (446 nm), respectively. The A and B exciton peaks are generated due to the direct excitonic transitions between the maxima of split valence bands and the conduction band at the K point of the Brillouin zone.[44] The C exciton peak is attributed to direct transitions from the deep valence band to the conduction band in 1L-MoS_2. The absorption spectrum of HS illustrates a significant enhancement in absorption compared to the sum of the individual contribution to the absorption by 1L-MoS_2 and Bi_2O_2Se layers. The higher absorption in the HS may be attributed to the interface scattering and the interlayer coupling of light-material interaction in the HS.[45] The absorption spectra were taken on a large area sample on a sapphire (transparent) substrate with sapphire as the reference for absorption measurement. Any interference effect is very unlikely to occur here as the thickness of the samples is much smaller than the wavelength of the excitation light. Further, any interference effect would give rise to oscillatory data in the spectrum, which is absent in our case. To better visualize the resonating behaviour of the A, B exciton peaks in the HS, we extracted a second-order derivative of absorption spectra with respect to excitation energy. The

A, B exciton peaks appear with significant resonance, and a blue shift in the peak in the HS compared to that in pristine 1L-MoS_2 in differentiated absorption (d^2A/d^2E) spectrum can be seen in the inset of **Fig 5.6a**. Resonated A, B excitons with blue shift (11 meV in A and 7 meV in B) are attributed to a robust coupling between heterolayer with the p-n junction formation, which is consistent with the DFT calculations (discussed later). It may be noted that absorbance

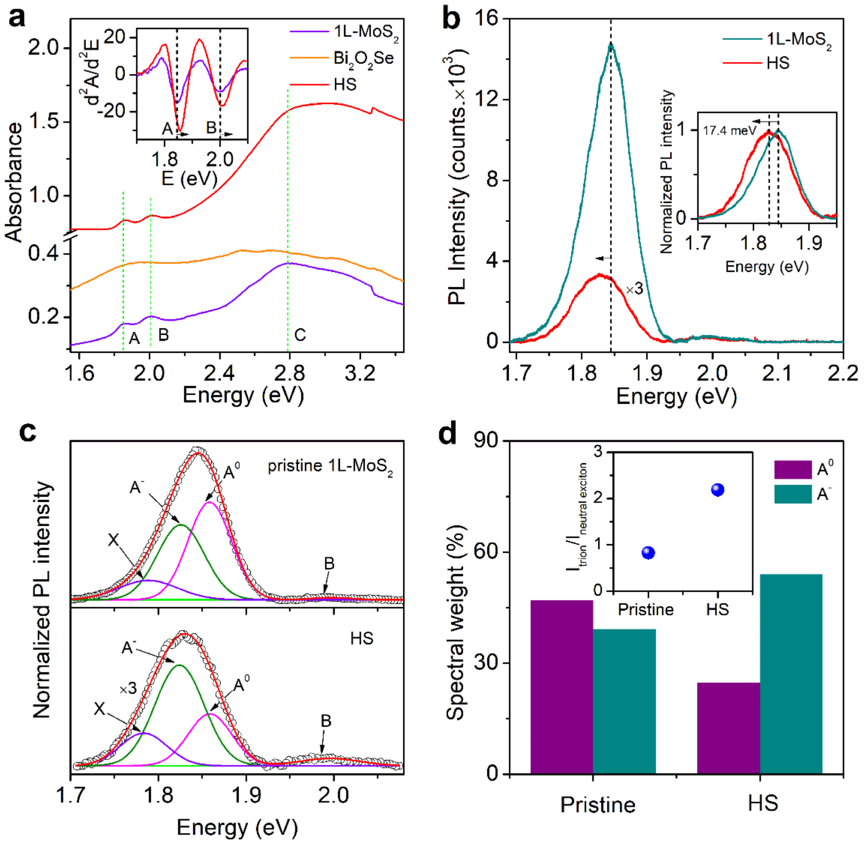

Fig. 5.6: (a) Comparison of absorption spectra for bare 1L-MoS_2, pristine Bi_2O_2Se, Bi_2O_2Se/1L-MoS_2 heterostructure. Inset shows the second derivative of absorption spectra with respect to perturbed energy. (b) Comparisons of PL spectra for pristine 1L-MoS_2, and heterostructure. Inset depicts the normalized PL curves for 1L-MoS_2 and HS showing the peak shift. (c) PL spectra fitted with Gaussian peaks for pristine MoS_2 and heterostructure. (d) Spectral weight of neutral exciton (A^0, violet), trion (A^-, dark cyan) in pristine 1L-MoS_2 and HS. Inset represents the intensity ratio of trion and neutral exciton.

spectra were collected over a few mm^2 of area, giving the overall excitonic feature of the full HS sample. The excitonic peaks are consistent with the PL emission spectra of the pristine MoS_2 and the HS. To study the interlayer CT adequately, PL spectra were recorded for pristine 1L-MoS_2 and the HS (**Fig. 5.6b**). 1L- MoS_2 shows a highly intense PL due to the A and B excitonic direct optical transitions at ~ 1.86 eV and ~1.99 eV, respectively.[46] In the HS, we observed a drastic quenching of 73.5 % in PL (shown in **Fig. 5.6b**). The dramatic quenching with a significant red shift (17.4 meV, shown in the inset of **Fig. 5.6b**) of PL peak in the HS is due to the CT across the interface. The HS-induced change in the dielectric environment may have some contribution to the PL peak shift due to a modification of electron-electron and electron-hole Coulomb interactions across the layers. Bi_2O_2Se with a relatively high dielectric constant (~20) [47] at 2.3 eV (532 nm) is stacked on a low dielectric constant (~6.3) [48] 1L-MoS_2, which might increase dielectric screening from immediate environment.[49]

To identify the contribution of different excitons in the PL emission, the PL spectra were deconvoluted with a Gaussian line shape, as shown in **Fig. 5.6c**. The PL spectral weight of A^0, A^- excitons peak in pristine MoS_2 and HS is presented in **Fig. 5.6d**. In pristine 1L-MoS_2, the A^0 neutral exciton contribution is much higher (47.0%) than that of the HS (24.7%). In contrast, the A^- trion contribution is higher for HS (54.0%) than for bare MoS_2 (39.2%) due to the charge separation and transfer of photogenerated electrons from Bi_2O_2Se layer to 1L-MoS_2. In HS, the spectral weightage of neutral exciton has decreased by approximately 47.5 %, and trion contribution has been ramped up by 37.8 %. The intensity ratio of trion to neutral exciton (I_{A^-}/I_{A^0}) increased from 0.83 to 2.19 (inset of **Fig. 5.6d**) in the HS. The significant increment (1.36) in (I_{A^-}/I_{A^0}) signifies that a significant amount of CT occurs in the HS. This is primarily due to the transfer of electrons from Bi_2O_2Se layer to 1L-MoS_2, which promotes the formation of trions (charged excitons) at the cost of reduction of the neutral excitons. The spectral weightage of excitonic peaks (B, A^0, A^-, X) is tabulated in **Table 5.2**. The contribution from defect-bound exciton (X) also increases (29.7%) due to enhanced radiative recombination of bound excitons in the defect-related trap states. Thus, defect contribution is not negligible, and these defects may trap the charge carriers, and accordingly the actual amount of CT is less than that expected from a defect-free MoS_2 layer. We believe that the defects partially quench the neutral excitonic emission and increase the trion population. Excess addition of B exciton contribution in HS may relate to the formation of B trion.[50] B-excitonic contribution is significantly less than A^0 and A^- excitons for pristine 1L-MoS_2 grown on a sapphire substrate, consistent with the earlier report.[51] Moreover, PL mapping (**Fig. 5.7**) was recorded to visualize

Table 5.2 *Relative weightage of excitons obtained via Gaussian deconvolution of PL spectra in pristine 1L-MoS_2 and HS sample.*

	Spectral weight of excitonic peaks (%)			
	B	A^0	A^-	X
1L-MoS_2	1.0	47.0	39.2	12.8
HS	4.8	24.7	54.0	16.6

the uniformity of the PL quenching of 1L-MoS_2 in the HS. During the photon irradiation, the photogenerated electrons in Bi_2O_2Se are transferred to 1L-MoS_2 due to the favorable band bending, resulting in more n-type nature of MoS_2.

To identify the chemical composition and interface status, we performed XPS analysis. The survey scan XPS spectra of different samples (**Fig. 5.8**) reflect that the samples consist of characteristics XPS peaks of Bi, O, Se, Mo, and S elements, as expected. High-resolution XPS spectra (**Fig. 5.9 (a-c))** were collected to identify the interlayer status. The spectral shift in the individual peaks reveals that a static electric field was introduced at the interface due to

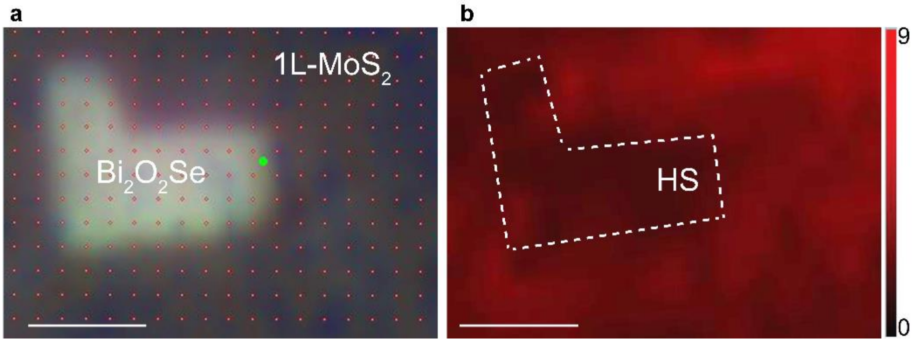

Fig. 5.7: (a) Optical image of HS where PL mapping was conducted. (b) The PL mapping of pristine 1L-MoS_2 and HS (marked with white dashed line). The scale bar is 2 μm.

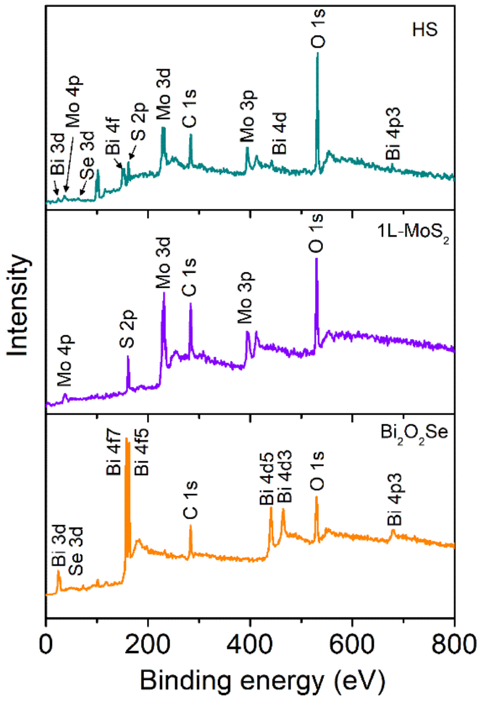

Fig. 5.8: XPS survey spectra of Bi_2O_2Se, 1L-MoS_2, and HS (bottom to top).

interlayer coupling in the HS.[52] **Fig. 5.9a** shows the deconvoluted Mo 3d XPS spectra for pristine MoS_2 and HS. Mo $3d_{5/2}$ and Mo $3d_{3/2}$ binding energies (BEs) are 228.7 eV, and 231.8 eV and 228.6 eV, 231.8 eV in the pristine MoS_2 and HS, respectively. In the HS, Mo $3d_{5/2}$ BE (228.7 eV) becomes lower by 0.1 eV without altering the higher BE (231.8 eV) of Mo $3d_{3/2}$. The shift of only Mo $3d_{5/2}$ (outer electron) without affecting Mo $3d_{3/2}$ (inner electron) might be attributed to the stronger electrostatic stacking at the interface. At the same time, the BE shift (0.1 eV) of Mo $3d_{5/2}$ indicates the formation of chemical bond across the two heterolayers and the electron transfer from Bi_2O_2Se to 1L-MoS_2.[53] The deconvoluted spectrum shows additional Mo 6+ peaks at 230.3 eV and 232.7 eV in pristine MoS_2, while the peaks appear at 230.6 eV and 233.0 eV in the HS. The peak shift (0.3 eV) toward the higher BE indicates the formation of a Mo-O bond, which might be ascribed to the incorporation of O atom from Bi_2O_2Se, and it is consistent with the presence of B_{2g} mode in the Raman spectrum. Proper bond formation of O atoms with Mo can result in n-type doping in MoS_2 in HS. According to first principle calculation, the substitution of an S atom by an oxygen atom in a monolayer MoS_2 lowers the conduction band edge concerning the Fermi level of monolayer MoS_2 without affecting the valence band edge resulting in n-type doping.[54] ‘O’ from Bi_2O_2Se can be bonded with ‘Mo’ at the sulfur vacant sites of the CVD-grown MoS_2, eventually resulting in electron doping at the interface. Additionally, the Mo (6+) peak at 234.9 eV in pristine is unchanged in HS, indicating that the already formed Mo-O bond (due to the unwanted MoO_3 residue from the CVD growth) before HS fabrication is not affected.[21] S 2s peak positions (226.1 eV and 226.0 eV, **Fig. 5.9a**) are red-shifted by 0.1 eV in HS, indicating the accumulation of electrons via n-type doping. [55] Since S 2p and Bi 4f binding energies are close to each other, the spectra are deconvoluted to obtain each binding energy (**Fig. 5.9b**). S $2p_{3/2}$ and S $2p_{1/2}$ BEs are 161.4 eV and 162.6 eV, respectively, for pristine MoS_2 and 161.5 eV and 162.6 eV for the HS. Careful observation shows that the S$2p_{3/2}$ peak is shifted (by 0.1 eV) toward higher BE. It suggests that due to the stacking of nvdW Bi_2O_2Se, the S 2p state becomes more electronegative in the HS due to the induced electric field at the interface after contact, consistent with theoretical charge density difference (CDD) calculations. Such an interfacial electric field results in band bending, which promotes CT. Therefore, S 2s with higher BE (elimination of the inner electron) get red-shifted, while S 2p with lower BE (elimination of outer electron) get blue-shifted. More explicitly, the mechanism is that after contact between the hetero layers, they form a positively charged MoS_2 site and a negatively charged Bi_2O_2Se site at the interface, which initially makes S 2p electronegative, but at the same time, due to favorable band bending, electron transfers from Bi_2O_2Se to MoS_2 result in the red shift of S 2s. For Bi $4f_{7/2}$ and $4f_{5/2}$, the BEs are 157.7 eV and

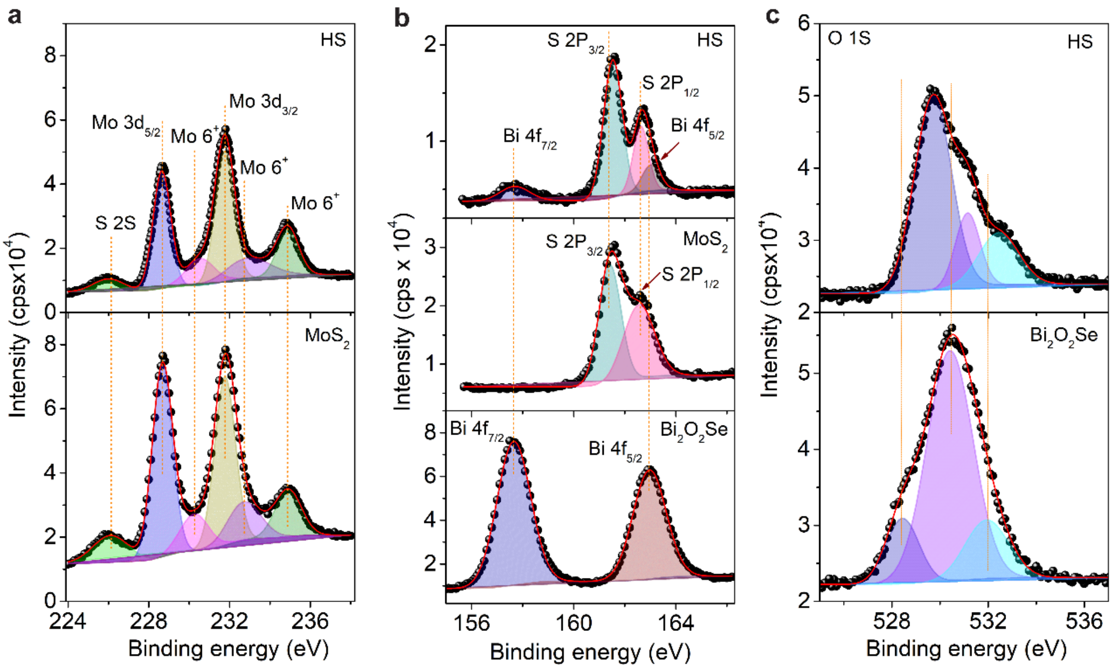

Fig. 5.9: (a) XPS spectra of Mo 3d for 1L-MoS_2 and HS. (b) S 2p and Bi 4f spectra for pristine Bi_2O_2Se, 1L-MoS_2, and HS. (c) O 1s spectra for pristine Bi_2O_2Se and HS. Symbols indicate the experimental data, while the solid line represents the fitted spectra with Shirley's baseline.

163.0 eV, the same for bare Bi_2O_2Se and the HS (**Fig. 5.9b**). O 1s peaks are at 528.4, 530.4, 531.9 eV for Bi_2O_2Se and 529.7, 531.2, and 532.4 eV for the HS (**Fig. 5.9c**). The blue shift of O1s is ascribed to interlayer electron transfer at an atomically sharp interface from Bi_2O_2Se to 1L-MoS_2 in the HS through the band bending effect and partially through the formation of a formal Mo-O bond.

The knowledge of the work function/Fermi level of individual and heterostructure materials is fundamental to understanding the type of HS and band bending.[56, 57] The energy offset between CBM or VBM induces interfacial charge transfer at the heterolayer interface. To find the origin of the interface's static electric field and the type of HS formed, we conducted KPFM measurement on the HS transferred on an indium tin oxide (ITO) substrate. Work function can be calculated using the following equation,

$$eV_{CPD} = \Phi_{tip} - \Phi_{sample} \qquad (5.2)$$

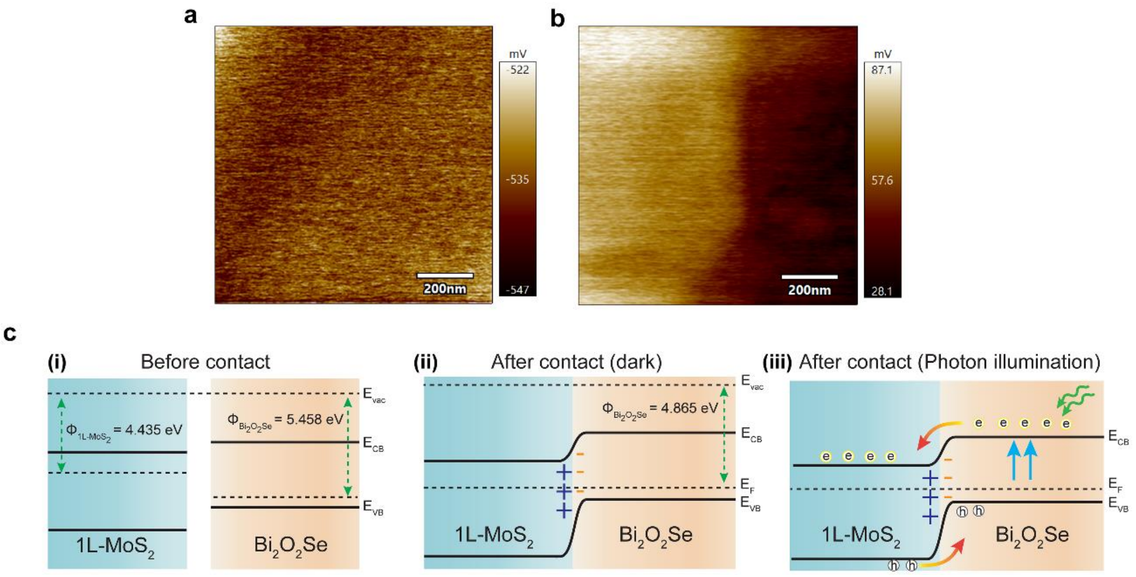

Fig. 5.10: (a, b) Surface contact potential difference topography of the Bi_2O_2Se and HS sample, respectively. (c) Band alignment for the HS, (i) before, and (ii, iii) after contact.

where V_{CPD} is the contact potential difference measured from KPFM, and Φ_{tip} and Φ_{sample} are the work function of the tip used during measurement and the sample, respectively. The calibrated work function of the Ti/Ir coated silicon tip (Φ_{tip}) is 4.95 eV. From **Fig. 5.10a**, the contact potential difference (V_{CPD}) of the layered Bi_2O_2Se is 535 mV. The calculated work function of Bi_2O_2Se is 5.485 eV by inserting the values in **equation (5.2)**. Previous studies reported that the theoretical work function of Bi_2O_2Se is 4.23 eV (2 Layer) and 4.15 eV (1L), whereas the experimental value varies between 4.37 and 4.45 eV.[58-60] In contrast, we find the work function of Bi_2O_2Se as 5.485 eV, which is much higher. This is attributed to the trapping of the electron in the defect states in Bi_2O_2Se and the corresponding movement of the Fermi level away from the conduction band minimum (E_{CBM}) and, thus, the increase in work function.[61] Similarly, the work function of 1L-MoS_2 is 4.435 eV, as reported in our previous study.[21] **Fig. 5.10b** displays that the V_{CPD} of Bi_2O_2Se in the HS is ~85 mV. Thus, the calculated work function of Bi_2O_2Se for the HS is 4.865 eV using **equation (5.2)**. The apparent reduction (~0.62 eV) in the work function of Bi_2O_2Se in HS is attributed to charge accumulation at the Bi_2O_2Se side and charge depletion at the MoS_2 side after contact, which is consistent with the theoretical CDD analysis. Due to the formation of HS, the Fermi level aligns across the junction leading to band bending, as shown in **Fig. 5.10c.** The schematic of the band alignment of the HS under different conditions (before contact and after contact in the dark and photon illumination) is depicted in **Fig. 5.10c**. **Fig. 5.10c(i)** denotes the energy band positions of 1L-

MoS_2 and Bi_2O_2Se before making contact. **Fig. 5.10c(ii)** implies the band alignment after contact (dark). It suggests a type-II band bending upon HS formation. After contact, Fermi levels of heterolayers become 4.865 eV, which is higher than of 1L-MoS_2 and lower than that of ultrathin Bi_2O_2Se. Since the work function of MoS_2 is lower than that of Bi_2O_2Se, the electrons will flow from MoS_2 to Bi_2O_2Se after the contact. Consequently, electrons are accumulated at the Bi_2O_2Se side, and holes/positive charges are created at the MoS_2 side (shown in F**ig. 5.10c(ii)**). Under equilibrium with equalized Fermi level, a built-in electric field directed from MoS_2 to Bi_2O_2Se will be established at the interface, and at the same time, band bending will occur. The band alignment from the configuration at equilibrium indicates a type-II heterojunction. A p-n junction with type-II band bending will facilitate the efficient photogenerated electron (hole) transfer from 2D Bi_2O_2Se (1L-MoS_2) to 1L-MoS_2 (2D Bi_2O_2Se). Moreover, the work function difference between 1L-MoS_2 and Bi_2O_2Se is ~50 meV ((**Fig. 5.10b**), obtained from the contrast difference at the HS junction), which indicates a low contact resistance of vdW/nvdW heterojunction. It further suggests that the carrier injection at the interface is favorable for efficient CT. Recently, Tan et al. reported a low-resistance contact between the 2D Bi_2O_2Se and the graphene for efficient photodetectors[62], which is consistent with our explanation.

To identify the nature of band alignment and the formation of p-n type junction, we calculated charge density difference (CDD) across the hetero-layers using density functional theory (DFT) calculation, including van der Waals correction. The individual unit cell structures of MoS_2, Bi_2O_2Se, and HS are depicted in **Fig. 5.11a**. The Bi_2O_2Se/MoS_2 HS was modeled by keeping the Bi_2O_2Se above the MoS_2 surface with lattice constant a = 3.53 Å and b = 3.41 Å. The optimized interlayer distance between the two layers was confirmed by the potential energy curve (PEC), as shown in **Fig. 5.11b**. **Fig. 5.11c** depicts the Bi_2O_2Se/MoS_2 heterostructure with the optimized interlayer distance (2.7 Å). A 3×3 supercell of HS was considered to calculate the CDD. The calculated CDD plot and the plane-average charge density of the MoS_2/Bi_2O_2Se HS are shown in **Fig. 5.11d**. Systematic accumulation and depletion of charge across the HS indicate that CT occurs between the two layers [63] (**Fig. 5.11c),** when two phases acquire equalized Fermi level. Further, in the plane average of charge density plot (**Fig. 5.11d**), charge accumulation and depletion reflect the respective positive and negative values. The sharp peak in the charge accumulation region present in the Se-layer of the Bi_2O_2Se indicates that significant charge carriers are located in that site, whereas in the S-layer of MoS_2, sharp peaks are present in the charge depletion region. It suggests that when the

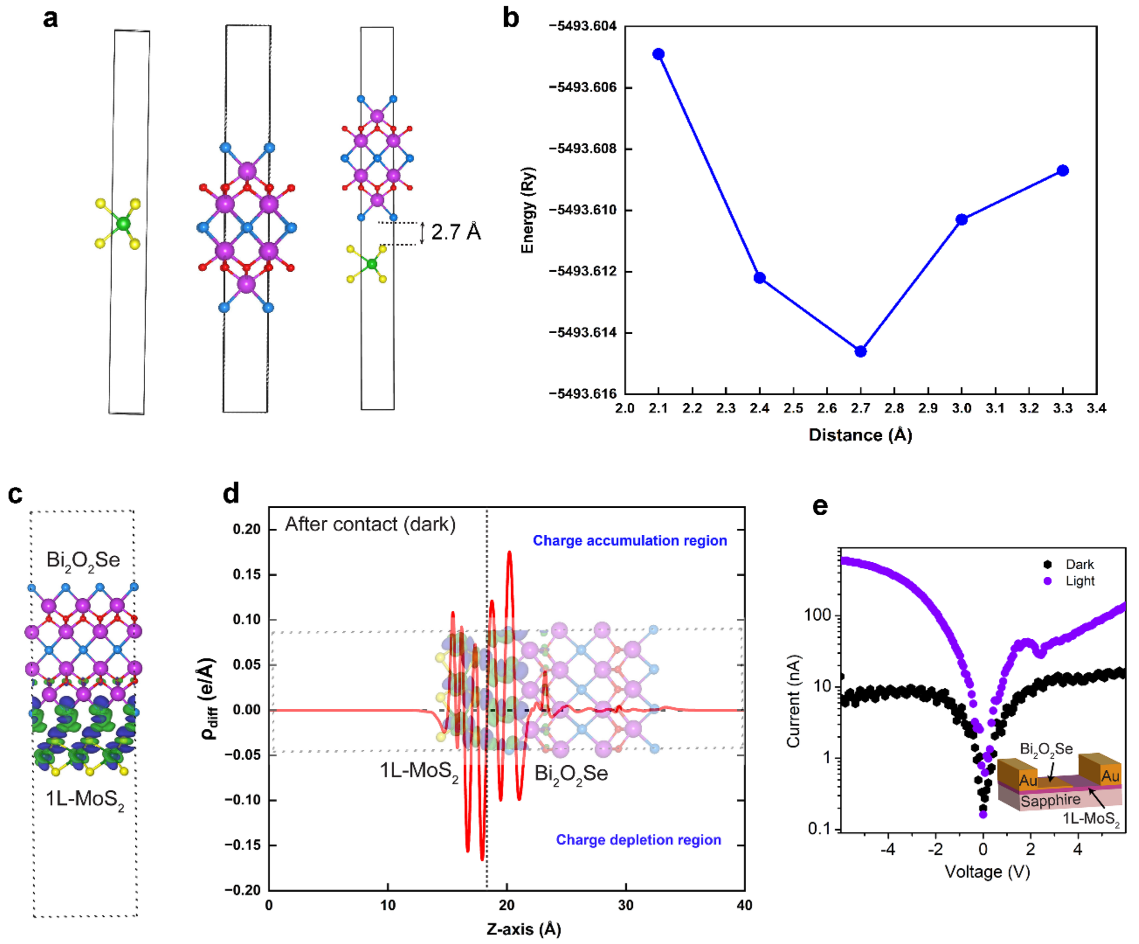

Fig. 5.11: (a) Unit cell of (a) MoS_2 monolayer, (b) Bi_2O_2Se bilayer, and (c) Bi_2O_2Se/MoS_2 hetero structure. Green, yellow, purple, red and blue balls depict Mo, S, Bi, O, and Se-atoms respectively. (b) Potential energy curve (PEC) of Interlayer distance between MoS_2 and Bi_2O_2Se in Bi_2O_2Se/MoS_2 hetero structure. (d) Charge density difference (CDD) plot of HS. Blue and green colour depicts charge depletion and accumulation region in iso-surface value 0.0001 e/bohr^3. (e) Plane-average charge density difference plot. (f) I-V characteristics of HS device under dark and light. The inset shows a schematic of the fabricated HS device.

two layers come in contact with each other, charge transfer occurs from the MoS_2 monolayer to the Bi_2O_2Se bilayer. It is calculated that an amount of 0.06 e per unit cell charge transfers from the MoS_2 to Bi_2O_2Se, which is quite reasonable.[64] The charge (electron) accumulation in the Se-site of Bi_2O_2Se, and charge (electron) depletion in S-sites of MoS_2 shows that electron is being transferred from the MoS_2 layer to the Bi_2O_2Se layer due to the alignment of the Fermi level forming an electrostatic interface, fully consistent with our experimental observation. The established built-in electric field across the hetero-layers forms p-n type junction and type-II HS that escalates the photogenerated CT from 2D Bi_2O_2Se to 1L-MoS_2. Note that as-grown 1L-MoS_2 is intrinsically n-type, and the 2D Bi_2O_2Se is p-type in this case, justifying the p-n junction behaviour.

Under light illumination, the type-II band alignment across the junction enables the photogenerated electrons in the conduction band of Bi_2O_2Se to transfer to the conduction band of 1L-MoS_2 due to suitable band bending (see **Fig. 5.10c(iii)**). The electrical coupling at the interface enhances electrons transfer from Bi_2O_2Se to MoS_2 under light resulting in high photocurrent under reverse bias. An HS-based device was fabricated (inset of **Fig. 5.11e**) to validate CT and type-II band alignment via current-voltage analysis. We followed the earlier technique to fabricate the HS device with metal electrodes.[27] **Fig. 5.11e** shows the forward and reverse bias photocurrent as a function of applied bias. The voltage was spread across the HS on the sapphire substrate via gold (Au) electrodes. In dark condition, the I-V curve shows a nearly symmetrical nature under reverse and forward bias due to two back-to-back junctions formed by the metal contact. However, the I–V curve under 405 nm illumination shows an asymmetric diode-like rectifying behaviour (**Fig. 5.11e**), consistent with the type–II HS formation. Surprisingly, the construction of HS suppresses Bi_2O_2Se dark current to an ultralow value <10 nA at 5V. Consequently, the HS photodetector shows a high on/off ratio (current) of 10^2 at room temperature. Lower dark current in the HS may be attributed to the depletion layer/built-in electric field across the hetero-layers. A p-n junction with type-II band alignment under photoexcitation stimulates electron transfer under reverse bias, and excess electron density increases with light intensity.

5.4.4. Low-temperature PL study and estimation of charge doping density

We conducted low-temperature PL measurements to comprehend the interfacial exciton dynamics in the heterolayered system. **Fig. 5.12a** shows the PL spectral evolution of HS from room temperature (293 K) down to 93 K. The results reveal a significant quenching of the PL intensity in the HS with respect to the pristine 1L-MoS_2 due to the CT, and the temperature-dependent data show an apparent redshift in the PL peak with increasing temperature. We calculated the PL quenching factor ($\mathrm{I}_{1L-MoS_2}(T) \big/ \mathrm{I}_{HS}(T)$) in the temperature range of 93-293 K (**Fig. 5.12b**), where $\mathrm{I}_{1L-MoS_2}(T)$ and $\mathrm{I}_{HS}(T)$ are the total integrated PL intensity of 1L-MoS_2 and the HS, respectively, at temperature T. The quenching factor increases exponentially from 2.5 to 8.3 with a decrease in temperature, indicating enhanced CT at lower temperatures. As the temperature decreases, the interlayer contraction is quite likely between the monolayer MoS_2 and Bi_2O_2Se surface.[65] Reduction in interlayer separation enhances the CT.[66] The interlayer spacing shrinks due to induced lattice anharmonicity during a change in temperature. In this case, the built-in electric field at the interface of the heterolayers and chemical bonding (Mo-O) across the heterolayers probably favours the contraction through electrostatic interaction, and eventually the interfacial interaction results in a larger quenching factor that reflects a robust interfacial coupling.[65] Significant change in the quenching factor due to a change in temperature indicates interlayer CT is the dominant

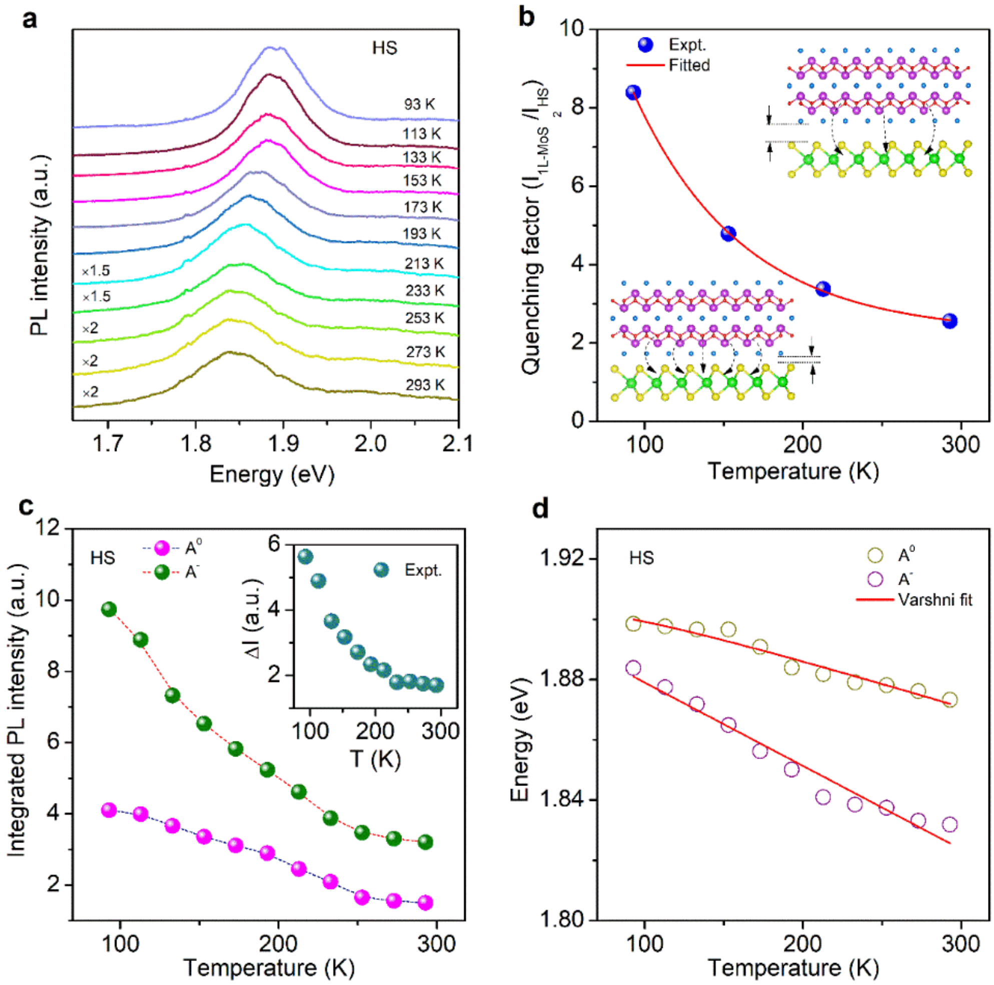

Fig. 5.12: (a) Temperature-dependent PL spectra of the heterostructure. 253 K, 273 K, 293 K spectra are multiplied by 2 and 213 K, 233 K spectra are multiplied by 1.5 for better clarity. (b) PL quenching factor i.e. the PL ratio of pristine 1L-MoS_2 and HS is plotted as a function of temperature. The solid line shows the exponential fitting curve. Upper inset demonstrates comparatively higher interlayer spacing results lower quenching factor due to lesser CT and lower inset depicts contracted interlayer spacing results higher quenching factor due to higher CT. (c) Integrated PL intensity of neutral exciton and trion vs. T plot. Inset represents the plot of difference between the integrated PL intensity of charged exciton (trion, A-) and neutral exciton as function of temperature which demonstrate the contribution from trion is much higher than neutral exciton at lower temperature. (d) Variation of PL peak energy for A^0, A^- as a function of temperature. The solid line represents the Varshni fit. The symbols are the experimental data.

process over other factors, such as the substrate, absorption, scattering, surface quality doping from absorbates, etc.[65, 67]

To further understand the CT due to interlayer coupling, the integrated PL intensity of neutral exciton (A^0) and trion (A^-) is plotted as a function of temperature, shown in **Fig. 5.12c.** It is apparent that the weightage of both the excitons (neutral and charged) increases with lowering of temperature. Noticeably, the variation in spectral weight is much higher due to trions than for neutral excitons in the low-temperature region. To visualize the increment better, the quantitative differences of trion and exciton weightage have been extracted for each temperature and are plotted in the inset of **Fig. 5.12c**. The higher increment in spectral weight of trion is attributed to the CT across the interface due to a reduction in interlayer spacing with lowering of temperature. It is obvious that the trion formation increases at lower temperatures due to its higher stability at low temperatures. It can be speculated that due to favourable band alignment, the exciton formation may occur between the positive charge lying at VBM of Bi_2O_2Se and the negative charge at CBM of MoS_2 that is interlayer exciton. However, due to the low intensity of PL, it is difficult to distinguish the interlayer excitons that are usually observed at ultralow temperatures.

Temperature-dependent PL analysis also enables the evaluation of the electron-phonon/ exciton-phonon coupling in the HS. For this purpose, the spectral energy (peak positions) of the neutral excitons (A^0) and trions (A^-) is plotted as a function of temperature in **Fig. 5.12d**. We use the modified Varshni equation[68, 69] for fitting the temperature vs. energy plot,

$$E_g(T) = E_g(0) - S\langle\hbar\omega\rangle\left[\coth\left(\frac{\langle\hbar\omega\rangle}{2K_BT}\right) - 1\right] \qquad (5.3)$$

which describes the behavior of electron-phonon coupling with temperature for many semiconductors. The parameter, S, is called Huang–Rhys factor, implying the strength of electron/exciton-phonon coupling[70], ħ, and K_B are Planks and Boltzmann constants, respectively. $\langle\hbar\omega\rangle$ is average photon energy. $E_g(0)$ is the emission energy of exciton at an absolute zero temperature. The energy shifts of the neutral exciton and trion peak were fitted via **equation 5.3**. The fitted parameters are; $E_g(0)$ = 1.90 eV and S = 0.94 for neutral exciton (A^0), and $E_g(0)$ =1.90 eV, S = 1.60 for trion (A^-). The higher S value for trion than the neutral exciton signifies that the trions contribute more to electron-phonon coupling than neutral excitons in the HSs. The observations of the higher S value corresponding to trions than the neutral exciton suggest that trion-phonon coupling is stronger than the exciton phonon coupling. However, to the best of our knowledge, there is no report on the trion-phonon coupling in the literature and it may require further investigation. It may be noted that due to the additional one electron in the trion than the neutral exciton, there may be more sites for interaction between electrons and phonons, which may give rise to the higher coupling constant (S) for trions. The A^0 exciton emission peak shifts from 1.87 to 1.90 eV (**Fig. 5.12d**) with increasing temperature, which is attributed to the lattice expansion at higher temperatures and also additional binding to defects, either via impurities at the sample surface or the Bi_2O_2Se/MoS_2 interface.[71, 72]

To further estimate the doping density, we followed a four-energy-level model as reported by Mawlong et al.[21] for 2D MoS_2/WS_2 system. The corresponding rate equations are

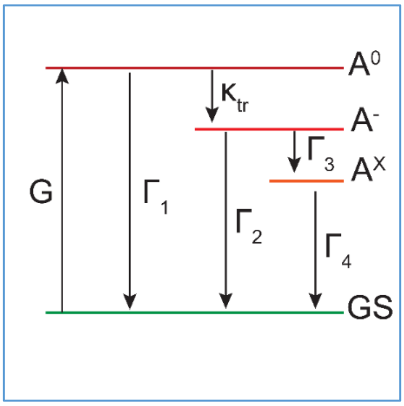

Fig. 5.13: Charge transfer through four energy level model representing the generation rate (G), trion formation rate (k_{tr}), decay rate of neutral exciton (Γ_1) trion (Γ_2, Γ_3), defect bound exciton (Γ_4).

$$\frac{dN_{A^0}}{dt} = G - [\Gamma_1 + k_{A^-}]N_{A^0} \qquad (5.4)$$

$$\frac{dN_{A^-}}{dt} = k_{A^-}N_{A^0} - [\Gamma_2 + \Gamma_3]N_{A^-} \qquad (5.5)$$

$$\frac{dN_X}{dt} = \Gamma_3 N_{A^-} - \Gamma_4 N_X \qquad (5.6)$$

Where G depicts the optical generation rate of excitons. k_{A^-} is the formation rate of trion from exciton. $\Gamma_1, \Gamma_2, \Gamma_3, \Gamma_4$ are the decay rate of neutral exciton, trion, and defect excitons (**Fig.**

5.13). By solving **equations 5.4-6**, we obtain the population of excitons (N_{A^0}), trions (N_{A^-}), defect exciton (N_X) in the steady-state,

$$N_{A^0} = \frac{G}{\Gamma_1 + k_{A^-}} \tag{5.7}$$

$$N_{A^-} = \frac{k_{A^-}}{(\Gamma_2 + \Gamma_3)} \frac{G}{(\Gamma_1 + k_{A^-})} \tag{5.8}$$

$$N_X = \frac{\Gamma_3}{\Gamma_4} \frac{k_{A^-}}{(\Gamma_2 + \Gamma_3)} \frac{G}{(\Gamma_1 + k_{A^-})} \tag{5.9}$$

Assuming the PL intensity of excitons and trions is proportional to their populations, the integrated PL intensity of exciton, trion, and defect-bound exciton can be expressed as

$$I_{A^0} = \frac{AG\gamma_0}{\Gamma_1 + k_{A^-}} \tag{5.10}$$

$$I_{A^-} = \frac{k_{A^-}}{(\Gamma_2 + \Gamma_3)} \frac{AG\gamma_-}{(\Gamma_1 + k_{A^-})} \tag{5.11}$$

$$I_X = \frac{\Gamma_3}{\Gamma_4} \frac{k_{A^-}}{(\Gamma_2 + \Gamma_3)} \frac{AG\gamma_X}{(\Gamma_1 + k_{A^-})} \tag{5.12}$$

where γ_0, γ_-, and γ_X are the radiative decay rate of the neutral exciton, trion, and defect-bound exciton, respectively. A is the collection efficiency of the luminescence.

The link between the population of the neutral exciton (N_{A^0}), trions (N_{A^-}), and the charge density n_e can be explained using the law of mass-action

$$\frac{N_{A^0} n_e}{N_{A^-}} = \left(\frac{4 m_{A^0} m_e}{\pi \hbar^2 m_{A^-}}\right) \mathrm{K}_B \mathrm{T} \exp\left(-\frac{E_b}{\mathrm{K}_B T}\right) \tag{5.13}$$

where m_{A^0}, m_e, and m_{A^-} are the effective masses of the neutral exciton, electron, and trion, respectively. $\hbar$ and K_B are the reduced Planck's constant and Boltzmann's constant. T and E_b define the temperature and trion binding energy, respectively. The effective masses for the studied system are $m_e = 0.35m_0$, $m_h = 0.45m_0$, $m_{A0} = m_e+m_h = 0.8m_0$, and $m_{A-} = 2m_e+m_h = 1.15m_0$, where m_0 is the free electron mass. Using these parameters in **equations 5.10-12**, the neutral exciton PL spectral weight can be formulated as

$$\left.\frac{I_{A^0}}{I_{total}}\right|_{pristine} = \frac{1}{1+\frac{N_{A^-}\gamma_-}{N_{A^0}\gamma_0}+\frac{N_X\gamma_X}{N_{A^0}\gamma_0}} \approx \frac{1}{1+3.2\times10^{-14}n_e} \qquad (5.14)$$

$$\left.\frac{I_{A^0}}{I_{total}}\right|_{hs} \approx \frac{1}{1+9.3\times10^{-14}n_e} \qquad (5.15)$$

Where $I_{total} = (I_{A^0} + I_{A^-} + I_X)$. $\frac{\gamma_-}{\gamma_0} = 0.11$ and $\frac{\gamma_X}{\gamma_0} = 0.01$ for a pristine sample; $\frac{\gamma_-}{\gamma_0} = 0.33$ and $\frac{\gamma_X}{\gamma_0} = 0.06$ for HS (calculated using **equations 5.10-12**). The parameters used for the calculation are $\Gamma_1 = 0.002$ ps^{-1}, $\Gamma_2 = 0.02$ ps^{-1}, $\Gamma_3 = 0.05$ ps^{-1}, $\Gamma_4 = 0.01$ ps^{-1} and $k_{A^-} = 0.5$ ps^{-1} based on the earlier reports.[21, 73] The value of $\frac{\gamma_-}{\gamma_0}$ (0.33) in HS is higher compared to pristine sample (0.11), which is ascribed to the formation of trions via efficient CT. Inserting all the values in **equations 5.14 and 5.15**, we obtain $n_e = 2.99\times10^{13}$ cm^{-2} for pristine 1L-MoS_2 and 3.32×10^{13} cm^{-2} for the HS. Therefore, the charge doping density (Δn_e) is ~ 3.3×10^{12} cm^{-2}. It may be noted that doping density in the present case is relatively lower than the case of other vdW-vdW HSs, and this may be due to the electrostatic interaction between the vdW-nvdW layers. This is consistent with the observation of relatively small red shift of the Raman peak caused by the CT. In the case of MoS_2/WS_2 QDs, this doping density was reported as 1.5×10^{13} cm^{-2}, which is substantially higher than the present case.[21]

5.5. Conclusions

We have demonstrated that the strong interfacial coupling between vdW and nvdW HS renders interlayer CT at the 2D Bi_2O_2Se/1L-MoS_2 HS interface. A narrow depletion width is formed, and the built-in electric field is directed from MoS_2 to Bi_2O_2Se. The charge transport through the heterolayers is governed by type-II band bending, which accelerates the carrier transfer from Bi_2O_2Se to 1L-MoS_2. Experimentally, the interlayer CT between 1L-MoS_2 and Bi_2O_2Se was substantiated by Raman, PL, and XPS measurements. Analysis of the relative contribution of the excitonic emissions revealed that a significant amount of CT occurs in the HS by conversion of excitons to trions. The XPS analyses shows that an electrostatic interface with a probable Mo-O bond is created that promotes CT across the surface. Experimentally work function analyses from KPFM measurement and theoretically DFT calculations suggest that initially (dark), a significant CT occurs at the interface after contact formation from 1L-MoS_2 to Bi_2O_2Se and forms an electric field across the interface that eventually forms a p-n junction with type-II band bending. In addition, asymmetric diode-like rectifying behavior confirms type-II HS formation between the layers. I-V characteristics provide an ultralow dark current of 10^{-8} A. As a result, this HS photodetector shows a high on/off ratio of 10^2 at room temperature (300 K). Temperature-dependent PL analysis of HS reveals a larger formation rate of trion (due to CT) with decreasing temperature due to the interlayer contraction and stronger coupling effect. A higher value of the Huang–Rhys factor for trions indicates that trion-phonon coupling is stronger than exciton-phonon coupling in the HS. Considering the four-energy level model, the estimated n-type doping density (Δn_e) is ~ 3.3×10^{12} cm^{-2}, which is quite consistent with the theoretical estimate from DFT calculation. We believe the proposed 2D Bi_2O_2Se/1L-MoS_2 HS extends its promising potential in optoelectronics based on its intriguing CT properties. Moreover, our work opens up a viable strategy for understanding the interlayer coupling in van der Waals / non-van der Waals systems, which will benefit the development of heterostructure-based nanodevices.

References

1. K. S. Novoselov, A. Mishchenko, A. Carvalho and A. H. Castro Neto, *Science*, 2016, **353**, aac9439.
2. M. Gibertini, M. Koperski, A. F. Morpurgo and K. S. Novoselov, *Nature Nanotechnology*, 2019, **14**, 408-419.
3. Y. Liu, S. Zhang, J. He, Z. M. Wang and Z. Liu, *Nano-Micro Letters*, 2019, **11**, 13.
4. X. Cai, S. Wang and L.-M. Peng, *Nano Research Energy*, 2023, DOI: 10.26599/NRE.2023.9120058.
5. K. S. Novoselov and A. H. Castro Neto, *Physica Scripta*, 2012, **T146**, 014006.
6. K. Chen, X. Wan, J. Wen, W. Xie, Z. Kang, X. Zeng, H. Chen and J.-B. Xu, *ACS Nano*, 2015, **9**, 9868-9876.
7. J. He, C. Wang, B. Zhou, Y. Zhao, L. Tao and H. Zhang, *Materials Horizons*, 2020, **7**, 2903-2921.
8. D. Jariwala, T. J. Marks and M. C. Hersam, *Nature Materials*, 2017, **16**, 170-181.
9. J. Zhang, H. Hong, C. Lian, W. Ma, X. Xu, X. Zhou, H. Fu, K. Liu and S. Meng, *Advanced Science*, 2017, **4**, 1700086.
10. T. Zheng, P. Valencia-Acuna, P. Zereshki, K. M. Beech, L. Deng, Z. Ni and H. Zhao, *ACS Applied Materials & Interfaces*, 2021, **13**, 6489-6495.
11. Z. Ji, H. Hong, J. Zhang, Q. Zhang, W. Huang, T. Cao, R. Qiao, C. Liu, J. Liang, C. Jin, L. Jiao, K. Shi, S. Meng and K. Liu, *ACS Nano*, 2017, **11**, 12020-12026.

12. K. Wang, B. Huang, M. Tian, F. Ceballos, M.-W. Lin, M. Mahjouri-Samani, A. Boulesbaa, A. A. Puretzky, C. M. Rouleau, M. Yoon, H. Zhao, K. Xiao, G. Duscher and D. B. Geohegan, *ACS Nano*, 2016, **10**, 6612-6622.
13. X. Hong, J. Kim, S.-F. Shi, Y. Zhang, C. Jin, Y. Sun, S. Tongay, J. Wu, Y. Zhang and F. Wang, *Nature Nanotechnology*, 2014, **9**, 682-686.
14. H. Chen, X. Wen, J. Zhang, T. Wu, Y. Gong, X. Zhang, J. Yuan, C. Yi, J. Lou, P. M. Ajayan, W. Zhuang, G. Zhang and J. Zheng, *Nature Communications*, 2016, **7**, 12512.
15. L. Li, R. Long and O. V. Prezhdo, *Chemistry of Materials*, 2017, **29**, 2466-2473.
16. L. Wang, M. Tahir, H. Chen and J. B. Sambur, *Nano Letters*, 2019, **19**, 9084-9094.
17. C. Trovatello, G. Piccinini, S. Forti, F. Fabbri, A. Rossi, S. De Silvestri, C. Coletti, G. Cerullo and S. Dal Conte, *npj 2D Materials and Applications*, 2022, **6**, 24.
18. Z. Chen, Q. Chen, Z. Chai, B. Wei, J. Wang, Y. Liu, Y. Shi, Z. Wang and J. Li, *Nano Research*, 2022, **15**, 4677-4681.
19. T. Jena, M. T. Hossain and P. K. Giri, *Journal of Materials Chemistry C*, 2021, **9**, 16693-16708.
20. X. Wu, X. Wang, H. Li, Z. Zeng, B. Zheng, D. Zhang, F. Li, X. Zhu, Y. Jiang and A. Pan, *Nano Research*, 2019, **12**, 3123-3128.
21. L. P. L. Mawlong, A. Bora and P. K. Giri, *Scientific Reports*, 2019, **9**, 19414.
22. J. Zhang, J. Wang, P. Chen, Y. Sun, S. Wu, Z. Jia, X. Lu, H. Yu, W. Chen, J. Zhu, G. Xie, R. Yang, D. Shi, X. Xu, J. Xiang, K. Liu and G. Zhang, *Advanced Materials*, 2016, **28**, 1950-1956.
23. X. Zhu, N. R. Monahan, Z. Gong, H. Zhu, K. W. Williams and C. A. Nelson, *Journal of the American Chemical Society*, 2015, **137**, 8313-8320.
24. C. R. Dean, A. F. Young, I. Meric, C. Lee, L. Wang, S. Sorgenfrei, K. Watanabe, T. Taniguchi, P. Kim, K. L. Shepard and J. Hone, *Nature Nanotechnology*, 2010, **5**, 722-726.
25. A. K. Geim and I. V. Grigorieva, *Nature*, 2013, **499**, 419-425.
26. M. T. Hossain and P. K. Giri, *Journal of Applied Physics*, 2021, **129**, 175102.
27. M. T. Hossain, M. Das, J. Ghosh, S. Ghosh and P. K. Giri, *Nanoscale*, 2021, **13**, 14945-14959.
28. P. Giannozzi, S. Baroni, N. Bonini, M. Calandra, R. Car, C. Cavazzoni, D. Ceresoli, G. L. Chiarotti, M. Cococcioni, I. Dabo, A. Dal Corso, S. de Gironcoli, S. Fabris, G. Fratesi, R. Gebauer, U. Gerstmann, C. Gougoussis, A. Kokalj, M. Lazzeri, L. Martin-Samos, N. Marzari, F. Mauri, R. Mazzarello, S. Paolini, A. Pasquarello, L. Paulatto, C. Sbraccia, S. Scandolo, G. Sclauzero, A. P. Seitsonen, A. Smogunov, P. Umari and R. M. Wentzcovitch, *Journal of Physics: Condensed Matter*, 2009, **21**, 395502.
29. P. E. Blöchl, *Physical Review B*, 1994, **50**, 17953-17979.
30. J. P. Perdew, K. Burke and M. Ernzerhof, *Physical Review Letters*, 1996, **77**, 3865-3868.
31. H. J. Monkhorst and J. D. Pack, *Physical Review B*, 1976, **13**, 5188-5192.
32. J. Moellmann and S. Grimme, *The Journal of Physical Chemistry C*, 2014, **118**, 7615-7621.
33. Q. Wei, R. Li, C. Lin, A. Han, A. Nie, Y. Li, L.-J. Li, Y. Cheng and W. Huang, *ACS Nano*, 2019, **13**, 13439-13444.
34. S. Thomas, V. Kumar, D. R. Roy and M. A. Zaeem, *ACS Applied Nano Materials*, 2020, **3**, 10073-10081.
35. K. Momma and F. Izumi, *Journal of Applied Crystallography*, 2008, **41**, 653-658.
36. H. Lin, Y. Li, H. Li and X. Wang, *Nano Research*, 2017, **10**, 1377-1392.
37. L. Seguin, M. Figlarz, R. Cavagnat and J. C. Lassègues, *Spectrochimica Acta Part A: Molecular and Biomolecular Spectroscopy*, 1995, **51**, 1323-1344.
38. Z. Hu, X. Liu, P. L. Hernández-Martínez, S. Zhang, P. Gu, W. Du, W. Xu, H. V. Demir, H. Liu and Q. Xiong, *InfoMat*, 2022, **4**, e12290.
39. H. Park, G. H. Shin, K. J. Lee and S.-Y. Choi, *Nano Research*, 2020, **13**, 576-582.
40. S. Bae, N. Sugiyama, T. Matsuo, H. Raebiger, K.-i. Shudo and K. Ohno, *Physical Review Applied*, 2017, **7**, 024001.
41. A. P. Richter, J. R. Lombardi and B. Zhao, *The Journal of Physical Chemistry C*, 2010, **114**, 1610-1614.

42. J. R. Lombardi and R. L. Birke, *The Journal of Physical Chemistry C*, 2008, **112**, 5605-5617.
43. V. Natarajan, M. Ahmad, J. Paul Sharma, A. Sathya, P. Kumar Sharma and R. Thangaraj, *Applied Surface Science*, 2021, **550**, 149356.
44. K. F. Mak, C. Lee, J. Hone, J. Shan and T. F. Heinz, *Physical Review Letters*, 2010, **105**, 136805.
45. W. Wang, K. Li, Y. Wang, W. Jiang, X. Liu and H. Qi, *Applied Physics Letters*, 2019, **114**, 201601.
46. A. M. van der Zande, P. Y. Huang, D. A. Chenet, T. C. Berkelbach, Y. You, G.-H. Lee, T. F. Heinz, D. R. Reichman, D. A. Muller and J. C. Hone, *Nature Materials*, 2013, **12**, 554-561.
47. Y. Li, K. Dai, L. Gao, J. Zhang, A. Cui, K. Jiang, Y. Li, L. Shang, L. Zhu and Z. Hu, *Nanoscale*, 2023, DOI: 10.1039/D2NR05775A.
48. J. Koo, S. Gao, H. Lee and L. Yang, *Nanoscale*, 2017, **9**, 14540-14547.
49. X. Zhu, J. He, R. Zhang, C. Cong, Y. Zheng, H. Zhang, S. Wang, H. Zhao, M. Zhu, S. Zhang, S. Li and L. Chen, *Nano Research*, 2022, **15**, 2674-2681.
50. R. Kaupmees, H.-P. Komsa and J. Krustok, *physica status solidi (b)*, 2019, **256**, 1800384.
51. K. K. Paul, L. P. L. Mawlong and P. K. Giri, *ACS Applied Materials & Interfaces*, 2018, **10**, 42812-42825.
52. Z. Jiang, W. Zhang, L. Jin, X. Yang, F. Xu, J. Zhu and W. Huang, *The Journal of Physical Chemistry C*, 2007, **111**, 12434-12439.
53. J. Meyer, P. R. Kidambi, B. C. Bayer, C. Weijtens, A. Kuhn, A. Centeno, A. Pesquera, A. Zurutuza, J. Robertson and S. Hofmann, *Scientific Reports*, 2014, **4**, 5380.
54. L. Qi, Y. Wang, L. Shen and Y. Wu, *Applied Physics Letters*, 2016, **108**, 063103.
55. P. Zhang, Y. Li, Y. Zhang, R. Hou, X. Zhang, C. Xue, S. Wang, B. Zhu, N. Li and G. Shao, *Small Methods*, 2020, **4**, 2000214.
56. R. R. Rojas-Lopez, J. C. Brant, M. S. O. Ramos, T. H. L. G. Castro, M. H. D. Guimarães, B. R. A. Neves and P. S. S. Guimarães, *Applied Physics Letters*, 2021, **119**, 233101.
57. I. Sharma and B. R. Mehta, *Applied Physics Letters*, 2017, **110**, 061602.
58. S. Liu, L. Xu, Y. Pan, J. Yang, J. Li, X. Zhang, L. Xu, H. Pang, J. Yan, B. Shi, X. Sun, H. Zhang, L. Xu, J. Yang, Z. Zhang, F. Pan and J. Lu, *Advanced Theory and Simulations*, 2019, **2**, 1800178.
59. P. Luo, F. Wang, J. Qu, K. Liu, X. Hu, K. Liu and T. Zhai, *Advanced Functional Materials*, 2021, **31**, 2008351.
60. S. Liu, D. He, C. Tan, S. Fu, X. Han, M. Huang, Q. Miao, X. Zhang, Y. Wang, H. Peng and H. Zhao, *Small*, 2022, **18**, 2106078.
61. L.-Y. Dang, M. Liu, G.-G. Wang, D.-Q. Zhao, J.-C. Han, J.-Q. Zhu and Z. Liu, *Advanced Functional Materials*, 2022, **n/a**, 2201020.
62. C. Tan, S. Xu, Z. Tan, L. Sun, J. Wu, T. Li and H. Peng, *InfoMat*, 2019, **1**, 390-395.
63. R. Singh, U. Gupta, V. S. Kumar, M. M. Ayyub, U. V. Waghmare and C. N. R. Rao, *ChemPhysChem*, 2019, **20**, 1728-1737.
64. H. Li, K. Yu, C. Li, Z. Tang, B. Guo, X. Lei, H. Fu and Z. Zhu, *Scientific Reports*, 2015, **5**, 18730.
65. L. Zhang, H. Yan, X. Sun, M. Dong, T. Yildirim, B. Wang, B. Wen, G. P. Neupane, A. Sharma, Y. Zhu, J. Zhang, K. Liang, B. Liu, H. T. Nguyen, D. Macdonald and Y. Lu, *Nanoscale*, 2019, **11**, 418-425.
66. J. Kang, W. Liu, D. Sarkar, D. Jena and K. Banerjee, *Physical Review X*, 2014, **4**, 031005.
67. F. Wang, J. Wang, S. Guo, J. Zhang, Z. Hu and J. Chu, *Scientific Reports*, 2017, **7**, 44712.
68. K. P. O'Donnell and X. Chen, *Applied Physics Letters*, 1991, **58**, 2924-2926.
69. S. Tongay, J. Zhou, C. Ataca, K. Lo, T. S. Matthews, J. Li, J. C. Grossman and J. Wu, *Nano Letters*, 2012, **12**, 5576-5580.
70. S. Helmrich, R. Schneider, A. W. Achtstein, A. Arora, B. Herzog, S. M. de Vasconcellos, M. Kolarczik, O. Schöps, R. Bratschitsch, U. Woggon and N. Owschimikow, *2D Materials*, 2018, **5**, 045007.
71. H. Li, X. Zhu, Z. K. Tang and X. H. Zhang, *Journal of Luminescence*, 2018, **199**, 210-215.
72. T. Korn, S. Heydrich, M. Hirmer, J. Schmutzler and C. Schüller, *Applied Physics Letters*, 2011, **99**, 102109.

73. S. Mouri, Y. Miyauchi and K. Matsuda, *Nano Letters*, 2013, **13**, 5944-5948.

Chapter 6

Defect-Induced Photogating Effect and its Modulation in Ultrathin Free-standing Bi_2O_2Se Nanosheets with Visible-to-Near-Infrared Photoresponse

In this chapter, we have explored the unique structural and optoelectronic functionalities of ultrathin Bi_2O_2Se nanocrystals, synthesized via a scalable chemical reaction process with high reproducibility, and their modulation through vacuum annealing. The as-prepared nanosheets (NS) with monolayer to few-layer thickness possess different kinds of defects (e.g., Bi-antisites at Se vacancies, Se vacancies, interstitial O, O antisites at Se vacancies) due to their free-standing nature with Se-terminated charged surface. Our study reveals that vacuum annealing improves the crystal quality through defect passivation, basically through the inter-layer self-assembly via electrostatic interaction. Interestingly, we observed self-powered negative persistent photoconductivity (PPC) in as-grown defect-containing Bi_2O_2Se NS and positive photoconductivity (PC) in annealed Bi_2O_2Se NS containing fewer defects. The mechanistic origin of such conversion from negative PPC to positive PC is discussed in detail, where the energy levels created by the defects serve as photo-gates. In addition, photoresponsivity (vis-NIR) measurements show a photo-gating effect created by defects that play a key role in modulating the wavelength-dependent photoconductivity. The peak responsivity of the device is shown to be 0.4 AW^{-1} at 808 nm. This work highlights the possible origin of crystallinity improvement of non-van der Waals Bi_2O_2Se nanosheets through vacuum annealing and their intriguing photoresponse properties in visible-to-near-infrared range, which are of fundamental importance and practical application in cutting-edge optoelectronics.

6.1. Introduction

Low-dimensional materials are promising for the next generation devices due to their tunable structural[1], and unique optical [2, 3], and electronic properties[4, 5]. Interestingly, these properties depend highly on the crystallinity[6], thickness[7, 8], and defects[9] of the material. Among low-dimensional materials, 2D nanosheets have attracted significant attention due to their fascinating optoelectronic properties.[10-12] Newly emerging nvdW Bi_2O_2Se has shown competitive optoelectronic properties[13-16] comapred with its vdW-2Ds (such as MoX_2, WX_2, PdX_2 where X= S, Se, Te). Different synthesis techniques have been adopted to obtain the high crystal quality and scalable production of 2D Bi_2O_2Se (discussed in **Chapter 1**).[14, 17-21] Based on its application, researchers have adopted various synthesis/growth routes, such as CVD-grown milli-meter-sized single crystal of Bi_2O_2Se for phototransistors[17], the catalyst-free CVD-growth of Bi_2O_2Se nanoribbons for phototransistors[22], the solution-based top-down synthesis of Bi_2O_2Se quantum dots for cancer photothermal therapy[23], *etc*. However, further investigations are necessary to bridge the gap between synthesis and applications in an orderly manner by unraveling the hidden properties of Bi_2O_2Se nanostructures. Many inherent properties, such as bolometric effect[24], low lattice thermal conductance[25-27], high carrier mobility[28, 29], room-temperature ferroelectricity[18, 30], and excimer formation[31] have been reported in semiconducting Bi_2O_2Se.

Generally, in semiconductors, photoexcitation leads to surplus charge carriers, which increases the electrical conductivity known as positive photoconductivity (PC). However, in exceptional circumstances, negative PC may appear due to a diminished conductivity under illumination. So far, many semiconductor nanostructures have exhibited negative PC, e.g., as in p-type single-walled carbon nanotubes[32], Bi-doped p-type ZnSe nanowires[33], n-type InAs nanowires[34], n-type InN thin films[35], Bi_2Se_3 nanosheets[36], etc. Many theoretical predictions and experimental studies have been reported and debated to determine the origin of negative PC in such semiconductors.[37-41] Grillo et al. have observed the coexistence of negative PC and positive PC in p-type few-layer $PtSe_2$ due to the physisorption of oxygen at the surface.[42] For p-type material, photon-assisted oxygen desorption leaves electrons that further recombine with holes and reduce the carrier (hole) concentration, resulting in negative PC. By contrast, negative PC in an n-type material cannot be explained following such a mechanism because the desorption of oxygen leaves electrons and increases electron concentration, which will result in positive PC. However, negative PC has also been reported in n-type semiconductors, explained in some cases through light-assisted hot electron trapping[34] and light-induced positively charged gap states[35]. Other mechanisms, such as the built-in-electric field[43, 44], the presence of DX (D: donor atom, X: unspecified lattice defect) like centers[45], etc, have been reported to explain this negative PC. Although different origins of negative PC have been reported in different materials, the observation of negative PC in Bi_2O_2Se is novel, and understanding its origin is imperative because of its unique nvdW characteristics. Besides being a superior optoelectronic candidate, the intrinsic defects and structural tuning via vacuum annealing in Bi_2O_2Se are interesting to explore because they can profoundly affect the transport properties of Bi_2O_2Se. In addition, these defects can produce Janus structures compared with conventional oxide passivation in metal chalcogenides nanostructures[46]. The dissimilarity in non-vdW materials can create several applications, including ferroelectricity, piezoelectricity, etc.[47, 48]

In this work, we report negative PC in Bi_2O_2Se nanosheets (NS) in their pristine form, synthesized via a one-pot chemical synthesis process. We study the conversion of negative PC to positive PC via vacuum annealing of the as-grown Bi_2O_2Se nanosheets, and explore the origins behind this systematic conversion. Unlike previously reported p-type systems, oxygen desorption can hardly explain the origin of negative PC in our study, since the as-grown Bi_2O_2Se contains intrinsic defects (mainly Bi-antisites at Se vacancies/Se vacancies/interstitial O/O antisites at Se vacancies), as confirmed from energy-dispersive X-ray spectroscopy and X-ray photoelectron spectroscopy measurements. Interestingly, after vacuum annealing, the defect density is substantially reduced. X-ray diffraction pattern and Raman analyses have been adopted to understand the mechanism of the improved crystallinity of Bi_2O_2Se after annealing. We provide evidence of defect healing in free-standing Bi_2O_2Se through self-assembly during vacuum annealing. Atomic resolution transmission electron microscopy provides evidence for inter-layer merging of two layers during vacuum annealing, which reduces the defects. We show that the defect-induced shallow energy states serve as a photo-gate that controls the negative PC via increasing electron-hole recombination and the trapping of free carriers. Thus, the photo-gating effect plays a significant role in tuning the electronic properties of chemically synthesized Bi_2O_2Se NS. We also study the performance of the annealed NS as a photodetector.

6.2. Experimental details

6.2.1. Materials

The following materials have been used for the preparation of Bi_2O_2Se nanosheets: 100 mg of $Bi(NO_3)_3.5H_2O$ (Sigma Aldrich) and 13 mg $SeC(NH_2)_2$ (Sigma Aldrich), 306.8 mg EDTA, 120 mg KOH, and 320 mg NaOH.

6.2.2. Preparation

Fig. 6.1 shows the schematic diagram of the synthesis process. At first, 100 mg of bismuth nitrate pentahydrate ($Bi(NO_3)_3$,$5H_2O$) was placed in a beaker containing 20 ml of distilled water. This was mixed using a magnetic stirrer on a hot plate at 150 1C at 550 rpm for 10 minutes. Subsequently, 13 mg of selenouria was added, and the experiment was continued for 10 minutes. Next, 306.8 mg of EDTA was added and the reaction continued for 10 minutes. The, 120 mg of KOH and 320 mg of NaOH were added, and the reaction was continued for another 15 minutes. Later, the product was rinsed with ethanol and DI water. Finally, the product was centrifuged at 9000 rpm with ethanol and DI water 4 times consecutively. In the end, the product was kept inside a hot air oven for 24 hours with a heat of 80°C and, finally, the Bi_2O_2Se nanosheets are obtained. For vacuum annealing, the sample were kept inside a single zone tube (quartz) furnace, where the tube was maintained at a vacuum of 8.5×10^{-3} mbar. Annealing was carried out for 1 hour at temperature of 200°C, 300°C, 400°C.

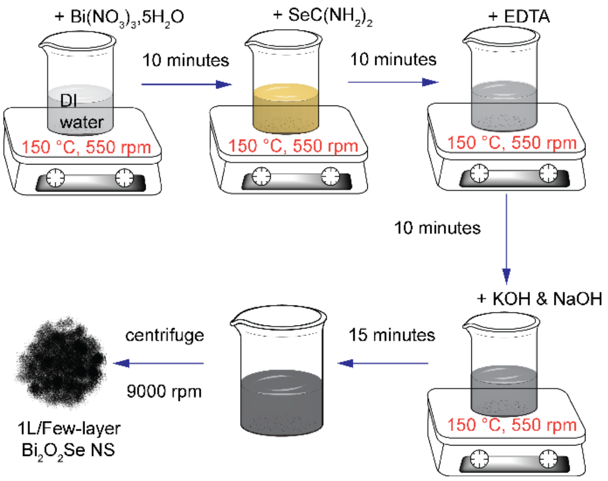

Step I: $Bi(NO_3)_3 + H_2O \rightarrow BiONO_3 + 2H^+ + 2NO_3^-$
Step II: $SeC(NH_2)_2 + OH^- \rightarrow Se^{2-} + H_2NCN + H_2O$
Step III: $2BiONO_3 + Se^{2-} \rightarrow Bi_2O_2Se + 2NO^{3-}$

Fig. 6.1: Schematic of the synthesis process of Bi_2O_2Se NS.

6.2.3. Characterization techniques

Micro-Raman spectroscopy (LabRam HR800, Jobin Yvon) was carried out to characterize the unannealed and annealed Bi_2O_2Se NS with an excitation wavelength (λ_{ex}) of 532 nm with 100× objective lens with a typical spot size of 1 µm. X-ray diffraction (instrument details same as **section 2.2.3**) patterns were collected to extract the crystal information. The thickness of the samples has been measured with atomic force microscopy (AFM; Cypher, Oxford Instruments) imaging in non-contact mode scanning. XPS and ultraviolet photoelectron spectroscopy (UPS) measurements were performed using a PHI 5000VersaProbe III instrument (ULVAC-PHI, INC). The morphology of unannealed and annealed Bi_2O_2Se NS was studied using a field emission scanning electron microscope (FESEM) (Sigma, Zeiss). FETEM, including high-resolution TEM operated at 200 KV, was performed to study the morphology, layer, and self-merging of the Bi_2O_2Se nanosheets. Energy-dispersive X-ray spectroscopy (EDS) of the Bi_2O_2Se NCs was performed using a scanning transmission electron microscope (STEM; JEM 2100F, 200 kV). The Bi_2O_2Se layer was drop cast onto a TEM Cu grid for the TEM measurements and baked on a hot plate at 50 °C for 30 minutes. Absorbance spectra were acquired with a UV-VIS spectrophotometer (Lambda 950, PerkinElmer). The transfer characteristics of the photodetectors were measured using a microprobe station (ECOPIA EPS-500) with 808 nm, 532 nm, and 405 nm lasers. Photoresponse data were collected at 808 nm and 405 nm facilitated with TTL modulation (CNI Laser) and I-V measurement system (Keithley 4200). The spectral photo-responsivity of the photodetector was measured using a Xenon lamp (Newport) with a manual monochromator (Newport) and source-measure unit (Keithley 2400).

6.3. Results and Discussion

6.3.1. Synthesis and characterization

Bi_2O_2Se NS was synthesized via a chemical process using bismuth nitrate ($Bi(NO_3)_3$) and selenourea ($SeC(NH_2)_2$) at 150 °C in a laboratory atmosphere. A schematic of the synthesis process has been depicted in **Fig. 6.1**. Typically, in step I, bismuth nitrate goes through a hydrolysis process in the aqueous medium and forms $BiONO_3$. Subsequently, the addition of selenourea decomposes into selenium ions (Se^2) in the aqueous medium in step II. In step III, $BiONO_3$ reacts with Se^{2-} and produces Bi_2O_2Se. Thus, bismuth nitrate and selenourea produce $[Bi_2O_2]^{2+}$ and $[Se]^{2-}$ ions, which further covalently bond and form a layered electrostatic structure of Bi_2O_2Se. **Fig. 6.2a** shows the electrostatic stacking of $[Bi_2O_2]^{2+}$ and $[Se]^{2-}$ layers atomically. As shown in **Fig. 6.2b** (unannealed) and **6.1c** (annealed), free-standing nanosheet's are obtained, as captured via FESEM imaging. A mixture of few-layer (**Fig. 6.2d**) to multilayer, including monolayer (**Fig. 6.2e**), was observed in the as-prepared nanosheets (NS). In **Fig. 6.2d**, an edge of the Bi_2O_2Se flake shows the 5 consecutive layers with a spacing of 0.6 nm, confirming the few-layer Bi_2O_2Se. The inset of **Fig. 6.2e** demonstrates the thickness of 0.6 nm, a single layer thickness of Bi_2O_2Se.[49] To confirm the crystallinity of the NS, we carried out Raman spectroscopy on the as-grown Bi_2O_2Se NS. Observation of characteristic A_{1g} Raman mode at 154.7 cm^{-1} indicates the formation of the tetragonal phase of Bi_2O_2Se.[18, 26, 50]

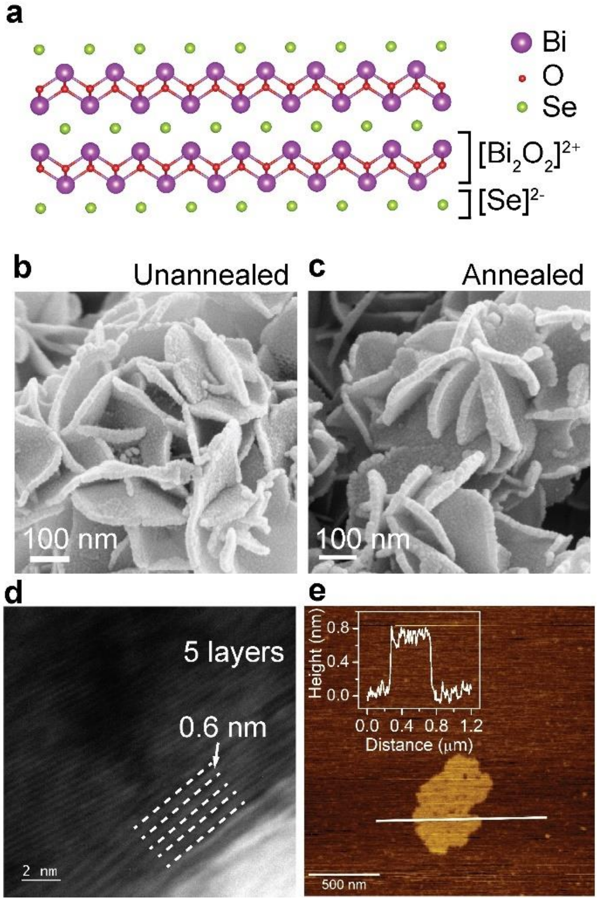

Fig. 6.2: (a) Atomic crystal structure of Bi_2O_2Se showing the electrostatic stacking of $[Bi_2O_2]^{2+}$ and $[Se]^{2-}$ (b, c) FESEM images of as-synthesized free-standing nanosheet before and after annealing. (d) TEM image showing an edge of Bi_2O_2Se NS containing 5 layers (3 nm thickness). (e) Atomic force microscopy image of a single monolayer Bi_2O_2Se nanosheet. Inset shows the corresponding height profile of monolayer Bi_2O_2Se.

6.3.2. Evidence for intrinsic defects and their control via vacuum annealing

Although we observe the characteristic A_{1g} Raman mode, there exists a broad asymmetric tail of A_{1g} mode (**Fig. 6.3a**). To understand the origin of the tail, we carried out vacuum (10^{-3} mbar) annealing of the sample at different temperatures (200-400 °C). Interestingly, the broadening (FWHM) of the A_{1g} mode decreases with the annealing temperature. With an increasing annealing temperature, the FWHM of A_{1g} mode decreases systematically from 19.2 cm^{-1} (unannealed) to 17.8 cm^{-1} (200 °C, annealed), 14.8 cm^{-1} (300 °C, annealed), and 11.0 cm^{-1} (400 °C, annealed) (**Fig. 6.3b**). The atomic out-of-plane vibration of the Bi-atom about the $[Bi_2O_2]$ plane is the origin of the A_{1g} mode (154.7 cm^{-1}). The in-plane vibration of the Bi atom with respect to the Se atom causes the E_{2g} mode in Bi_2Se_3 at ~131 cm^{-}

^{1}.[51] From the Lorentzian fitted spectra (**Fig. 6.3a**), the extra broad peak at ~138.3 cm^{-1} (in the as-grown Bi_2O_2Se), 138.9 cm^{-1} (200 °C), 143.4 cm^{-1} (300 and 400 °C)) corresponds to neither the E_{2g} peak of Bi_2Se_3 nor the A_{1g} peak of Bi_2O_2Se. Now, what is the origin of the ~138.3 cm^{-1} mode? The intrinsic defect could probably be passivated via vacuum annealing due to the quasi-Se-terminated charged surface of Bi_2O_2Se. Hence, the broad peak at ~138.3 cm^{-1} indicates the defective bismuth oxiselenide state. We assigned it to a defect peak. The intensity ratio ($\frac{I_{A_{1g}}}{I_{defect}}$) of A_{1g} mode and the defect mode (~138.3 cm^{-1}) is found to increase from 1.44 (before annealing) to 1.55 (200 °C), 2.1 (300 °C), and 3.2 (400°C) after annealing, as shown in **Fig. 6.3c**. The vibrational mode caused by defects at ~138.3 cm^{-1} is reduced significantly after annealing. Upon vacuum annealing, the decrease in FWHM and the increase in $\frac{I_{A_{1g}}}{I_{defect}}$ suggest an improvement in crystallinity through defect reduction due to built-in electrostatic interactions among the layers.

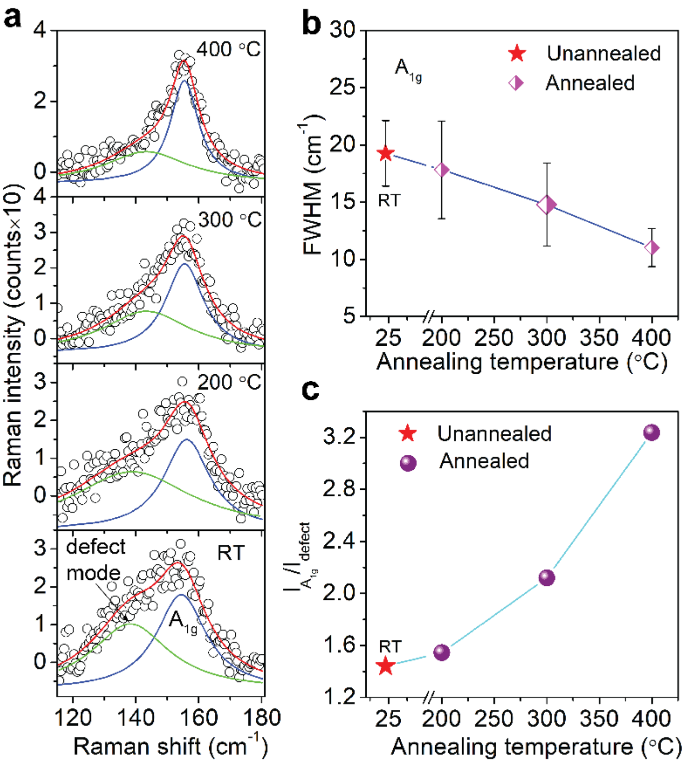

Fig. 6.3: (a) Comparison of Raman spectra of unannealed & annealed Bi_2O_2Se samples. (b) FWHM of A_{1g} mode as a function of annealing temperature. (c) Intensity ratio of A_{1g} Raman mode to defect-induced mode as the function of annealing temperature reflecting that A_{1g} becomes prominent with increasing annealing temperature.

To find the mechanism of defect reduction, elemental mapping was carried out. **Fig. 6.4a (i-iv)** shows the STEM mapping of each element of unannealed Bi_2O_2Se NS, and the corresponding EDX spectrum is depicted in **Fig. 6.4b** with atomic percentage. **Fig 6.4a(i)** shows a cluster of free-standing nanosheets, and **Fig 6.4a(ii-iv)** shows the corresponding Bi (yellow), O (green), and Se (red) colour mapping, which shows elemental uniformity over the cluster. The atomic percentage of Bi, O, and Se is 45.8 %, 40.7 %, and 13.5 %, respectively, for the pristine sample. This deviates from the ideal Bi_2O_2Se crystal with an atomic ratio of 2:2:1 and reflects the formation of the Se poor and Bi-rich state. The formation of such Se-poor, Bi-rich state probably arises due to low-temperature chemical growth. According to DFT, considering 90 atom's Bi_2O_2Se supercell, under Se-poor and Bi-rich conditions, besides the Se vacancies and O vacancies, the formation of ‘Bi antistites at Se vacancies’ and ‘presence of interstitial oxygen’ is most likely.[52] In addition, Wei et al. found from the first-principle

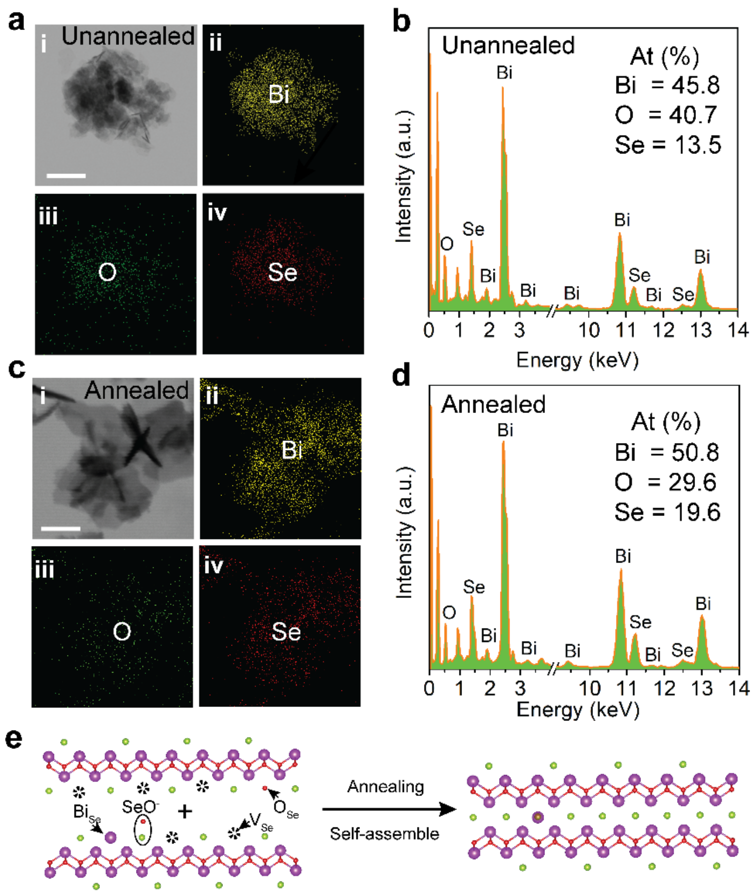

Fig. 6.4: (a, c) Bright-field TEM image of unannealed and annealed Bi_2O_2Se NS (i-iv) corresponding STEM mapping of Bi (yellow), O (green), Se (red) in each case. (b, d) STEM EDX spectra showing the atomic percentage of different elements in unannealed and annealed samples, respectively. (e) Plausible route of structural modification after annealing. Left panel: Defects present in unannealed NS. Right panel: Self-assembly of atomic layers after annealing showing defect passivation.

calculations that the formation energy of O antisite at Se vacancy (O_{Se}) is slightly higher than the Se vacancy.[53] In line with this, we found the atomic stoichiometry of unannealed NS to be $Bi_2O_{1.78}Se_{0.59}$, which reveals the possible presence of multiple point defects, such as Se vacancies (V_{Se}), oxygen vacancies (V_O), Bi antisites at Se vacancies (Bi_{Se}), interstitial oxygen, O antisites at Se vacancies (O_{Se}). By contrast, elemental mapping of the annealed Bi_2O_2Se cluster shows an improved elemental uniformity, as revealed from **Fig. 6.4c(i-iv).** In annealed Bi_2O_2Se NS, the atomic percentage of Bi, O, and Se are 50.8 %, 29.6 %, and 19.6 %, respectively, as shown in **Fig. 6.4d**. After annealing, the oxygen concentration decreases, and the Se-poor, Bi-rich conditions remain similar, although the crystallinity improves. In the unannealed sample, Bi : Se is 3.4, and in the annealed sample, the ratio decreases to 2.6 (closer to the ideal value of 2.0), indicating defect healing (Bi antisites at Se vacancy). The evolution of O : Se = 3.0 (unannealed) to 1.5 (annealed) indicates the partial removal of interstitial oxygen atoms and the passivation of O_{Se} during annealing. The changed atomic stoichiometry (from $Bi_2O_{1.78}Se_{0.59}$ in the unannealed NS to $Bi_2O_{1.17}Se_{0.77}$ in the annealed NS) suggests that Se vacancies are reduced in the annealed sample.

To better illustrate the defect healing, in **Fig. 6.4e** we present a schematic representation of the four types of defect (Bi_{Se}, O_{in}, O_{Se}, and V_{Se}) in the unannealed sample and their healing upon annealing. These defects are reduced via self-assembly and form better crystals (favorably even numbers of layers to terminate as the complete unit cells) after annealing due to built-in electrostatic interaction between the layers of Bi_2O_2Se, as shown in the right panel of **Fig. 6.4e**. In an ideal scenario, two monolayer surface with 50% Se vacancies can self-assemble through electrostatic interaction under vacuum annealing to form one Se-layer with no vacancies between two $[Bi_2O_2]^+$ layers.[54] The oxygen concentration is reduced in the annealed sample (1.17) compared with the unannealed sample (1.78), indicating partial removal of loosely bound surface oxygen during annealing, which is consistent with the XPS analysis discussed below. Due to these defects, a lower frequency Raman mode is observed for the defects at ~138.3 cm^{-1}.

To confirm our claim of intrinsic defects in the as-grown Bi_2O_2Se NS, we conducted XPS measurements on unannealed and annealed (400 °C) Bi_2O_2Se NS. The XPS spectra of Bi 4f, O 1s, Se 3d, and C 1s are presented in **Fig. 6.5(a-d),** and their deconvoluted peak positions are tabulated in **Table 6.1**. In the unannealed NS, deconvoluted Bi 4f peak positions are located at 158.1 eV (Bi $4f_{7/2}$) and 163.4 eV (Bi $4f_{5/2}$) (**Fig. 6.5a**, lower panel). In the annealed NS, the respective peak positions are at 153.2 and 163.5 eV (**Fig. 6.5b**, upper panel). The spectral shift

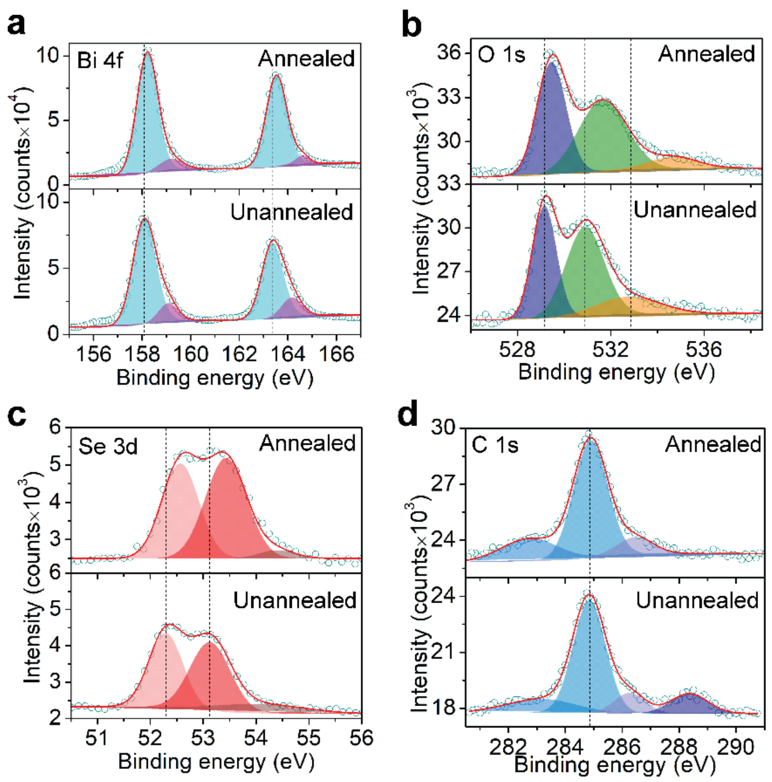

Fig. 6.5: (a-d) XPS spectra of Bi 4f, O 1s, Se 3d and C 1s, respectively, of unannealed (lower panel) and annealed (upper panel) NS.

(0.1 eV) of Bi 4f towards higher binding energy is attributed to interlayer self-assembly. In addition, the peaks centred at 159.1 eV (159.2 eV), and 164.2 eV (164.6 eV) in the unannealed (annealed) NS indicate the presence of Bi antisites at Se vacancies (**Fig. 6.5**). The lower BE of the peaks at 159.1 eV and 164.2 eV in the unannealed NS compared with the annealed NS at 159.2 eV and 164.6 eV suggests that the Bi_{Se} located at the outer surface merges and forms intra-layer Bi_{Se} after annealing (see **Fig. 6.4e** right panel). The O 1s spectra in unannealed NS are deconvoluted into three peaks located at 529.1 eV (O 1s I), 531.0 eV (O 1s II), and 532.8 eV (O 1s III), and those in the annealed NS are at 529.4 eV (O 1s I), 531.6 eV (O 1s II), and 533.6 eV (O 1s III) (**Fig. 6.5b**). The peak shifts of 0.3 eV (O 1s I), 0.6 eV (O 1s II), and 0.8 eV (O 1s III) are attributed to the self-assembly or amalgamation of layers, consistent with the Bi 4f peak shift. O 1s I is attributed to O^{2-} (lattice oxygen), and O 1s II originated from O^{-} state, indicating the presence of O_{Se} and interstitial oxygen (SeO^{-} ions).[55] Upon annealing, the intensity ratio of O 1s I and O 1s II increased from 0.78 (unannealed) to 0.98 (annealed) NS. Hence, the higher ratio of O1s I and O1s II suggests that the lattice crystallinity improves via the partial removal of interstitial (SeO^{-} ions) and O_{Se}. Although annealing decreases the oxygen-to-selenium ratio (O/Se) from 3.0 to 1.5 (as obtained via elemental analysis), atmospheric exposure before XPS measurement possibly creates an oxide layer over the NS surface, which results in an O 1s II peak in annealed NS.[56] The additional peak centred at 532.8 eV (O 1s III) may be associated with loosely bound surface oxygen, which might be integrated during the chemical reaction process.[57] The annealing process partially removes such functional groups and, consequently, the areal intensity of O 1s III decreases from 14 % (unannealed) to 7 % (annealed), consistent with the STEM analysis. To confirm the presence of loosely bonded surface oxygen, we deconvoluted the C 1s spectra with four peaks (unannealed) and three peaks (annealed), as shown in **Fig. 6.5d**. In the unannealed NS, the extra peak at 288.4 eV arises due to the chemi-adsorbed oxygen functional group (C-(O)-C).[58] The corresponding peak is absent in annealed NS, which indicates the removal of oxygen functional groups in the annealed NS. The oxygen at the top surface is integrated with the C element during the reaction process from the carbon-containing selenourea, and those oxygen functional groups are removed after annealing. In the unannealed NS, the deconvoluted Se 3d peaks are located at 52.3 eV (Se $3d_{5/2}$), 53.1 eV (Se $3d_{3/2}$), and 54.0 eV (**Fig. 6.5c**, lower panel). In the annealed NS, the respective peaks are at 52.6 eV, 53.4 eV, and 54.4 eV (**Fig. 6.5c**, upper panel). The lower binding energy of Se 3d in the unannealed NS compared with the annealed NS indicates the presence of Se-vacancies (V_{Se}) at the outer surface. In the annealed NS, the binding energy of Se 3d increases by 0.3 eV (Se $3d_{5/2}$), 0.5 eV (Se $3d_{3/2}$), and 0.4 eV, which is ascribed to inter-layer self-assembly (the outer surface of two Se layers merges and forms one Se layer and therefore the binding energy of Se 3d increases in the annealed NS), which is consistent with Bi 4f and O 1s peak shifts. Thus, the lattice crystallinity and the chemical environment of the as-synthesized NS evolve and improve after vacuum annealing.

Table 6.1: *XPS peak positions of all elements of unannealed and annealed NS.*

Element		Binding energy (eV)	
		Unannealed NS	Annealed NS
Bi 4f	Bi $4f_{7/2}$	158.1	153.2
	Bi $4f_{5/2}$	163.4	163.5
O 1s	O 1s (I)	529.1	529.4
	O 1s (II)	531.0	531.6
	O 1s (III)	532.8	533.6
Se 3d	Se $3d_{5/2}$	52.3	52.6
	Se $3d_{3/2}$	53.1	53.4
C 1s	C 1s	284.8	284.8
	C-(O)-C	288.4	absent

Furthermore, an XRD pattern was collected to investigate the phase evolution of the as-synthesized NS after annealing (200°C- 400°C). A broad peak is observed in the range of 15-35˚ for the unannealed Bi_2O_2Se NS, which is consistent with the earlier report by Ghosh et al.[18] With increasing annealing temperature (200-400°C), the characteristics XRD peaks of the tetragonal phase of Bi_2O_2Se (space group: I4/mmm) start to appear, as shown in **Fig. 6.6a**. The XRD peak positions lie at 29.1˚ (004), 31.7˚ (103), 44.3˚ (006), 46.9˚ (200), and 57.8˚ (213) for the tetragonal Bi_2O_2Se after annealing. The intensity of the XRD peak is higher for the 400 °C annealed sample. The appearance of an XRD peaks after annealing is due to defect reduction in the electrostatic layers. The positively charged surface of Bi_2O_2 and the negatively charged Se surface influence the free-standing layers to self-assemble/merge. As annealing at 400 °C yields the highest peak intensity, we carried out FETEM analysis of the sample to better understand the mechanism of defect reduction. **Fig. 6.6b** shows a low-resolution FETEM image of free-standing nanosheets of Bi_2O_2Se lying tilted on a TEM grid. To find the crystal

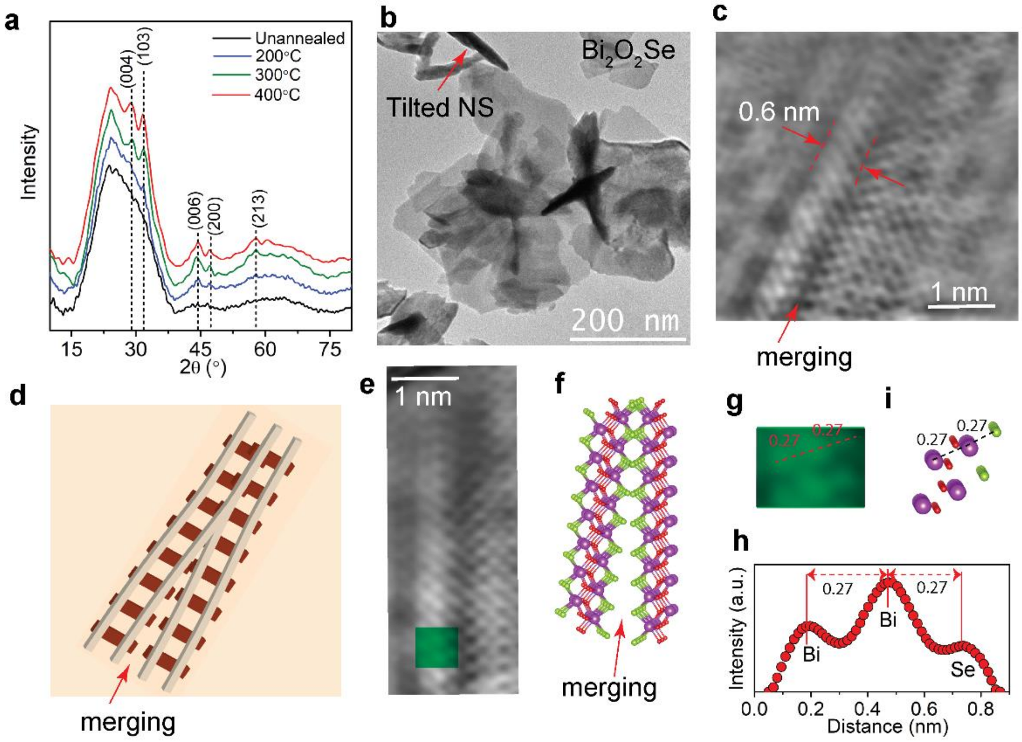

Fig. 6.6: (a) XRD pattern of Bi_2O_2Se crystals before and after annealing at different temperatures. (b) Low-resolution TEM image of free-standing Bi_2O_2Se NS after annealing. (c) Atomic resolution TEM image of tilted Bi_2O_2Se NS showing Se layers of two monolayers merge and form one Se layer. (d) The corresponding model of merging of two railway tracks resembling the present case. (e, f) experimental observation and atomic model of merging of layers. (g) Two Bi-Bi-Se rows of fig. (e) showing spacing of Bi-Bi is 0.27 nm and of Bi-Se is 0.27 nm, (h) the corresponding intensity profile along the red dotted line. (i) Atomic model of two Bi-Bi-Se rows denoting Bi-Bi distance of 0.27 nm and Bi-Se distance of 0.27 nm.

structure, atomic resolution analysis of a tilted edge of the annealed NS was carried out. The outer surface with Se layer of two Bi_2O_2Se NS merges and completes the tetragonal phase, as shown in **Fig. 6.6c**. Unlike van der Waals gap materials, in Bi_2O_2Se, 50% Se of one surface can merge with another surface and form one Se layer without having any gap within the layers.[54] Due to its symmetrical crystal structure, it can merge along the a-c plane/a-b plane/b-c plane, which enhances the possibility of quick self-merging. This resembles the merging of two railway tracks, as shown in **Fig. 6.6d**. **Fig. 6.6e** shows the merging of two monolayers as represented by the atomic model in **Fig. 6.6f**. **Fig. 6.6g** shows an expanded portion of the region highlighted in green in **Fig. 6.6e**. The experimentally observed atomic spacing of Bi-Bi for a free-standing NS is 0.27 nm, and that of Bi-Se is 0.27 nm (as shown in **Fig. 6.6h**), which matches well with the atomic structure of Bi_2O_2Se (as depicted in **Fig. 6.6i**). Therefore, we attribute the defect reduction in annealed Bi_2O_2Se to self-merging caused by the built-in electrostatic interaction. As the sample annealed at 400°C shows better crystallinity, further experiments are carried out with the 400°C-annealed sample and compared with the unannealed samples.

6.3.3. Photoresponse properties of unannealed and annealed Bi_2O_2Se NS

We measured the photoconductivity of unannealed and annealed Bi_2O_2Se nanosheets to compare their optoelectronics properties. To fabricate a two-terminal device, we drop-casted the free-standing nanosheets over commercially procured interdigitated Au electrodes. **Fig. 6.7a** shows the I-V characteristics of the unannealed NS under the dark and 808 nm laser illumination (50 mW/cm^2) under ambient conditions. Interestingly, we observe negative photoconductivity (negative PC) effect, i.e., the current under illumination is lower than the dark current. The lower inset of **Fig. 6.7a** shows a photograph of the measurement set up for measuring the transfer characteristics.

Negative PC has been observed earlier in inorganic/organic materials, and different origins of negative PC have been reported, such as the photogating effect[40, 59, 60], bolometric effect[61], and the interaction of adsorbates[42, 62]. The origin also depends on factors such as relative humidity, composition, and measuring environment (temperature, pressure). As we conducted our experiments under ambient conditions, oxygen adsorption is likely from the atmosphere. However, the STEM elemental distribution recorded under a high vacuum reveals that the oxygen concentration is higher in the unannealed NS than in the annealed NS. Therefore, oxygen adsorbates are introduced mainly during the chemical preparation of

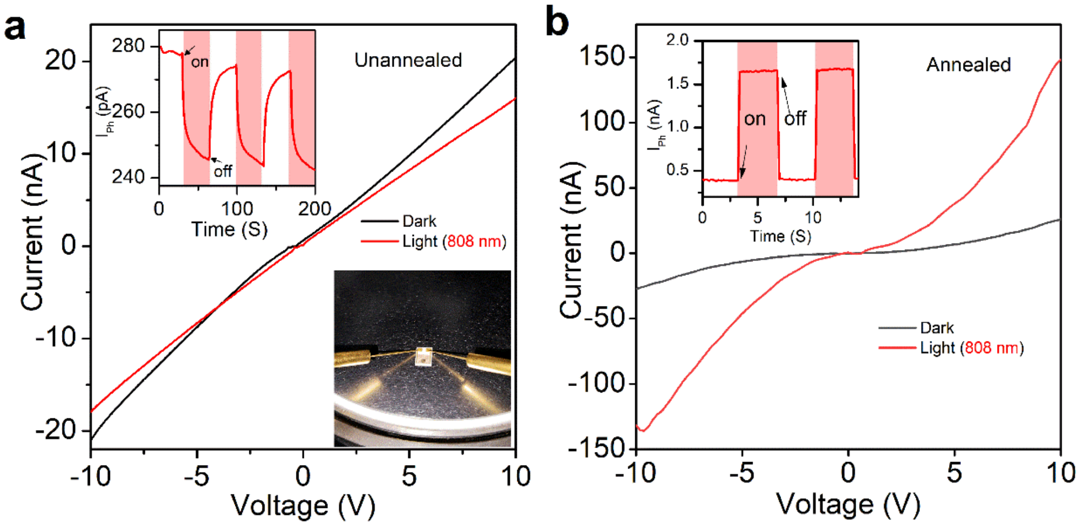

Fig. 6.7: (a) Dark and photo I-V characteristics of unannealed Bi$_2$O$_2$Se NS. The lower inset shows the photograph of microprobe system for I-V measurement. The upper inset shows the photocurrent under 808 nm excitation at 2V, showing current decreases when light is turned on implying negative photoconductivity. (b) Dark and photo I-V characteristics of annealed Bi$_2$O$_2$Se NS sample. The inset shows the positive photoconductivity under 808 nm excitation at 1 V.

Bi$_2$O$_2$Se nanosheets, instead of the ambient exposure. From the first-principle calculation, Li et al. found that interstitial O (O$_{in}$) is energetically favorable and forms SeO^{-2+q} ion (where charge state, q varies from -2 to +2).[52] We have observed O antisites at Se vacancies (O$_{Se}$) in the STEM and XPS analyses of our sample. In addition, Li et al. suggested that Se vacancy dimers of the Bi$_2$O$_2$Se surface are active adsorption sites for oxygen molecules[63], which integrate functional groups, as understood via XPS analysis (described in the preceding section). This additional oxygen can decrease the photo-carrier density and mobility of 2D Bi$_2$O$_2$Se. Therefore, the channel resistance increases significantly. Consequently, we observe lower/higher channel current/resistance before annealing.

Interestingly, after vacuum annealing, we do not observe any negative PC even under ambient conditions, which is primarily due to the reduction of defects. This is also partly due to the desorption of O$_{Se}$/O$_{in}$/oxygen molecules from the outer surface atomic layers, and the assembly of such inter-layers is consistent with atomic stoichiometry observed from the elemental analysis. The upper inset of **Fig. 6.7a** shows the unannealed device on/off current under pulsed illumination, measured at 2V. At equilibrium, under dark condition, the dark current is 277 pA. When the light is on, the current decreases slowly and reaches a value of 245 pA. The behavior of decreasing conductivity under illumination involves the trapping of extrinsic photoelectrons with a slower response time (of the order of seconds) and the dominance of traps in the material. Subsequently, when the light is 'off', the current reaches

273 pA, and, again, when the light 'on' the current reduces to 244 pA. The change of the dark current in consecutive cycles indicates the loss of intrinsic carriers trapped by defect-induced photo-gate in the highly defective unannealed Bi_2O_2Se NS-device. In addition, we found a photocurrent, I_{ph}~ 3 pA (I_{dark}-I_{light}) without any external bias (0V), which reveals the self-powered feature of the unannealed NS-based device (shown in **Fig. 6.8a**). We ascribed this self-bias behavior to defect-induced photo-gating effect.

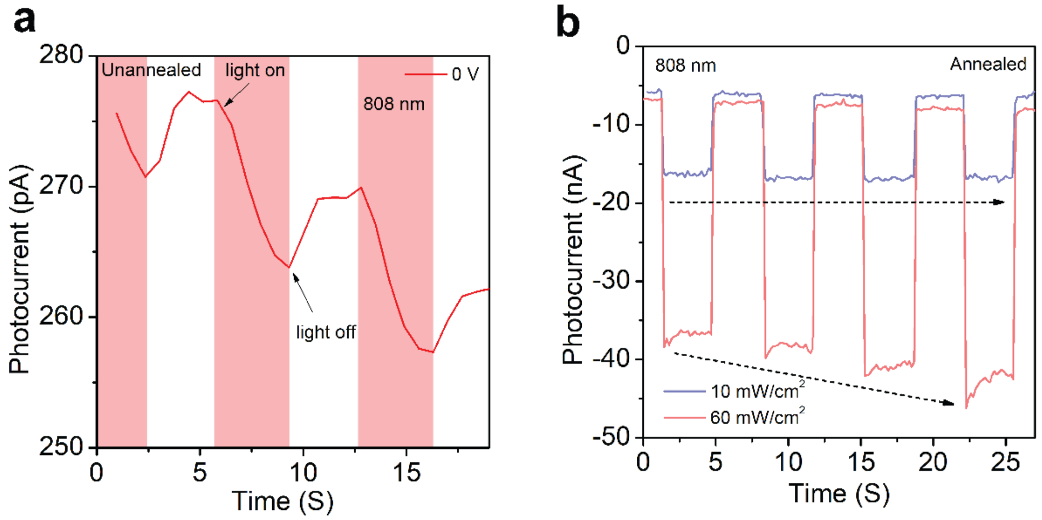

Fig. 6.8: (a) Photocurrent as a function of time at 0V for unannealed Bi_2O_2Se NS shows the self-powered feature. (b) Photocurrent as a function of time of annealed NS for two laser intensities showing the bolometric effect at a higher power.

By contrast, the device made of annealed Bi_2O_2Se exhibits positive photoconductivity under identical measuring conditions (a 808 nm laser with 50 mW/cm^2, room temperature), as shown in **Fig. 6.7b**. As revealed in our earlier analyses, the stoichiometry of bismuth oxiselenide changes after annealing, i.e., Se vacancies, O_{in}, O_{Se}, and Bi_{Se} in a unannealed NS are partly removed during annealing through inter-layer/intra-layer self-assemble/merging due to the electrostatic interaction within the Se-terminated charged surface. In the pristine sample, the photogenerated electrons are trapped by O-rich acceptor surface states act as a photo-gate. However, in an annealed sample, Se-vacancies/O_{in}/O_{Se}/Bi_{Se} were partly removed/passivated through inter/intra layer merging. Therefore, due to the reduced trapping of the carriers by the photo-gate, the photo-generated carriers escape recombination, which leads to positive photoconductivity. The inset of **Fig. 6.7b** shows the on/off cycles at 1V (low powered) in annealed Bi_2O_2Se. Under equilibrium, the dark current is 393 pA. When the light is turned on, the current increases promptly to 1644 pA. In contrast to unannealed Bi_2O_2Se, the conductivity rises upon illumination in annealed Bi_2O_2Se. And unlike unannealed Bi_2O_2Se-based device, the photocurrent (1251 pA) remains the same after the on/off cycle. However, at a high illumination intensity (50 mW/cm^2), the photocurrent increases over time (**Fig. 6.8b**). This arises due to the localized heating effect known as a bolometric effect.[24] Apparently, due to the laser light, the local temperature increases; therefore, the carrier density increases, and thus the photocurrent increases.

The mechanism of zero-biasd negative PC and biased positive PC is explained further in the unannealed and annealed Bi_2O_2Se NS. Photo-generated carriers (free electrons/holes) are the origin of photoconductivity, which is usually positive. Defects in the unannealed NS give rise to electron donor/acceptor surface states. The photo-generated electrons are trapped by the holes present at acceptor defect states for recombination. These donor/acceptor states act as localized floating gates and modulate the channel current. This phenomenon is known as the photo-gating effect.[40] Due to the presence of a floating gate, electrons can transfer from the conduction channel to the floating gate filled with holes. And due to more recombination than separation, the photocurrent decreases, which results in negative photoconductivity. A schematic of the mechanism of negative PC is illustrated in **Fig. 6.9a**. In the presence of defect-induced trap levels (E_{t1}, E_{t2}), the photocarriers (e/h) are trapped largely by those trap levels and therefore cannot take part to produce a photocurrent ('×', which symbolizes the elimination of carriers in **Fig. 6.9a**), and thus we observe negative PC. By contrast, partial removal of the defect trap levels in annealed NS results in low trapping, which creates a higher carrier separation than recombination/trapping, which causes the positive PC in the annealed NS, as

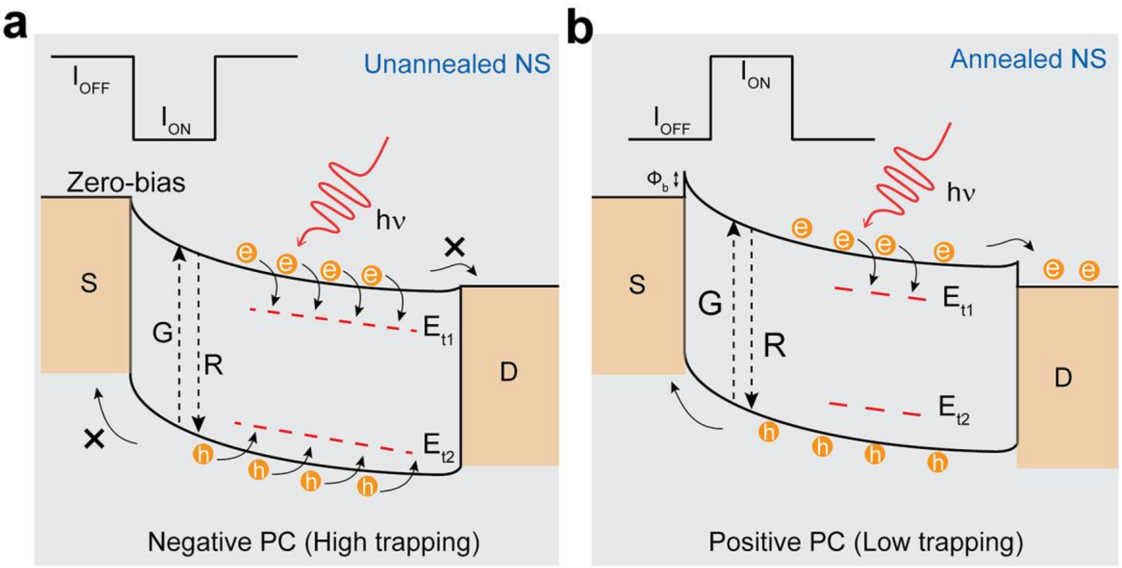

Fig. 6.9: Schematics of the mechanisms of (a) negative PC due to the high trapping of carriers in unannealed NS, and (b) positive PC in the presence of fewer traps in annealed NS.

shown in **Fig. 6.9b**. To further our understanding of the photo-gating effect in the unannealed Bi_2O_2Se device, we measured the negative PC over a prolonged period (53 min, which includes one light ON and one light OFF condition), as shown in **Fig. 6.10**. This reveals that the current under light illumination decreases monotonously and continues slowly, as monitored up to 1250 s, and when the light is turned OFF the current increases continuously and slowly (monitored up to 1950 s). Such a phenomenon of very slow change in PC is known as persistent photoconductivity (PPC), which causes a semiconductor material to remain conducive for hours/days, even without light.[64] Interestingly, in the present case, it is persistent negative photoconductivity (PNPC), which is primarily due to the presence of multiple point defects such as Bi_{Se}, V_{Se}, O_{in}, and O_{Se} in the NS. It has been reported that Bi-antisite (Bi_{Se}) defect (donor) levels occur 0.3 eV above the valence band maxima[52] and Se vacancies acting as a donor level lie below the conduction band[53], which can produce free electrons in the conduction band upon photon irradiation/thermal excitation.[45] When the light is turned on, initially, the electrons jump to the conduction band from (i) the valance band and (ii) the V_{Se}/Bi_{Se} defect donor level, which results in an initial spike in the photocurrent (shown in the inset of **Fig. 6.10**). At the same time, the presence of acceptor level created by O_{Se} and O_{in} (which stay in ionized form SeO^{-2+q} or in the form of oxygen functional groups) suppress the increase in positive PC (shown in the inset of **Fig. 6.10**) and form DX-like (D: donor, X: acceptor lattice defect) centers.

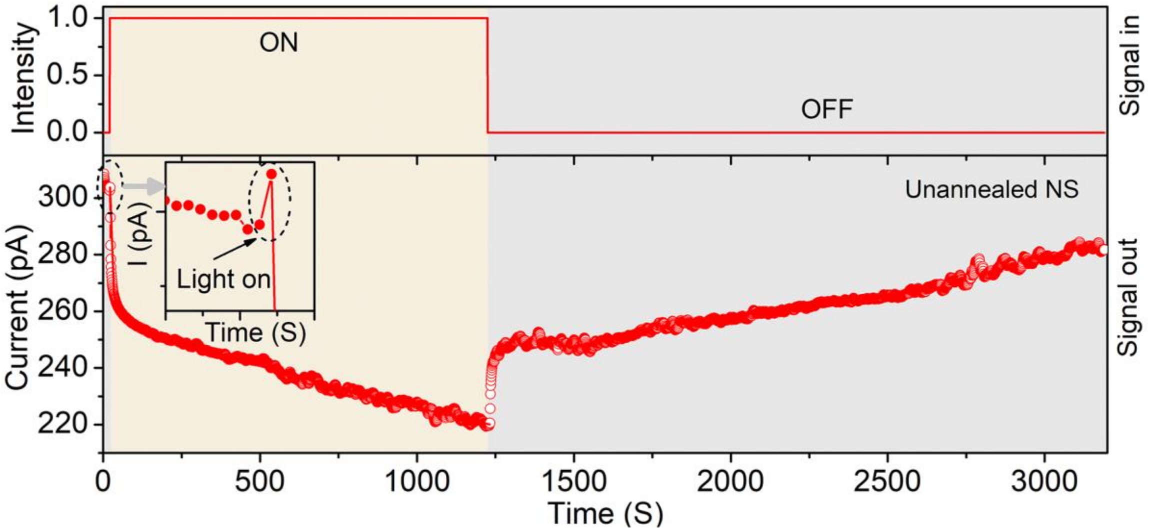

Fig. 6.10: Upper panel: the applied light pulse signal; lower panel: the output photocurrent signal, which represents the negative persistent photoconductivity effect.

The crystal defects responsible for the recombination and trapping of carriers, which reduce the free carrier density, are shown schematically in **Fig. 6.11a**. The defects, such as Bi_{Se}, and V_{Se}, are the electron donors, whereas O_{Se} is an electron acceptor. Upon photoexcitation, photogenerated carriers go through trapping as well as recombination, which is responsible for the reduction in free photocarrier density, and eventually, that reduces the photoconductivity below the dark current level, and this is dominant in the defect-rich Bi_2O_2Se NS.

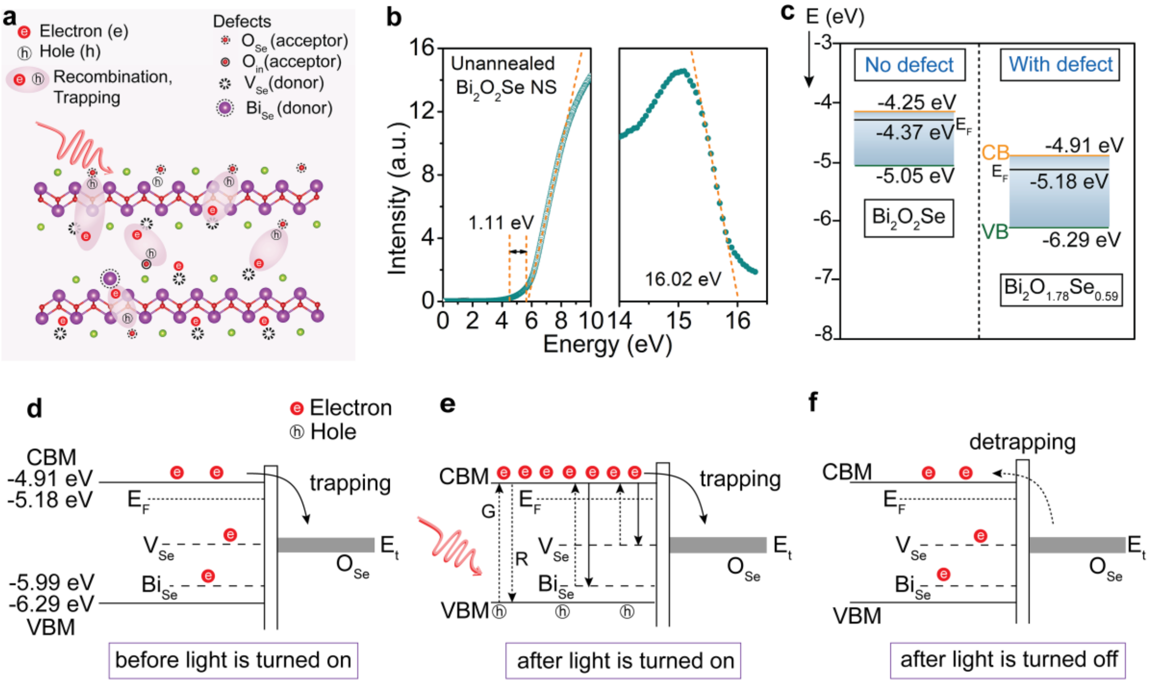

Fig. 6.11: (a) Schematic illustration showing the various kinds of crystal defect that are responsible for recombination and the trapping of carriers in unannealed Bi_2O_2Se NS, which reduces the free carrier density. (b) Ultraviolet photoelectron spectrum of unannealed Bi_2O_2Se NS showing its valence band edge (left panel) and work function (right panel). (c) Comparison of band positions for bulk Bi_2O_2Se and unannealed Bi_2O_2Se NS. (d–f) Persistent negative PC mechanism band diagrams. (d) For the trapping of free electrons from the CBM and donor levels (V_{Se}/Bi_{Se}) by trap the level (Et), resulting in a decreasing current with time before turning the light on. (e) Recombination and trapping of photo-excited electrons by the trap level (Et), and the acceptor (O_{Se}) level when the light is turned on. (f) De-trapping of the electrons after the light is turned off.

UPS measurements were carried out to construct the band diagram of unannealed and annealed NS for understanding the impact of defects on persistent negative PC. The work function and VB maximum values for unannealed NS are -5.18 eV and - 6.29 eV, respectively, which are extracted from the UPS spectrum (**Fig. 6.11b**). The bandgap the NS is found to be 1.38 eV. The band gap is higher (1.38 eV) than the bulk (~ 0.8 eV) due to few-layer thickness. Thus, the conduction band minimum is - 4.91 eV. The measured work function (-5.18 eV) of the nanosheets reveals that the Fermi level is closer to the conduction band minimum (-4.91 eV), which suggests that the nanosheets are intrinsically n-type in nature. The band diagrams of the unannealed nanosheets ($Bi_2O_{1.78}Se_{0.59}$) are drawn schematically in **Fig. 6.11b** and compared with the Bi_2O_2Se bulk. In the NS with defects, the work function is higher than for the pure Bi_2O_2Se bulk, and the Fermi level moves away from the CB, suggesting that the NS becomes less n-type, which is attributed to defect-induced trapping.[65] To explain the PNPC effect, we propose the band diagrams shown in **Fig. 6.11(d-f)** that illustrate the different processes taking place in the absence and presence of light. The band positions/alignments in **Fig. 6.11d** are drawn based on the preceding discussion. The Bi_{Se} defect level appears between the VBM and CBM (at 5.99 eV, considering that the value exists 0.3 eV above the VBM[52]), V_{Se} and O_{Se} appear between the VBM and CBM[53]. Before the light is turned on, the current decreases with time (inset of **Fig. 6.10**) due to the continuous trapping of electrons by the acceptor levels (such as, O_{Se} and O_{in}). When the light is turned on, the photogeneration (G) of carriers takes place and the donor levels (such as Bi_{Se}, V_{Se}) provide extra carriers, which initially increases the photocurrent instantaneously (inset of **Fig 6.10**). Besides the band-to-band recombination (R), the photo-excited electrons from the Bi_{Se}/V_{Se} donor level can recombine with the holes produced by O_{Se}/SeO^{-2+q} acceptor level, and thus, we see a fast decay of PC resulting in negative PC initially, and to become energetically stable, the acceptor levels trap the electrons (see **Fig. 6.11e**) further; hence we observe persistent negative photoconductivity. Next, again when the light is turned off, photo-excited electrons are not generated monotonously. However, due to the de-trapping of electrons/holes (see **Fig. 6.11f**), a persistent conductivity is observed during dark conditions after several minutes of light irradiation, and the current increases slowly (see **Fig. 6.10**). In addition, light-induced trap centers may contribute to the PNPC. To acquire any signature of light-induced trap centers, the absorption spectra are acquired for different (light) exposure times, as shown in **Fig. 6.12**. The systematic increase in effective absorption with increasing exposure time of light indicates the generation of light-induced trap centers and the absorption of photons, which are responsible for persistent negative photoconductivity. According to literature[66], three different mechanisms of PPC are proposed; i) a macroscopic barrier (MB) that is usually found in heterostructures, ii) large lattice relaxation (LLR), and iii) random-local-potential fluctuations (RLPF). Both LLR and RLPF may play some roles in the present case. RLPF may be induced by compositional fluctuations and may result in PNPC in unannealed NS.[67] However, we do not observe PPC in annealed NS, which indicates that the LLR model may dominate in the present case due to the likely formation of DX-centers in unannealed sample. In annealed samples, such DX-like centers are absent due to defect annealing/passivation. Although we do not observe persistent photoconductivity in annealed Bi_2O_2Se, the presence of defects in Se poor, Bi-rich conditions introduces photo-gating effect, and slows down the photoresponse.

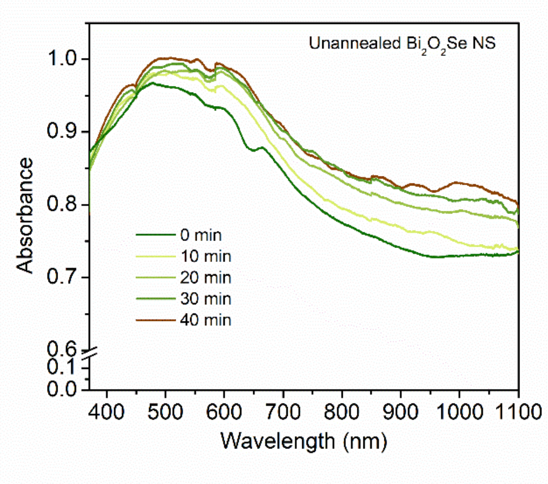

Fig. 6.12: Absorbance spectra of unannealed Bi_2O_2Se NS after different light exposure times.

To determine photo-response under different intensity of light, photocurrent has been measured and plotted as a function of light intensity. Usually, the power law $I \propto P^{\theta}$ is followed for the photocurrent (I), where P is the incident light intensity and θ measures the response capability of a photodetector. For an ideal photodetector, θ =1, as it corresponds to the linear nature. We found that unannealed Bi_2O_2Se NS exhibits θ value of 0.67 with negative PC under 808 nm (**Fig. 6.13a**). The lower θ (0.67) is attributed to the photo-gating effect as it tends to reduce the θ. In annealed Bi_2O_2Se, the logarithmic I_{ph} vs. intensity plot shows a sub-linear nature with θ values 0.54 and 0.94 under low and high intensity illumination of 808 nm, respectively, as shown in **Fig. 6.13b**. The lower θ (0.54) at the lower intensity (10-50 mW/cm^2) is ascribed to the photo-gating effect, and the higher θ (0.94) at the higher intensity illumination (50-70 mW/cm^2) is attributed to the bolometric effect (the change in resistance due to localized heating). Briefly, with high-intensity light, localized heating modulates the carrier concentration and increases the photocurrent with time/multiple on-off cycles, as shown in **Fig. 6.8b**. Interestingly, the measured θ value under 405 nm illumination is 1.01 (inset of **Fig. 6.13a**), suggesting a better photoresponse of unannealed Bi_2O_2Se NS than with 808 nm illumination. This indicates that photoelectron de-trapping is greater with 405 nm (3.06 eV) illumination due to its higher energy excitation compared with 808 nm (1.53 eV). However, for the annealed NS, θ = 0.52 under 405 nm, which is less than that with 808 nm illumination (inset of **Fig. 6.13b**), indicating the partial removal of the defect acceptor levels. These defect levels act as photo-gate and regulate the device response time.

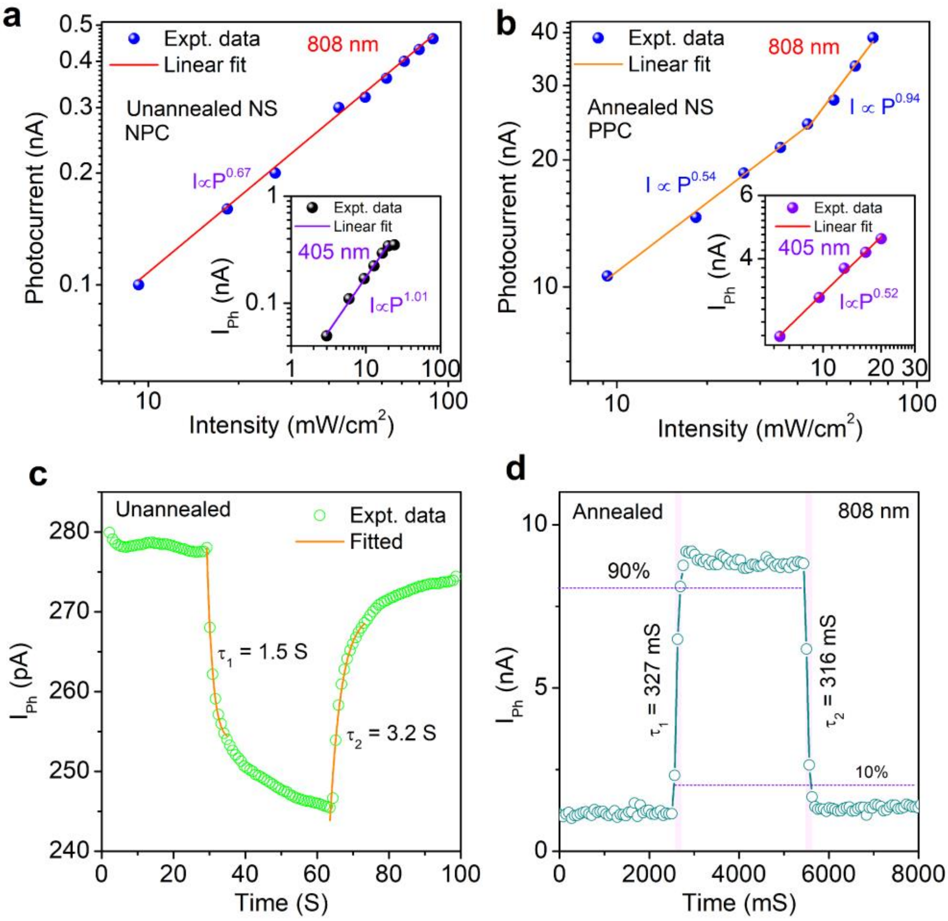

Fig. 6.13: Logarithmic plot of photocurrent vs. illuminated intensity with 808 nm laser for (a) unannealed (b) annealed Bi_2O_2Se-based photodetectors. The solid line represents the linear fitting of the power law. (c) Photocurrent response time (decay and rise) of unannealed Bi_2O_2Se photodetector under 808 nm pulsed laser. The solid line depicts the dual exponential fitting. (d) Photocurrent response time (rise and decay) of annealed Bi_2O_2Se photodetector with faster photo response.

To quantify the response time of an unannealed photodetector (**Fig. 6.13c**), a single exponential function fitting has been adopted to represent the initial decay, $I(t) = A_1 exp\left(-\frac{t}{\tau_1}\right)$, and $I'(t) = A_2\left(1 - exp\left(\frac{t}{\tau_2}\right)\right)$ for the growth of the photocurrent, where τ_1 and τ_2 are the decay and growth time constants, and A_1, and A_2 are constants, respectively. We obtain the decay (recombination) time constant of 1.5 s (τ_1) and the growth (recovery) time of 3.2 s (τ_2) under exposures at 808 nm. Note that due to the persistent current, only the initial portions of the current decay and growth are considered for the fitting. Similarly, the values are 1.4 sec (τ_1) and 1.7 sec (τ_2) under 405 nm pulsed laser.[68] For 532 nm laser illumination, the values are 1.6 sec (τ_1) and 2.0 sec (τ_2) in unannealed NS-based device.[68] Interestingly, for the annealed NS-based device, the growth and decay times are, respectively, 327 ms and 316 ms for 808 nm (**Fig. 6.13d**), 350 ms and 318 ms for 405 nm, and 343 ms and 329 ms for 532 nm, as obtained from calculating the time requirement of the maximum photocurrent increasing from 10% to 90%.[68] Hence, the response time is much faster in annealed sample with a positive PC than that with a negative PC of unannealed sample. We attribute the slower response to the photo-gating effect/trapping of free electrons by the defect state generated mainly by O_{Se}/O_{in} causes less trapping of free electrons, leading to a faster response time with positive PC. Furthermore, annealed samples exhibit a much slower response time (327/316 mS) than the CVD synthesized Bi_2O_2Se (a few milliseconds to microseconds; **Table 6.2**), which is ascribed to the higher defects, multi-grain boundaries, channel width, etc. in chemically grown NS compared with the CVD-grown Bi_2O_2Se.

Further, we studied the photoresponse properties of annealed Bi_2O_2Se to gain an insight into the photo-gating effect on it (annealed Bi_2O_2Se) and its impact on figures of merit of a photodetector (e.g., the photocurrent, responsivity, detectivity, and EQE). **Fig. 6.14a** shows the positive photocurrent at different bias voltages from -1V to -8V for the annealed NS device. Note that the current value is rescaled (multiplied with -1) and plotted in the positive y-axis. With increasing external bias, the current under light illumination (808 nm) increases with a monotonous increase in the dark current. Consistent with the I-V characteristics (**Fig. 6.7b**), the ‘dark current increase’/’higher carrier separation’ occurs due to the built-in electric field. Eventually, the current under light illumination increases while increasing the external bias voltage. In the I-V characteristics (**Fig. 6.7b**), at -8 V, the current under light illumination is 103 nA, and the dark current is 17 nA: the photocurrent is 86 nA. Nevertheless, in **Fig. 6.14a,** the current under light is 84 nA, and the dark current is 17 nA, showing a photocurrent of 67 nA with an on/off of 4.9 at -8 V. After replicated measurement, the photocurrent loss (103-84 =19 nA) might be attributed to electron-hole recombination at surface states. Photocurrent increases exponentially (inset of **fig. 6.14a**) from 1.3 nA at -1 V to 67 nA at -8V while varying bias in Au-annealed Bi_2O_2Se-Au device under pulsed 808 nm laser with an intensity of 50 mW/cm^{-2}. Furthermore, we verified the photodetection of annealed Bi_2O_2Se under 405 nm, 532 nm, and 808 nm laser at 3V external bias for measuring the photocurrent quantitively. At 3 V external bias, under 405 nm illumination the photocurrent is 2 nA (I_{on}/I_{off} = 1.3); under 532 nm illumination, it is 8 nA (I_{on}/I_{off} = 2.3), and under 808 nm, it is 34 nA (I_{on}/I_{off} = 6.4). The higher on/off ratio with 808 nm than 532 nm and 405 nm wavelength may be attributed to the lower carrier trapping due to the lower energy excitation. In addition, wavelength-dependent responsivity is extracted using the formula $R = \frac{I_{ph}}{SP}$ (where I_{ph} is the photocurrent, S is the exposed effective area under the light, P is the light intensity), as shown in **Fig. 6.14c** (left y-axis). The higher responsivity of annealed Bi_2O_2Se photodetector exhibited over the visible-to-near-IR region is ascribed to the inherent absorption and lower recombination in Bi_2O_2Se over the region (shown in **Fig. 6.14c**, right y-axis). In the wavelength region of ~750 to 850 nm, the absorption spectrum and responsivity spectrum are in parallel, indicating that most of the generated photoelectrons rake part in generating the photocurrent. However, in the low wavelength regions (~380-700 nm), more trapping of the generated photoelectron (via photo-absorption) at the defect (surface) states is consistent with the lower θ value observed at 405 nm compared with 808 nm (refer to **Fig. 6.14b**). Principally, the change in photocurrent with laser intensity is lower under 405 nm laser illumination than at 808 nm. In the case of 405 nm, the transition of electrons from the valance band to the conduction band must occur for a high

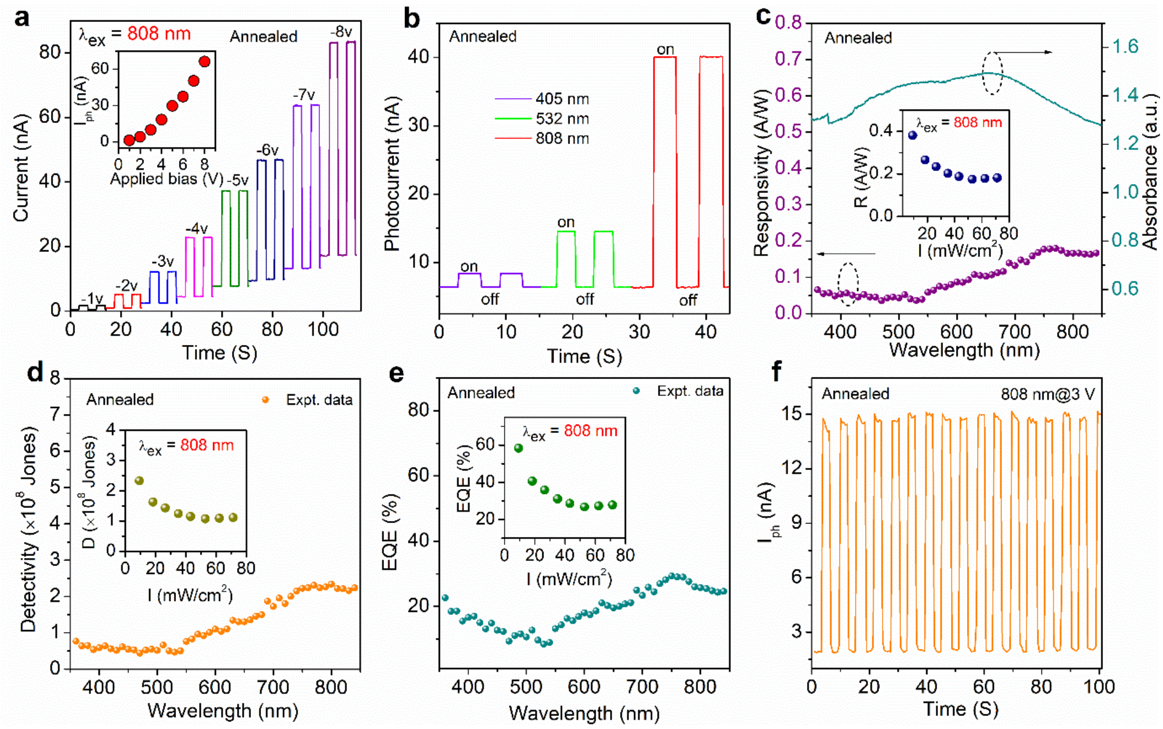

Fig. 6.14: (a) Pulsed photoconductivity of annealed Bi_2O_2Se under 808 nm excitation at different applied biases. Inset represents the photocurrent as a function of applied bias voltage. (b) On/off photocurrent of the annealed samples under 405 nm, 532 nm, and 808 nm excitations showing UV-visible to NIR photoresponse. (c) Spectral responsivity (left y-axis) and absorbance spectrum (right y-axis) of annealed Bi_2O_2Se NS. The inset shows the responsivity (R) as a function of illumination intensity at 808 nm. (d) Detectivity as a function of wavelength. The inset shows the detectivity (D) as a function of illumination intensity at 808 nm. (e) EQE as a function of wavelength. The inset shows the EQE as a function of illumination intensity at 808 nm. (f) Photocurrent response with long duration exposure to 808 nm excitation at frequency of 2 Hz of the annealed device showing the high stability of the device.

energy gap (3.06 eV) and consequently more defect (surface) states than the low energy gap (1.53 eV) are caused at 808 nm. Hence, carrier trapping is favourable under 405 excitation, which has a higher energy. Accordingly, we observe lower responsivity at lower-wavelength (higher-energy) regions even though high absorption occurs. In the visible-to-near-IR region, the responsivity varies from 35 mA/W at 470 nm to 180 mA/W at 770 nm. The responsivity is higher at a lower illumination intensity (808 nm), as shown in the inset of **Fig. 6.14c**. Furthermore, detectivity (D) is evaluated using the following formula, $D = \frac{R_\lambda}{(2qJ_d)^{1/2}}$, where R_λ and J_d represent the photoresponsivity and the dark current density of the photodetector, respectively. The detectivity of the annealed NS is found to be ~10^8 jones, as shown in **Fig. 6.14d**. The detectivity value is 0.4×10^8 Jones at 470 nm and reaches to 2.3×10^8 Jones at 800 nm. The detectivity decreases slightly with the increase in illuminating light intensity, as shown in the inset of **Fig 6.14d**. This may be attributed to the higher recombination rate and the reduction of lifetime of photogenerated carriers under strong light exposure.[69] The external quantum efficiency (EQE) value evaluates the conversion efficiency of incident photons into participating electrons involved in photocurrent. The EQE is calculated using, $EQE = \frac{hcR_\lambda}{e\lambda}$ where R_λ is the photoresponsivity at wavelength λ, and h, c and e are the Planck constant, the light velocity, and the electron charge, respectively. The wavelength-dependent EQE is shown in **Fig. 6.14e**. EQE reaches a maximum value of 29 % at 770 nm. The dependence of the EQE on the incident light intensity is shown in the inset of **Fig. 6.14e**. Furthermore, the device's on/off ratio is consistent for a long duration of light exposure, as shown in **Fig. 6.14f**. The constant photocurrent with constant dark and light currents over multiple cycles proves the good stability of the annealed NS device. Although Bi_2O_2Se NS has been utilized for high-performance photodetection earlier[13, 70] due to their inherent defect-rich electronic properties, the optoelectronics properties are sensitive to the defects. Apart from photodetector application, these defect-rich nanosheets can be potential candidate for several sensing applications, e.g., gas sensing, biosensing, non-volatile memories, and others.

Table 6.2: *Comparison of photoconductivity types with device parameters (detection wavelength, response time) found in differently synthesized* Bi_2O_2Se. τ_1 *and* τ_2 *are the rise and fall-time constants of the photocurrent in the device.*

Materials	**Synthesis process**	**Photoconductivity type**	**Illuminated wavelength (nm)**	**Response time** Rise/fall τ_1/τ_2	**Ref**
Unannealed Bi_2O_2Se	Colloidal	NPC	405 nm 532 nm 808 nm	1.4 s/1.7 s 1.6 s/2.0 s 1.5 s/3.2 s	This work
Annealed Bi_2O_2Se	Colloidal	PPC	405 nm 532 nm 808 nm	350/318 mS 343/329 mS 327/316 mS	This work
Bi_2O_2Se	CVD	PPC	808 nm	3.2/4.6 mS	[13]
Bi_2O_2Se	CVD	PPC	405 nm	62/601 μS	[71]
Bi_2O_2Se nanoribbons	CVD	PPC	650 nm	2.1/3.2 μS	[70]
Bi_2O_2Se nanowires	CVD	PPC	808 nm	4.31/4.74 mS	[72]

6.4. Conclusions

We have demonstrated an inherent photo-gating effect in defect-containing Bi_2O_2Se NS synthesized via a facile chemical reaction process. Raman, XPS, XRD, and TEM analyses reveal that the unannealed Bi_2O_2Se NS contains multiple defects ($V_{Se}/O_{in}/Bi_{Se}/O_{Se}$), which are partially removed upon vacuum annealing to improve the crystallinity via inter-layer merging due to the ubiquitous non-van der Waals characteristics of the NS. Those defects serve as photo-gate. The origin of persistent negative photoconductivity is attributed to the formation of donor-acceptor trap centers created by intrinsic defects in unannealed Bi_2O_2Se NS, and the LLR model of PPC is affirmed to dominates over the RLPFs model in the present case. The conversion of negative to positive photoconductivity is ascribed to defect passivation/partial desorption of oxygen in annealed Bi_2O_2Se. The observation of negative photoconductivity without any external bias in pristine Bi_2O_2Se, indicates potential self-bias photodetection nature, which may also be beneficial for sensing, e.g., gas sensing and biosensing. The annealed Bi_2O_2Se NS exhibits a faster response time with positive photoconductivity. The photo responsivity observed (in the vis-NIR region) shows the photo-gating effect created by defects, which play a key role in modulating the wavelength-dependent photoconductivity. Photodetectors prepared with annealed samples showed a peak responsivity of 0.4 A/W at 808 nm, which is significant. Thus, we demonstrated the interesting, defect-controlled features of chemically synthesized Bi_2O_2Se nanosheets, which can be exploited in future optoelectronics. We believe these findings shed light on the fundamentals of optoelectronics properties of novel Bi_2O_2Se and will help in the tuning of those properties for ensuing applications such as in optoelectronic synapses, optical memory, holography, and artificial intelligence.

References

1. S. Yang, F. Liu, C. Wu and S. Yang, *Small*, 2016, **12**, 4028-4047.
2. X. Liu, Q. Guo and J. Qiu, *Advanced Materials*, 2017, **29**, 1605886.
3. H. Wang, J. Guo, J. Miao, W. Luo, Y. Gu, R. Xie, F. Wang, L. Zhang, P. Wang and W. Hu, *Small*, 2022, **18**, 2103963.
4. B. Sacépé, M. Feigel'man and T. M. Klapwijk, *Nature Physics*, 2020, **16**, 734-746.
5. J. Wu, N. Wang, X. Yan and H. Wang, *Nano Research*, 2021, **14**, 1863-1877.
6. Q. Weng, G. Li, X. Feng, K. Nielsch, D. Golberg and O. G. Schmidt, *Advanced Materials*, 2018, **30**, 1801600.
7. H. Liu, Y. Du, Y. Deng and P. D. Ye, *Chemical Society Reviews*, 2015, **44**, 2732-2743.
8. C. Soldano, A. Mahmood and E. Dujardin, *Carbon*, 2010, **48**, 2127-2150.
9. L. Vicarelli, S. J. Heerema, C. Dekker and H. W. Zandbergen, *ACS Nano*, 2015, **9**, 3428-3435.
10. H. Wang, C. Li, P. Fang, Z. Zhang and J. Z. Zhang, *Chemical Society Reviews*, 2018, **47**, 6101-6127.
11. S. Kang, D. Lee, J. Kim, A. Capasso, H. S. Kang, J.-W. Park, C.-H. Lee and G.-H. Lee, *2D Materials*, 2020, **7**, 022003.
12. T. Mueller and E. Malic, *npj 2D Materials and Applications*, 2018, **2**, 29.
13. J. Li, Z. Wang, Y. Wen, J. Chu, L. Yin, R. Cheng, L. Lei, P. He, C. Jiang, L. Feng and J. He, *Advanced Functional Materials*, 2018, **28**, 1706437.
14. Y. Sun, J. Zhang, S. Ye, J. Song and J. Qu, *Advanced Functional Materials*, 2020, **30**, 2004480.
15. T. Tong, Y. Chen, S. Qin, W. Li, J. Zhang, C. Zhu, C. Zhang, X. Yuan, X. Chen, Z. Nie, X. Wang, W. Hu, F. Wang, W. Liu, P. Wang, X. Wang, R. Zhang and Y. Xu, *Advanced Functional Materials*, 2019, **29**, 1905806.
16. Y. Chen, W. Ma, C. Tan, M. Luo, W. Zhou, N. Yao, H. Wang, L. Zhang, T. Xu, T. Tong, Y. Zhou, Y. Xu, C. Yu, C. Shan, H. Peng, F. Yue, P. Wang, Z. Huang and W. Hu, *Advanced Functional Materials*, 2021, **31**, 2009554.
17. U. Khan, Y. Luo, L. Tang, C. Teng, J. Liu, B. Liu and H.-M. Cheng, *Advanced Functional Materials*, 2019, **29**, 1807979.
18. T. Ghosh, M. Samanta, A. Vasdev, K. Dolui, J. Ghatak, T. Das, G. Sheet and K. Biswas, *Nano Letters*, 2019, **19**, 5703-5709.
19. D. Vrushabendrakumar, H. Rajashekhar, S. Riddell, A. P. Kalra, K. M. Alam and K. Shankar, *Nanotechnology*, 2021, **32**, 485602.
20. X. Pang, Y. Zhao, X. Gao, G. Wang, H. Sun, J. Yin and J. Zhu, *Chinese Chemical Letters*, 2021, **32**, 3099-3104.
21. A. Bora, S. Paul, M. T. Hossain and P. K. Giri, *The Journal of Physical Chemistry C*, 2022, **126**, 12623-12634.
22. U. Khan, L. Tang, B. Ding, L. Yuting, S. Feng, W. Chen, M. J. Khan, B. Liu and H.-M. Cheng, *Advanced Functional Materials*, 2021, **31**, 2101170.

23. H. Xie, M. Liu, B. You, G. Luo, Y. Chen, B. Liu, Z. Jiang, P. K. Chu, J. Shao and X.-F. Yu, *Small*, 2020, **16**, 1905208.
24. H. Yang, C. Tan, C. Deng, R. Zhang, X. Zheng, X. Zhang, Y. Hu, X. Guo, G. Wang, T. Jiang, Y. Zhang, G. Peng, H. Peng, X. Zhang and S. Qin, *Small*, 2019, **15**, 1904482.
25. J. Sun, M. Hu, C. Zhang, L. Bai, C. Zhang and Q. Wang, *Advanced Functional Materials*, 2022, **32**, 2209000.
26. F. Yang, R. Wang, W. Zhao, J. Jiang, X. Wei, T. Zheng, Y. Yang, X. Wang, J. Lu and Z. Ni, *Applied Physics Letters*, 2019, **115**, 193103.
27. M. T. Hossain and P. K. Giri, *Journal of Applied Physics*, 2021, **129**, 175102.
28. J. Wu, C. Qiu, H. Fu, S. Chen, C. Zhang, Z. Dou, C. Tan, T. Tu, T. Li, Y. Zhang, Z. Zhang, L.-M. Peng, P. Gao, B. Yan and H. Peng, *Nano Letters*, 2019, **19**, 197-202.
29. C. Chen, M. Wang, J. Wu, H. Fu, H. Yang, Z. Tian, T. Tu, H. Peng, Y. Sun, X. Xu, J. Jiang, N. B. M. Schröter, Y. Li, D. Pei, S. Liu, S. A. Ekahana, H. Yuan, J. Xue, G. Li, J. Jia, Z. Liu, B. Yan, H. Peng and Y. Chen, *Science Advances*, **4**, eaat8355.
30. J.-M. Yan, J.-S. Ying, M.-Y. Yan, Z.-C. Wang, S.-S. Li, T.-W. Chen, G.-Y. Gao, F. Liao, H.-S. Luo, T. Zhang, Y. Chai and R.-K. Zheng, *Advanced Functional Materials*, 2021, **31**, 2103982.
31. J. Yu, Y. Han, H. Zhang, X. Ding, L. Qiao and J. Hu, *Advanced Materials*, 2022, **34**, 2204227.
32. R. J. Chen, N. R. Franklin, J. Kong, J. Cao, T. W. Tombler, Y. Zhang and H. Dai, *Applied Physics Letters*, 2001, **79**, 2258-2260.
33. X. Zhang, J. Jie, Z. Wang, C. Wu, L. Wang, Q. Peng, Y. Yu, P. Jiang and C. Xie, *Journal of Materials Chemistry*, 2011, **21**, 6736-6741.
34. Y. Yang, X. Peng, H.-S. Kim, T. Kim, S. Jeon, H. K. Kang, W. Choi, J. Song, Y.-J. Doh and D. Yu, *Nano Letters*, 2015, **15**, 5875-5882.
35. P.-C. Wei, S. Chattopadhyay, M.-D. Yang, S.-C. Tong, J.-L. Shen, C.-Y. Lu, H.-C. Shih, L.-C. Chen and K.-H. Chen, *Physical Review B*, 2010, **81**, 045306.
36. S. Paul, M. T. Hossain, A. K. Mia and P. K. Giri, *ACS Applied Nano Materials*, 2021, **4**, 12527-12540.
37. C. H. Lui, A. J. Frenzel, D. V. Pilon, Y. H. Lee, X. Ling, G. M. Akselrod, J. Kong and N. Gedik, *Physical Review Letters*, 2014, **113**, 166801.
38. A. S. Chaves and H. Chacham, *Applied Physics Letters*, 1995, **66**, 727-729.
39. N. K. Tailor, C. A. Aranda, M. Saliba and S. Satapathi, *ACS Materials Letters*, 2022, **4**, 2298-2320.
40. B. Cui, Y. Xing, J. Han, W. Lv, W. Lv, T. Lei, Y. Zhang, H. Ma, Z. Zeng and B. Zhang, *Chinese Physics B*, 2021, **30**, 028507.
41. A. I. Yakimov, A. V. Dvurechenskii, A. I. Nikiforov, O. P. Pchelyakov and A. V. Nenashev, *Physical Review B*, 2000, **62**, R16283-R16286.
42. A. Grillo, E. Faella, A. Pelella, F. Giubileo, L. Ansari, F. Gity, P. K. Hurley, N. McEvoy and A. Di Bartolomeo, *Advanced Functional Materials*, 2021, **31**, 2105722.
43. N. K. Tailor, P. Maity and S. Satapathi, *ACS Photonics*, 2021, **8**, 2473-2480.
44. Y. Yuan, Q. Yao, J. Zhang, K. Wang, W. Zhang, T. Zhou, H. Sun and J. Ding, *Physical Chemistry Chemical Physics*, 2020, **22**, 14276-14283.
45. M. A. Haque, J.-L. Li, A. L. Abdelhady, M. I. Saidaminov, D. Baran, O. M. Bakr, S.-H. Wei and T. Wu, *Advanced Optical Materials*, 2019, **7**, 1900865.
46. K. Xu, B. Y. Zhang, M. Mohiuddin, N. Ha, X. Wen, C. Zhou, Y. Li, G. Ren, H. Zhang, A. Zavabeti and J. Z. Ou, *Nano Today*, 2021, **37**, 101096.
47. Z. Ma, P. Huang, J. Li, P. Zhang, J. Zheng, W. Xiong, F. Wang and X. Zhang, *npj Computational Materials*, 2022, **8**, 51.
48. L. Gogoi, W. Gao, P. M. Ajayan and P. Deb, *Physical Chemistry Chemical Physics*, 2023, **25**, 1430-1456.
49. J. Wu, C. Tan, Z. Tan, Y. Liu, J. Yin, W. Dang, M. Wang and H. Peng, *Nano Letters*, 2017, **17**, 3021-3026.

50. T. Cheng, C. Tan, S. Zhang, T. Tu, H. Peng and Z. Liu, *The Journal of Physical Chemistry C*, 2018, **122**, 19970-19980.
51. J. Zhang, Z. Peng, A. Soni, Y. Zhao, Y. Xiong, B. Peng, J. Wang, M. S. Dresselhaus and Q. Xiong, *Nano Letters*, 2011, **11**, 2407-2414.
52. H. Li, X. Xu, Y. Zhang, R. Gillen, L. Shi and J. Robertson, *Scientific Reports*, 2018, **8**, 10920.
53. Q. Wei, C. Lin, Y. Li, X. Zhang, Q. Zhang, Q. Shen, Y. Cheng and W. Huang, *Journal of Applied Physics*, 2018, **124**, 055701.
54. Q. Wei, R. Li, C. Lin, A. Han, A. Nie, Y. Li, L.-J. Li, Y. Cheng and W. Huang, *ACS Nano*, 2019, **13**, 13439-13444.
55. L. Q. Wu, Y. C. Li, S. Q. Li, Z. Z. Li, G. D. Tang, W. H. Qi, L. C. Xue, X. S. Ge and L. L. Ding, *AIP Advances*, 2015, **5**, 097210.
56. M. Gao, W. Wei, T. Han, B. Li, Z. Zeng, L. Luo and C. Zhu, *ACS Applied Materials & Interfaces*, 2022, **14**, 15370-15380.
57. S. Gandla, S. R. Gollu, R. Sharma, V. Sarangi and D. Gupta, *Applied Physics Letters*, 2015, **107**, 152102.
58. R. Das, S. Parveen, A. Bora and P. K. Giri, *Carbon*, 2020, **160**, 273-286.
59. H. Zhang, H. Li, F. Wang, X. Song, Z. Xu, D. Wei, J. Zhang, Z. Dai, Y. Ren, Y. Ye, X. Ren and J. Yao, *ACS Applied Electronic Materials*, 2022, **4**, 5177-5183.
60. Y. Han, X. Zheng, M. Fu, D. Pan, X. Li, Y. Guo, J. Zhao and Q. Chen, *Physical Chemistry Chemical Physics*, 2016, **18**, 818-826.
61. J. Miao, B. Song, Q. Li, L. Cai, S. Zhang, W. Hu, L. Dong and C. Wang, *ACS Nano*, 2017, **11**, 6048-6056.
62. C. Biswas, F. Güneş, D. D. Loc, S. C. Lim, M. S. Jeong, D. Pribat and Y. H. Lee, *Nano Letters*, 2011, **11**, 4682-4687.
63. T. Li and H. Peng, *Accounts of Materials Research*, 2021, **2**, 842-853.
64. S. Jeon, S.-E. Ahn, I. Song, C. J. Kim, U. I. Chung, E. Lee, I. Yoo, A. Nathan, S. Lee, K. Ghaffarzadeh, J. Robertson and K. Kim, *Nature Materials*, 2012, **11**, 301-305.
65. L.-Y. Dang, M. Liu, G.-G. Wang, D.-Q. Zhao, J.-C. Han, J.-Q. Zhu and Z. Liu, *Advanced Functional Materials*, 2022, **32**, 2201020.
66. A. Sumanth, K. Lakshmi Ganapathi, M. S. Ramachandra Rao and T. Dixit, *Journal of Physics D: Applied Physics*, 2022, **55**, 393001.
67. H. X. Jiang and J. Y. Lin, *Physical Review B*, 1989, **40**, 10025-10028.
68. M. T. Hossain, T. Jena, S. Debnath and P. K. Giri, *Journal of Materials Chemistry C*, 2023, DOI: 10.1039/D3TC01129A.
69. M. Yu, C. Fang, J. Han, W. Liu, S. Gao and K. Huang, *ACS Applied Materials & Interfaces*, 2022, **14**, 13507-13515.
70. Y. Wei, C. Chen, C. Tan, L. He, Z. Ren, C. Zhang, S. Peng, J. Han, H. Zhou and J. Wang, *Advanced Optical Materials*, 2022, **n/a**, 2201396.
71. M. T. Hossain, M. Das, J. Ghosh, S. Ghosh and P. K. Giri, *Nanoscale*, 2021, **13**, 14945-14959.
72. J. Li, Z. Wang, J. Chu, Z. Cheng, P. He, J. Wang, L. Yin, R. Cheng, N. Li, Y. Wen and J. He, *Applied Physics Letters*, 2019, **114**, 151104.

Chapter 7

Summary and Outlook

This chapter summarizes the whole thesis highlighting the key findings on newly emerged nvdW 2D Bi_2O_2Se and their future scopes for further fundamental studies and multifunctional applications.

7.1. Summary and Highlights of Thesis

We have systematically investigated the CVD and chemical growth of 2D nvdW Bi_2O_2Se and its structural, optical, electrical, and thermal properties, including photodetector applications. CVD-growth of ultrathin Bi_2O_2Se has been optimized for controlled growth, and ultrathin layers are exploited for finding in-plane thermal conductivity through an optical technique (Chapter 2). Optical properties are thoroughly studied on CVD-grown Bi_2O_2Se on arbitrary growth substrates, and interestingly we observe room temperature exciton formation established through the spectroscopic studies and theoretical calculations (Chapter 3). Hybrid integration of 2D Bi_2O_2Se with $CsPbBr_3$ NC has been exploited for understanding interfacial charge transfer and its application in superior photodetection (Chapter 4). Layer by Layer stacking of vdW MoS_2 (monolayer) and nvdW Bi_2O_2Se has been constructed to investigate photo-induced charge transfer at the atomically sharp 2D interface (Chapter 5). Finally, free-standing ultrathin nanosheets of Bi_2O_2Se are chemically synthesized for photoconductivity study that discovers unexplored physical phenomenon (negative PPC) in highly defective Bi_2O_2Se (Chapter 6).

The significant contributions of the thesis are listed below.

A. Temperature-dependent Raman studies and Thermal conductivity of direct CVD grown non-van der Waals layered Bi_2O_2Se

We demonstrated the controlled CVD growth of 2D ultrathin Bi_2O_2Se with high structural and chemical uniformity despite its challenging growth on the mica substrate due to the weak electrostatic interaction among the layers. The growth temperature is tuned to obtain ultra-smooth single crystals of few-layer Bi_2O_2Se. Temperature-dependent (78 - 293 K) Raman studies reveal that the A_{1g} phonon mode of Bi_2O_2Se varies linearly with the temperature with a first-order temperature coefficient (α) of $-0.017\ 87 \pm 0.0011$ $cm^{-1}K^{-1}$. The in-plane thermal conductivity is estimated to be ~1.6 W/mK, which is significantly low compared to graphene

(~4840 W/mK) and other 2D materials. It demonstrates the potential of 2D Bi_2O_2Se as a suitable thermoelectric material. The results of this chapter elucidate the CVD growth of ultrathin Bi_2O_2Se on mica substrate and develop insights into electron-phonon and phonon-phonon interactions in nvdW 2D materials. *This work has been published in "J. Appl. Phys. 129, 175102 (2021)".*

B. Room Temperature Exciton Formation and Robust Optical Properties of CVD-Grown Ultrathin Bi_2O_2Se Crystals on Arbitrary Substrates

We demonstrate the CVD growth of ultrathin Bi_2O_2Se on various substrates (mica, sapphire, SiO_2, quartz, glass) and its impact on structural and optoelectronic properties, including morphology, lattice strain, optical bandgap, and photo-carrier dynamics. Through careful analysis, we discover the formation of multiple excitons, even at room temperature, resulting in broadband absorption and PL in the visible to near-infrared (NIR) region in nvdW Bi_2O_2Se. These results are significant for developing nvdW Bi_2O_2Se for ensuing applications. *This work has been published in "Nanoscale 15, 11222-11236 (2023)".*

C. Interfacial Charge Transfer in the CVD-grown $Bi_2O_2Se/CsPbBr_3$ Nanocrystal Heterostructure and its Exploitation in Superior Photodetection

We investigated interfacial charge transfer dynamics in the $Bi_2O_2Se/CsPbBr_3$ hybrid structure. Here, we integrated $CsPbBr_3$ nanocrystals (a high light-harvesting perovskite) on top of a few-layer Bi_2O_2Se nanosheet (a superior electron mobility material) for efficient charge separation and broadband photodetection. The band alignment reveals a type-I heterojunction, and the device under illumination and reverse bias display a fast response time of 12 µs/24 µs (rise time/fall time) and an improved responsivity in the 390 to 840 nm range due to the effective interfacial charge transfer and efficient interlayer coupling at the $Bi_2O_2Se/CsPbBr_3$ interface. A photodetector with a better light on/off ratio and a peak responsivity of $\sim 10^3$ AW^{-1} was achieved in the $Bi_2O_2Se/CsPbBr_3$ hybrid photodetector due to the synergistic effects in the hybrid structure under ambient conditions. The DFT analysis of the density of states and charge density plots in the hybrid structure revealed a net transfer of electrons from perovskite nanocrystals to Bi_2O_2Se layers and additional density of states in Bi_2O_2Se. These results are significant for developing nvdW hybrid structure-based high-performance, low-powered photodetectors. *This work has been published in "Nanoscale 13, 14945 – 14959 (2021)".*

D. Interlayer Charge-Transfer-Induced Photoluminescence Quenching and Enhanced Photoconduction in Two-Dimensional Bi_2O_2Se/MoS_2 Type-II Heterojunction

We demonstrate layer-by-layer stacking of a vdW 2D MoS_2 (monolayer) on a nvdW Bi_2O_2Se layer and study the interlayer electron-phonon coupling and charge transfer across the hetero-layer interface. The unique combination of nvdW 2D Bi_2O_2Se and vdW MoS_2 hetero-layer interface offers significant photogenerated charge transfer due to the favorable type-II band alignment via forming a p-n junction. Low-temperature PL studies reveal that the robust interlayer coupling between the hetero-layers enhances the charge transfer process. Our study reveals that upon photoexcitation, the trion-phonon coupling is stronger than the exciton-phonon coupling in the heterogeneous system. These results are significant for understanding the interaction between vdW and nvdW 2D heterostructures and further exploration of such vdW/nvdW 2D heterostructures in future optoelectronic applications. *This work has been published in "ACS Appl. Nano Mater. (2023) DOI: 10.1021/acsanm.3c00759".*

E. Defect-Induced Photogating Effect and its Modulation in Ultrathin Free-standing Bi_2O_2Se Nanosheets with Visible to Near-Infrared Photoresponse

We studied the structural/optoelectronic properties of ultrathin Bi_2O_2Se nanocrystals synthesized via a chemical reaction process (colloidal synthesis). It provides the scalable and rapid synthesis of free-standing Bi_2O_2Se nanosheets with controllable defects. Vacuum annealing is a simple but effective way to control intrinsic defects of Bi_2O_2Se. Interestingly, we found an unusual physical phenomenon: self-powered negative persistent photoconductivity (negative PPC) in highly defective Bi_2O_2Se and positive photoconductivity (positive PC) in annealed/less defective Bi_2O_2Se. The origin of conversion from negative PPC to positive PC is the defect-induced photo-gating effect in ultrathin Bi_2O_2Se nanosheets. The observation of negative PPC in Bi_2O_2Se is novel. The intrinsic defect-induced photo-gating effect plays a significant role in tuning the electronic properties of chemically synthesized Bi_2O_2Se. Besides being a superior optoelectronic material, the inherent defects and further structural tuning via vacuum annealing in Bi_2O_2Se can profoundly affect its transport properties, which are fundamental to electronic devices. These findings shed light on the next-generation novel Bi_2O_2Se-based electronics devices. *This work has been published in "J. Mater. Chem. C, 11, 6670-6684 (2023)".*

7.2. Future scopes

In the present thesis, we have demonstrated the controlled growth of ultrathin Bi_2O_2Se and integrated them with perovskite nanocrystals, monolayer MoS_2 for optoelectronic properties, and broadband photodetection. However, the development of 2D Bi_2O_2Se is at a preliminary stage compared to graphene and other 2D materials; many more opportunities exist to explore 2D Bi_2O_2Se. A few of the scopes are listed below,

1. Ultrathin Bi_2O_2Se exhibits ultralow lattice thermal conductivity, enabling the scope for studying the thermoelectric properties of 2D-Bi_2O_2Se.
2. 2D Bi_2O_2Se could be used for high-performance photovoltaic devices due to low exciton binding energy with multiple exciton generations, as established in Chapter 3.
3. Heterostructuring with other 0D/1D/2D materials like perovskites, GO, TMD, Black phosphorus, h-BN, and Mxene could tune their photoelectrical properties to enable high-performance Bi_2O_2Se-based devices.
4. The defect-rich Bi_2O_2Se nanosheets could be utilized for applications like gas sensing, biosensing, non-volatile memories, etc. Defects (e.g., Se vacancies) in Bi_2O_2Se nanosheets enable the adsorption of foreign molecules, rendering the scope for gas sensing or biosensing. In addition, functionalizing them with carbon dots and metal nanoparticles may be advantageous for highly selective sensors. The defect-rich Bi_2O_2Se exhibits negative persistent photoconductivity and ferroelectric properties, which suggest its applicability in memory devices.
5. Since 2D Bi_2O_2Se possesses electronic properties comparable to matured silicon, the 2D Bi_2O_2Se could be an alternative for next-generation optoelectronics, energy storage, and other applications.